

# LINEAR AND NONLINEAR GLOBAL GYROKINETIC STUDY OF MICROINSTABILITIES IN TOKAMAKS

By  
**Jugal Chowdhury**

INSTITUTE FOR PLASMA RESEARCH, BHAT, GANDHINAGAR,  
GUJARAT, INDIA

A thesis submitted to the  
Board of Studies in Physical Sciences

In partial fulfillment of the requirements

For the Degree of

**DOCTOR OF PHILOSOPHY**

*of*

**HOMI BHABHA NATIONAL INSTITUTE**



September 2011

# Homi Bhabha National Institute

## Recommendations of the Viva Voce Board

As members of the Viva Voce Board, we recommend that the dissertation prepared by **Jugal Chowdhury** entitled “**Linear and Nonlinear Global Gyrokinetic Study of Microinstabilities in Tokamaks**” may be accepted as fulfilling the dissertation requirement for the Degree of Doctor of Philosophy.

----- Date :25/01/2012  
External Examiner: Prof. Avinash Khare  
Delhi University, Delhi, India

----- Date :25/01/2012  
Chairman : Prof. Predhiman Krishan Kaw  
Institute for Plasma Research  
Bhat, Gandhinagar-382428, India

----- Date :25/01/2012  
Convener (Guide): Dr. Rajaraman Ganesh  
Institute for Plasma Research  
Bhat, Gandhinagar-382428, India

----- Date :25/01/2012  
Member : Prof. Abhijit Sen  
Institute for Plasma Research  
Bhat, Gandhinagar-382428, India

----- Date :25/01/2012  
Member : Prof. Amita Das  
Institute for Plasma Research  
Bhat, Gandhinagar-382428, India

----- Date :25/01/2012

Member : Dr. Sudip Sengupta  
Institute for Plasma Research  
Bhat, Gandhinagar-382428, India

----- Date :25/01/2012

Dean Academics : Dr. Subroto Mukherji  
Institute for Plasma Research  
Bhat, Gandhinagar-382428, India

Final approval and acceptance of this dissertation is contingent upon the candidate's submission of the final copies of the dissertation to HBNI.

I hereby certify that I have read this dissertation prepared under my direction and recommend that it may be accepted as fulfilling the dissertation requirement.

----- Date :25/01/2012

Guide : Dr. Rajaraman Ganesh  
Institute for Plasma Research  
Bhat, Gandhinagar 382428, India

## CERTIFICATION FROM GUIDE

This is to certify that the corrections as suggested by the Referees in the thesis evaluation report have been incorporated in the copy of the thesis submitted to HBNI.

Dr. Rajaraman Ganesh  
Guide

Date: 25/01/2012.

## DECLARATION

I, hereby declare that the investigation presented in the thesis has been carried out by me. The work is original and the work has not been submitted earlier as a whole or in part for a degree/diploma at this or any other Institution or University.

Jugal Chowdhury

## STATEMENT BY AUTHOR

The dissertation has been submitted in partial fulfilment of requirements for a Ph.D. degree at Homi Bhabha National Institute (HBNI) and is deposited in the library to be made available to borrowers under rules of HBNI.

Brief quotations from this dissertation are allowable without special permission, provided that proper acknowledgement of source is made. Requests for permission for extended quotation from or reproduction of this manuscript in whole or in part may be granted by the competent authority of HBNI when in his/her judgement the proposed use of the material is in the interest of scholarship. In all other instances, however, permission must be obtained from the author.

Jugal Chowdhury

To Maa-Deuta.....

## ACKNOWLEDGEMENTS

At the very outset, I convey my hearty gratitude to my thesis supervisor Dr. Rajaraman Ganesh. His diligent support and guidance from the initial phase of my work to date have been the source of inspiration for me. I must not forget his care and the way he nurtured me during this long endeavor. His enthusiasm, availability for discussion at any time and friendly nature have made my journey easier. I am also thankful to him for providing me enough independence during my work. I will remain indebted to him for involving me in couple of fruitful collaborations.

I am obliged to Prof. P. K. Kaw, Prof. Abhijit Sen, Prof. Amita Das, and Dr. Sudip Sengupta for consenting to be my doctoral committee members. I always feel privileged to have them in my doctoral committee. Their critiques during my yearly reviews have helped enormously to improve my work.

I would like to thank Dr P. Vasu, Dr. R. Ganesh, Dr, P. Chattopadhyay, Dr. R. Srinivasan, Dr. S. Sengupta, Dr. D. Raju, Prof. R. Jha, Dr. S. Chaturvedi, Prof. Amita Das, Dr. Manoj Warriar, Dr. S. K. Pathak, Dr. S. Deshpande, Dr. S. Pradhan, Dr. D. Ahalpara, and Prof. D. Bora for their endurance while teaching us during the first year course work.

Many other people remain the source of motivation during this period. Dr. Subroto Mukherjee, Dr. N. Ramshubramanian (Mani), Dr. Joydeep Ghosh, Dr. Rajiv Goswami, Dr. Devendra Sharma, and Dr. Sambaran Pahari are among them.

I am indebted to my collaborators from CRPP-EPFL, Dr. Stephan Brunner and Prof. Laurent Villard for their advice and guidance. I thank Dr. Xavier Lapillonne for helping me learn the code GENE. I appreciate the numerous help of Edith Grueter and Dr. Sudheer Jawla during my stay at CRPP-EPFL.

I also owe the people in PPPL; Dr. Weixing Wang for giving me an opportunity to work with him, Dr. Stephane Ethier for his numerical help and Dr. Janardhan Manickam for giving his valuable time discussing various physics and other issues. Many thanks are due to Dr. W. W. Lee for his warm and friendly nature towards me. Special thanks go to Jennifer Jones for her nice arrangement of my accommodation and sustenance without which my stay at PPPL would not have been so

pleasant one.

The library staff, computer staff and administrative staff of IPR have always remained cooperative. I convey my thanks to Mrs. Sutapa Ranjan, Mr. Shailendra Trivedi, Mr. Arvind Singh, Mr. Hemant Joshi, Mr. Gaurav Garg, Mr. Saroj Das, Mr. Shravan Kumar, Ms. Smita Parmar, Mrs. Arundhati Das, Mr. M. Sourabhan, Mr. M. H. Vartak, Mr. H. K. Sharmah, Mr. H. C. Khanduri, Mr. Hitesh Mehta, Mr. Dinesh Nair, Mr. Silel Shah, and Ms. Shirin Bhesania for their help in numerous occasions.

I can not forget the warm, cordial and friendly ambience in the hostel. Greetings and best wishes to my dear Jyotirmoy Pramanik, Pintu Banerjee (Bubaida), Niraj Jain, Shyama Mukherjee, Ritu Dey, Suraj Sinha, Manash Paul, Rajneesh Yadav, Anand Srivastav, Santosh Dhanpat, Bhaskar Choudhury, Vijay Srivastav, Anurag Mishra, Surendra Prasad, Vikrant, Kishor, Maya, Subhash, Satya, Sharad, Shekar, Sunita, Puraram, Kshitish, Deepak, Vikram, Prabal, Ashwin, Ujjwal, Sita, Tayyab, Rameswar, Sushil, Sanat, Pravesh, Shayak, Manjit, Sauman, Aditya, Iliyas, and Vikram Pensia Singh Dharodi. I will miss you people a lot!

I take this opportunity to thank my teachers during my M.Sc., especially, Dr. Buddhadeb Bhattacharjee, Dr. Bosanta Ranjan Baruah and Dr. Pratyush Purakayastha for their encouragement and for motivating me to pursue further studies in the field of Physics.

When I look back through my academic carrier I see many other people who always encourage me and wish me the best. Mr. Siva Mohan Bhuyan, Dr. Bhagirath Handique, Dr. Chandra Chutia, and Dr. Jiten Dutta are among them.

My friends Simanta Hazarika, Debananda Phukan, Pranjal Mahanta, and Uday Sankar Senapati need a special mention here for being by my side always.

Rameswar has spent his valuable time in proofreading the draft. Thanks a lot to him.

Finally, my heartfelt gratitude to my parents and family for their goodwill and support all through my life.

**Jugal Chowdhury**

## LIST OF PUBLICATIONS

### Publications:

- [1] “**Nature of energetic ion transport by ion temperature gradient driven turbulence and size scaling**”, J. Chowdhury, W. Wang, S. Ethier, J Manickam and R. Ganesh  
*Under review, Physics of Plasmas.*
- [2] “**Radial transport of energetic ions in the presence of trapped electron mode turbulence**”, J. Chowdhury, W. Wang, S. Ethier, J Manickam and R. Ganesh, *Physics of Plasmas* **18**, 112510 (2011).
- [3] “**Nonlinear Short Wavelength Ion Temperature Gradient turbulence**”, J. Chowdhury, S Brunner, R. Ganesh, X Lapillone, L. Villard and F. Jenko.  
*Research Report 520, September, 2011, Institute for Plasma Research.*  
*To be submitted to Physics of Plasmas.*
- [4] “**Toroidal universal drift instability: A global gyrokinetic study**”, J. Chowdhury, R. Ganesh, S. Brunner, J. Vaclavik, and L. Villard, *Physics of Plasmas* **17**, 102105 (2010).
- [5] “**Nonlocal effects in gyrokinetic turbulence simulations using GENE**”, T. Gorler, X. Lapillonne, S. Brunner, J. Chowdhury, T. Dannert, F. Jenko, B. F. McMillan, F. Merz, D. Told and L. Villard, *Journal of Physics: Conference Series* **260**, 012011 (2010).
- [6] “**Gyrokinetic simulations of turbulent transport: size scaling and chaotic behaviour**”, L. Villard, A. Bottino, S. Brunner, A. Casati, J. Chowdhury, T. Dannert, R. Ganesh, X. Garbet, T. Gorler, V. Grandgirard, R. Hatzky, Y. Idomura, F. Jenko, S. Jolliet, S. K. Aghdam, X. Lapillonne, G. Latu, B. F. McMillan, F. Merz, Y. Sarazin, T. M. Tran and T. Vernay, *Plasma Phys. Control. Fusion* **52**, 124038 (2010).
- [7] “**Sluggish response of untrapped electrons and global electrostatic micro-instabilities in a tokamak**”, J. Chowdhury, R. Ganesh, P. An-

- gelino, J. Vaclavik, L. Villard and S. Brunner, Journal of Physics: Conference Series **208**, 012058 (2010).
- [8] “**Short wavelength ion temperature gradient mode and coupling with trapped electrons**”, J. Chowdhury, R. Ganesh, J. Vaclavik, S. Brunner, L. Villard, and P. Angelino, Physics of Plasmas **16**, 082511 (2009).
- [9] “**A comprehensive gyrokinetic description of global electrostatic microinstabilities in a tokamak**”, J. Chowdhury, R. Ganesh, S. Brunner, J. Vaclavik, L. Villard, and P. Angelino, Physics of Plasmas **16**, 052507 (2009).
- [10] “**Role of nonadiabatic untrapped electrons in global electrostatic ion temperature gradient driven modes in a tokamak**”, J. Chowdhury, R. Ganesh, P. Angelino, J. Vaclavik, L. Villard, and S. Brunner, Physics of Plasmas **15**, 072117 (2008).

## ABSTRACT

The present dissertation is dedicated to the study of the stability and transport properties of many microinstabilities which play an important role in causing anomalous transport of energy and particles in tokamaks using global, linear and nonlinear, gyrokinetic formulations. In particular, it highlights (1) *effects of the nonadiabatic passing electrons on the ion temperature gradient (ITG) mode, trapped electron coupled ion temperature gradient mode (ITG-TEM) and trapped electron mode (TEM) by linear, global, gyrokinetic numerical study*; (2) *the behaviour of the ion temperature gradient driven modes in the presence of highly steep density profile typically observed in the transport barriers inside the tokamak; a linear and nonlinear gyrokinetic study on the occurrence of the short wavelength ion temperature gradient mode (SWITG)*; (3) *a linear, global, gyrokinetic stability analysis of the universal toroidal mode, which although is thought to be ubiquitous, yet overshadowed by the temperature gradient driven modes*; (4) *the stabilization of the microinstabilities by the hot ions (those ions having temperature higher than the thermal ions), and finally, the redistribution of the hot ions by microturbulence with the help of linear and nonlinear, global, gyrokinetic simulations.*

The role of the nonadiabatic passing electrons on the ion temperature gradient and trapped electron modes has been studied. Addressing the fully nonadiabatic passing electrons in time dependent linear and nonlinear codes has been an uphill task in the presence of full ion dynamics with true ion to electron mass ratio in terms of the computational cost. These particles are therefore considered either adiabatic or nonadiabatic with reduced ion to electron mass ratio. Thus, the effect of these nonadiabatic passing electrons on the growth rate and global mode structures of the ITG mode, ITG-TEM and TEM is often overlooked. With a global, spectral, gyrokinetic model it is possible to incorporate the full dynamics of the passing nonadiabatic electrons in the linear limit without any assumption regarding the ion to electron mass ratio. Strong effects of these nonadiabatic passing electrons near the mode rational surfaces where  $k_{\parallel} \rightarrow 0$  on the ITG mode, ITG-TEM and TEM have been observed.

The veracity of a nonadiabatic passing electron model is established only if it can produce modes inherent to the nonadiabatic passing electrons, one of which is the electron temperature gradient driven (ETG) mode. We have thus, extended

our study from the ion scales of ITG mode, ITG-TEM and TEM to the electron scales of the ETG mode and compared it with the already known results on the ETG mode. With the inclusion of the space charge effect in the form of Debye shielding, the model enables one to study the pure ETG mode in the presence of fully nonadiabatic ions.

The density gradient driven instability, known as the universal drift instability, is studied in the toroidal geometry and its linear properties have been discussed in both electrostatic and electromagnetic limit. The global mode structure and stability properties of the low- $n$  (toroidal mode number) toroidal universal mode along with its coupling to the trapped electrons have been studied perhaps for the first time to our knowledge.

Although ions are considered adiabatic at shorter wavelength or high wave number regime, they can behave nonadiabatically giving rise to a temperature gradient driven mode even at the high wave number regime. This mode, hitherto known to be slab like, is named as the short wavelength ion temperature gradient (SWITG) mode and studied only in the local limit. We have presented a linear, global, gyrokinetic study of the mode and shown that in the presence of trapped electrons this mode can be further unstable and exhibit toroidal nature. A nonlinear, flux tube, gyrokinetic simulation of the SWITG mode also has been carried out which shows that in spite of the linear dominance of the mode compared to the standard ITG mode, the former has very low contribution to the net thermal ion transport.

The behaviour of the energetic ions in tokamak plasmas is another issue that has derived much attention in the fusion community. Presence of these particles are inevitable in the fusion grade plasmas because of the various auxiliary heating schemes and fusion produced  $\alpha$  particles. The study of the influence of these energetic ions on the kinetic ballooning mode (KBM), toroidal Alfvén eigenmode (TAE), etc., is very much important. These particles can give rise to the unstable modes on their own, for example, energetic particle modes (EPM). We as a first step, have incorporated a second species of ions with higher energy than the thermal ions to an existing linear, global, gyrokinetic model and studied its effects on the ITG modes. It is observed that these energetic particles stabilize the ITG mode strongly. The He ions are found to be more stabilizing. Conversely, the effect of the microturbulence driven by the ITG mode and TEM on the energetic

ions is studied considering the energetic species as passive tracers using a global, nonlinear, gyrokinetic simulation. Microturbulence plays an important role in the redistribution of the energetic ions. The system size dependence and energy scaling of the energetic ions have been discussed. The transport of passing and trapped energetic ions is found to display different energy scalings.

# Contents

List of Figures . . . . .	iii
List of Tables . . . . .	xviii
<b>1 Introduction</b>	<b>1</b>
1.1 Magnetically Confined Fusion and Its Prospects . . . . .	1
1.2 Brief Review of Earlier Works . . . . .	5
1.3 Thesis Outline . . . . .	15
<b>2 Role of nonadiabatic/kinetic passing electrons in global electrostatic ion temperature gradient driven modes in a tokamak</b>	<b>17</b>
2.1 Introduction . . . . .	17
2.2 Model Equations . . . . .	19
2.2.1 Diagnostics: Eigenmode-averaged quantities . . . . .	27
2.2.2 Normalization for full radius calculation . . . . .	27
2.3 Eigenvalue finding method . . . . .	28
2.4 Results and Discussion . . . . .	29
2.4.1 $n$ -scan: Effect of variation of $\eta_e$ , multiscale features and mixing length transport . . . . .	29
2.4.2 $\eta_i$ scan: Nonadiabatic electrons cause down-shift of critical $\eta_i$	37
2.5 Conclusion . . . . .	38
<b>3 Trapped Electron Coupled Ion Temperature Gradient Mode And Trapped Electron Mode In The Presence Of Nonadiabatic Passing Electrons</b>	<b>40</b>
3.1 Introduction . . . . .	40
3.2 Model equations . . . . .	42
3.3 Results and Discussion . . . . .	46

3.3.1	Trapped Electron Mode . . . . .	54
3.4	Conclusion . . . . .	59
<b>4</b>	<b>Modes inherent to nonadiabatic/kinetic passing electrons</b>	<b>62</b>
4.1	Introduction . . . . .	62
4.2	Electron Temperature Gradient Driven Mode . . . . .	64
4.2.1	Profiles and Parameters . . . . .	64
4.2.2	Pure ETG Mode . . . . .	65
4.2.3	Mixing length estimate of flux . . . . .	76
4.3	Toroidal Universal Drift Instability: A Global Gyrokinetic Study . .	79
4.3.1	Model equations . . . . .	79
4.3.2	Results and Discussion . . . . .	81
4.4	Conclusions . . . . .	96
<b>5</b>	<b>Short wavelength ion temperature gradient mode and coupling with trapped electrons</b>	<b>101</b>
5.1	Introduction . . . . .	101
5.2	Linear SWITG . . . . .	103
5.2.1	Model Equations . . . . .	103
5.2.2	$k_\theta \rho_{Li}$ Scan . . . . .	105
5.2.3	$\epsilon_n$ Scan . . . . .	113
5.2.4	$\eta_i$ Scan . . . . .	118
5.2.5	$\tau$ Scan . . . . .	121
5.2.6	Mixing Length Estimation . . . . .	122
5.3	Nonlinear SWITG . . . . .	123
5.3.1	The Model . . . . .	123
5.3.2	Results . . . . .	128
5.4	Conclusion . . . . .	136
<b>6</b>	<b>Interaction of microturbulence with energetic ions</b>	<b>140</b>
6.1	Introduction . . . . .	140
6.2	Effect of energetic ions on the stability of temperature gradient driven mode of thermal ions. . . . .	143
6.2.1	Model equations . . . . .	144
6.2.2	Profiles and Parameters: . . . . .	145

6.2.3	Wave number scan for the mode frequency and growth rate .	146
6.2.4	Effect of density fraction of energetic ions . . . . .	148
6.2.5	Effect of temperature of the energetic ions . . . . .	150
6.2.6	Mixing length estimate of transport . . . . .	152
6.3	Size and energy scaling of hot ion transport in the presence of ion temperature gradient driven turbulence. . . . .	154
6.3.1	Simulation Model . . . . .	157
6.3.2	Parameters and profiles . . . . .	158
6.3.3	Heat flux of thermal ions . . . . .	158
6.3.4	Mean Squared Displacement of hot ions . . . . .	161
6.3.5	Nature of transport: Energy Scaling . . . . .	163
6.3.6	Nature of Transport: Size scaling . . . . .	164
6.3.7	Check for quasisteady state and robustness of the results . .	171
6.3.8	Plausible explanation for subdiffusion . . . . .	178
6.4	Radial transport of energetic ions in the presence of trapped electron mode turbulence. . . . .	180
6.4.1	Simulation Model . . . . .	181
6.4.2	Parameters and Profiles . . . . .	181
6.4.3	Isotropic hot ions . . . . .	182
6.4.4	Passing Hot Ions . . . . .	191
6.4.5	Trapped Hot Ions . . . . .	192
6.4.6	Nature of Transport . . . . .	193
6.4.7	Energy Scaling of Hot Ions . . . . .	196
6.5	Conclusion . . . . .	199

## 7 Conclusion

<b>and Future Direction</b>	<b>203</b>
7.1 Conclusions . . . . .	203
7.2 Future Work . . . . .	207
Bibliography . . . . .	209

# List of Figures

2.1	Equilibrium profiles for global ITGs stability studies (parameters for Table 2.1: Normalized density, temperature, $\eta_{i,e}$ (left), Safety factor $q$ and magnetic shear $\hat{s}$ (right) profiles as functions of normalized radius $s = r/a$ . Note that $\eta$ peaks at $s = \rho/a = s_0 = 0.6$ . . . . .	30
2.2	Growth rates and frequencies for profiles in Fig. 2.1: Growth rate $\gamma$ and real frequency $\omega_r$ for $\eta_i(s_0) = 2$ with adiabatic electron model and nonadiabatic electron model characterized by increasing $\eta_e$ . . .	31
2.3	Two-dimensional eigenmode structure of global ITG at $n = 9$ , $\eta_i(s_0) = 2$ for adiabatic electron response (left panel) and nonadiabatic electron response (right panel) at $\eta_e(s_0) = 2$ . Global nature of the mode is clearly visible covering about 30% of the minor radius. . . . .	32
2.4	The poloidal Fourier components for electrostatic mode shown in Fig. 2.3. Note that at each radial location, there are several poloidal harmonics coupled. A few locations where $k_{\parallel m,n} = 0$ (i.e, $nq = m$ ) are indicated on the top axis. Nonadiabatic electrons introduce sharp structure near these points. . . . .	33
2.5	Radial Fourier harmonics for each poloidal mode for the electrostatic mode shown in Fig. 2.3. Here we have used 144 modes. For numerical convergence, we have tested with larger number of radial harmonics and observe that the results are converged. . . . .	34

2.6	Typical per-mode phase velocity $\omega_r/k_{  m,n}$ versus normalized minor radius $s = r/a$ for equilibrium profile of $q$ shown in Fig. 2.1 with $\eta_e(s_0) = 8$ , $\eta_i(s_0) = 2$ , $n = 9$ . Locations of peaks ( $r = r_{MRS}$ ) indicate mode rational surfaces. The horizontal dashed lines are the electron thermal velocities $v_{the}^{min}$ and $v_{the}^{max}$ at radial locations at the beginning ( $s=0.4$ ) and end ( $s=0.7$ ) of mode structure, respectively. The horizontal dashed-dotted lines are ion thermal speeds at same locations as the electrons. . . . .	35
2.7	Closeup of two dimensional eigenmode structure of global ITG at $n = 9$ , $\eta_i = 2$ for (a) adiabatic electron response, (b) nonadiabatic electron response at $\eta_e(s_0) = 2$ and (c) same as (b) at $\eta_e = 8(s_0)$ . . .	35
2.8	Eigenmode averaged normalized mode numbers $\langle k_\theta \rho_{Li} \rangle$ (squares), $\langle k_r \rho_{Li} \rangle$ (diamonds), $\langle k_\perp \rho_{Li} \rangle$ (stars) as a function of toroidal mode number $n$ at $\eta_i(s_0) = 2$ ; (a) adiabatic electron response, (b) nonadiabatic electron response at $\eta_e(s_0) = 2$ , and (c) same as (b) at $\eta_e(s_0) = 8$ . . . . .	36
2.9	Mixing length estimate for transport coefficient $D_{ML} = \gamma / \langle k_\perp^2 \rangle$ in gyro-Bohm units as a function of toroidal mode number $n$ ; $\eta_i(s_0) = 2$ for (a) adiabatic electron response (solid line), (b) nonadiabatic electron response at $\eta_e(s_0) = 2$ (dashed line), and (c) same as (b) at $\eta_e(s_0) = 8$ (dot-dashed line). . . . .	36
2.10	For the highest growth rate mode toroidal mode number $n = 9$ , $\eta_i$ scan is performed for three cases of electron model: (a) Adiabatic electron response (solid line), (b) nonadiabatic electron response at $\eta_e(s_0) = 2$ (dashed line), and (c) same as (b) at $\eta_e(s_0) = 8$ (dot-dashed line). Results clearly show that $\eta_{i,crit}$ is downshifted. . . . .	37
3.1	Growth rate $\gamma$ (dashed line) and real frequency $\omega_r$ (solid line) for $\eta_i(s_0) = 2$ (i) for pure ITG with adiabatic electron model (squares),(ii) ITG-TEM without nonadiabatic passing electrons (diamonds), and (iii) ITG-TEM with nonadiabatic passing electrons at $\eta_e(s_0) = 2.0$ (filled circles). . . . .	46

3.2	Two dimensional eigenmode structure of global ITG at $n = 8$ and $\eta_i(s_0) = 2$ for (a) pure ITG with adiabatic electrons, (b) ITG-TEM without nonadiabatic passing electrons, and (c) ITG-TEM with nonadiabatic passing electron at $\eta_e(s_0) = 2.0$ . . . . .	47
3.3	Closeup of two dimensional eigenmode structure for (a) pure ITG with adiabatic electrons, (b) ITG-TEM without nonadiabatic passing electrons, and (c) ITG-TEM with nonadiabatic passing electrons at $\eta_e(s_0) = 2.0$ . . . . .	49
3.4	Poloidal Fourier components for electrostatic modes shown in Fig. 3.2 (a) ITG with adiabatic electrons, (b) ITG-TEM without nonadiabatic passing electrons, and (c) ITG-TEM with nonadiabatic passing electrons at $\eta_e(s_0) = 2.0$ . Note that at each radial location, there are several poloidal harmonics coupled. A few locations where $k_{\parallel m,n} = 0$ (i.e., $nq = m$ ) are indicated on the top axis. Nonadiabatic electrons introduce sharp structure near these points. . . . .	50
3.5	Upper panel: Radial Fourier harmonics for each poloidal mode for the electrostatic mode shown in Fig. 3.2 for (a) pure ITG with adiabatic electron response and (b) ITG-TEM without nonadiabatic passing electrons. Lower panel: Radial Fourier harmonics for each poloidal mode for the electrostatic mode shown in Fig. 3.2(c) for ITG-TEM with nonadiabatic passing electrons at $\eta_e(s_0) = 2.0$ . . . . .	52
3.6	Eigenmode-averaged normalized mode numbers $\langle k_{\theta} \rho_{Li} \rangle$ (squares), $\langle k_r \rho_{Li} \rangle$ (diamonds), and $\langle k_{\perp} \rho_{Li} \rangle$ (stars) at $\eta_i(s_0) = 2$ ; (a) pure ITG with adiabatic electron response, (b) ITG-TEM without nonadiabatic passing electrons, and (c) ITG-TEM with nonadiabatic passing electrons at $\eta_e(s_0) = 2.0$ . . . . .	53
3.7	Mixing length estimate for transport coefficient $D_{ML} = \gamma / \langle k_{\perp}^2 \rangle$ in gyro-Bohm units as a function of $k_{\theta} \rho_{Li}$ for $\eta_i(s_0) = 2$ ; (a) pure ITG with adiabatic electron response (solid line with squares), (b) ITG-TEM without nonadiabatic passing electrons (divided by 8) (solid line with diamonds), and (c) ITG-TEM with nonadiabatic passing electrons at $\eta_e(s_0) = 2$ (dashed line with filled circles). . . . .	53

3.8	Growth rate $\gamma$ (dashed line) and real frequency $\omega_r$ (solid line) versus $\eta_i$ at $\eta_e(s_0) = 2$ (i) for pure ITG with adiabatic electrons (squares), (ii) ITG-TEM without nonadiabatic passing electrons (diamonds), and (iii) ITG-TEM with nonadiabatic passing electrons (filled circles). . . . .	54
3.9	Growth rate $\gamma$ (dashed line) and real frequency $\omega_r$ (solid line) for $\eta_i(s_0) = 2$ ; (i) for TEM without nonadiabatic passing electron model (squares) and (ii) for TEM with nonadiabatic passing electron model at $\eta_i(s_0) = \eta_e(s_0) = 2.0$ (open circles). . . . .	55
3.10	Two dimensional eigenmode structure for (a) TEM without nonadiabatic passing electron response and (b) TEM with nonadiabatic passing electron response at $n = 7$ and $\eta_i(s_0) = \eta_e(s_0) = 2.0$ . . . . .	56
3.11	Closeup of two dimensional eigenmode structure of (a) TEM without nonadiabatic electron response and (b) TEM with nonadiabatic passing electron response for $n = 7$ and $\eta_i(s_0) = \eta_e(s_0) = 2.0$ . . . . .	56
3.12	Poloidal Fourier components for electrostatic mode shown in Fig. 3.10. Note that at each radial location, there are several poloidal harmonics coupled. A few locations where $k_{\parallel m,n} = 0$ (i.e., $nq = m$ ) are indicated on the top axis. Nonadiabatic electrons introduce sharp structure near these points. . . . .	57
3.13	Right panel: Radial Fourier harmonics for each poloidal mode for the electrostatic mode shown in Fig. 3.10(a) for TEM without nonadiabatic passing electron response. Left panel: Radial Fourier harmonics for each poloidal mode for the electrostatic mode shown in Fig. 3.10(b) for TEM with nonadiabatic passing electron response. . . . .	58
3.14	Eigenmode-averaged normalized mode numbers $\langle k_{\theta} \rho_{Li} \rangle$ (squares), $\langle k_r \rho_{Li} \rangle$ (diamonds), and $\langle k_{\perp} \rho_{Li} \rangle$ (stars) as a function of $k_{\theta} \rho_{Li}$ at $\eta_i(s_0) = 2$ : (a) TEM without nonadiabatic passing electron response and (b) TEM with nonadiabatic passing electrons at $\eta_e(s_0) = 2.0$ . . . . .	58

3.15	Mixing length estimate for transport coefficient $D_{ML} = \gamma / \langle k_{\perp}^2 \rangle$ in gyro-Bohm units as a function of $k_{\theta}\rho_{Li}$ with $\eta_i(s_0) = 2.0$ for (a) TEM without nonadiabatic passing electron response (dashed line with squares) and (b) TEM with nonadiabatic passing electron response at $\eta_e(s_0) = 2.0$ (dashed line with open circles). . . . .	60
4.1	The normalized real frequency $\omega_r$ (upper panel) and growth rate $\gamma$ (lower panel) for the ETG mode as function of $\eta_e$ for $k_{\theta}\rho_e \simeq 0.5$ , $\epsilon_n = L_n/R = 0.2$ , and $\tau = 1.0$ . The lines with squares represent manually extracted points from Horton <i>et al.</i> [21] which uses local kinetic formulation. The lines with open circles depict the results from our global linear gyrokinetic model. . . . .	66
4.2	Figures 3 and 4 from Horton <i>et al.</i> [21] . . . . .	67
4.3	The normalized real frequency $\omega_r$ (upper panel) and growth rate $\gamma$ (lower panel) for the ETG with and without Debye shielding for $\eta_e(s_0) = 2$ . Ions are considered adiabatic. . . . .	68
4.4	$\eta_e(s_0)$ scan for the growth rate of the ETG mode with and without Debye shielding for $n = 250$ and $380$ , respectively. . . . .	69
4.5	Upper panel: The normalized real frequency $\omega_r$ for the ETG mode without Debye shielding $\eta_e(s_0) = 2.0$ with adiabatic ions and nonadiabatic ions. $\eta_i(s_0)$ takes values 2, 4, 6, 8 for nonadiabatic ions. Lower panel: The corresponding growth rates $\gamma$ . . . . .	70
4.6	Upper panel: the normalized frequency $\omega_r$ for the ETG mode with Debye shielding for $\eta_e(s_0) = 2.0$ with adiabatic ions and nonadiabatic ions. $\eta_i(s_0)$ takes values 2, 4, 6, 8 for nonadiabatic ions. Lower panel: the corresponding growth rates $\gamma$ . . . . .	71
4.7	Upper panel: the normalized frequency $\omega_r$ for the ITG mode for $\eta_i(s_0) = 2.0$ with adiabatic and nonadiabatic electrons. $\eta_e(s_0)$ takes values 2, 4, 6, 8 for nonadiabatic electrons. Debye shielding is not included for these runs. Lower panel: the corresponding normalized growth rates $\gamma$ . . . . .	72

4.8	Mode structures for the ITG mode for $\eta_i(s_0) = 2.0$ (left) and ETG mode for $\eta_e(s_0) = 2.0$ with (middle) and without (right) Debye shielding on the poloidal cross section of a tokamak for the maximum growth rates. The other species (electron for ITG, ion for ETG) is considered adiabatic. . . . .	73
4.9	Closeup view of Fig. 4.8 . . . . .	74
4.10	Poloidal Fourier harmonics for the modes shown in Fig. 4.8 . . . . .	74
4.11	Top panel: mixing length estimate for transport coefficient $D_{ML} = \gamma / \langle k_{\perp}^2 \rangle$ in electron gyro-Bohm units as a function of $k_{\theta}\rho_{Li}$ for the ETG mode without Debye shielding at $\eta_e(s_0) = 2$ with adiabatic ions and nonadiabatic ions for $\eta_i(s_0) = 2, 4, 6, 8$ ; Middle panel: mixing length estimate for transport coefficient $D_{ML} = \gamma / \langle k_{\perp}^2 \rangle$ in electron gyro-Bohm units as a function of $k_{\theta}\rho_{Li}$ for the ETG mode with Debye shielding at $\eta_e(s_0) = 2$ with adiabatic ions and nonadiabatic ions for $\eta_i(s_0) = 2, 4, 6, 8$ ; Bottom panel: mixing length estimate for transport coefficient $D_{ML} = \gamma / \langle k_{\perp}^2 \rangle$ in ion gyro-Bohm units as a function of $k_{\theta}\rho_{Li}$ ; $\eta_i(s_0) = 2$ , with adiabatic electrons and nonadiabatic electrons for $\eta_e(s_0) = 2, 4, 6, 8$ . . . . .	77
4.12	Left panel: normalized perpendicular wave numbers $k_r, k_{\theta}, k_{\perp}$ vs toroidal mode number $n$ for the ETG mode without Debye shielding. Right panel: normalized perpendicular wave numbers $k_r, k_{\theta}, k_{\perp}$ vs toroidal mode number $n$ for the ETG mode with Debye shielding. . . . .	78
4.13	Equilibrium profiles to study the global toroidal universal drift instability mode (for parameters in Table I): (a) normalized density (dots), temperature (circle), $\eta_{i,e}$ (triangle), (b) Safety factor $q$ (circle) and magnetic shear $\hat{s}$ (dots) profiles as functions of normalized radius $s = r/a$ . Note that $q(s_0) = 2.0$ , $\hat{s}(s_0) = 0.40$ , $\epsilon_n(s_0) = 0.1$ , and $\tau(s_0) = 3.0$ for $s_0 = 0.6$ . . . . .	81
4.14	Real frequency and growth rate for the electrostatic case corresponding to the parameters in the Table I and profiles shown in Fig. 4.13. . . . .	82

4.15	Upper panel: (Left) The electrostatic mode structure for toroidal mode number $n = 10$ , $k_\theta \rho_{Li} = 0.58$ , corresponding to the parameters in the Table I and profiles shown in Fig. 4.13. (Right) poloidal component of $\tilde{\phi}$ in (top) radial Fourier representation and (bottom) radial direct space. Lower panel: A closeup view of the mode structure. . . . .	84
4.16	The effect of electron and ion Landau resonance for the mode $n = 10$ corresponding to $k_\theta \rho_{Li} = 0.58$ . This is done by weighting the Landau resonance term by $\alpha$ and running it from 0 to 1 for one species, and keeping $\alpha = 1.0$ for the other species and vice versa. . . . .	85
4.17	Effect of ion and electron magnetic drift resonance for the mode $n=10$ corresponding to $k_\theta \rho_{Li} = 0.58$ . This is done by weighting the magnetic drift term by $\alpha$ and running it from 0 to 1, and keeping $\alpha = 1.0$ for the other species and vice versa. . . . .	86
4.18	Shear scan for the mode $n = 10$ corresponding to $k_\theta \rho_{Li} = 0.58$ at position $s = s_0 = 0.6$ , where the density gradient peaks. For these scans the safety factor at $s = s_0$ is kept at the fixed value $q = 2.0$ . . . . .	87
4.19	Real frequency and growth rate for $\epsilon_n = L_n/R$ for the parameters and profiles as in the Table I and Fig. 4.13 in the case of mode $n = 10$ corresponding to $k_\theta \rho_{Li} = 0.58$ . Note that $a$ , $L_n$ , $Rq$ and $nq$ are kept constant in this scan. . . . .	88
4.20	Real frequency and growth rate for $\tau = T_e/T_i$ and for the parameters and profiles of Table I and Fig. 4.13 in the case of the mode $n = 10$ corresponding to $k_\theta \rho_{Li} = 0.58$ . . . . .	89
4.21	Real frequency and growth rate in the case of a temperature gradient scan for the parameters and profiles of Table I and Fig. 4.13 for the mode $n = 10$ corresponding to $k_\theta \rho_{Li} = 0.58$ . The flat temperature profile in Table I, has been replaced by one with $\delta_{sT} = 0.2$ instead of 0 for the previous cases. . . . .	90
4.22	Real frequency and growth rate for the electrostatic (dashed curve) and electromagnetic case (solid curve) for the parameters in Table I and profiles as shown in Fig. 4.13. The value of $\beta$ considered here is 0.001. . . . .	91

4.23	(Upper panel) The global mode structure for the $\tilde{\phi}$ component in the poloidal cross section in the electromagnetic case for $n = 10$ , $k_{\theta}\rho_{Li} = 0.58$ , and $\beta = 0.001$ . (Lower panel) Poloidal component of $\tilde{\phi}$ in (top) radial Fourier representation and (bottom) radial direct space. . . . .	93
4.24	(Upper panel) The global mode structure for the $\tilde{A}_{\parallel}$ component in the poloidal cross section in the electromagnetic case for $n = 10$ , $k_{\theta}\rho_{Li} = 0.58$ , and $\beta = 0.001$ . (Lower panel) Poloidal component of $\tilde{\phi}$ in (top) radial Fourier representation and (bottom) radial direct space. . . . .	94
4.25	$\beta$ scan for the mode frequency and growth rate for the parameters and profiles as in Table I and Fig. 4.13 for the mode $n = 10$ corresponding to $k_{\theta}\rho_{Li} = 0.58$ . . . . .	95
4.26	Electromagnetic ratio with increasing function of $\beta$ for the parameters and profiles as in Table I and Fig. 4.13 for the mode $n = 10$ corresponding to $k_{\theta}\rho_{Li} = 0.58$ . . . . .	95
4.27	The real frequency and growth rate vs temperature gradient for different unstable modes in the presence of trapped electrons in the same regime defined by the parameters and profiles of Table I and Fig. 4.13 for the mode $n = 10$ corresponding to $k_{\theta}\rho_{Li} = 0.58$ . The flat temperature profile in Table I, has been replaced by one with $\delta s_T = 0.2$ instead of 0 for the previous cases. The three dashed curves (circle, square, diamond) are for universal mode without trapped electrons (same as Fig. 4.21), three solid lines (circle, square, diamond) are for universal mode in the presence of trapped electrons (UNV-TE), the dashed curve with triangles is for ion temperature gradient mode with trapped electrons (ITG-TE) and the solid curve with stars is for pure trapped electron mode (TEM). . .	97

5.1	Equilibrium profiles to study the global SWITG mode( for parameters in Table I): (a) normalized density (square), temperature (circle), $\eta_{i,e}$ (triangle), (b) Safety factor $q$ (circle) and magnetic shear $\hat{s}$ (diamond) profiles as functions of normalized radius $s = r/a$ . Note that $\eta$ peaks at $s = \rho/a = s_0 = 0.6$ and is equal to 2.5. Also $q(s_0 = 0.6) = 2.0$ , $\hat{s}(s_0 = 0.6) = 1.0$ , $\epsilon_n(s_0 = 0.6) = 0.1$ , and $\tau(s_0 = 0.6) = 1.0$ . . . . .	104
5.2	The normalized growth rate $\tilde{\gamma}$ of the ITG (first peak) and of the SWITG (second peak) mode with (solid line+square) and without (solid line + circle) the trapped electrons from the global as well as local formulation (dotted line + diamond, for the case with the trapped electrons and dotted line + circle, for the case without the trapped electrons.) $\eta_{e,i}(s_0) = 2.5$ , $q(s_0) = 2.0$ , $\hat{s}(s_0) = 1.0$ , $\tau = 1.0$ , and $\epsilon_n = 0.1$ . Upper axis shows the corresponding toroidal mode numbers. . . . .	105
5.3	The normalized real frequency $\tilde{\omega}_r$ of the ITG and of the SWITG mode with (solid line+square) and without (solid line+circle) the trapped electrons from the global as well as local formulation (dotted line+diamond, for the case with the trapped electrons and dotted line + circle, for the case without the trapped electrons.) $\eta_{e,i}(s_0) = 2.5$ , $q(s_0) = 2.0$ , $\hat{s}(s_0) = 1.0$ , $\tau = 1.0$ , and $\epsilon_n = 0.1$ . Upper axis shows the corresponding toroidal mode numbers. . . . .	107
5.4	Two dimensional eigenmode structures of (a) the ITG mode at $k_\theta \rho_{Li} \approx 0.5$ , $n = 9$ , (b) the SWITG mode at $k_\theta \rho_{Li} \approx 1.3$ , $n = 21$ without the trapped electrons both corresponding to the maximum growth rate. The mode structure of the SWITG mode is finer than the ITG mode but yet global enough. . . . .	110
5.5	Two dimensional eigenmode structures of (a) the ITG mode at $k_\theta \rho_{Li} \approx 0.4$ , $n = 7$ , (b) the SWITG mode at $k_\theta \rho_{Li} \approx 1.3$ , $n = 21$ with the trapped electrons, both for the maximum growth rates respectively. The mode structure of the SWITG mode is finer than the ITG mode but still global enough. . . . .	111

5.6	A closeup view of the eigenmode structures of (a) the ITG mode at $k_\theta \rho_{Li} \approx 0.5$ , $n = 9$ , (b) the SWITG mode at $k_\theta \rho_{Li} \approx 1.3$ , $n = 21$ without the trapped electrons shown in Fig. 5.4. . . . .	112
5.7	A closeup of the two dimensional eigenmode structures of (a) the ITG mode at $k_\theta \rho_{Li} \approx 0.4$ , $n = 7$ , (b) the SWITG mode at $k_\theta \rho_{Li} \approx 1.3$ , $n = 21$ with the trapped electrons shown in Fig. 5.5. . . . .	114
5.8	Poloidal Fourier components for electrostatic modes shown in Figs. 5.4 and 5.5, (a) the ITG mode at $k_\theta \rho_{Li} \approx 0.5$ , $n = 9$ , (b) the SWITG mode at $k_\theta \rho_{Li} \approx 1.3$ , $n = 21$ , both without the trapped electrons, (c) the ITG mode at $k_\theta \rho_{Li} \approx 0.4$ , $n = 7$ , and (d) the SWITG mode at $k_\theta \rho_{Li} \approx 1.3$ , $n = 21$ , both with the trapped electrons. . . . .	115
5.9	Radial Fourier components for electrostatic modes shown in Fig. 5.4 and 5.5, (a) the ITG mode at $k_\theta \rho_{Li} \approx 0.5$ , $n = 9$ , (b) the SWITG mode at $k_\theta \rho_{Li} \approx 1.3$ , $n = 21$ , both without the trapped electrons, (c) the ITG mode at $k_\theta \rho_{Li} \approx 0.4$ , $n = 7$ , and (d) the SWITG mode at $k_\theta \rho_{Li} \approx 1.3$ , $n = 21$ , both with the trapped electrons. . . . .	116
5.10	Normalized growth rates $\tilde{\gamma}$ vs. $\epsilon_n$ scan for the SWITG mode at $k_\theta \rho_{Li} \approx 1.3$ with (solid line + square) and without (solid line + circles) the trapped electrons (from the global gyrokinetic model). $\eta_{e,i}(s_0) = 2.5$ , $q(s_0) = 2.0$ , $\hat{s}(s_0) = 1.0$ , $\tau = 1.0$ , $L_n = 0.2$ , and $a = 0.5$ . . . . .	117
5.11	Normalized real frequency $\tilde{\omega}_r$ vs. $\epsilon_n$ scan for the SWITG mode at $k_\theta \rho_{Li} \approx 1.3$ with (solid line + square) and without (solid line + circles) the trapped electrons (from the global gyrokinetic model). $\eta_{e,i}(s_0) = 2.5$ , $q(s_0) = 2.0$ , $\hat{s}(s_0) = 1.0$ , $\tau = 1.0$ , $L_n = 0.2$ , and $a = 0.5$ . . . . .	117
5.12	Normalized growth rates $\tilde{\gamma}$ vs. $\eta_i$ scan for the SWITG mode at $k_\theta \rho_{Li} \approx 1.3$ with (solid line + square) and without (solid line + circles) the trapped electrons (from the global gyrokinetic model). $\eta_e(s_0) = 2.5$ , $q(s_0) = 2.0$ , $\hat{s}(s_0) = 1.0$ , $\tau = 1.0$ , and $\epsilon_n = 0.1$ . . . . .	118
5.13	Normalized real frequency $\tilde{\omega}_r$ vs. $\eta_i$ scan for the SWITG mode at $k_\theta \rho_{Li} \approx 1.3$ with (solid line + square) and without (solid line + circles) the trapped electrons (from the global gyrokinetic model). $\eta_e(s_0) = 2.5$ , $q(s_0) = 2.0$ , $\hat{s}(s_0) = 1.0$ , $\tau = 1.0$ , and $\epsilon_n = 0.1$ . . . . .	119

5.14	Normalized growth rates $\tilde{\gamma}$ vs. $\tau$ scan for the SWITG mode at $k_{\theta}\rho_{Li} \approx 1.3$ with (solid line + square) and without (solid line + circles) the trapped electrons (from the global gyrokinetic model). $\eta_{e,i}(s_0) = 2.5$ , $q(s_0) = 2.0$ , $\hat{s}(s_0) = 1.0$ , and $\epsilon_n = 0.1$ . . . . .	120
5.15	Normalized real frequency $\tilde{\omega}_r$ vs. $\tau$ scan for the SWITG mode at $k_{\theta}\rho_{Li} \approx 1.3$ with (solid line + square) and without (solid line + circles) the trapped electrons (from the global gyrokinetic model). $\eta_{e,i}(s_0) = 2.5$ , $q(s_0) = 2.0$ , $\hat{s}(s_0) = 1.0$ , and $\epsilon_n = 0.1$ . . . . .	120
5.16	Mixing length estimate for transport coefficient $D_{ML} = \gamma / \langle k_{\perp}^2 \rangle$ of the ions in the ion gyro-Bohm units as a function of $k_{\theta}\rho_{Li}$ ; (a) the ITG and the SWITG mode without the trapped electrons (solid line + circle) (b) the ITG and the SWITG mode with the trapped electrons (solid line + square) (from the global gyrokinetic model). Note that this curve is scaled down by a factor of 8. The upper axis presents the corresponding toroidal mode numbers. . . . .	121
5.17	(a) Real frequency $\omega_r$ , and (b) growth rate $\gamma$ versus wave number $k_y\rho_s$ of the linear short wavelength ion temperature gradient mode (SWITG) for different values of $R/L_n$ . Here $\eta_i = 2.5$ , $q = 2.0$ , $\hat{s} = 1.0$ , $\tau = 1.0$ in these simulations. . . . .	127
5.18	Time (in units of $R/c_s$ ) evolution of ion heat flux $Q$ normalized by $Q_{norm} = p_{ref}c_s\rho_s^2/R^2$ for SWITG simulation, with $R/L_n = 5$ and $R/L_n = 10$ . The black dashed lines represent the time average of the heat flux between $t = 100 R/c_s$ and $t = 330 R/c_s$ . For $R/L_n = 5$ the average $Q = 195 Q_{norm}$ and for $R/L_n = 10$ the average $Q = 302 Q_{norm}$ . . . . .	128
5.19	(a) Time averaged ion heat flux versus normalized wavenumber $k_y$ for $R/L_n = 5$ and $R/L_n = 10$ in lin-lin plot. (b) Time averaged ion heat flux as a function of normalized wavenumber $k_y$ for $R/L_n = 5$ and $R/L_n = 10$ in log-log plot. $Q$ is normalized with respect to $Q_{norm} = p_{ref}c_s\rho_s^2/R^2$ . . . . .	130
5.20	Cumulative sum of heat flux for $R/L_n = 10$ . The standard ITG contribution to the heat flux is for $k_y\rho_s \leq 1$ and SWITG contribution to the heat flux is for $k_y\rho_s \geq 1$ . $Q_{c.s.}$ is normalized with respect to $Q_{norm} = p_{ref}c_s\rho_s^2/R^2$ . . . . .	132

5.21	Cumulative sum of heat flux for $R/L_n = 5$ . The standard ITG contribution to the heat flux is for $k_y \rho_s \leq 1$ and SWITG contribution to the heat flux is for $k_y \rho_s \geq 1$ . $Q_{c.s.}$ is normalized with respect to $Q_{norm} = p_{ref} c_s \rho_s^2 / R^2$ . . . . .	132
5.22	Snapshots of the potential (top) and perturbed density (bottom) of the SWITG mode for $R/L_n = 5$ taken at $t = 330 R/c_s$ . . . . .	134
5.23	Snapshots of the potential (top) and perturbed density (bottom) of the SWITG mode for $R/L_n = 10$ taken at $t = 330 R/c_s$ . . . . .	135
5.24	Time traces of the zonal flow shearing rate $\omega_E = dv_{E,y}/dx$ , in units of $c_s/R$ for the SWITG modes with (a) $R/L_n = 5$ and (b) $R/L_n = 10$ . . . . .	137
6.1	Left panel: the equilibrium density and temperature profiles along with the $\eta$ profile of the thermal ions and electrons. Right panel: the safety factor profile and shear profile. The $\eta$ profile peaks at $s_0 = 0.7$ with the magnitude $\eta = 2.0$ . The safety factor $q$ and shear value $\hat{s}$ at this point, respectively, are 2.0 and 1.0. . . . .	144
6.2	The $\eta$ profiles considered for the energetic ions with respect to the background profiles of the thermal ions and electrons. While the thermal ion and electron $\eta$ profiles are kept the same, energetic ion profiles are considered for three different cases, namely, flat $\eta$ profile (green curve), peaked $\eta$ profile (red curve) and same $\eta$ profile (blue curve) as the thermal ions. . . . .	145
6.3	The wavenumber scan for the mode frequency $\omega_r$ (left panel) and growth rate $\gamma$ (right panel) of the ITG mode is presented for the cases, viz., (i) without energetic ions (magenta line), (ii) with singly charged energetic ions with flat $\eta$ profile (green line), steeper $\eta$ profile (red line), same $\eta$ profile (blue line) as the thermal ions and (iii) with energetic He ions (brown line). . . . .	147
6.4	A typical electrostatic mode structure for $n = 8$ , $k_\theta \rho_{Li} = 0.4$ corresponding to the maximum growth rate of the ITG mode with nonadiabatic electrons and energetic ions. . . . .	148

6.5	The mode frequency $\omega_r$ and growth rate $\gamma$ are plotted as a function of density fraction of the energetic ions compared to background density of electron for the mode with $n = 8$ , $k_\theta \rho_{Li} = 0.4$ for the cases, viz., (i) with singly charged energetic ions with flat $\eta$ profile (green line), steeper $\eta$ profile (red line), same $\eta$ profile (blue line) as the thermal ions and (ii) with energetic He ions (brown line). . . . .	149
6.6	The mode frequency $\omega_r$ and growth rate $\gamma$ are plotted as a function of temperature fraction of the energetic ions compared to the temperature of the thermal ions for the mode characterized by the toroidal mode number $n = 8$ , corresponding to $k_\theta \rho_{Li} = 0.4$ for the cases, viz., (i) with singly charged energetic ions with flat $\eta$ profile (green line), steeper $\eta$ profile (red line), same $\eta$ profile (blue line) as the thermal ions and (ii) with energetic He ions (brown line). . . . .	150
6.7	A mixing length based estimation of transport in gyroBohm units is presented for the cases, viz., (i) without energetic ions (magenta line), (ii) with singly charged energetic ions with flat $\eta$ profile (green line), steeper $\eta$ profile (red line), same $\eta$ profile (blue line) as the thermal ions and (iii) with energetic He ions (brown line). . . . .	152
6.8	Different domains of anomalous diffusion, defined through the mean squared displacement $\langle \sigma^2 \rangle = A t^p$ , and parameterized by the anomalous diffusion exponent $p$ : (a) subdiffusion for $0 < p < 1$ , (b) superdiffusion for $1 < p < 2$ . On the threshold between sub- and superdiffusion is the normal Brownian diffusion located. Another special case is ballistic motion $p = 2$ [169]. . . . .	156
6.9	Time evolution of heat flux, measured at $r = 0.5a$ , for system size (a) $a/\rho_i = 157$ , (b) $a/\rho_i = 315$ , and (c) $a/\rho_i = 500$ . . . . .	159
6.10	The typical snapshots of mode structure in the linear (left panel) and nonlinear (right panel) regime of the ITG turbulence for the system size $a/\rho_i = 157$ . . . . .	160
6.11	The typical snapshots of mode structure in the linear (left panel) and nonlinear (right panel) regime of the ITG turbulence for the system size $a/\rho_i = 315$ . . . . .	160

6.12	The typical snapshots of mode structure in the linear (left panel) and nonlinear (right panel) regime of the ITG turbulence for the system size $a/\rho_i = 500$ . . . . .	161
6.13	Mean squared displacement of the hot ions for system size a) $a/\rho_i = 157$ (upper left panel), b) $a/\rho_i = 315$ (upper right panel), c) $a/\rho_i = 500$ (lower panel). . . . .	162
6.14	$D_h = \delta < \sigma^2 > / \delta t$ versus energy of hot ions. . . . .	164
6.15	$D_h$ versus $a/\rho_i$ . . . . .	165
6.16	Exponent $p$ in $< \sigma^2 > \propto t^p$ versus $a/\rho_i$ . . . . .	166
6.17	Upper panel: PDF for hot ions for $a/\rho_i = 157$ . Lower panel: $< \sigma^2 > / t^p$ as a function of $t$ for $a/\rho_i = 157$ . . . . .	168
6.18	Upper panel: PDF for hot ions for $a/\rho_i = 315$ . Lower panel: $< \sigma^2 > / t^p$ as a function of $t$ for $a/\rho_i = 315$ . . . . .	169
6.19	Upper panel: PDF for hot ions for $a/\rho_i = 500$ . Lower panel: $< \sigma^2 > / t^p$ as a function of $t$ for $a/\rho_i = 500$ . . . . .	170
6.20	Heat flux for $a/\rho_i = 157$ and $315$ . . . . .	172
6.21	Mean squared displacement for $a/\rho_i = 157$ and $315$ . . . . .	173
6.22	Probability distribution function for $a/\rho_i = 157$ . . . . .	175
6.23	Probability distribution function for $a/\rho_i = 315$ . . . . .	175
6.24	Upper panel: $< \sigma^2 > / t^p$ as a function of $t$ for $a/\rho_i = 157$ . Lower panel: $< \sigma^2 > / t^p$ as a function of $t$ for $a/\rho_i = 315$ . . . . .	177
6.25	Time history of electron particle flux . . . . .	183
6.26	The typical snapshots of mode structure in the linear (left panel) and nonlinear (right panel) regime of the TEM turbulence for the system size $a/\rho_i = 157$ . . . . .	183
6.27	The spatio-temporal evolution of turbulent field intensity due to TEM turbulence . . . . .	184
6.28	Hot ions are inserted at $t = 0L_n/c_s$ , (a) when there is no TEM activity (left panel) and (b) when TEM turbulence is ON (right panel). . . . .	185
6.29	Hot ions are inserted at $t = 70L_n/c_s$ (a) without TEM turbulence (left panel) and (b) in the presence of TEM turbulence (right panel). . . . .	186
6.30	Probability distribution function of hot ions for isotropic distribution . . . . .	187
6.31	$< \sigma^2 > / t^p$ as a function of $t$ for isotropic hot ions. . . . .	187

6.32	$D_h$ versus energy of the hot ions for isotropic distribution; (a) in linear scale (upper panel) and (b) in log-log scale (lower panel). . .	190
6.33	Passing hot ions are inserted at $t = 0L_n/c_s$ (a) without TEM turbulence (left panel) and (b) in the presence of TEM turbulence (right panel). . . . .	191
6.34	Trapped hot ions are inserted at $t = 0L_n/c_s$ (a) without TEM turbulence (left panel) and (b) in the presence of TEM turbulence (right panel). . . . .	192
6.35	(a) Upper panel: PDFs for hot ions with passing distribution, (b) lower panel: PDFs for hot ions with trapped distribution . . . . .	194
6.36	$\langle \sigma^2 \rangle / t^p$ as a function of t for passing hot ions. . . . .	195
6.37	$\langle \sigma^2 \rangle / t^p$ as a function of t for trapped hot ions. . . . .	195
6.38	(a) Upper panel: $D_h$ versus energy of the hot ions for passing distribution, (b) Lower panel: $D_h$ versus energy of the hot ions for trapped distribution in linear scale. . . . .	197
6.39	(a) Upper panel: $D_h$ versus energy of the hot ions for passing distribution, (b) Lower panel: $D_h$ versus energy of the hot ions for trapped distribution in log-log scale. . . . .	198

# List of Tables

2.1	Profiles and parameters . . . . .	30
4.1	Profiles and parameters . . . . .	64
4.2	Profiles and parameters . . . . .	82
5.1	Profiles and parameters . . . . .	104
5.2	Normalization of dependent variables. . . . .	124
5.3	Normalization of independent variables. . . . .	125
6.1	Profiles and parameters . . . . .	146
6.2	New values of mean $p$ and values measured in Section 6.3.6 (see Fig. 6.16) for $a/\rho_i = 157$ . . . . .	174
6.3	New values of mean $p$ and values measured in Section 6.3.6 (see Fig. 6.16) for $a/\rho_i = 315$ . . . . .	175
6.4	Energy, standard deviation, kurtosis, skewness, exponent $p$ for isotropic hot ions . . . . .	188
6.5	Energy, standard deviation $\sigma$ , kurtosis $k$ , skewness $s$ and exponent $p$ in $\langle \sigma^2 \rangle \propto t^p$ for the passing hot ions . . . . .	193
6.6	Energy, standard deviation $\sigma$ , kurtosis $k$ , skewness $s$ and exponent $p$ in $\langle \sigma^2 \rangle \propto t^p$ for the trapped hot ions . . . . .	195

# Chapter 1

## Introduction

### 1.1 Magnetically Confined Fusion and Its Prospects

In view of the much speculated dearth of energy in near future leading to an imbalance between demand and supply, the focus of energy research has largely shifted to the nuclear fusion of deuterium and tritium<sup>1</sup> in the plasma state, which is envisaged to generate virtually limitless energy with minimal adverse environmental impact. Although, the phenomenon of nuclear fusion is quite common in our universe (for example, the sun in our solar system provides light and heat via fusion reaction naturally), the natural occurrence of fusion on earth is inhibited by the need of the very high temperature propitious for the fusion reaction. One has to arrange, therefore, laboratory plasma experiments to harness energy from fusion on earth. And at the same time, one also has to look for ways that prevent direct contact of this high temperature plasma with the container wall. Since fusion needs high temperature and density, a material shielding therefore is incapable to contain the hot fuel, as the high heat load on the container wall will apparently make the latter unable to withstand so much of heat. For this reason, one has to devise ingenious confinement methods to avert such a situation.

There are various special confinement schemes that have been able to allure researchers in the field. Some of them are magnetically confined fusion (MCF) [1], inertial confinement fusion (ICF) [2], etc. Here we focus on MCF which has been able to garner significant attention and resources since its inception.

---

<sup>1</sup>  ${}^2_1H + {}^3_1H = {}^4_2He + {}^1_0n + 17.4 \text{ Mev}$

## Chapter 1: Introduction

The MCF method relies on using powerful magnets to confine plasma in a donought-shaped high-vacuum vessel named as **Tokamak**. The concept of such a scheme is to heat deuterium tritium (D-T) ions to a very high temperature of the order of hundred million degrees of centigrade and then confine the system using curved and closed magnetic field for long enough time such that the two species of ions can fuse effectively overcoming the Coulomb barrier to release energy in the range of MeV, which then can be extracted by proper arrangements (For example, Test Blanket Module (TBM) [3].), and made commercially available for civil purposes. Since its realization during 1960s, scientists have acquired much expertise on tokamak and have therefore moved one step ahead to build ITER [3] to test fusion with gain factor more than one. As is apparent, efficient heating and then long confinement are two key factors that determine the success of such an endeavor<sup>2</sup>.

The heating process starts with the ohmic heating mechanism and then in the later phase where ohmic heating is no longer effective due to reduced collisions, heating is supported by various auxiliary methods. Among the various auxiliary heating schemes, neutral beam injection (NBI) and RF heating (For example, ion cyclotron resonance heating (ICRH), electron cyclotron resonance heating (ECRH), etc.), where the energy is first transferred to the thermal electrons and then to the ions, are very often used. These heating schemes thus incorporate large amount of hot ions into the system of thermal ions and electrons. Moreover, once the fusion is accomplished, the tokamak itself becomes populated with fusion produced Helium ions or  $\alpha$  particles of MeV energy. In the self ignition phase, these helium ions are required to transfer their energy to the thermal ions. Thus it is clear that for efficient heating of the thermal ions and subsequent fusion, one requires that the hot ions (along with the thermal ions and electrons) be confined in the system for long enough time, and transfer their energy to the thermal ions which are eventually going to fuse.

The major hurdle in maneuvering fusion in a plasma laboratory, however, appears to be the poor confinement of plasmas brought about by the exotic behavior of these extremely hot and dense charged particles in the presence of magnetic field. Various physical mechanisms which are self-generated in the plasma throw parti-

---

<sup>2</sup>Lawson criterion requires  $nT\tau_E > 3 \times 10^{21}$  keV sec/m<sup>3</sup>, where,  $n$ ,  $T$  and  $\tau_E$  are, respectively, density, temperature of plasma and plasma confinement time.

## Chapter 1: Introduction

cles and heat out of the system undermining the confinement and hence blurring the hope of realistic fusion machines.

These mechanisms, often referred to as instabilities, are broadly classified as macroinstabilities and microinstabilities [4, 5] depending upon their scale-length and frequency compared to the Larmor radius and gyrofrequency of the constituent charged particles. Macroinstability generally refers to the large-scale magnetohydrodynamics (MHD) instabilities. They can quench the plasma in microseconds which otherwise would have been several seconds long lived [6]. Though with proper field configuration this class of instabilities can be suppressed, the plasma is still subject to fine-scale instabilities, often referred to as microinstabilities driving loss of energy and particle. These instabilities are equally capable to influence the dynamics of the energetic ions. Thus, in order to learn how to tame these instabilities, researchers, before constructing real fusion reactors, would want to understand the basic confinement, stability and transport issues of charged particles in a relatively simpler environment. To that end, many tokamaks<sup>3</sup> have been built around the world which exploit the magnetic confinement to lighter charge particles, e.g., hydrogen in extreme conditions of temperature and density to investigate the inherent stability and transport issues of toroidal plasma.

The motion of the charged particles in a magnetic field, in the simplest case, is confined to a helical path along the magnetic field line [7]. The maximum step size of any movement across the magnetic field, therefore, is equal to their Larmor radii. The collisions among themselves, although infrequent (as the system is very hot), bring in random walks in the system. As a result of this, the charge particles jump from one position to another with the step size of Larmor radius resulting in what is called classical diffusion. However, the magnitude of such classical diffusion of particles and their thermal energy across the magnetic field lines is about thousand times lower than that observed in regular tokamak experiments [1].

The classical model of diffusion is nevertheless modified and made complex by the presence of the curved magnetic field in tokamaks. The curved magnetic field can trap charge particles leading to a larger step size of random walks, of the order of radius of banana orbits [1] of the trapped particles, enhancing the amount of transport. This modifies the estimate of the classical diffusion and termed as

---

<sup>3</sup>For example, JET, DIII-D, ASDEX, JT60, etc.

## Chapter 1: Introduction

neoclassical diffusion process. However, the experimentally observed diffusion rate is still order of magnitude higher than that predicted by the neoclassical theory [1]. This discrepancy between the theoretical prediction and experimental observation in diffusion rate of energy and particles is termed as “anomalous” due to the lack of understanding of the physics issues imparting this anomaly.

Even when plasmas are maintained free from MHD instabilities, they are far from being quiescent. As confined plasmas are invariably associated with inhomogeneities in density and temperature, they are, therefore, always in the state of tremulous movement induced by some fine scale (of the order of Larmor radius of the charge particles) and low frequency fluctuations (smaller than the gyrofrequency of the ions). These turbulent, fine scale and low frequency fluctuations, generally defined as microinstabilities, are capable to transport energy and charged particles out of the system at a rate faster than the classical and neoclassical diffusion. Such a transport, in general, is the consequence of random walks of the constituent charged particles with an enhanced step size and reduced correlation time in the presence of turbulence resulting from the microinstabilities, and perhaps accounts for the observed anomaly in transport via ion and electron channels.

Among the various microinstabilities, ion temperature gradient (ITG) modes [4, 8, 9, 10, 11, 12, 13, 14, 15, 16, 17, 18] are now firmly believed to cause anomalous transport of thermal ions, while, electron temperature gradient driven (ETG) [19, 20, 21, 23, 24] modes and trapped electron modes (TEM) [11, 25, 26, 27, 28] are observed to produce anomalous transport of electrons. The ITG modes are driven by the free energy available in the gradient of temperature profile of thermal ions, while ETG and TEM draw free energy from the gradient of temperature profile of electrons. Universal toroidal modes which live on the free energy available in the inhomogeneity of electron density, and hence seem to be ubiquitous, are also another class of microinstabilities driving electron transport.

While electron transport exhibits a multiscale feature ranging from the electron Larmor radius ( $k_{\perp}\rho_{Li} \gg 1$ ) of the ETG mode to the ion Larmor radius ( $k_{\perp}\rho_{Li} \leq 1$ ) of the TEM, ion transport driven by the ITG mode, on the other hand, is hitherto known to be unstable only at one scale length on the order of the ion Larmor radius ( $k_{\perp}\rho_{Li} \leq 1$ ). However, of late, a new mode [29] propagating in the ion diamagnetic direction, on the intermediate scale between ITG and ETG mode with  $k_{\perp}\rho_{Li} > 1$  joins the group of microinstabilities imparting multi-scale

## Chapter 1: Introduction

feature to the thermal ion transport. This mode is generally referred to as the short wavelength ion temperature gradient (SWITG) mode following its occurrence in the shorter wavelength side of the dispersion spectrum of microinstabilities.

Concerted efforts of theory, experiment and simulation to understand, both qualitatively and quantitatively, the behavior of the plasmas in a tokamak are under way among the fusion communities. Attempt to compose simulation models to make quantitative predictions of transport is very much sought. As tokamak experiments themselves are very much expensive, a proper modeling of the mechanisms could prove very useful in identifying and separating the various underlying physics issues one by one without pursuing repeated experiments for that purpose. However, due to the disparate masses of the constituting particles such as ions and electrons, a consistent numerical study of transport via ion and electron channels simultaneously has proved to be a formidable task. When one attempts to model a phenomenon, where both electrons and ions are nonadiabatic, one has to take into account the larger spatial scales (*i.e.* Larmor radius) and slower time scales (*i.e.* gyro period) of ions on one hand, and the finer spatial scales and faster time scales of electrons on the other hand for a given temperature and magnetic field, which sometimes goes beyond the computational resources available, in particular, in the case of nonlinear, time-evolving, numerical models using kinetic theory. Moreover, the instabilities are often found to be nonlocal spreading over a substantial fraction of the tokamak cross section both in the linear and nonlinear phase, the comprehensive study of which invariably demands global simulation aggravating the situation. A minimal nontrivial linear, global, gyrokinetic numerical model can be enormously useful to that effect, at least, to identify and understand physical mechanisms in the simplest case. However, one needs eventually to validate them with respect to the nonlinear turbulent models.

### 1.2 Brief Review of Earlier Works

Anomalous transport in collisionless hot tokamak plasmas is believed to be due to the drift waves driven by the density and temperature gradients [4, 5] of the charge particles in a magnetically confined plasma. While the turbulent heat flux of ions is believed to be driven by the ion temperature gradient (ITG) mode, the

## Chapter 1: Introduction

electron heat and particle flux, on the other hand, is expected largely to be driven by the trapped electron mode (TEM) in the low magnetic field side of a tokamak on ion scales (of the order of ion Larmor radius) and by the electron temperature gradient (ETG) mode on electron scales (of the order of electron Larmor radius). Enormous effort has been put to understand the underlying physics issues both theoretically and computationally and then to match the predicted transport flux with that observed experimentally.

The study of ion transport by the ITG mode has started with simple models [30, 31], where electrons are treated adiabatic. The next step is then to incorporate the nonadiabatic electrons. This has been achieved in the form of trapped electrons included to the background model of nonadiabatic ions and adiabatic passing electrons. This has extended the study of this class of microinstabilities to the trapped electron coupled ITG mode (ITG-TEM) [11, 12, 13, 14, 15, 16, 17, 18] mode and TEM [11, 25, 26, 28, 32]. The new models with trapped electrons give growth rate two to three times larger than that in the case of simple adiabatic electron models. At the same time, the transport flux is observed to rise substantially. A comparison of gyrofluid [33] and continuum gyrokinetic [34] simulation of transport in realistic geometry with experiments has been carried out, and the electron thermal diffusivity, ion thermal diffusivity and perturbed density fluctuation level are found to exceed the experimental value by factors more than two. The reason of this deviation is speculated to be due to the *non-local* behavior owing to the variation of plasma gradients.

Following this, sophisticated flux ribbon codes have come up with advanced features [35, 36] to reduce the discrepancy between experiments and computational results [37]. The kinetic electron simulation with trapped particles using generalized split weight scheme to  $\delta f$  gyrokinetic particle method has been carried out [38]. The results show significant increase in the ion heat diffusivity in comparison with that in the case of the adiabatic electron model in line with the increased growth rate. However, the experimentally observed ion diffusivity [39] is much lower than that predicted by the adiabatic electron models. Thus, more comprehensive gyrokinetic models that treat electrons and ions on the same physics footing with global profile effects are required to address such anomaly.

The major problem with the incorporation of full dynamics of electrons including even the passing fraction nonadiabatically or kinetically in a time dependent

## Chapter 1: Introduction

model is their fast parallel motion. The high mobility of these electrons needs higher resolution in their response time scale, and is a formidable task in the presence of full ion dynamics, the issue of which is discussed elaborately in Ref. [40]. With advances in the computational facilities significant progress has been achieved to this end to treat the electrons fully kinetically [36, 157, 139]. However, sometimes simulations choose reduced mass ratios of ion and electron to downsize the computational cost [32, 40, 42].

While ion transport can be brought down to neoclassical level by the formation of internal transport barriers (ITBs) [67, 68], the electron transport still remains orders of magnitude above the neoclassical level. The electron anomalous transport is an issue of paramount concern in the fusion plasma because of the fact that the electrons will be heated dominantly by the collisional relaxation of the highly energetic  $\alpha$  particles and the instabilities inherent to electrons can deteriorate the process of confinement of the plasma.

The experiments on electron transport [69] observe stiffness in the electron temperature profile and suggest a threshold in the electron temperature gradient  $\nabla T_e/T_e$  above which the turbulent transport takes place. This supports two theoretically proposed modes, namely, the TEM and ETG mode.

The existence of such a threshold has been established and its experimental determination is achieved by further experiments [70, 71, 72]. Although, a complete radial profile of transport threshold has been evaluated in Ref. [73], whether the observed transport is because of TEMs or ETG modes remains difficult to determine unambiguously, as both modes exhibit threshold in  $\nabla T_e/T_e$ .

The TEMs have their origin in the precession of trapped electrons on the weaker side of the magnetic field and been studied extensively, both experimentally [69, 73, 74, 75, 76, 77] and theoretically [25, 26, 27, 28, 78, 79, 80, 81]. The TEMs have wave number in the range of ITG modes; they have dependence on the gradient threshold, fraction of trapped electrons, and collisionality; they are active when  $\tau(= T_e/T_i) > 1$ .

The other source of electron transport, the ETG mode was studied initially in the sheared slab geometry [19, 20] and then in the toroidal geometry [21]. With the advanced diagnostics, now a days, it has been possible to identify the ETG mode even in experiments [82, 83]. The ETG mode because of its small scale, initially was not expected to contribute significantly to the electron transport. But

## Chapter 1: Introduction

the electron heat diffusivity is usually found to be of orders of magnitude higher than the simple mixing length estimate. The works in Refs. [23, 24, 84, 85, 86, 87] showed that in spite of its small scale length, the ETG mode can indeed contribute to the electron particle and heat losses comparable to the experimental level by the formation of radially elongated structures or convective cells nonlinearly or through electromagnetic inverse cascade processes. While the ITG mode is suppressed by the  $E \times B$  shear [88, 89] in ITBs, the electron transport is still observed to be anomalous as it is barely affected by the  $E \times B$  shear [90]. Under special circumstances, such as reverse shear, one may be able to reduce TEM induced transport but ETG is nonetheless expected to remain unaffected because of its higher growth rate than the  $E \times B$  shearing rate.

Earlier studies on microinstabilities, in general, proceed with a tacit assumption that the mode under consideration is independent of other members of the class. But, studies of the ITG mode in the presence of the trapped electrons, i.e., ITG-TEM [11, 12, 13, 14, 15, 16, 17, 18] have shown that one mode can have strong effect on the other. For example, often ions are considered adiabatic while studying the ETG mode. The ions, because of their larger Larmor radius, can attain adiabaticity by moving across the magnetic field. However, recent works in Refs. [36, 37, 91, 92, 93, 94] showed that the ion dynamics can play an important role in the ETG scale transport and help achieving saturation of electron flux. Although ITG coupled to the trapped electrons has been studied in details, studies of ETG coupled to TEM (ETG-TEM) have been very few [91, 92].

In the absence of temperature gradients, there can be another class of instabilities, which is driven even by the slightest density gradient of the electrons in the plasma and therefore called the universal drift instability. In the late 1980s, there had been a large effort to understand the basic physics of the universal drift instability. The motivation was that the universal drift mode was thought to be the dominant microinstability at that time and thus source of plasma transport in the various confining devices, such as, tandem mirror, tokamak, spheromak, stellarator, etc. In situations where the density profile is steeper than the temperature profile, one can indeed have fluctuations and associated transport dominated by the universal drift instability. Moreover, the universal instability is the simplest one in the class of drift waves and a thorough understanding of the mode can help get insight in the other modes of the family as well.

## Chapter 1: Introduction

The study of the universal drift wave had started with a very simple model, the shearless slab model [95, 96], that revealed that the collisionless universal drift instability is always unstable in the presence of a density gradient and absence of shear. The driving mechanism in this case is the wave particle resonance by the electrons coupled with the density gradients. The mode remains unstable, in the presence of weak but reasonable shear, when studied in the framework of the adiabatic electron model. Thus, up to that point, the speculation was that the universal mode without or with weak shear is always unstable. However, in contradiction to all previous works, Ross *et al.* [97] and Tsang *et al.* [98] reported that the universal instability or collisionless drift instability in the presence of magnetic shear is always stable in the slab geometry, irrespective of the strength of the shear or transverse wave number when one takes into account the full electron dispersion function. The observed stability is attributed primarily to the stabilizing influence of the nonresonant electrons. These issues had further been addressed by Chen *et al.* [99] who concluded that the mode can be damped and marginally stable depending upon the strength of the shear and magnitude of the transverse wave number  $k_y$ . For example, in the case of sufficiently weak shear, i.e., with  $L_s/L_n$  greater than a critical value (where  $L_s$  and  $L_n$  are, respectively, the measure of shear and density gradient scale length) collisionless drift waves are marginally stable at shorter wavelength or high wave number regime, where the electron dynamics usually play the pivotal role in determining the nature of an eigenmode. In the opposite limit, i.e., at longer wavelength or lower wave number regime where ion dynamics dominate, the eigenmode is damped. For strong shear, on the other hand, the eigenmodes are always stable irrespective of the wave number or wavelength. However, even in a sheared magnetic field, an absolute instability can be observed by the elimination of the stabilization produced by the off-resonant electrons by the turbulent diffusion near the mode rational surfaces [100].

The investigation of the various properties of the universal drift instability in a more complex situation such as in the presence of finite toroidicity was undertaken by Cheng *et al.* [101]. Two eigenmodes were found to coexist that are brought about by the equilibrium variation along the field line. One mode is not localized in the ballooning coordinate and gets strongly stabilized due to the magnetic shear, much like the slab version of the mode. The other eigenmode is observed to have no slab counterpart. It was shown to be intrinsically driven by the toroidicity,

## Chapter 1: Introduction

partly localized, and weakly affected by the stabilization of the magnetic shear. It was shown that while it is rendered as an absolute instability by the electron Landau resonance, ion Landau damping on the other hand has a stabilizing effect on the mode. It is important to note that the formulation in Ref. [101] uses the ballooning formalism applicable only in the high  $n$  (toroidal mode number) limit, considers  $k_{\perp}\rho_{Li} \ll 1$  and keeps the toroidal coupling effect only through the ion  $\nabla B$  and curvature drift. The ion drift frequency, however, is assumed very small compared to the mode frequency  $\omega$  and ion drift resonance is thus ignored. Studies involving more complex geometries, such as in small aspect ratio tokamaks or spheromaks [102] were reported later. Modes are found to be less localized at different positions of poloidal angle when one removes the large aspect ratio assumption. However, except for the presence of more than one mode along the poloidal direction because of the strong equilibrium variations along the field line, the results are qualitatively the same as for the case of former large aspect ratio. The role of ion magnetic drift resonance and electron Landau resonance are discussed by Chep *et al.* [103] using the ballooning formalism with gyrokinetic theory. The conclusion is that along with magnetic drift resonance, one requires electron Landau resonance to make the mode unstable. However, this study precludes the role of the transit frequency of the thermal ions by assuming the mode frequencies to be higher than the transit frequency of the thermal ions. Berk *et al.* [104] showed that the universal drift instability is stabilized by the presence of finite plasma  $\beta$ . This can be understood to result from the coupling of the universal drift wave to the Alfvén mode and from the effect of ion Landau damping. Hastings *et al.* [105], considering a slab geometry with finite  $\nabla B$  and using gyrokinetic theory, find two mechanisms of stabilization of the mode by finite  $\beta$ : (1) for small values of  $\beta$  in the range  $m_e/m_i < \beta \ll 1$ , the stabilization is brought about by the coupling to the Alfvén wave and (2) for  $\beta \sim O(1)$ , the stabilization is due to the compression of the perturbed plasma motion.

While electron transport exhibits a multiscale feature ranging from the electron Larmor radius ( $k_{\perp}\rho_{Le} \gg 1$ ) of the ETG mode to the ion Larmor radius ( $k_{\perp}\rho_{Li} \leq 1$ ) of the TEM, ion transport driven by the ITG mode, on the contrary, is hitherto known to be unstable only at one scale length on the order of the ion Larmor radius ( $k_{\perp}\rho_{Li} \leq 1$ ). However, of late, a new mode, with mode frequency in the direction of the ion diamagnetic drift frequency, on the intermediate scale between

## Chapter 1: Introduction

ITG and ETG mode with  $k_{\perp}\rho_{Li} > 1$  has been identified [29]. This mode is found to be driven by the temperature gradient of the ions in the presence of the Landau resonance/inverse resonance in a slab geometry and by the toroidal drift resonance in a toroidal geometry, in combination with the nonmonotonic behavior of the mode frequency with respect to the perpendicular wave number. Because of its occurrence in the short wavelength limit and due to the nonadiabaticity of ions, the mode is named as short wavelength ion temperature gradient (SWITG) mode to distinguish it from the conventional ITG mode at longer wavelength. It is generally speculated that in the limit  $(k_{\perp}\rho_{Li})^2 \gg 1$ , there should be no mode intrinsic to the ion nonadiabaticity, since ion dynamics in this limit is expected to be adiabatic. However, if the scale length of the inhomogeneity is such that  $\omega_{*i}$ , the ion diamagnetic drift frequency becomes larger than the mode frequency  $\omega$ , there can be an instability related to the inhomogeneity in the ions even in this shorter limit [106].

Initially, the mode was thought to be of hybrid type [106, 107], requiring both  $\eta_i$  and  $\eta_e$  (ratio of the density to temperature scale length of the ions and electrons respectively) to be above a threshold. Later parametric study by Gao *et al.* [108] demonstrated that the electron nonadiabaticity is not an essential ingredient for the mode to develop. Effect of the nonadiabatic electrons is only to enhance the growth rate of the mode. The theoretical study of this mode started with the work of Smolyakov *et al.* [29] in a sheared slab and toroidal geometry using a local formulation. The work was then extended by Hirose *et al.* [106] using a kinetic integral code based on ballooning formalism. This was followed by the study of the mode in the sheared slab [107] and then in the toroidal geometry [108] by Gao *et al.* Effects of shear flows on this mode have been studied in the sheared slab geometry and found to have strong stabilizing impact on the mode [109]. However, it is expected that the toroidal SWITG mode will need higher rate of EXB flow shear for stabilization than the conventional toroidal ITG mode as the former has higher frequency [108]. The dependence of the critical gradient on the various physical parameters such as temperature ratio, toroidicity, magnetic shear and safety factor has been studied for this mode [110]. It is to be noted that such a double hump behavior was pointed out a long way back by Pu *et al.* [111] while studying the ion mixing mode. The main conclusions, from the past works are the following. (1) In the slab limit (small toroidicity  $\epsilon_n = L_n/R$ ), a strong temperature gradient

## Chapter 1: Introduction

driven mode exists in the regime  $(k_{\perp}\rho_{Li})^2 \gg 1$ . The instability requires both  $\eta_i$  and  $\eta_e$  to be above a critical value [106, 107]. But later study [108] reveals that it is inherently an ion mode and exists even if the electrons are adiabatic. The same is observed in the work of Smolyakov *et al.* [29]. (2) Toroidicity has strong stabilizing effect on the mode [106]. Stabilization occurs at  $\epsilon_n \geq 0.15$ . (3) The instability is driven by magnetic shear and the growth rate is approximately proportional to  $\sqrt{|s|}$  [106] where  $s$  stands for the shear. But a broader parameter scan [108] finds that the growth rate initially increases and then starts decreasing with shear. (4) Similar to the conventional ITG, it is also stabilized by a modest  $\alpha$ , the ballooning parameter. (5) Nonadiabatic circulating electron dynamics provide destabilization. (6)  $E \times B$  flow shear has strong stabilizing effect on the mode.

The microinstabilities discussed above not only throw out the thermal ions and electrons but also the energetic ions produced by the auxiliary heating schemes and  $\alpha$  particles of energy in the MeV range produced as the fusion product. These energetic particles constitute a considerable fraction of the total plasma, and thus a sound understanding of the role of these energetic ions on the plasma confinement through the interaction with the background instabilities is very much required. The various magnetohydrodynamics (MHD) events are observed to transport and redistribute the energetic ion population via resonant and nonresonant phenomena [115, 116]. For example, resonant MHD activities such as fishbone, toroidal Alfvén mode (TAE), etc., can cause large transport of the energetic ions. Similarly, high  $\beta$  sawteeth can also produce loss of the energetic ions. The low frequency MHD modes such as neoclassical tearing modes (NTM) are equally capable to drive both passing and trapped energetic ion loss [117, 118]. The toroidal field ripples and stochastic magnetic field are also among the other mechanism of fast ion losses. The energetic ions can in turn also alter the stability of the plasma by exciting and sometimes suppressing the MHD events. One may, for example, note the observed stabilization of sawteeth by perpendicular energetic ion population, the destabilization of internal kink mode, TAE, fishbone, etc. The energetic ions also can give rise to modes on their own which are generally named as energetic particle modes (EPM) [119].

Though much understanding and confidence have been gained in the case of the interplay between MHD and energetic ions via theory and experiments, little attention is paid toward the interaction of these energetic ions with the microtur-

## Chapter 1: Introduction

bulence induced by the ITG mode, TEM, ETG mode, etc. One partial reason could perhaps be the observation of very weak diffusivities of the energetic ions and  $\alpha$  particles in comparison with the thermal ions experimentally [115, 116, 120] as well as theoretically [121]. The reason for it, as speculated, is that the energetic ions do not stay in resonance with these microturbulence driven fluctuations as their drift orbit radii are far higher than the radial correlation length of these fluctuations, and therefore average over the fluctuation spectrum temporally and spatially. These phenomena are generally defined as drift averaging and gyroradius averaging [115]. On the contrary, recent numerical experiments [122] have shown that  $\alpha$  particle and energy loss could be higher than the corresponding losses of thermal ions and large orbit averaging is not strong enough to ignore the interaction of the  $\alpha$  particles with ITG turbulence. However, it is a recent experiment [123] reporting evidence of correlation between microturbulence and redistribution of energetic ions that has spurred a fresh interest among the researchers in the subject. Even in the absence of any MHD activity, fast radial broadening of the current profile driven by the off axis neutral beam injection (NBI) has been observed supporting the fact that there must indeed be some correlation between redistribution of energetic ions and background microturbulence. This has been further studied in Refs. [124, 125]. Following this, numerical analysis [126] on the interaction of energetic ions with ITG turbulence observes  $1/E$  dependence for the passing energetic ion diffusion, where,  $E$  is the energy of the energetic ions and  $1/E^2$  dependence for the trapped energetic ion diffusion. Similar study [127] found  $1/E$  dependence of diffusion for the beam energetic ions in the presence of electrostatic fluctuation. In contrast, the diffusion of the energetic ions in the presence of magnetic fluctuations [127] has been found to be independent of the particle energy, and therefore, may play more important role than the electrostatic fluctuations in redistributing the energetic ions. The reciprocal dependence of diffusivity on the particle energy of the energetic ions could be one of the reasons for the superficial effect of microturbulence on the energetic ions observed in the earlier experiments. The difference in the born energy of the energetic ions between the earlier and recent experiments can be a likely explanation of the difference in the observations regarding the effect of microturbulence on these energetic ions. Note that such phenomena of redistribution of hot ions by microturbulence is not confined to only toroidal devices like tokamaks; experiments on linear system also confirm

## Chapter 1: Introduction

the interaction of hot ions with density gradient driven turbulence [172]. Astrophysical plasmas also encounter similar phenomena resulting from interaction of the energetic ions with turbulent field [129].

Coming back to the back reaction of energetic ions on microturbulence, one may cite latest experiments [130] that has reported signature of internal transport barrier (ITB) in the ion channel even in the absence of reverse shear. The formation of the ITB has been observed to have correlation with the transport suppression mechanism by the injected energetic ions with a lifetime of the order of slowing down time of the beam ions. Similar observation of the ITG mode suppression by the energetic ions produced by ion cyclotron resonance heating (ICRH) and concurrent formation of the ITB triggered by these energetic ions in a plasma with monotonic safety factor profile has been reported in Ref. [131].

In the backdrop of this wide, complex and nonlocal scenario of plasma behavior in MCF systems the present dissertation is dedicated to the study of the stability properties of few microinstabilities which usually play the pivotal role in causing anomalous transport of energy and particles in tokamaks. In particular, it highlights (1) effects of the nonadiabatic passing electrons on the ion temperature gradient (ITG) mode, trapped electron coupled ion temperature gradient mode (ITG-TEM) and trapped electron mode (TEM) by linear, global, gyrokinetic numerical study; (2) the behaviour of the ion temperature gradient driven modes in the presence of highly steep density profile typically observed in the transport barriers inside the tokamak; a linear and nonlinear gyrokinetic study on the occurrence of the short wavelength ion temperature gradient mode (SWITG); (3) a linear, global, gyrokinetic stability analysis of the universal toroidal mode, which although is thought to be ubiquitous, yet overshadowed by the temperature gradient driven modes; (4) the stabilization of the microinstabilities by the hot ions (those ions having temperature higher than the thermal ions), and finally, the redistribution of the hot ions by microturbulence with the help of linear and nonlinear, global, gyrokinetic simulations.

### 1.3 Thesis Outline

As the title says, the present dissertation studies the linear and nonlinear properties of the temperature and density gradient driven microinstabilities using global, linear and nonlinear, gyrokinetic models.

Chapter 2 details the linear, global, gyrokinetic model which is the core of the linear gyrokinetic spectral code EM-GLOGYSTO [11, 44]. The nonadiabatic/kinetic passing electrons are introduced to the electrostatic model. The rest of the sections of Chapter 2 thus elucidates the observed effect of the nonadiabatic/kinetic electrons on the various properties of the linear global ITG mode.

In Chapter 3, the new nonadiabatic/kinetic model introduced in Chapter 2 for passing electrons is used to study the trapped electron coupled ITG (ITG-TEM) mode and trapped electron mode using the code EM-GLOGYSTO. The effect on the linear growth rate and real frequency, global electrostatic mode structure, critical temperature gradient, etc., have been discussed for the ITG-TEM and TEM in separate sections.

Chapter 4 discusses the modes inherent to nonadiabatic passing electrons, namely, the electron temperature gradient mode (ETG) driven by the temperature gradient of the passing electrons and universal drift mode driven by the density gradient of the passing electrons. For ETG, the basic properties of the mode have been studied with and without the Debye shielding effect. The results obtained for the linear ETG mode are well known [21, 22]. We then move to use the nonadiabatic electron model to study the universal toroidal drift instability, which is overshadowed by the temperature gradient driven modes. We have discussed the various linear properties of the mode and its presence amid the temperature gradient driven modes. It has been observed that this mode can coexist with the ITG and TEM, and can contribute to the electron transport which is usually thought to be from the ETG and TEM only.

A new branch of the ITG mode has been reported recently. This mode is unstable at  $k_y \rho_i > 1$ , where,  $k_y$  and  $\rho_i$  are, respectively, poloidal wavenumber and ion Larmor radius, and therefore named as the short wavelength ion temperature gradient (SWITG) mode. A linear global gyrokinetic study has been carried out for the first time, using the spectral code EM-GLOGYSTO. The various linear properties and global mode structure have been studied with and without the

## Chapter 1: Introduction

presence of trapped electrons. The results are presented in Chapter 5. Corresponding nonlinear study is carried out using the flux tube version of the global, nonlinear, Eulerian, gyrokinetic code Gyrokinetic Electromagnetic Numerical Experiment (GENE) [32, 84]. It is observed that although linearly the SWITG mode can be as strong as the standard ITG (with  $k_y \rho_i \leq 1$ ), nonlinearly the mode has very weak contribution to the net thermal ion heat transport compared to the standard ITG mode.

The study of the interaction of the microturbulence and energetic ions has emerged as a very important area of research following experiments in ASDEX and DIII-D. In Chapter 6, the interaction between the energetic ions and microturbulence generated by the temperature gradient driven modes has been studied. The chapter comprises of three sections. In the first section, the effect of energetic ions on the linear ITG mode is studied nonperturbatively using the spectral code EM-GLOGYSTO. A third species of ions has been added to the existing two species version nonperturbatively, and the effect of the energetic ions on the linear properties of the ITG mode has been studied. The second section deals with the nonlinear study on the effect of the turbulent field generated by the ITG mode on the energetic ions. For the purpose we have used the global, nonlinear, gyrokinetic, first principle based (PIC method) code Gyrokinetic Tokamak Simulation (GTS) [139, 140]. The energetic ions are introduced to the code as passive tracers that exhibit random walks in the presence of the equilibrium and turbulent fields. The energy and system size dependence of the energetic ions have been evaluated in the presence of the ITG mode turbulence. In the third section of the chapter, the influence of the TEM turbulence is studied using the code GTS and same passive tracer method. Three different distributions for the energetic species, namely, isotropic, passing and trapped distributions have been considered and the respective transport properties have been investigated. The different energy scalings for different types of distribution mentioned above are estimated and the nature of transport is studied.

## Chapter 2

# Role of nonadiabatic/kinetic passing electrons in global electrostatic ion temperature gradient driven modes in a tokamak

### 2.1 Introduction

Tokamak plasmas, which are stable to ideal magnetohydrodynamic (MHD) disturbances, exhibit transport of particles and energy across magnetic flux surfaces. On longer time scales compared to particle and energy confinement times, such transport phenomena, which arise due to equilibrium inhomogeneities, are attributed to the low frequency drift waves in the plasma.

Among others, toroidal ion temperature gradient driven drift modes (ITG) [8], trapped electron modes [25], high- $n$  Alfvén ion temperature gradient driven modes or high- $n$  kinetic ballooning modes [43] ( $n$  is the toroidal mode number) have been studied extensively both in linear and nonlinear regimes. For large  $n$ , where it is expected that the mode structure would be localized to a magnetic flux surface, the ballooning formalism is a commonly used technique. For global modes with small  $n$  values, the profile effects do play a role, and therefore, the usual ballooning formalism fails to retain these effects. The global linear and nonlinear gyrokinetic models then become necessary.

## Chapter 2: Role of nonadiabatic/kinetic passing electrons in global electrostatic ion temperature gradient driven modes in a tokamak

For ITGs, such global gyrokinetic models show that the linear growth rate peaks between  $n \simeq 3$  and 15 such that  $k_{\theta}\rho_{Li} \approx 0.5$ . For example, for typical tokamak parameters, the global electrostatic toroidal gyrokinetic spectral model GLOGYSTO [11, 44] and time-evolving gyrokinetic codes [45] report typical toroidal mode numbers in the range  $3 \leq n \leq 15$  with eigenmode structure occupying a good fraction of the minor radius  $a$ . These eigenmodes span several mode rational surfaces (MRS)  $r = r_{MRS}$  defined as  $k_{||m,n}(r = r_{MRS}) = 0$ . In these models, the passing and trapped ions respond nonadiabatically while passing electrons are assumed adiabatic.

An electromagnetic version of GLOGYSTO called EM-GLOGYSTO has been developed by including passing drift kinetic electrons coupled to  $A_{||}$  fluctuations [46] followed by fully gyrokinetic electron dynamics coupled to  $A_{||}$  fluctuations and equilibrium flows [47]. The code EM-GLOGYSTO was generalized by including fully gyrokinetic nonadiabatic passing ion and electron dynamics which couple to  $A_{\perp}$  fluctuations, Shafranov shift effects [48], followed by trapped electron dynamics coupled to  $A_{\perp}$  fluctuations [11, 49]. It has been shown that when passing drift kinetic electrons couple only to  $A_{||}$  [46, 55], finite- $\beta$  effects have a benign effect on ITGs with adiabatic electron response. Using the same model, unstable Alfvén ITGs (AITGs) or Kinetic Ballooning modes (KBMs) [43, 50, 51, 52, 53, 54] are shown to become more unstable with increasing  $\beta$  [46, 48]. Subsequent studies [55] with more accurate gyrokinetic nonadiabatic passing electron dynamics coupled to  $A_{||}$  fluctuations have shown about 10 % change in growth rates of AITGs. However, in all the above-mentioned studies, the effect of nonadiabatic passing electrons when coupled to electrostatic fluctuations  $\tilde{\phi}$  has not been explored.

In time-evolving gyrokinetic particle simulations where ions are pushed by solving the first principle laws, the difference in mass ratio of ions and electrons imposes a stringent constraint on the numerical time-stepping. The assumption of adiabatic electron response simplifies the computational demands enormously. However, on a given magnetic flux surface, adiabatic electron model is known to introduce spurious charge accumulation and zonal flows if electron adiabaticity is not carefully imposed [56]. If one were to push electrons with finite mass in a numerically consistent fashion, then such problems can be avoided. Because of the ion to electron mass ratio, the necessity of using small time-steps is seen as a difficulty in time-evolving linear and nonlinear gyrokinetic particle codes. It goes without saying

## Chapter 2: Role of nonadiabatic/kinetic passing electrons in global electrostatic ion temperature gradient driven modes in a tokamak

that the above mentioned mass-ratio related physics issues are equally relevant to gyrokinetic Vlasov codes as well. For trapped electrons, more sophisticated models [13, 14, 15] are being developed, whereas for passing nonadiabatic electrons very few models exist.

Coming back to the global linear spectral models [11, 46, 48, 55] mentioned earlier, the above-said difficulties encountered in time-evolving gyrokinetic linear/nonlinear codes are avoided as time-evolution is replaced by frequency response of the system. As a result, at least for the linear regime, both ions and electrons can be handled on exactly the same physics footing. This situation provides a strong advantage in favor of the linear global gyrokinetic spectral models both physics-wise and also as a stringent numerical test case for time-evolving nonlinear gyrokinetic codes with nonadiabatic electrons. We bring out interesting qualitative and quantitative differences between ITGs with the usual adiabatic electron response and with the nonadiabatic passing electrons response.

To this end, we focus on the electrostatic version of the fully gyrokinetic, fully electromagnetic global linear stability model EM-GLOGYSTO extensively studied and reported in [11, 46, 48, 55] as applicable to large aspect ratio tokamaks. For the purposes of this study, Shafranov shift, equilibrium flows, trapped electron effects,  $B_{\perp}$ , and  $B_{\parallel}$  fluctuations are dropped, while particle nonadiabaticity for passing ions and passing electrons, Landau damping of passing species, finite Larmor radius (FLR) effects to all orders for all species, trapped and transit resonances, and poloidal and radial coupling of modes due to particle drifts across magnetic flux surfaces are included.

## 2.2 Model Equations

To describe tokamak plasmas, collisionless Vlasov-Maxwell equations are used. In the following, we invoke the standard technique of *gyrokinetic* change of variables as employed by Catto *et al.* [57] with an *eikonal or spectral ansatz* to obtain a gyrokinetic Vlasov equation. Among others, a self-consistent and energy conserving theoretical framework was given by Hahm [58] based on Hamiltonian and Lie transformations, and more recently a variational formulation for gyrokinetic Vlasov-Maxwell system was given by Brizard [59] resulting in gyrokinetic

**Chapter 2: Role of nonadiabatic/kinetic passing electrons in global electrostatic ion temperature gradient driven modes in a tokamak**

equations and gyro-averaged Maxwell's equations for finite- $\beta$  plasmas. The theoretical formulations used here are discussed in detail in Refs. [44] and [55]. For the sake of completeness, we redo the formulation with one major change, namely, the addition of the proper gyrokinetic nonadiabatic passing electron response to the electrostatic potential fluctuation. As our interest is in the passing nonadiabatic electron dynamics in electrostatic limit, in the following we are redoing a description of only the electrostatic formulation [44].

As appropriate for a linear stability study, the full distribution function  $f_j(\mathbf{r}, \mathbf{v}, t)$  of species  $j$  is linearized about a suitable equilibrium  $f_{0j} = f_{0j}(\mathbf{r}, \mathbf{v})$  such that  $f_j(\mathbf{r}, \mathbf{v}, t) = f_{0j}(\mathbf{r}, \mathbf{v}) + \tilde{f}_j(\mathbf{r}, \mathbf{v}, t)$  with the assumption that  $\tilde{f}_j/f_{0j} \ll 1$ . Retaining terms up to the first order, we get ;

$$\left. \frac{D}{Dt} \right|_{u.t.p.} f_{0j}(\mathbf{r}, \mathbf{v}) = 0, \quad \text{where} \quad \left. \frac{D}{Dt} \right|_{u.t.p.} \equiv \frac{\partial}{\partial t} + \mathbf{r} \cdot \nabla + \frac{q_j}{m_j} (\mathbf{v} \times \mathbf{B}) \cdot \nabla_{\mathbf{v}}, \quad (2.1)$$

and

$$\left. \frac{D}{Dt} \right|_{u.t.p.} \tilde{f}_j(\mathbf{r}, \mathbf{v}, t) = -\frac{q_j}{m_j} \tilde{\mathbf{E}} \cdot \nabla_{\mathbf{v}} f_{0j}. \quad (2.2)$$

Here *u.t.p* implies unperturbed trajectories of particles. As the formulation is linear, the trajectories of the particles remain unperturbed. Also, note that  $\mathbf{B} = \nabla \times \mathbf{A} = B \hat{e}_{\parallel}$  is the equilibrium toroidal magnetic field,  $\tilde{\mathbf{E}}$  is the perturbed electrostatic field,  $q_j$  and  $m_j$  are the electric charge and mass of the species  $j$ , respectively. Expressing  $\tilde{\mathbf{E}}$  in terms of  $\tilde{\varphi}$  and defining the following change of variables:  $(\mathbf{r}, \mathbf{v}) \rightarrow (\mathbf{r}, \xi = v^2/2, \mu = v_{\perp}^2/2B)$  and using particle canonical angular momentum for the species  $j$ , i.e.,  $\psi_{0j} = \hat{e}_{\phi} \cdot [\mathbf{r} \times (\mathbf{A} + m_j \mathbf{v}/q_j)] = \psi + m_j r v_{\phi}/q_j$ , one can write  $f_{0j}(\mathbf{r}, \mathbf{v}) = f_{0j}(\mathbf{r}, \xi, \mu, \psi_{0j})$ . Here cylindrical coordinates  $\mathbf{r} \equiv (r, \phi, z)$  have been introduced and  $\psi = r A_{\phi}$  is the poloidal flux function per unit radian. Such a transformation would enable one to express  $f_{0j}$  in terms of single particle constants of motion. Thus,  $\nabla_{\mathbf{v}} f_{0j}$  term on the right hand side of Eq. (2.2) becomes

$$\begin{aligned} \nabla_{\mathbf{v}} f_{0j}(\mathbf{r}, \xi, \mu, \psi_{0j}) &= \mathbf{v} \left( 1 + \frac{m_j r v_{\phi}}{q_j} \frac{\partial}{\partial \psi_{0j}} \right) \frac{\partial f_{0j\psi}}{\partial \xi} + \frac{\mathbf{v}_{\perp}}{B} \frac{\partial f_{0j\psi}}{\partial \mu} \\ &+ \frac{m_j r \hat{e}_{\phi}}{q_j} \frac{\partial f_{0j}}{\partial \psi_{0j}} \Bigg|_{\psi_0=\psi}, \end{aligned} \quad (2.3)$$

**Chapter 2: Role of nonadiabatic/kinetic passing electrons in global electrostatic ion temperature gradient driven modes in a tokamak**

where  $f_{0j\psi} \equiv f_{0j}(\psi_{0j} = \psi)$  and  $\hat{e}_\phi$  is the toroidal unit vector. To obtain Eq. (2.3),  $f_{0j}$  is Taylor expanded to first order in  $\{m_j r v_\phi / q_j\}$  around  $\psi_{0j} = \psi$ . Then, the following gyrokinetic ordering is used:  $\omega / w_{cj} \ll 1$ ,  $k_\perp \varrho_{Lj} \simeq O(1)$ ,  $k_\parallel \varrho_{Lj} \simeq \varrho_{Lj} / L_{eq} \ll 1$ , where  $k_\perp^{-1}$ ,  $k_\parallel^{-1}$ , and  $\varrho_{Lj}$  are perpendicular perturbation scales, parallel perturbation scales and Larmor radius of the species  $j$ , respectively, and  $L_{eq}$  is a typical equilibrium scale length. Rewriting  $\tilde{f}_j$  in Eq. (2.2), using the change of variables defined by

$$\tilde{f}_j = h_j^{(0)} + \tilde{\varphi} \frac{q_j}{m_j} \left[ \left( 1 - \frac{v_\phi}{\Omega_{pj}} \nabla_n \right) \frac{\partial f_{0j\psi}}{\partial \xi} + \frac{1}{B} \frac{\partial f_{0j\psi}}{\partial \mu} \right], \quad (2.4)$$

and then invoking gyro-ordering followed by some standard vector algebra, we arrive at

$$\begin{aligned} \left. \frac{D}{Dt} \right|_{u.t.p} h_j^{(0)}(\mathbf{r}, \mathbf{v}, t) &= -\frac{q_j}{m_j} \left[ \frac{\partial f_{0j\psi}}{\partial \xi} \frac{\partial}{\partial t} + \frac{v_\parallel}{B} \frac{\partial f_{0j\psi}}{\partial \mu} \hat{e}_\parallel \cdot \nabla \right. \\ &\quad \left. + \frac{1}{\Omega_{pj}} \nabla_n f_{0j} \right]_{\psi} \hat{e}_\phi \cdot \nabla \tilde{\varphi} + O(\epsilon). \end{aligned} \quad (2.5)$$

In Eqs. (2.4) and (2.5), we have introduced the following definitions:  $\Omega_{pj} = w_{cj} B_p / B$ ,  $w_{cj} = q_j B / m_j$ ,  $\nabla_n = -r B_p \partial / \partial \psi$ ,  $B_p = |\nabla \psi| / r$  and  $h_j^{(0)}$  is the zeroth order term of the perturbative series in the ‘‘inverse gyro-frequency expansion’’ of the nonadiabatic part

$$h_j = h_j^{(0)} + \frac{1}{w_{cj}} h_j^{(1)} + \frac{1}{w_{cj}^2} h_j^{(2)} \dots$$

Note that since  $D/Dt \simeq O(w_{cj})$ , only  $h_j^{(0)}$  is retained which is independent of  $w_{cj}$  and hence the gyroangle (defined below). In the rest of this chapter  $h_j^{(0)}$  is referred to simply as  $h_j$ . Equation (2.5) is our starting equation. Now let us proceed with the gyro-averaging procedure. In a large aspect ratio tokamak geometry, velocity  $\mathbf{v}$  of a particle gyrating around a field line is  $\mathbf{v} = v_\perp (\hat{e}_\rho \cos \alpha + \hat{e}_\theta \sin \alpha) + v_\parallel \hat{e}_\parallel$ , where unit vectors  $(\hat{e}_\rho, \hat{e}_\theta, \hat{e}_\phi)$  define the toroidal coordinates and  $\alpha$  is the gyroangle. We

**Chapter 2: Role of nonadiabatic/kinetic passing electrons in global electrostatic ion temperature gradient driven modes in a tokamak**

define the gyro-averaging of a quantity “Q” as

$$\langle Q \rangle = \frac{1}{2\pi} \int_0^{2\pi} d\alpha Q(\alpha; ..).$$

In Eq. (2.5), the terms in square brackets [..], on the right hand side, are all *equilibrium quantities* and are independent of  $\alpha$ . Thus, only the electrostatic potential is to be gyroaveraged. Similarly, on the left hand side,  $h_j$  is independent of  $\alpha$ , hence only  $D/Dt|_{u.t.p}$  is to be gyro-averaged. Therefore,

$$\left. \frac{D}{Dt} \right|_{u.t.p} \xrightarrow{\text{gyro-averaging}} \left. \frac{D}{Dt} \right|_{u.t.g} \equiv \frac{\partial}{\partial t} + (v_{\parallel} \hat{e}_{\parallel} + \mathbf{v}_{\mathbf{d}j}) \cdot \frac{\partial}{\partial \mathbf{R}},$$

where  $\mathbf{v}_{\mathbf{d}j} = (v_{\perp}^2/2 + v_{\parallel}^2) \hat{e}_z / (r w_{cj})$ , *u.t.g.* implies *unperturbed trajectory of guiding centers*, and  $\mathbf{R}$  is defined by  $\mathbf{R} = \mathbf{r} + \mathbf{v} \times \hat{e}_{\parallel} / w_{cj}$ . Therefore,

$$\langle \tilde{\varphi} \rangle = \frac{1}{2\pi} \int_0^{2\pi} d\alpha \left[ \tilde{\varphi}(\mathbf{r}[\alpha], t) \right] \Bigg|_{\mathbf{r}=\mathbf{R}-\mathbf{v} \times \hat{e}_{\parallel} / w_{cj}}.$$

Since  $\tilde{\varphi}(\mathbf{r}[\alpha], t)$  is an unknown function, the gyro-averaging is performed by first Fourier decomposing these functions, then representing the particle coordinate  $\mathbf{r}$  by gyro-center  $\mathbf{R}$  and remembering that

$$J_p(x) = \frac{1}{2\pi} \int_0^{2\pi} d\alpha \exp[\iota(x \sin \alpha - p\alpha)],$$

With the above-mentioned procedure, one obtains the following *gyrokinetic equation*:

$$\begin{aligned} \left. \frac{D}{Dt} \right|_{u.t.g} h_j(\mathbf{R}, \mathbf{v}, t) &= - \left( \frac{q_j}{m_j} \right) \left[ \frac{\partial f_{0j\psi}}{\partial \xi} \frac{\partial}{\partial t} + \frac{v_{\parallel}}{B} \frac{\partial f_{0j\psi}}{\partial \mu} \hat{e}_{\parallel} \cdot \nabla \right. \\ &\quad \left. + \frac{1}{\Omega_{pj}} \nabla_n f_{0j} \Bigg|_{\psi} \hat{e}_{\phi} \cdot \nabla \right] (\tilde{\varphi}(\mathbf{k};) J_0(k_{\perp} \varrho_{Lj})) + O(\epsilon). \quad (2.6) \end{aligned}$$

The solution to Eq. (2.6) is obtained by the *Green function technique* (unit source solution *say*  $\mathcal{P}$ ) [60]. An explicit form of  $\mathcal{P}$  is obtained analytically by the method of characteristics of unperturbed trajectories of guiding centers (*u.t.g.*) and followed

## Chapter 2: Role of nonadiabatic/kinetic passing electrons in global electrostatic ion temperature gradient driven modes in a tokamak

by a perturbative technique for the guiding center velocity [44]. Moreover, the unit source solution,  $\mathcal{P}$ , to Eq. (2.6) is independent of the type of perturbation (electrostatic or electromagnetic) and solely depends on the considered *equilibrium*. We assume for equilibrium  $f_{0j}$  a local Maxwellian of the form

$$f_{0j}(\xi, \mu, \psi) = f_{Mj}(\xi, \psi) = \frac{N(\psi)}{\left(\frac{2\pi T_j(\psi)}{m_j}\right)^{3/2}} \exp\left(-\frac{\xi}{T_j(\psi)/m_j}\right),$$

so that  $\partial f_{0j}/\partial \mu \equiv 0$  by choice and density profile  $N(\psi)$  is independent of the species type  $j$ . Thus, for a “sinusoidal” time dependence, the solution to Eq. (2.6) in guiding center coordinates  $\mathbf{R}$  is

$$h_j(\mathbf{R}, \mathbf{v}, \omega) = -\left(\frac{q_j F_{Mj}}{T_j}\right) \int d\mathbf{k} \exp(\iota \mathbf{k} \cdot \mathbf{R} (\omega - \omega_j^*)) (\iota \mathcal{P}_j) \tilde{\varphi}(\mathbf{k}; \cdot) J_0(k_\perp \varrho_{Lj}) + O(\epsilon).$$

Here,  $\mathbf{k} = \kappa \hat{e}_\rho + k_\theta \hat{e}_\theta + k_\phi \hat{e}_\phi$  and  $\kappa = (2\pi/\Delta\rho) k_\rho$ , with  $\Delta\rho = \rho_u - \rho_l$  which defines the radial domain,  $k_\phi = n/r$  and  $k_\theta = m/\rho$ ;  $\omega$  is the *eigenvalue* and

$$\omega_j^* = \omega_{nj} \left[ 1 + \frac{\eta_j}{2} \left( \frac{v_{\parallel}^2}{v_{thj}^2} - 3 \right) + \frac{\eta_j v_\perp^2}{2 v_{thj}^2} \right],$$

with  $\omega_{nj} = (T_j \nabla_n \ln N k_\theta)/(q_j B)$  is the *diamagnetic drift frequency* and  $\eta_j = (d \ln T_j)/(d \ln N)$ . Note also that since the large aspect ratio equilibria considered are axisymmetric, the toroidal mode number “ $n$ ” can be fixed and the problem is effectively two dimensional in  $(\rho, \theta)$  (configuration space) or  $(\kappa, k_\theta)$  (Fourier space).

As our interest is in the nonadiabatic passing electrons, let us now proceed to the construction of the propagator for passing gyrokinetic species. For trapped ions one can see Ref. [44]. Since a gyroaveraged Vlasov equation can be solved using the method of integration along its *u.t.g.*, for our special class of “sinusoidal” time dependence, the solution  $\mathcal{P}$  for a given  $(\mathbf{k}, \omega)$  is simply

$$\begin{aligned} \mathcal{P}(\mathbf{R}, \mathbf{k}, \epsilon, \mu, \sigma, \omega) &= \int_{-\infty}^t dt' \exp(\iota [\mathbf{k} \cdot (\mathbf{R}' - \mathbf{R}) - \omega t']) \\ &= \int_{-\infty}^t dt' \exp\left(\iota \int^t dt'' \mathbf{k} \cdot \mathbf{v}_g(t'') - \iota \omega t'\right), \end{aligned} \quad (2.7)$$

**Chapter 2: Role of nonadiabatic/kinetic passing electrons in global electrostatic ion temperature gradient driven modes in a tokamak**

where guiding center velocity  $d\mathbf{R}/dt = \mathbf{v}_g = \mathbf{v}_\parallel + \mathbf{v}_d$  and  $\mathbf{R}(t)$  is to be obtained by solving for guiding center trajectories as an “initial value problem” in equilibrium considered above. This is done by first assuming that the cross-field drift terms  $[\mathbf{v}_d]$  are small and drop them at the zeroth order and to include them iteratively at the next order. This procedure gives us  $\mathcal{P}$ ,

$$\iota\mathcal{P} = \sum_{p,p'} \frac{J_p(x_{tj}^\sigma)J_{p'}(x_{tj}^\sigma)}{\omega - \sigma k_\parallel v_\parallel - p\omega_t} \exp(\iota(p - p')(\theta - \bar{\theta}_\sigma)), \quad (2.8)$$

where  $x_{tj}^\sigma = k_\perp \xi_\sigma$ ,  $\xi_\sigma = v_d/\omega_t$ ,  $v_d = (v_\perp^2/2 + v_\parallel^2)/(\omega_c R)$ ,  $\omega_t = \sigma v_\parallel/(q(s)R)$ ,  $\sigma = \pm 1$  (sign of  $\mathbf{v}_\parallel$ ),  $k_\perp = \sqrt{\kappa^2 + k_\theta^2}$ ,  $k_\parallel = [nq(s) - m]/(q(s)R)$  and  $\bar{\theta}_\sigma$  is defined as  $\tan \bar{\theta}_\sigma = -\kappa/k_\theta$  and  $s = \rho/a$ ,  $a$ —is the minor radius. A few points to be noted here are as follows: (1) Note that the grad-B and curvature drift effects appear through the argument of Bessel functions ( $x_{tj}^\sigma = k_\perp v_d/\omega_t$ ) of Eq. 2.8. Thus, for example, “radial and poloidal coupling” vanishes if  $x_{tj}^\sigma = 0$  in Eq. 2.8 and one would arrive at “cylindrical” results. Hence in our model, Bessel functions in Eq. 2.8 bring about coupling between neighboring flux surfaces and also couple neighboring poloidal harmonics. (2) The argument of Bessel functions  $J_p$ ’s in Eq. (2.8) i.e.,  $x_{tj}^\sigma = k_\perp \xi_\sigma$ , also depends on transit frequency  $\omega_t$ ,  $x_{tj}^\sigma$  can become  $x_{tj}^\sigma \simeq \mathcal{O}(1)$ . Hence transit harmonic orders are to be chosen accordingly. (3) While performing the numerical calculations, we have approximated the particle speeds in  $\xi_\sigma$  by their local thermal velocity values and hence use  $\xi_\sigma = \langle \xi_\sigma \rangle$  where  $\langle \xi_\sigma \rangle = 2\sigma \text{sign}(q_j)q(s)\varrho_{Lj}$ . (4) The parallel velocity  $v_\parallel$  of the particles are considered to be independent of time. That means that the passing particles are modelled as deeply passing. In this form,  $\mathcal{P}$  contains effects such as transit harmonic and its coupling, parallel velocity resonances and poloidal mode coupling.

To obtain the particle density fluctuation  $\tilde{n}_j(\mathbf{r};\omega)$ , one requires to go from the guiding center (GC) coordinate  $\mathbf{R}$  to the *particle coordinate*  $\mathbf{r}$  using  $\mathbf{R} = \mathbf{r} + \mathbf{v} \times \hat{e}_\parallel/w_{cj}$ , by replacing  $h_j$  using Eq. (2.4) followed by the integration over  $\mathbf{v}$  keeping in mind the *gyroangle* integration over  $\alpha$ . This last integration on  $\alpha$  yields an additional Bessel function “ $J_0$ ” for  $\tilde{\varphi}$ . Thus, in real space  $\mathbf{r}$ , for species  $j$ , we

**Chapter 2: Role of nonadiabatic/kinetic passing electrons in global electrostatic ion temperature gradient driven modes in a tokamak**

finally have

$$\tilde{n}_j(\mathbf{r}; \omega) = - \left( \frac{q_j N}{T_j} \right) \left[ \tilde{\varphi} + \int d\mathbf{k} \exp(\iota \mathbf{k} \cdot \mathbf{r}) \times \int d\mathbf{v} \frac{f_{Mj}}{N} (\omega - \omega_j^*) (\iota \mathcal{P}_j) \tilde{\varphi}(\mathbf{k};) J_0^2(x_{Lj}) \right], \quad (2.9)$$

where  $x_{Lj} = k_{\perp} \rho_{Lj}$ . It may be worthwhile to emphasize that the equilibrium effects (incorporated in  $\mathcal{P}$ ) and perturbation effects are clearly delineated in the formulation. Equations are finally closed by invoking the *quasineutrality condition*,

$$\sum_j \tilde{n}_j(\mathbf{r}; \omega) \simeq 0. \quad (2.10)$$

Equation (2.10) defines a generalized eigenvalue problem with eigenvalue  $\omega$  and eigenvector  $\tilde{\varphi}$ . This eigenvalue problem is conveniently solved in Fourier space. By Fourier decomposing the potential in Eq. (2.10) and then taking Fourier transform, we obtain a convolution matrix in Fourier space. If we assume a hydrogen-like plasma (i.e., single charged) with ions, electrons, trapped ions, we have

$$\sum_{\mathbf{k}'} \sum_{j=i,e,tr-i} \hat{\mathcal{M}}_{\mathbf{k},\mathbf{k}'}^j \tilde{\varphi}_{\mathbf{k}'} = 0, \quad (2.11)$$

where  $\mathbf{k} = (\kappa, m)$  and  $\mathbf{k}' = (\kappa', m')$ . Note that we have three species: Passing ions ( $i$ ), passing electrons ( $e$ ), and trapped ions ( $tr-i$ ).

In the following, we discuss in detail the formulation for nonadiabatic passing species. With the definitions,  $\Delta\rho = \rho_u - \rho_l$  (upper and lower radial limits),  $\Delta_{\kappa} =$

**Chapter 2: Role of nonadiabatic/kinetic passing electrons in global electrostatic ion temperature gradient driven modes in a tokamak**

$\kappa - \kappa'$  and  $\Delta_m = m - m'$  the matrix elements are given as follows.

$$\begin{aligned} \hat{\mathcal{M}}_{\mathbf{k},\mathbf{k}'}^i &= \frac{1}{\Delta\rho} \int_{\rho_l}^{\rho_u} d\rho \exp(-\iota\Delta_\kappa\rho) \\ &\times \left[ \alpha_p \delta_{mm'} + \exp(\iota\Delta_m\bar{\theta}) \sum_p \hat{I}_{p,i}^0 \right], \end{aligned} \quad (2.12)$$

$$\begin{aligned} \hat{\mathcal{M}}_{\mathbf{k},\mathbf{k}'}^e &= \frac{1}{\Delta\rho} \int_{\rho_l}^{\rho_u} d\rho \exp(-\iota\Delta_\kappa\rho) \\ &\times \left[ \frac{\alpha_p}{\tau(\rho)} \delta_{mm'} + \frac{\exp(\iota\Delta_m\bar{\theta})}{\tau(\rho)} \sum_p \hat{I}_{p,e}^0 \right], \end{aligned} \quad (2.13)$$

where

$$\begin{aligned} \hat{I}_{p,j}^l &= \frac{1}{\sqrt{2\pi}v_{th,j}^3(\rho)} \int_{-v_{max,j}(\rho)}^{v_{max,j}(\rho)} v_{||}^l dv_{||} \exp\left(-\frac{v_{||}^2}{v_{th,j}^2(\rho)}\right) \times \\ &\left\{ \frac{N_1^j I_{0,j}^\sigma - N_2^j I_{1,j}^\sigma}{D_1^{\sigma,j}} \right\}_{p'=p-(m-m')}, \end{aligned} \quad (2.14)$$

$$\begin{aligned} I_{n,j}^\sigma &= \int_0^{v_{\perp max,j}(\rho)} v_{\perp}^{2n+1} dv_{\perp} \exp\left(-\frac{v_{\perp}^2}{2v_{th,j}^2(\rho)}\right) \times \\ &J_0^2(x_{Lj}) J_p(x'_{tj}{}^\sigma) J_{p'}(x'_{tj}{}^\sigma). \end{aligned} \quad (2.15)$$

We have introduced the following definitions:  $v_{\perp max,j}(\rho) = \min(v_{||}/\sqrt{\epsilon}, v_{max,j})$  which is “trapped particle exclusion” from  $\omega$ -independent perpendicular velocity integral  $I_{n,j}^\sigma$ ;  $\alpha_p = 1 - \sqrt{\epsilon/(1+\epsilon)}$  is the fraction of passing particles;  $\hat{I}_{p,j}^l$  is  $\omega$  - dependent parallel integrals;  $x_{tj}^\sigma = k_{\perp} \xi_{\sigma}$ . Also,

$$\begin{aligned} N_1^j &= \omega - w_{n,j} [1 + (\eta_j/2)(v_{||}^2/v_{th,j}^2) - 3], \\ N_2^j &= w_{n,j} \eta_j / (2v_{th,j}^2), \quad \text{and} \\ D_1^{\sigma,j} &= \langle w_{t,j}(\rho) \rangle (nq_s - m'(1-p)(\sigma v_{||}/v_{th,j}) - \omega, \end{aligned}$$

where  $\langle w_{t,j}(\rho) \rangle = v_{th,j}(\rho)/(rq_s)$ , is the average *transit frequency* of the species  $j$ . As integrals  $I_{n,j}^\sigma$  are independent of  $\omega$  and dependent only on  $v_{\perp}$ ,  $\sigma$  and other equilibrium quantities, one may choose to calculate and store them as interpolation

## Chapter 2: Role of nonadiabatic/kinetic passing electrons in global electrostatic ion temperature gradient driven modes in a tokamak

tables (memory intensive) or, alternatively, one may choose to calculate them when needed (CPU-time intensive). In the next section, we will specify some diagnostics and normalizations used in the code.

### 2.2.1 Diagnostics: Eigenmode-averaged quantities

Simple diagnostics for various physical quantities are computed as averages over the eigenmode. For example, mode-averaged poloidal, radial and perpendicular components of the wave vector  $\vec{k}$  of the most unstable mode can be evaluated as

$$\langle k_\theta \rangle^2 = \frac{\int d\rho \sum_m \left| \frac{m}{\rho} \varphi_{(k,m)} \right|^2}{\int d\rho \sum_m |\varphi_{(k,m)}|^2},$$

$$\langle k_\rho \rangle^2 = \frac{\sum_{(k,m)} |\phi_{(k,m)}(k2\pi/\Delta\rho)|^2}{\sum_{(k,m)} |\varphi_{(k,m)}|^2},$$

and

$$\langle k_\perp \rangle^2 = \langle k_\rho \rangle^2 + \langle k_\theta \rangle^2$$

where quantities with suffix “ $(k, m)$ ” imply Fourier weights of the corresponding perturbations.

### 2.2.2 Normalization for full radius calculation

Distances are normalized to minor radius “ $a$ ”; i.e.,  $s = \rho/a$ . Radial position where  $\eta_j$  peaks is represented as  $s = s_0$ . Frequencies and growth rates are normalized to  $\omega_{d0} = v_{thi}(s = s_0)\varrho_{Li}/a^2$ ,  $k_\perp$  is normalized to its local (ion/electron) inverse Larmor radius  $\varrho_{Lj}^{-1}(s)$ ,  $k_\parallel$  to  $L_n^{-1}$  (inverse density gradient length scale), magnetic field  $B$  to  $B(s = 0)$ , density to  $N(s = s_0)$ , temperature  $T$  to  $T(s = s_0)$ , and velocities ( $v_\perp, v_\parallel$ ) to  $v_{thi}(s)$  (i.e., to their radially local thermal values).

All input quantities to the code EM-GLOGYSTO are in SI units, except temperature of given species which is in eV. Hence, for example,  $v_{thi}$  is computed using  $v_{thi}^2(\text{in } m/s) = T_i(\text{in Joule})/m_i(\text{in Kg}) = |e|T_i(\text{in eV})/m_i(\text{in Kg})$ , where  $|e|$  is

**Chapter 2: Role of nonadiabatic/kinetic passing electrons in global electrostatic ion temperature gradient driven modes in a tokamak**

absolute value of electronic charge. Thus, for example, for parameters throughout this chapter, we have  $\omega_{d0} \simeq 3 \times 10^4 \text{ s}^{-1}$ .

## 2.3 Eigenvalue finding method

The eigenvalue solver is devised by Brunner *et al.* [11] applying the method proposed by Davies [176] along with further optimization. For the sake of completeness we elucidate the method again as follows.

The method uses the advantage of the fact that  $D(\omega)$  is analytic. Let us consider that  $h(z)$  is an analytic function inside a closed positively oriented contour  $C$ . If it is possible to determine the number  $N$  of the enclosed zeros  $a_i$ ,  $i = 1, \dots, N$  using the principle of argument, the method is then based on the evaluation of an equivalent number of integrals:

$$S_n = \frac{1}{2i} \int_C z^n \frac{h(z)}{h'(z)} dz \quad n = 1, \dots, N,$$

which have the property

$$S_n = \sum_{i=1}^N a_i^n, \quad n = 1, \dots, N. \quad (2.16)$$

The set of equations (2.16) is then solved finding the roots of the associated polynomial defined by

$$P_N(z) = \prod_{i=1}^N (z - a_i) = \sum_{i=1}^N A_i z^{N-i}.$$

One can calculate the coefficients  $A_n$  from  $S_n$  using a recursive relation as follows.

$$S_1 + A_1 = 0$$

$$S_2 + A_1 S_1 + 2A_2 = 0$$

$$S_k + A_1 S_{k-1} + A_2 S_{k-2} + \dots + kA_k = 0, \quad k = 1, \dots, N.$$

The original numerical technique by Davies is developed for circular contours. This has been generalized by Brunner *et al.* [11] to allow for more elongated curves in

## Chapter 2: Role of nonadiabatic/kinetic passing electrons in global electrostatic ion temperature gradient driven modes in a tokamak

the frequency plane. This is achieved by applying the above method along a unit circle to the function  $D(z) = D(\omega(z))$  with  $\omega(z)$  being a conformal transformation of the unit disc at origin. By considering,

$$\omega(z) = \tilde{\omega} + r z(Ez^2 + 1)$$

the unit circle in the  $z$ -plane is transformed to a more oval-shaped curve in the  $\omega$ -plane centered at  $\tilde{\omega}$  with average radius  $r$ . The elongation and orientation are defined by the complex parameter  $E$  ( $|E| \leq 0.1$ ). In this method the determinant must only be evaluated along a contour. Furthermore, up to ten roots inside a single curve can directly be obtained without any further refinement. To achieve accuracy, the number of equidistant sampling points along the unit circle is increased until the maximum jump in the argument of  $D(\omega(z))$  is less than  $\pi/2$ . Once an eigenfrequency  $\omega_i$  is identified, the corresponding eigenmode can be evaluated by considering an inhomogeneous right hand side in (2.11) by putting  $\omega = \omega_i$  and then solving the equation for  $\phi$ . The initial right hand side is taken as a first guess of the eigenvector structure which is then repeated iteratively until convergence is attained.

## 2.4 Results and Discussion

We choose profiles and parameters as presented in Table 2.1 to demonstrate the effect of nonadiabatic passing electrons on global ITGs. For these parameters equilibrium profiles are shown in Fig. 2.1. For the above-mentioned parameters, value of  $\rho^* \equiv \rho_{Li}(s = s_0)/a \simeq 0.0175$ .

### 2.4.1 $n$ -scan: Effect of variation of $\eta_e$ , multiscale features and mixing length transport

Growth rates  $\gamma$  and real frequencies  $\omega_r$  of global ITG mode as functions of  $k_\theta \rho_{Li}$  is shown in Fig. 2.2. Effect of adiabatic and nonadiabatic electron responses for various values of  $\eta_e$  is presented in the figure. Note that this kind of higher  $\eta_e$  values are often seen in electron internal transport barriers [63]. The growth peaks around  $n \simeq 9$ . This result shows that the electron nonadiabaticity indeed affects

## Chapter 2: Role of nonadiabatic/kinetic passing electrons in global electrostatic ion temperature gradient driven modes in a tokamak

Table 2.1: Profiles and parameters

Parameters:

- B-field :  $B_0 = 1.0$  Tesla
- Temperature :  $T_0 = T(s_0) = 7.5$  keV
- Major Radius :  $R = 2.0$  m
- Minor Radius :  $a = 0.5$  m
- radius :  $s = \rho/a$ ,  $0.01 < s < 1.0$ ,  $s_0 = 0.6$
- $L_{n0} = 0.4$  m,  $L_{T0} = 0.2$  m
- $\eta_{i,e}(s_0) = 2.0$ ,  $\epsilon_n = L_{n0}/R = 0.2$
- $\tau(s) = T_e(s)/T_i(s) = 1$ .

Equilibrium Profiles:

- N-profile and T-profile
 
$$\frac{N(s)}{N_0} = \exp\left(-\frac{a \delta s_n}{L_{n0}} \tanh\left(\frac{s-s_0}{\delta s_n}\right)\right)$$

$$\frac{T_{i,e}(s)}{T_0} = \exp\left(-\frac{a \delta s_T}{L_{T0}} \tanh\left(\frac{s-s_0}{\delta s_T}\right)\right)$$

$$\delta s_n = 0.35, \delta s_T = 0.2 \text{ at } s = s_0$$
- $q(s) = 1.25 + 0.67 s^2 + 2.38 s^3 - 0.06 s^4$   
such that  $q(s = s_0) = 2.0$ ;  
shear  $s = s_0$ ,  $\hat{s} = 1$ .

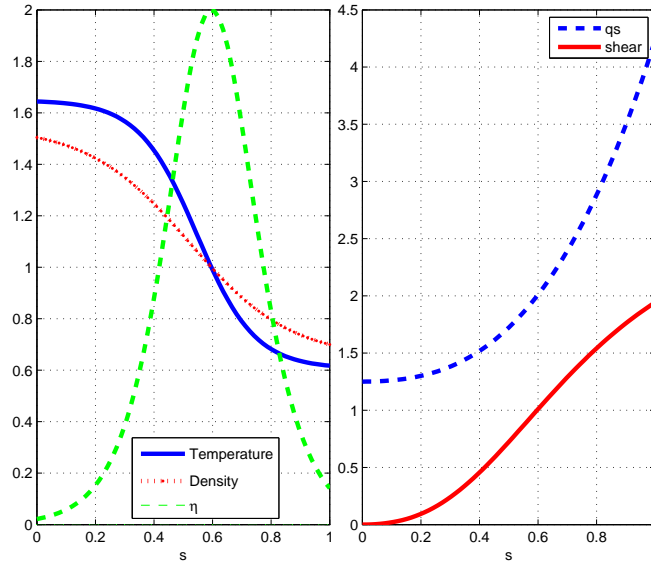


Figure 2.1: Equilibrium profiles for global ITGs stability studies (parameters for Table 2.1: Normalized density, temperature,  $\eta_{i,e}$  (left), Safety factor  $q$  and magnetic shear  $\hat{s}$  (right) profiles as functions of normalized radius  $s = r/a$ . Note that  $\eta$  peaks at  $s = \rho/a = s_0 = 0.6$

## Chapter 2: Role of nonadiabatic/kinetic passing electrons in global electrostatic ion temperature gradient driven modes in a tokamak

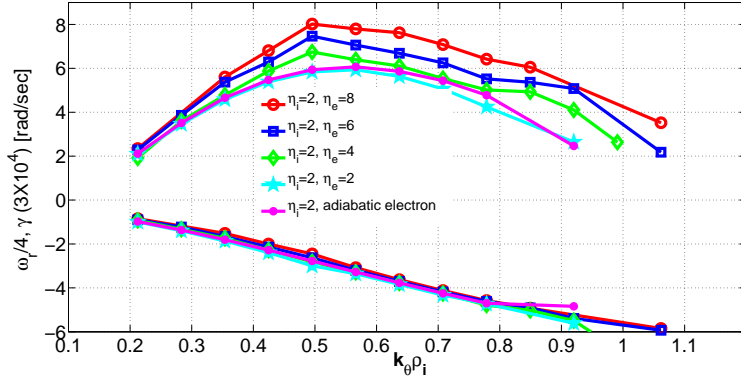


Figure 2.2: Growth rates and frequencies for profiles in Fig. 2.1: Growth rate  $\gamma$  and real frequency  $\omega_r$  for  $\eta_i(s_0) = 2$  with adiabatic electron model and nonadiabatic electron model characterized by increasing  $\eta_e$ .

the growth rates, in general. For finite time taken by passing electrons to respond to  $\mathbf{E}$ -perturbations, especially in regions where the magnetic surface is mode-rational (i.e., where  $k_{\parallel m,n} \simeq 0$ ), the nonadiabatic contribution is significant.

To elucidate this idea, for  $\eta_i = 2.0$ , we have computed the global eigenmode structures of ITG at  $n = 9$ , where the growth rate peaks. Again, for electrons we have two cases: (i) Adiabatic electron response and (ii) nonadiabatic electron response with increasing values for  $\eta_e$ . For example, in Fig. 2.3, eigenmode structures for the adiabatic electron case are compared with that for the case of nonadiabatic electron response with  $\eta_e = 2$ .

The “ballooning” nature of the modes on the “bad curvature” region is also clearly demonstrated. For example, unlike a “cylindrical” or “slab” ITG, here for each value of  $n$  there are about 10 poloidal mode numbers  $m$  coupled. This is again seen in Fig. 2.4, where at a radial location say  $s = r/a = 0.6$ , one can see a predominant Fourier contribution from several  $m$  numbers. The global nature of the mode is adequately demonstrated by projecting the eigenmode on to the poloidal plane. The mode width indeed occupies about 30 % of the minor radius  $a$  extending over several mode-rational surfaces  $r = r_{MRS}$ .

Note that at locations where  $k_{\parallel m,n} = 0$ , the mode structure is very sharp for ITGs with nonadiabatic electrons, whereas no such effect is detectable for ITGs with the usual adiabatic electrons. Consequently, the number of radial wavenum-

**Chapter 2: Role of nonadiabatic/kinetic passing electrons in global electrostatic ion temperature gradient driven modes in a tokamak**

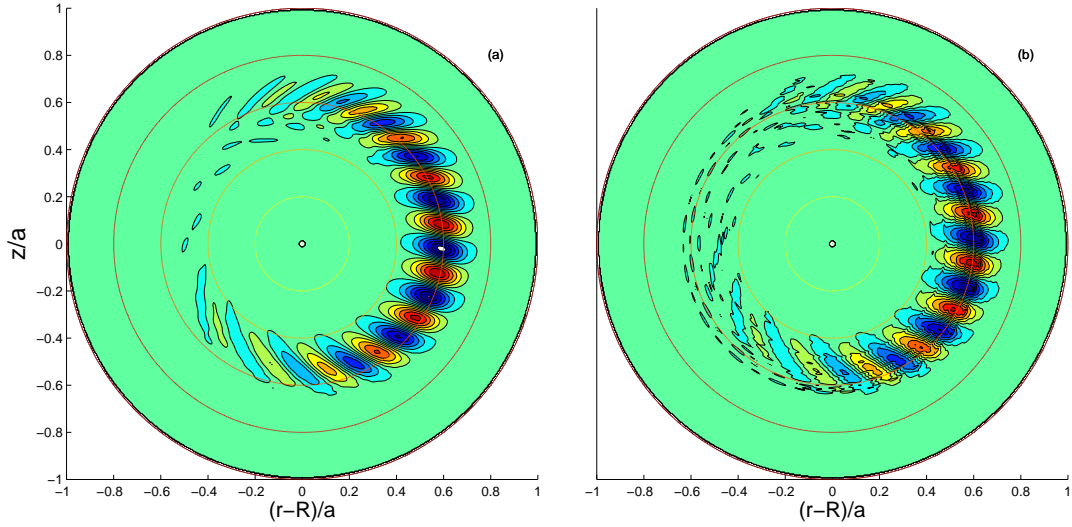


Figure 2.3: Two-dimensional eigenmode structure of global ITG at  $n = 9$ ,  $\eta_i(s_0) = 2$  for adiabatic electron response (left panel) and nonadiabatic electron response (right panel) at  $\eta_e(s_0) = 2$ . Global nature of the mode is clearly visible covering about 30% of the minor radius.

bers  $k_r$  needed to be resolved increases, as seen in Fig. 2.5.

To understand the structures, let us look at the mode-rational surfaces and phase velocity  $v_{m,n}^{ph}$  across the entire minor radius for equilibrium  $q$  profiles shown in the above table (Fig. 2.1). In Fig. 2.6 for  $n = 9$ ,  $\omega_r/k_{||m,n}$ , the per-mode phase velocity is plotted as function of normalized radius along with  $v_{the}$  and  $v_{thi}$ . If one assumes adiabatic electron response, as is usually done, then in both rapidly increasing regions of  $v_{m,n}^{ph}$  (i.e., as  $r \rightarrow r_{MRS}$ ) as well as in regular regions ( $r \neq r_{MRS}$ ), electrons are “forced” to respond “instantaneously”. However, as can be seen from Fig. 2.6, in regions close to  $r = r_{rms}$  electrons cannot respond instantaneously, but take finite time to respond. Thus, if the correct nonadiabatic response is incorporated then for all radial locations (i.e., for all per-mode phase velocities), there would be appropriate electron response. For example, for regions  $r \neq r_{MRS}$ , where  $v_{m,n}^{ph}$  is small compared to  $v_{the}(r)$ , automatically the response will be adiabatic. In the same way, as  $r \rightarrow r_{MRS}$ , the local phase velocity increases and hence strong deviations from adiabaticity occur, which will be automatically accounted for. Such nonadiabatic effects are indeed important for global ITGs as they alter both growth rate and mode structures remarkably.

Chapter 2: Role of nonadiabatic/kinetic passing electrons in global electrostatic ion temperature gradient driven modes in a tokamak

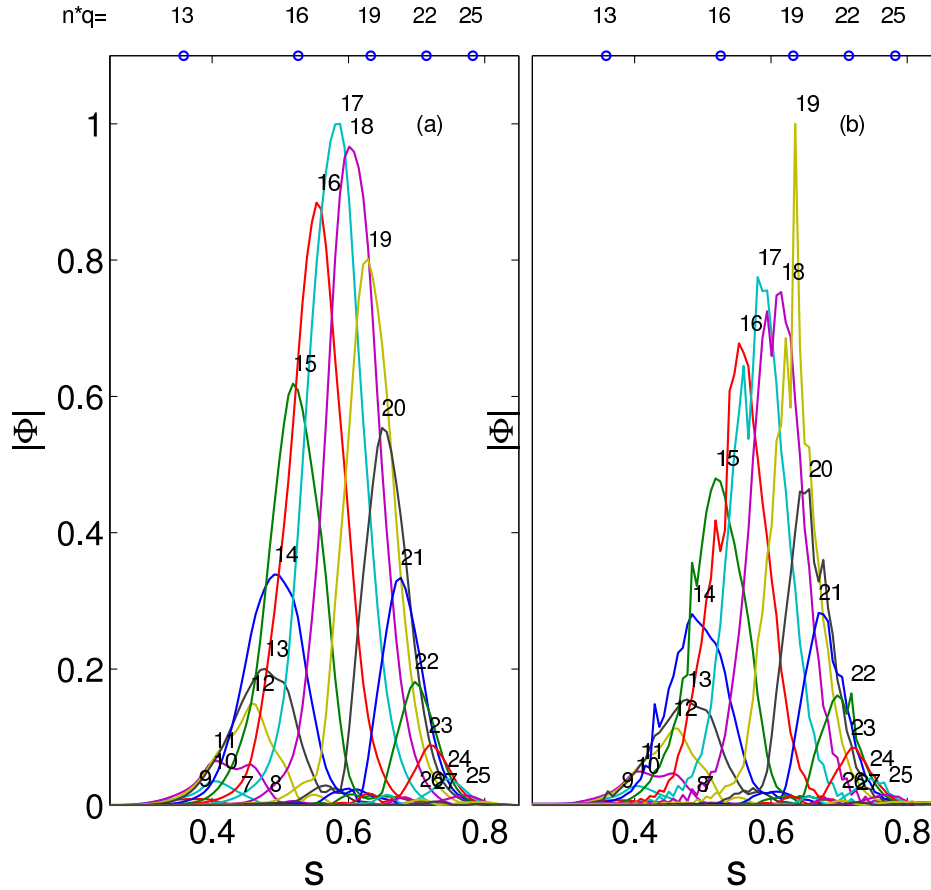


Figure 2.4: The poloidal Fourier components for electrostatic mode shown in Fig. 2.3. Note that at each radial location, there are several poloidal harmonics coupled. A few locations where  $k_{\parallel m,n} = 0$  (i.e.,  $nq = m$ ) are indicated on the top axis. Nonadiabatic electrons introduce sharp structure near these points.

## Chapter 2: Role of nonadiabatic/kinetic passing electrons in global electrostatic ion temperature gradient driven modes in a tokamak

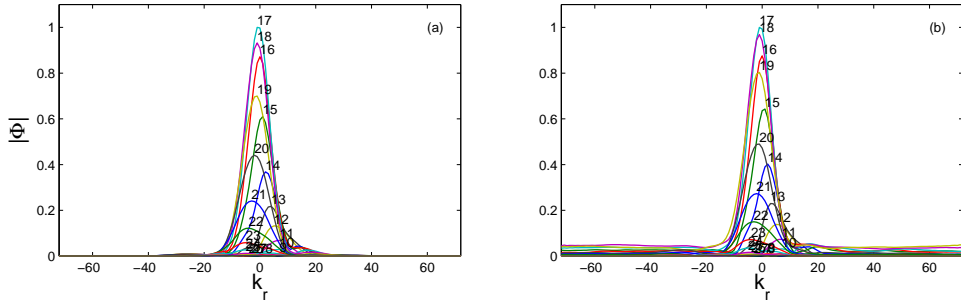


Figure 2.5: Radial Fourier harmonics for each poloidal mode for the electrostatic mode shown in Fig. 2.3. Here we have used 144 modes. For numerical convergence, we have tested with larger number of radial harmonics and observe that the results are converged.

An alternate way of understanding this situation is as follows: Nonadiabatic electron response allows residual unneutralized  $E$  field, and introduces phase delay between density and potential fluctuations and the concomitant growth. Multi-scale features seen in mode structure may remind one of nonlinear effects such as zonal flows, which “break up” the modes resulting in slower rates of growth for ITGs. However, here the exact opposite happens. The linear mode structure is “broken up” due to linear nonadiabatic response of electrons introducing phase delays and thus pronounced growth rates. In Fig. 2.7, we show a closeup of global eigenmodes with adiabatic and nonadiabatic electron responses.

These “broken up” structures, which we call as multiscale structures, in turn, increase the effective or mode-averaged wavenumber as compared to the adiabatic electron model. For example, eigenmode averaged  $k_r \rho_{Li}$ ,  $k_\theta \rho_{Li}$  and  $k_\perp \rho_{Li}$  for adiabatic electron model and nonadiabatic electron model with  $\eta_e = 2$  and  $\eta_e = 8$  are shown in Fig. 2.8 for various values of  $n$ . Note that due to the sharp radial structure introduced by nonadiabatic electrons, the effective  $k_\perp \rho_{Li}$  has been enhanced in both cases of  $\eta_e$ . It would then be interesting to construct the so-called “mixing length” transport for transport coefficient,  $D_{ML} = \gamma / \langle k_\perp^2 \rangle$  from the linear growth rate  $\gamma$  and mode-averaged  $k_\perp$ , i.e.,  $\langle k_\perp \rangle$ . In Fig. 2.9, we present the mixing-length estimates in the usual gyro-Bohm units as a function of the toroidal mode number  $n$ . It is found that compared to the adiabatic electron model, the

## Chapter 2: Role of nonadiabatic/kinetic passing electrons in global electrostatic ion temperature gradient driven modes in a tokamak

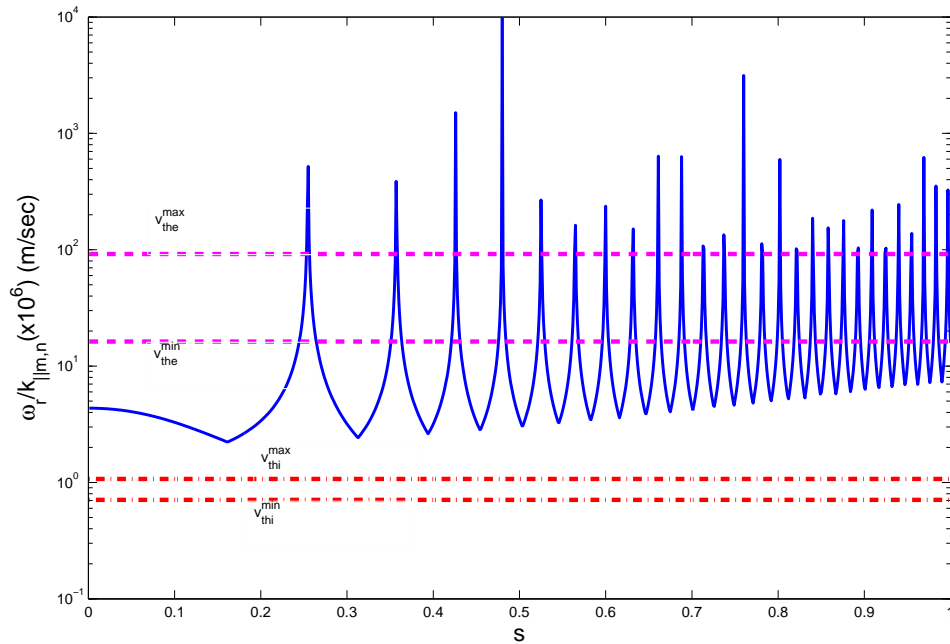


Figure 2.6: Typical per-mode phase velocity  $\omega_r/k_{||m,n}$  versus normalized minor radius  $s = r/a$  for equilibrium profile of  $q$  shown in Fig. 2.1 with  $\eta_e(s_0) = 8$ ,  $\eta_i(s_0) = 2$ ,  $n = 9$ . Locations of peaks ( $r = r_{MRS}$ ) indicate mode rational surfaces. The horizontal dashed lines are the electron thermal velocities  $v_{the}^{min}$  and  $v_{the}^{max}$  at radial locations at the beginning ( $s=0.4$ ) and end ( $s=0.7$ ) of mode structure, respectively. The horizontal dashed-dotted lines are ion thermal speeds at same locations as the electrons.

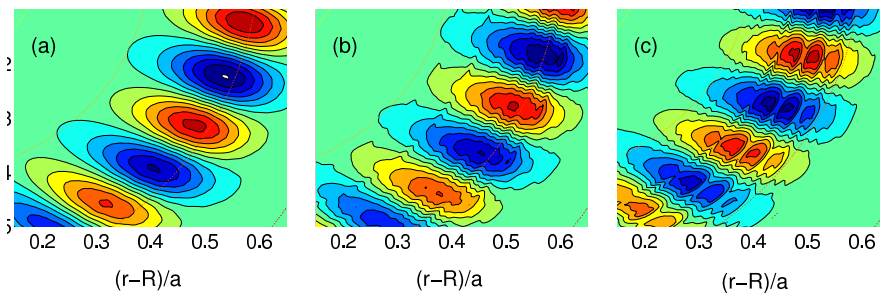


Figure 2.7: Closeup of two dimensional eigenmode structure of global ITG at  $n = 9$ ,  $\eta_i = 2$  for (a) adiabatic electron response, (b) nonadiabatic electron response at  $\eta_e(s_0) = 2$  and (c) same as (b) at  $\eta_e = 8(s_0)$ .

## Chapter 2: Role of nonadiabatic/kinetic passing electrons in global electrostatic ion temperature gradient driven modes in a tokamak

Figure 2.8: Eigenmode averaged normalized mode numbers  $\langle k_\theta \rho_{Li} \rangle$  (squares),  $\langle k_r \rho_{Li} \rangle$  (diamonds),  $\langle k_\perp \rho_{Li} \rangle$  (stars) as a function of toroidal mode number  $n$  at  $\eta_i(s_0) = 2$ ; (a) adiabatic electron response, (b) nonadiabatic electron response at  $\eta_e(s_0) = 2$ , and (c) same as (b) at  $\eta_e(s_0) = 8$ .

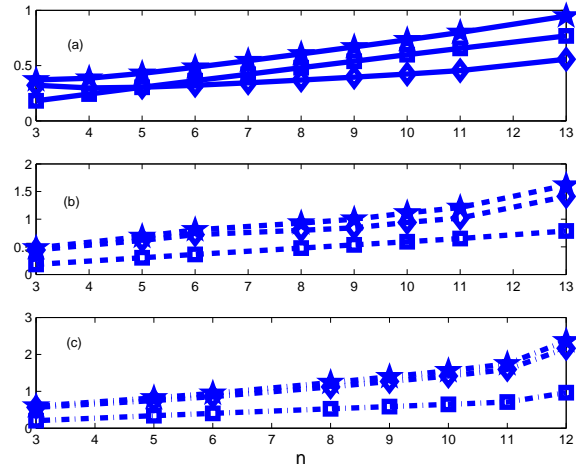
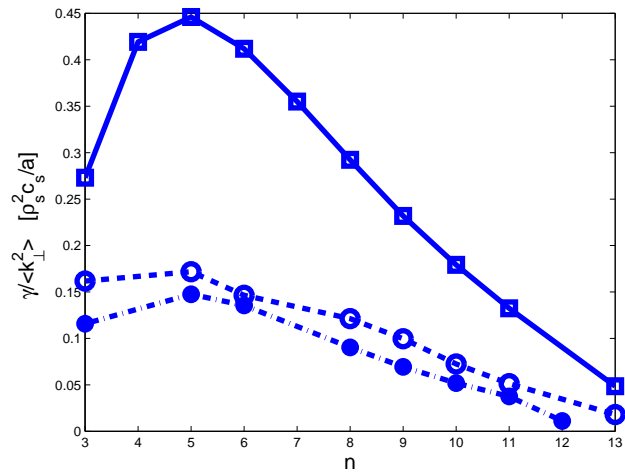


Figure 2.9: Mixing length estimate for transport coefficient  $D_{ML} = \gamma / \langle k_\perp^2 \rangle$  in gyro-Bohm units as a function of toroidal mode number  $n$ ;  $\eta_i(s_0) = 2$  for (a) adiabatic electron response (solid line), (b) nonadiabatic electron response at  $\eta_e(s_0) = 2$  (dashed line), and (c) same as (b) at  $\eta_e(s_0) = 8$  (dot-dashed line).



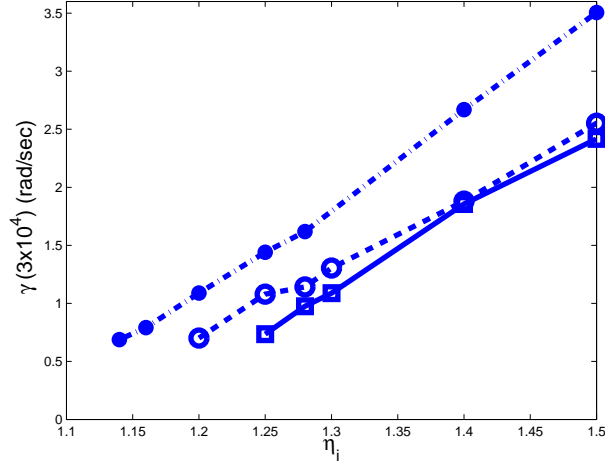


Figure 2.10: For the highest growth rate mode toroidal mode number  $n = 9$ ,  $\eta_i$  scan is performed for three cases of electron model: (a) Adiabatic electron response (solid line), (b) nonadiabatic electron response at  $\eta_e(s_0) = 2$  (dashed line), and (c) same as (b) at  $\eta_e(s_0) = 8$  (dot-dashed line). Results clearly show that  $\eta_{i,crit}$  is downshifted.

transport predicted from global ITGs for nonadiabatic electrons results in reduction in transport. It is important to note that the presence of nonadiabatic trapped electrons [11] may alter the levels of transport observed here due to nonadiabatic passing electrons.

It may be of interest to note that both nonlinearly generated zonal flows and linear but non adiabatic passing electrons "breakup" the mode structures. While the zonal flow breakup is not related to any particular surface ( $k_{\parallel} = 0$  everywhere for the  $m = 0, n = 0$  zonal flow potential perturbation), the presently studied effect occurs due to  $m \neq 0, n \neq 0$  but  $k_{\parallel} = 0$  mode-rational surfaces.

#### 2.4.2 $\eta_i$ scan: Nonadiabatic electrons cause down-shift of critical $\eta_i$

Next, we study the effect of nonadiabatic passing electrons on the critical ion temperature gradient parameter  $\eta_i$ . For adiabatic electrons, global ITGs are known to be unstable at about  $\eta_{i,crit} \simeq 1.1$ . Here, we follow the highest growth rate mode, namely,  $n = 9$ , and investigate the smallest value of  $\eta_i$  at which this mode becomes

## Chapter 2: Role of nonadiabatic/kinetic passing electrons in global electrostatic ion temperature gradient driven modes in a tokamak

unstable. We have studied again three cases: Global ITGs (i) with adiabatic electrons (ii) with nonadiabatic electrons at  $\eta_e = 2$ , and finally (iii) with nonadiabatic electrons with  $\eta_e = 8$ . We find that the critical  $\eta_i$  is *reduced* compared to the adiabatic electron model. This result is perhaps not surprising. As we have seen in the preceding section, nonadiabatic electrons tend to further destabilize global ITGs as compared to global ITGs with adiabatic electrons. Hence one may expect that a relatively weaker ion temperature gradient would destabilize global ITGs now as compared to the adiabatic electron model. This expectation is indeed shown to be true in Fig. 2.10. Physics-wise this result implies that, for example, for similar density profiles, in tokamaks with steeper electron temperature gradient than ions, global ITGs would become unstable for smaller values of  $\eta_i$  than predicted by adiabatic electron models, thus down-shifting the critical  $\eta_i$ . This linear phenomenon is in contrast to up-shifting of critical  $\eta_i$  when nonlinear zonal flows are allowed to evolve simultaneously with ITGs [5, 114].

## 2.5 Conclusion

We have presented a 2D global gyrokinetic stability study as applicable to large aspect ratio tokamaks. We have focused on the effect of treating electrons on the same physics footing as ions, meaning fully nonadiabatic electrons. For this study, we have included passing ions, trapped ions and passing electrons. The model includes arbitrary order FLR effects, kinetic effects such as Landau damping, transit/trapped particle resonances, poloidal and radial coupling, and magnetic resonances. With the above-mentioned model for electrons, we have reported the study of global toroidal ITGs for low toroidal mode numbers in the range  $3 < n < 15$ . There are several interesting new results:

- [1] For nearly the same values of  $\eta_i$  and  $\eta_e$ , the global mode structure is observed to change dramatically. With increasing  $\eta_e$  values, i.e., with more nonadiabaticity, growth rates also are seen to increase. Thus, we conclude that, in general, nonadiabatic passing electron dynamics destabilize global ITGs.
- [2] Important structural changes in the eigenmode structure appear near the mode-rational surfaces where per-mode  $k_{\parallel m,n}$  vanishes. On these surfaces, the local phase velocity grows quickly. Because the mode is global and

## Chapter 2: Role of nonadiabatic/kinetic passing electrons in global electrostatic ion temperature gradient driven modes in a tokamak

spans across several mode rational surfaces, generalizing electron dynamics, as done in the present study, introduces a multiscale nature in global ITG eigenmodes. These effects in turn alter the effective  $k_{\perp}$ . A combination of these effects appears to bring down the mixing length transport estimates as compared to global ITGs with adiabatic electron dynamics.

- [3] Finally, an important fall out is the down-shift of critical  $\eta_i$  values as compared to the adiabatic electron model.

## Chapter 3

# Trapped Electron Coupled Ion Temperature Gradient Mode And Trapped Electron Mode In The Presence Of Nonadiabatic Passing Electrons

### 3.1 Introduction

Anomalous transport in collisionless hot tokamak plasmas is believed to be due to the drift waves driven by the density and temperature gradients [4, 5] of the particles in a magnetically confined plasma. While the turbulent heat flux of ions is believed to be driven by the ion temperature gradient (ITG) mode, the electron heat and particle flux, on the other hand, is expected largely to be driven by the trapped electron mode (TEM) in the low magnetic field side of a tokamak on ion scales (of the order of ion Larmor radius) and by the electron temperature gradient (ETG) mode on electron scales (of the order of electron Larmor radius). Enormous effort has been put to understand the underlying physics issues both theoretically and computationally and then to match the predicted transport flux with that observed experimentally.

The study of ion transport by the ITG mode has started with simple mod-

### Chapter 3: Trapped Electron Coupled Ion Temperature Gradient Mode And Trapped Electron Mode In The Presence Of Nonadiabatic Passing Electrons

els [30, 31], where electrons are treated adiabatic. The next step is then to incorporate the nonadiabatic electrons. This has been achieved in the the form of trapped electrons included in the background model of nonadiabatic ions and adiabatic passing electrons. This has extended the study of this class of microinstabilities to the trapped electron coupled ITG mode (ITG-TEM) [11, 12, 13, 14, 15, 16, 17, 18] mode and TEM [11, 25, 26, 28, 32]. The new models with trapped electrons give growth rate two to three times larger than that in the case of simple adiabatic electron models. At the same time, the transport flux is observed to rise substantially. A comparison of gyrofluid [33] and continuum gyrokinetic [34] simulation of transport in realistic geometry with experiments has been carried out, and the electron thermal diffusivity, ion thermal diffusivity, and perturbed density fluctuation level are found to exceed the experimental value by factors of more than two. The reason of this deviation is speculated to be due to the *non-local* behavior owing to the variation of plasma gradients.

Following this, sophisticated flux ribbon codes have come up with advanced features [35, 36] to reduce the discrepancy between experiments and computational results [37]. The kinetic electron simulation with trapped particles using a generalized split weight scheme to  $\delta f$  gyrokinetic particle method is performed in Ref. [38]. The result shows significant increase in the ion heat diffusivity in comparison to that in the case of the adiabatic electron model in line with the increased growth rate. However, the experimentally observed ion diffusivity [39] is much lower than that predicted by the adiabatic electron models. Thus, a more complete gyrokinetic model that treats electrons and ions on the same physics footing with global profile effects is very much sought to address such anomaly.

The major problem with the incorporation of full dynamics of electrons including the passing fraction nonadiabatically or kinetically in a time dependent model is their fast parallel motion. The high mobility of these electrons needs higher resolution in their response time scale, and is a formidable task in the presence of full ion dynamics, the issue of which is discussed elaborately in Ref. [40]. With advances in computational facilities significant progress has been achieved to this end to treat the electrons fully kinetically [36, 157, 139]. However, sometimes simulations choose reduced ion to electron mass ratio to downsize the computational cost [32, 40, 42].

In the present chapter, we take into account the effect of the trapped elec-

### Chapter 3: Trapped Electron Coupled Ion Temperature Gradient Mode And Trapped Electron Mode In The Presence Of Nonadiabatic Passing Electrons

trons [11] in the model. The spirit is to show the role of kinetic electrons, which we term as “nonadiabatic” passing electrons, on the trapped electron coupled ion temperature gradient mode (ITG-TEM) and trapped electron mode (TEM). It is observed that inclusion of nonadiabatic passing electrons influences strongly the growth rate of the ITG-TEM and TEM and brings fine radial structures of the mode on the mode rational surfaces. A calculation of flux is done based on the mixing length estimation. It predicts transport level below those obtained from adiabatic electron models.

To serve our purpose, we use the electrostatic version of the fully gyrokinetic, fully electromagnetic global linear stability model EM-GLOGYSTO applicable to large aspect ratio tokamaks. We drop the parallel and perpendicular magnetic field perturbation, i.e.,  $B_{\perp}$  and  $B_{\parallel}$  fluctuations, Shafranov shift and equilibrium flows. Thus, particle nonadiabaticity for passing ions and trapped ions, passing electrons and trapped electrons, FLR effects to all orders for all species, kinetic resonances, viz., trapped and transit resonances, poloidal and radial coupling of modes due to particle drifts across magnetic flux surfaces are taken into account.

## 3.2 Model equations

In real space  $\mathbf{r}$ , for species  $j$ , the perturbed density can be expressed as due to adiabatic and nonadiabatic responses of the constituting particles. Thus, for our case, the perturbation in density for species  $j$  can be expressed as

$$\tilde{n}_j(\mathbf{r}; \omega) = - \left( \frac{q_j N}{T_j} \right) \left[ \tilde{\varphi} + \int d\mathbf{k} \exp(i\mathbf{k} \cdot \mathbf{r}) \int d\mathbf{v} \frac{f_{Mj}}{N} (\omega - \omega_j^*) (\iota \mathcal{P}_j) \tilde{\varphi}(\mathbf{k};) J_0^2(x_{Lj}) \right], \quad (3.1)$$

where the first term on right hand side corresponds to the adiabatic response, while the second term represents the nonadiabatic response of the particles to a perturbation with all its kinetic effects. Also,  $q_j$  and  $T_j$  are the charge and

### Chapter 3: Trapped Electron Coupled Ion Temperature Gradient Mode And Trapped Electron Mode In The Presence Of Nonadiabatic Passing Electrons

temperature for species  $j$ , respectively, and  $N$  is the equilibrium density.

$$\omega_j^* = \omega_{nj} \left[ 1 + \frac{\eta_j}{2} \left( \frac{v_{\parallel}^2}{v_{thj}^2} - 3 \right) + \frac{\eta_j v_{\perp}^2}{2 v_{thj}^2} \right],$$

where  $\omega_{nj} = (T_j \nabla_n \ln N k_{\theta}) / (q_j B)$  is the *diamagnetic drift frequency*;  $\eta_j = (d \ln T_j) / (d \ln N)$ ,  $v_{\parallel}$  and  $v_{\perp}$  represent parallel and perpendicular velocities, respectively, and  $v_{thj}$  is the thermal velocity of species  $j$ .  $J_0(x_{Lj})$  is the Bessel function of argument  $x_{Lj} = k_{\perp} \rho_{Lj}$ , presenting the FLR effect. We consider a local Maxwellian for each species of mass  $m_j$  as

$$f_{Mj}(\xi, \psi) = \frac{N(\psi)}{\left( \frac{2\pi T_j(\psi)}{m_j} \right)^{3/2}} \exp \left( -\frac{\xi}{T_j(\psi)/m_j} \right)$$

where  $\xi = v^2/2$ . Also in Eq.(4.3)  $\mathcal{P}_j$  represents the guiding center propagator for passing particles of type  $j = i, e$ . For details of the propagator for trapped particles the reader is referred to Ref. [11].

Introducing *quasineutrality condition*

$$\sum_j \tilde{n}_j(\mathbf{r}; \omega) \simeq 0; \quad , \quad (3.2)$$

one would finally end up with a generalized eigenvalue problem where  $\omega$  and  $\tilde{\varphi}$  respectively are the eigenvalue and eigenvector, which can then be conveniently solved in Fourier space by Fourier decomposing the potential in Eq.(6.1) first and then taking Fourier transform to eventually obtain a convolution matrix in Fourier space. With single charged passing ions ( $i$ ), electrons ( $e$ ) along with trapped ions ( $tr-i$ ) and electrons ( $tr-e$ ) we have

$$\sum_{\mathbf{k}'} \sum_{j=i} \hat{\mathcal{M}}_{\mathbf{k}, \mathbf{k}'}^j \tilde{\varphi}_{\mathbf{k}'} + \sum_{\mathbf{k}'} \sum_{j=tr-i} \hat{\mathcal{M}}_{\mathbf{k}, \mathbf{k}'}^j \tilde{\varphi}_{\mathbf{k}'} + \sum_{\mathbf{k}'} \sum_{j=e} \hat{\mathcal{M}}_{\mathbf{k}, \mathbf{k}'}^j \tilde{\varphi}_{\mathbf{k}'} + \sum_{\mathbf{k}'} \sum_{j=tr-e} \hat{\mathcal{M}}_{\mathbf{k}, \mathbf{k}'}^j \tilde{\varphi}_{\mathbf{k}'} = 0,$$

where  $\mathbf{k} = (\kappa, m)$  and  $\mathbf{k}' = (\kappa', m')$ .

### Chapter 3: Trapped Electron Coupled Ion Temperature Gradient Mode And Trapped Electron Mode In The Presence Of Nonadiabatic Passing Electrons

The trapped ion contribution to the matrix is given by [11]

$$M_{k,k'}^{tr-i} = \frac{1}{\Delta\rho} \int_{\rho_i}^{\rho_u} d\rho e^{-i(\kappa_\rho - \kappa'_\rho)\rho} \left( \frac{-Rq_s Nq^2}{B_0 T} \right) \left[ \alpha_b \delta_{m,m'} + \sqrt{\frac{2A^{-1}}{\pi}} \times \int_0^{+\infty} dE \sqrt{E} e^{-E} (\omega - \omega^*) J_0^2(x'_L) \frac{I_X(\tilde{x}_b(k', m), \tilde{x}_b(k' m'), p) e^{ip[\beta_b(k', m) - \beta_b(k', m')]} }{n < \dot{\phi} >_b - p\omega_b - \omega} \right] \quad (3.3)$$

where

$$\begin{aligned} I_X(\tilde{x}_b, \tilde{x}'_b, p) &= \int_0^1 dX J_p(x_b) J_p(x'_b) \\ &= \int_0^1 dX J_p(\sqrt{X}\tilde{x}_b) J_p(\sqrt{X}\tilde{x}'_b), \end{aligned}$$

$$\tilde{x}_b(k, m; \rho, \varepsilon) = 2\sqrt{(m - nq_s)^2 + \left(\frac{q_s k_\rho}{\Omega}\right)^2} \frac{\varepsilon}{A^{-1}},$$

$$\cos \beta_b(\vec{k}) = \frac{(m - nq_s)\theta_b}{x_b}, \quad \text{and} \quad \sin \beta_b(\vec{k}) = \frac{k_b \rho_b}{x_b}.$$

Also,

$$X = \frac{1 - \lambda B_{min}/B_0}{2\lambda A^{-1}},$$

For circulating particles,

$$0 < \lambda < \frac{B_0}{B_{min}} \iff 1 < X < +\infty,$$

and for trapped particles,

$$\frac{B_0}{B_{max}} < \lambda < \frac{B_0}{B} < \frac{B_0}{B_{min}} \iff 0 < \sin^2 \frac{\theta}{2} < X < 1,$$

where  $B_{max, min} = B_0(1 \pm A^{-1})$  and  $B = B_0(1 - A^{-1} \cos \theta)$  the magnetic field at

### Chapter 3: Trapped Electron Coupled Ion Temperature Gradient Mode And Trapped Electron Mode In The Presence Of Nonadiabatic Passing Electrons

the point of interest  $(\rho, \theta)$ . Furthermore, we use the following standard notations:

$E = \varepsilon/v_{th}^2$  is normalized energy variable,

$\varepsilon = v^2/2$  the kinetic energy,

$x_L = k_\perp \sqrt{2\varepsilon}/\Omega$ ,

$\Omega = qB/M$  the cyclotron frequency,

$v_{th} = \sqrt{T/M}$  the thermal velocity,

$\mu = v_\perp^2/2B$  the magnetic moment,

$\lambda = B_0\mu/\varepsilon$  the pitch angle variable,

$\omega_b = \sqrt{A^{-1}\varepsilon}/Rq_s$  the bounce frequency,

$\theta_b = 2\sqrt{X}$  the turning point angle of the trapped particles,

$\rho_b = 2q_s\sqrt{\varepsilon X}/\Omega\sqrt{A^{-1}}$  the half banana width,

and  $A^{-1} = \rho/R$  the inverse aspect ratio.

The toroidal precessional drift  $\langle \dot{\phi} \rangle_b$  for the large aspect ratio can be written as [177]

$$\langle \dot{\phi} \rangle_b = -\frac{\varepsilon}{R^2\Omega} \frac{q_s}{A^{-1}} G,$$

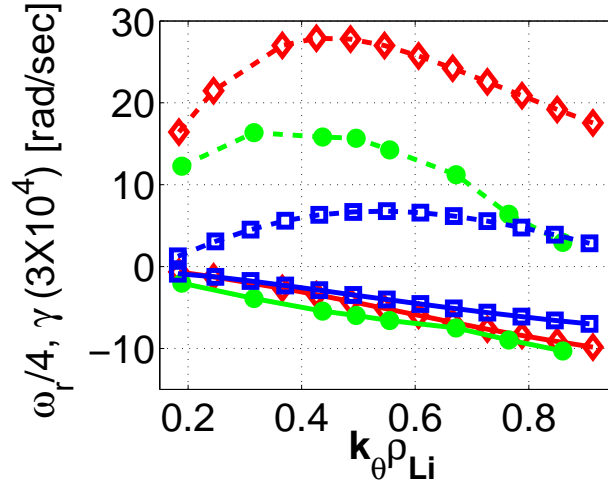
$$G(\rho, X) = 4\lambda \left\{ \hat{s} \left[ (X-1) + \frac{E(X)}{K(X)} \right] + \frac{1}{2} \left[ \frac{E(X)}{K(X)} - \frac{1}{2} \right] \right\}, \quad \text{for } 0 < X < 1,$$

where  $K(X)$  and  $E(X)$ , respectively, are complete elliptic integrals of first and second kind, and  $\hat{s} = d \ln q_s / d \ln \rho$  stands for magnetic shear. A single  $X$ -averaged value  $\langle G \rangle_X$  for each magnetic surface  $\rho$  is considered instead of considering the deeply trapped limit  $X \ll 1$  [11]. Note that the adiabatic term in Eq. (3.3) is weighted by the fraction  $\alpha_b$  of the trapped particles. For the electrons, a bounce averaged relation [178] is considered. Also the FLR and banana width effects can be neglected. Thus the simplified relation for trapped electrons [11] can be written as

$$M_{(k,k')}^{tr-e} = \frac{1}{\Delta\rho} \int_{\rho_i}^{\rho_u} d\rho e^{-i(\kappa_\rho - \kappa'_\rho)\rho} \left( \frac{-Rq_s Nq^2}{B_0 T} \right) \left[ \alpha_b \delta_{m,m'} + \sqrt{\frac{2A^{-1}}{\pi}} \times \int_0^1 dX \lambda \sqrt{\lambda} \frac{I_{\theta(m)} I_{\theta(m')}}{n \langle \dot{\phi} \rangle_{b0} K(X)} \times \left\{ \left[ \omega - \omega_{ne} \left( 1 - \frac{3}{2} \eta_e \right) \right] W(z) - \omega_{ne} \eta_e \left[ \frac{\omega}{n \langle \dot{\phi} \rangle_{b0}} W(z) + \frac{1}{2} \right] \right\} \right], \quad (3.4)$$

### Chapter 3: Trapped Electron Coupled Ion Temperature Gradient Mode And Trapped Electron Mode In The Presence Of Nonadiabatic Passing Electrons

Figure 3.1: Growth rate  $\gamma$  (dashed line) and real frequency  $\omega_r$  (solid line) for  $\eta_i(s_0) = 2$  (i) for pure ITG with adiabatic electron model (squares), (ii) ITG-TEM without nonadiabatic passing electrons (diamonds), and (iii) ITG-TEM with nonadiabatic passing electrons at  $\eta_e(s_0) = 2.0$  (filled circles).



where

$$W(z) = \frac{1}{2\pi} \int_{-\infty}^{+\infty} \frac{x}{x-z} \exp\left(\frac{-x^2}{2}\right) dx, \quad \text{Im}(z) > 0,$$

is the plasma dispersion function [179]. The other quantities are defined as follows.

$$I_\theta(m; \rho, X) = \int_0^{\theta_b} d\theta \frac{\cos(m - nq_s)\theta}{\sqrt{(X - \sin^2(\theta/2))}},$$

and

$$\tau_b = \frac{2Rq_s}{\sqrt{\varepsilon\lambda A^{-1}}} \int_0^{\theta_b} \frac{d\theta}{\sqrt{X - \sin^2(\theta/2)}} = \frac{4Rq_s}{\sqrt{\varepsilon\lambda A^{-1}}} K(X).$$

### 3.3 Results and Discussion

The effects of the nonadiabaticity of passing electrons on ITG mode have been explored and discussed in the preceding chapter. In the present chapter, we shall investigate the effects of nonadiabaticity of the passing electrons on ITG-TEM and TEM.

For this purpose we consider the same profiles and parameters presented in Table 2.1 of the preceding chapter. The equilibrium profiles corresponding to these parameters are shown in Fig. 2.1.

### Chapter 3: Trapped Electron Coupled Ion Temperature Gradient Mode And Trapped Electron Mode In The Presence Of Nonadiabatic Passing Electrons

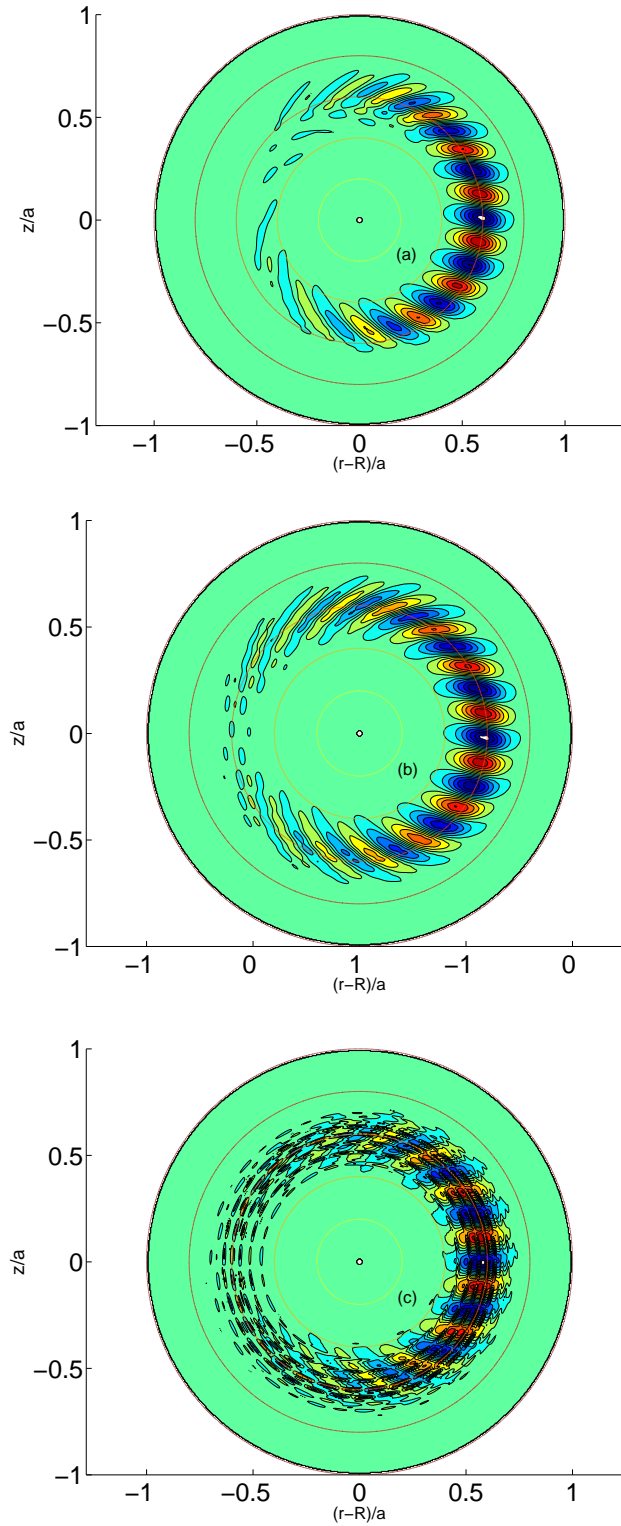


Figure 3.2: Two dimensional eigenmode structure of global ITG at  $n = 8$  and  $\eta_i(s_0) = 2$  for (a) pure ITG with adiabatic electrons, (b) ITG-TEM without nonadiabatic passing electrons, and (c) ITG-TEM with nonadiabatic passing electron<sup>47</sup> at  $\eta_e(s_0) = 2.0$ .

### Chapter 3: Trapped Electron Coupled Ion Temperature Gradient Mode And Trapped Electron Mode In The Presence Of Nonadiabatic Passing Electrons

The real frequency  $\omega_r$  and growth rates  $\gamma$  normalized by  $\omega_{d0} = v_{Ti}(s = s_0)\rho_{Li}/a^2$  for ITG-TEM are plotted in Fig. 3.1. Here we have shown (i) ITG-adiabEl (ITG mode with usual adiabatic electron response, i.e.,  $\tilde{n}/n = e\tilde{\phi}/T_e$ ), (dashed line for  $\tilde{\gamma}$  and solid line for  $\tilde{\omega}_r$  marked with squares), (ii) ITG-TEM without nonadiabatic passing electrons (dashed line for  $\tilde{\gamma}$  and solid line for  $\tilde{\omega}_r$  marked with diamonds), and (iii) ITG-TEM with the contribution from nonadiabatic passing electrons (dashed line for  $\tilde{\gamma}$  and solid line for  $\tilde{\omega}_r$  marked with filled circles). It is clear that the ITG-adiabEl mode is destabilized by the trapped electrons. The increase in the growth rate can be attributed to the following facts: (i) the presence of nonideal effects such as magnetic drift resonances [16], (ii) trapped electrons cannot respond adiabatically to the local variation of the scalar potential and consequently can not take part in charge cancellation[17], and (iii) an increase in real frequency reduces the ion Landau damping leading to an increase in the growth rate [18]. As can be seen, the growth rate peaks at around  $k_\theta\rho_{Li} = 0.5$  corresponding to the toroidal mode number  $n = 8$ . The plot for ITG-TEM along with a nonadiabatic contribution from passing electrons shows opposite effect of reducing the growth rate as compared to the ITG-TEM without nonadiabatic passing electrons. However, the growth rate is still at higher value than the ITG-adiabEl mode. Because of the nonadiabatic response of the passing electrons near the  $k_\parallel = 0$  surfaces to a perturbation, the electrons simply can not respond and short circuit the charge separation instantaneously because of which the mode gets finite amount of time to grow unstable. This sets the growth rate of ITG-TEM with nonadiabatic passing electrons higher than the ITG-adiabEl mode. The fact that it has growth rate lower than that of the ITG-TEM without nonadiabatic passing electrons can be explained as follows: the inclusion of trapped electrons increases the real frequency of the ITG-adiabEl mode such that there is an upshift of phase velocity  $\omega_r/k_\parallel$ , making ion Landau resonance regime narrower and thus increasing the growth rate. However, the inclusion of nonadiabatic passing electrons, in addition, increases the real frequency further thereby upshifting the phase velocity more. This makes the mode Landau resonate dominantly with electrons leading to the electron Landau damping of the growth rate. However, this damping is not sufficient enough to compensate for the increase in the growth rate produced due to weaker Landau resonance with ions. This can be attributed to the fact that the upshift of real frequency, when passing nonadiabatic electrons are included,

### Chapter 3: Trapped Electron Coupled Ion Temperature Gradient Mode And Trapped Electron Mode In The Presence Of Nonadiabatic Passing Electrons

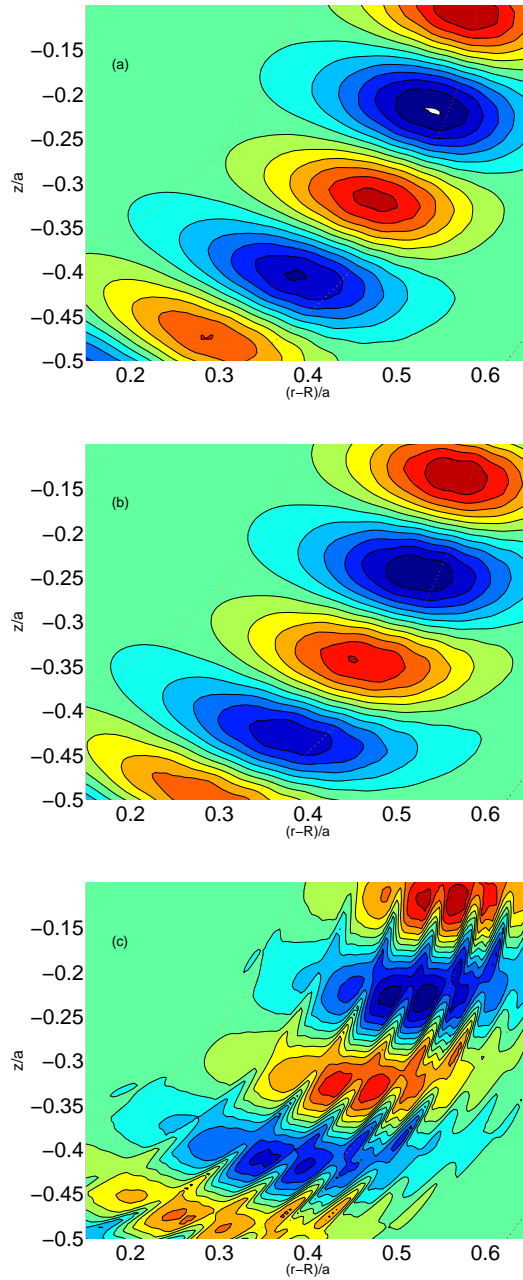


Figure 3.3: Closeup of two dimensional eigenmode structure for (a) pure ITG with adiabatic electrons, (b) ITG-TEM without nonadiabatic passing electrons, and (c) ITG-TEM with nonadiabatic passing electrons at  $\eta_e(s_0) = 2.0$ .

### Chapter 3: Trapped Electron Coupled Ion Temperature Gradient Mode And Trapped Electron Mode In The Presence Of Nonadiabatic Passing Electrons

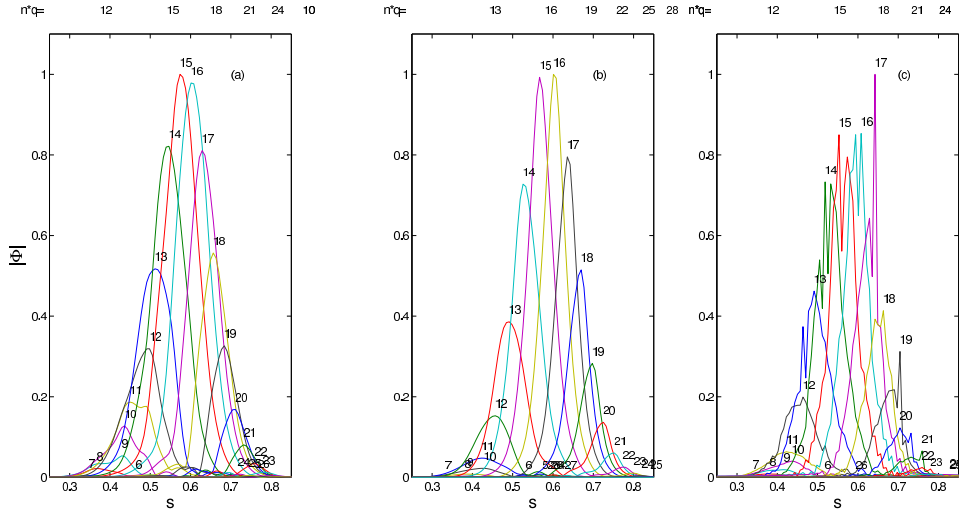


Figure 3.4: Poloidal Fourier components for electrostatic modes shown in Fig. 3.2 (a) ITG with adiabatic electrons, (b) ITG-TEM without nonadiabatic passing electrons, and (c) ITG-TEM with nonadiabatic passing electrons at  $\eta_e(s_0) = 2.0$ . Note that at each radial location, there are several poloidal harmonics coupled. A few locations where  $k_{\parallel m,n} = 0$  (i.e.,  $nq = m$ ) are indicated on the top axis. Nonadiabatic electrons introduce sharp structure near these points.

is not drastic, and only a fraction of the electrons resonate with the upshifted phase velocity of the mode. Hence stabilization due to Landau resonance of passing nonadiabatic electrons is weaker than the destabilization due to off-resonance of ions. This sets the growth rate of ITG-TEM with nonadiabatic passing electrons in between the ITG-adiabEl and ITG-TEM without nonadiabatic passing electrons. The eigenmode structures for the three cases of (i) the ITG-adiabEl mode, (ii) ITG-TEM without nonadiabatic passing electron, and (iii) ITG-TEM with nonadiabatic passing electrons are presented in Fig. 3.2. The mode structure is quite global so that it can pass through several mode rational surfaces. It reiterates our argument of pronounced nonadiabaticity of passing electrons near the  $k_{\parallel} = 0$  surfaces. One can see the changes in the eigenmode structure as one looks from Fig. 3.2(a) to Fig. 3.2(c). The mode acquires more and more global nature spreading toward good-curvature region as one goes from case (i) to case (ii) and finally to case (iii). A closeup look of the eigenmode structures on the poloidal plane is demonstrated in Fig. 3.3. As can be seen, the inclusion of nonadiabatic passing electrons introduces shorter scales in the eigenmode structures.

### Chapter 3: Trapped Electron Coupled Ion Temperature Gradient Mode And Trapped Electron Mode In The Presence Of Nonadiabatic Passing Electrons

These electrons near the  $k_{\parallel} = 0$  surfaces can not quench the charge separation, by moving along the field lines. So at those surfaces the charge separation leads to stronger  $E \times B$  drift and pronounced instability. This causes the linear eigenmode structure to break to shorter scale lengths. The increased strength of the electric field near these surfaces is apparent if one looks at Fig. 3.4, where amplitude of the potential corresponding to each poloidal harmonics is displayed along the minor radius for the three cases. The position of the mode rational surfaces (where  $m = nq$ ) is shown in the upper axis. Spikes in the potential are visible at those places where  $k_{\parallel} = 0$ , i.e., at the mode rational surfaces. One can easily see the coupling of poloidal harmonics at each radial location. The corresponding potential amplitudes in the Fourier space is shown in Fig. 3.5 for (i) ITG-adiabEl mode, (ii) ITG-TEM without nonadiabatic passing electrons and ITG-TEM with nonadiabatic passing electrons. Figure. 3.6 displays the mode-averaged measure of  $k_{\perp}$  along with its two components  $k_{\theta}$  and  $k_r$  for the three cases. The introduction of trapped electrons to the ITG-adiabEl mode and then nonadiabatic passing electrons to ITG-TEM enhances the effective  $k_{\perp}$  by bringing multiscale structures. Because of the increase in the mode-averaged perpendicular wave-number  $k_{\perp}$ , one requires more radial mode numbers for good resolution as well as convergence. Since the effect of the nonadiabatic passing electrons is to introduce short multiscale structures into the global eigen mode, thereby increasing effective  $k_{\perp}$ , one would like to see how it can affect the transport. Here we use the simple mixing length estimation for transport coefficient, where one requires calculating the parameter  $\mathcal{D}_{ML} = \gamma / \langle k_{\perp}^2 \rangle$ , with  $\gamma$  and  $\langle k_{\perp}^2 \rangle$  being the growth rate and mode averaged square of perpendicular wave number, respectively. This  $\mathcal{D}_{ML}$  is here plotted in gyro-Bohm units in Fig. 3.7 against  $k_{\theta}\rho_{Li}$ . While the transport coefficient first increases with  $k_{\theta}\rho_{Li}$  and peaks at  $k_{\theta}\rho_{Li} = 0.4$  and then starts falling for ITG-adiabEl, it, on the other hand, decreases monotonically with  $k_{\theta}\rho_{Li}$  for ITG-TEM without nonadiabatic passing electron response. To note that the parameter,  $\mathcal{D}_{ML} = \gamma / \langle k_{\perp}^2 \rangle$ , in this case, is divided by 8 to show it in the same figure. The inclusion of nonadiabatic passing electron physics into ITG-TEM reduces the transport but keeps the dependence on  $k_{\theta}\rho_{Li}$  same. Since the radial scale length of perturbation is shortened as is apparent from Fig. 3.3, the step size over which particles and energy can be thrown away is reduced. This leads to the decrease in the transport coefficient for the ITG-TEM with nonadiabatic passing electron response below the ITG-adiabEl level.

### Chapter 3: Trapped Electron Coupled Ion Temperature Gradient Mode And Trapped Electron Mode In The Presence Of Nonadiabatic Passing Electrons

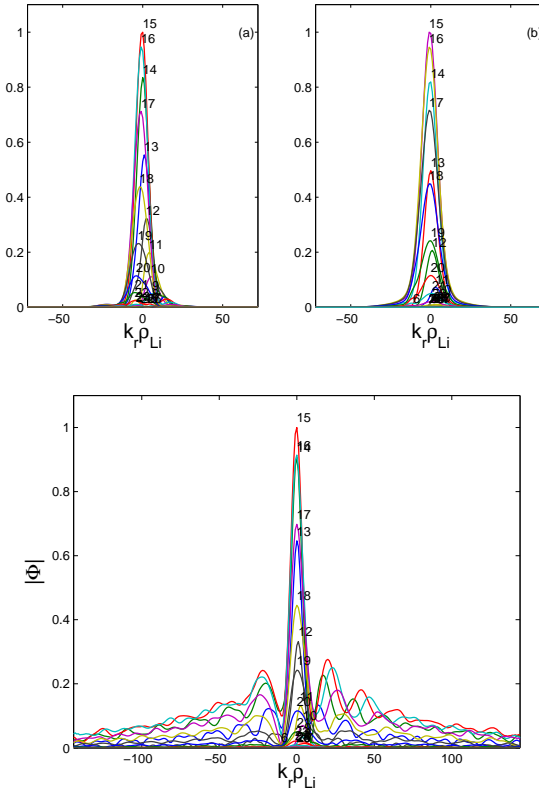


Figure 3.5: Upper panel: Radial Fourier harmonics for each poloidal mode for the electrostatic mode shown in Fig. 3.2 for (a) pure ITG with adiabatic electron response and (b) ITG-TEM without nonadiabatic passing electrons. Lower panel: Radial Fourier harmonics for each poloidal mode for the electrostatic mode shown in Fig. 3.2(c) for ITG-TEM with nonadiabatic passing electrons at  $\eta_e(s_0) = 2.0$ .

Chapter 3: Trapped Electron Coupled Ion Temperature Gradient Mode And Trapped Electron Mode In The Presence Of Nonadiabatic Passing Electrons

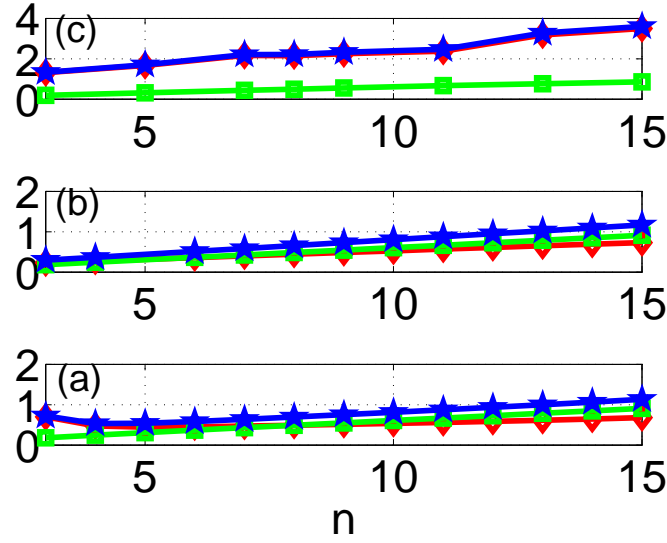


Figure 3.6: Eigenmode-averaged normalized mode numbers  $\langle k_{\theta}\rho_{Li} \rangle$  (squares),  $\langle k_r\rho_{Li} \rangle$  (diamonds), and  $\langle k_{\perp}\rho_{Li} \rangle$  (stars) at  $\eta_i(s_0) = 2$ ; (a) pure ITG with adiabatic electron response, (b) ITG-TEM without nonadiabatic passing electrons, and (c) ITG-TEM with nonadiabatic passing electrons at  $\eta_e(s_0) = 2.0$ .

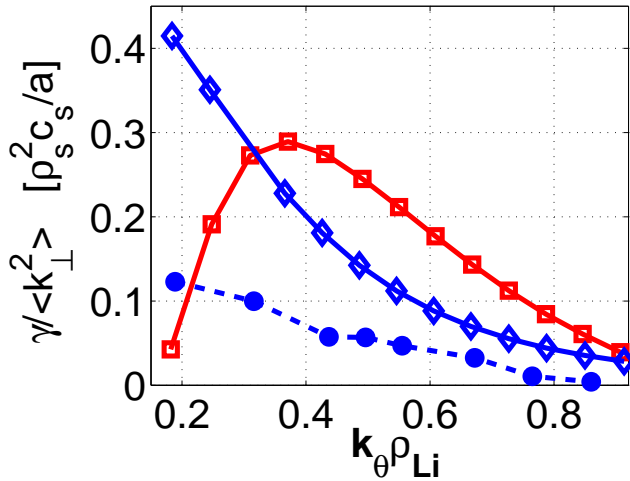


Figure 3.7: Mixing length estimate for transport coefficient  $D_{ML} = \gamma / \langle k_{\perp}^2 \rangle$  in gyro-Bohm units as a function of  $k_{\theta}\rho_{Li}$  for  $\eta_i(s_0) = 2$ ; (a) pure ITG with adiabatic electron response (solid line with squares), (b) ITG-TEM without nonadiabatic passing electrons (divided by 8) (solid line with diamonds), and (c) ITG-TEM with nonadiabatic passing electrons at  $\eta_e(s_0) = 2$  (dashed line with filled circles).

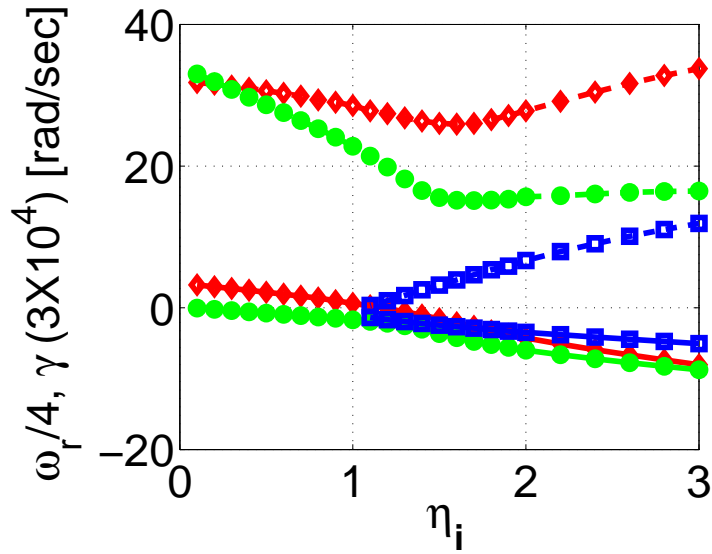


Figure 3.8: Growth rate  $\gamma$  (dashed line) and real frequency  $\omega_r$  (solid line) versus  $\eta_i$  at  $\eta_e(s_0) = 2$  (i) for pure ITG with adiabatic electrons (squares), (ii) ITG-TEM without nonadiabatic passing electrons (diamonds), and (iii) ITG-TEM with nonadiabatic passing electrons (filled circles).

An  $\eta_i$  scan for fixed  $\eta_e = 2.0$  for the three cases is presented in Fig. 3.8. The ITG-adiabatic mode becomes weaker and weaker as  $\eta_i$  is decreased and finally subsides. ITG-TEM without nonadiabatic passing electrons, on the other hand, transforms itself from dominantly ITG mode to dominantly TEM, as one reduces  $\eta_i$ . The reason is that with decreasing  $\eta_i$ , the free energy that drives the ITG mode becomes lesser and lesser, but the finite  $\eta_e$  provides the free energy to the trapped electrons so that mode inherent to trapped electrons starts becoming unstable. The transition occurs at  $\eta_i \sim 1.6$ . Nonadiabatic passing electrons resist the transition of the mode from ITG to TEM character and retain the real frequency in the ion diamagnetic direction with no critical  $\eta_i$ .

### 3.3.1 Trapped Electron Mode

TEMs are sustained by the trapped electron population in the bad-curvature region of a tokamak. Similar to the passing particles, the trapped particles can also produce unstable modes in the presence of density or temperature inhomogeneity.

**Chapter 3: Trapped Electron Coupled Ion Temperature Gradient Mode And Trapped Electron Mode In The Presence Of Nonadiabatic Passing Electrons**

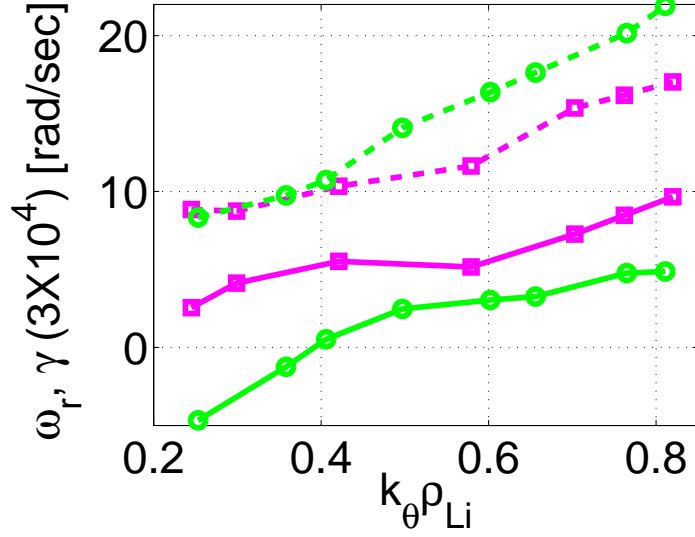


Figure 3.9: Growth rate  $\gamma$  (dashed line) and real frequency  $\omega_r$  (solid line) for  $\eta_i(s_0) = 2$ ; (i) for TEM without nonadiabatic passing electron model (squares) and (ii) for TEM with nonadiabatic passing electron model at  $\eta_i(s_0) = \eta_e(s_0) = 2.0$  (open circles).

genities. The TEM produced due to the presence of electron density gradient is driven by charge separation, while that produced due to the presence of electron temperature gradient is driven by compressibility. The passing fraction of electrons, when considered to respond adiabatically, can maintain the growth rate at a lower value. Recently, TEM in the presence of passing electrons has been studied nonlinearly in Ref. [32] which shows the signature of the persistence of linear mode structure in the non linear regime. We shall here show that nonadiabatic fraction of passing electrons significantly alters the stability properties of TEM. We start with the  $k_\theta \rho_{Li}$  scan of the real frequency and growth rate normalized by  $\omega_{d0} = v_{thi}(s = s_0) \rho_{Li} / a^2$  for the TEM for two cases, namely, (i) TEM without nonadiabatic passing electrons and (ii) TEM with nonadiabatic passing electrons in Fig. 3.9. The dashed line with squares represents the growth rate for case (i), while the solid line with squares represents corresponding real frequency. The dashed line with open circles is for growth rate for case (ii), with solid lines with open circles representing the corresponding real frequency. The scan reveals that nonadiabatic passing electrons destabilize the TEM further. The TEM whether

Chapter 3: Trapped Electron Coupled Ion Temperature Gradient Mode And Trapped Electron Mode In The Presence Of Nonadiabatic Passing Electrons

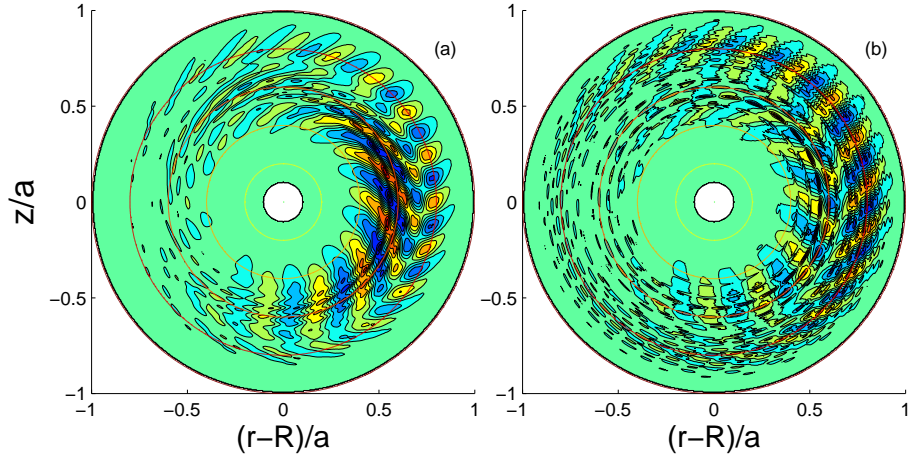


Figure 3.10: Two dimensional eigenmode structure for (a) TEM without nonadiabatic passing electron response and (b) TEM with nonadiabatic passing electron response at  $n = 7$  and  $\eta_i(s_0) = \eta_e(s_0) = 2.0$ .

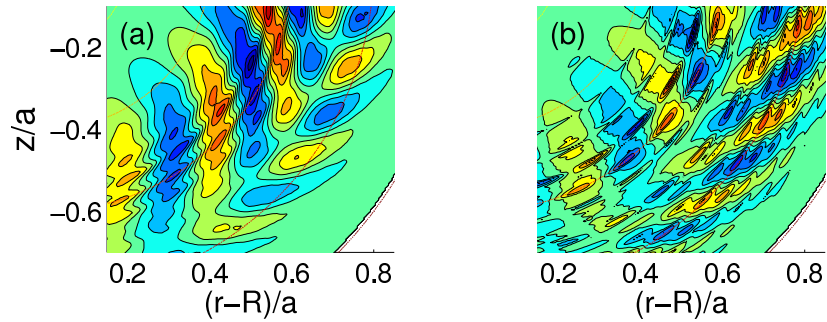


Figure 3.11: Closeup of two dimensional eigenmode structure of (a) TEM without nonadiabatic electron response and (b) TEM with nonadiabatic passing electron response for  $n = 7$  and  $\eta_i(s_0) = \eta_e(s_0) = 2.0$ .

### Chapter 3: Trapped Electron Coupled Ion Temperature Gradient Mode And Trapped Electron Mode In The Presence Of Nonadiabatic Passing Electrons

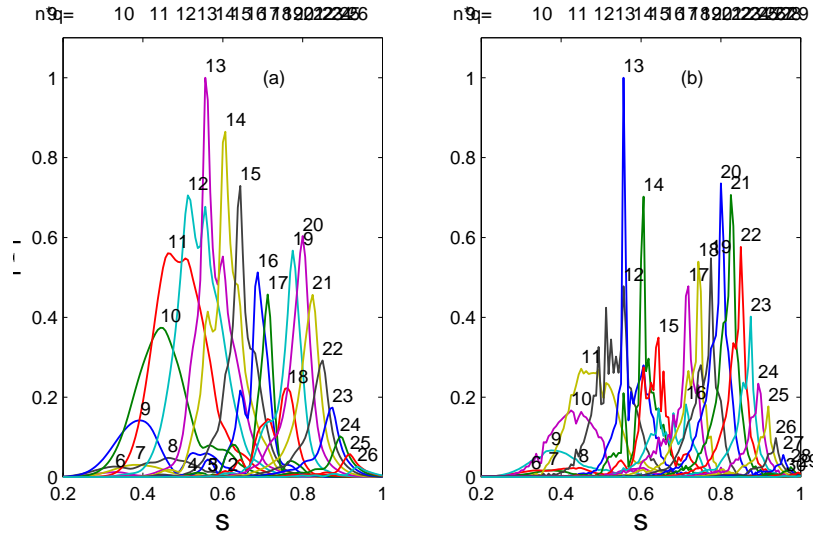


Figure 3.12: Poloidal Fourier components for electrostatic mode shown in Fig. 3.10. Note that at each radial location, there are several poloidal harmonics coupled. A few locations where  $k_{\parallel m,n} = 0$  (i.e.,  $nq = m$ ) are indicated on the top axis. Nonadiabatic electrons introduce sharp structure near these points.

produced due to density gradient or temperature gradient has  $E \times B$  drift at its root. When one considers passing electrons to be adiabatic, the moment charge separation is produced; these electrons move to the region of finite charge separation and wipe out the space charge, thus denying the possibility of building up of  $E \times B$  advection or reducing it. Nonadiabatic passing electrons, on the other hand, take finite time, especially near the  $k_{\parallel} = 0$  surfaces, to reach the region of  $E \times B$  advection, thereby allowing finite time for the mode to grow. The TEM thus gets enhanced when one considers the fraction of nonadiabatic passing electrons. One can expect similar effect of nonadiabaticity of passing electrons on density gradient driven trapped electron mode also.

Next we look at the change in the mode structures of TEM in the presence of these electrons. The global mode structures for the two cases without and with nonadiabatic passing electrons are shown in Fig. 3.10 with a closeup view presented in Fig. 3.11.

It is clear that the modes span through several mode rational surfaces. Non-

### Chapter 3: Trapped Electron Coupled Ion Temperature Gradient Mode And Trapped Electron Mode In The Presence Of Nonadiabatic Passing Electrons

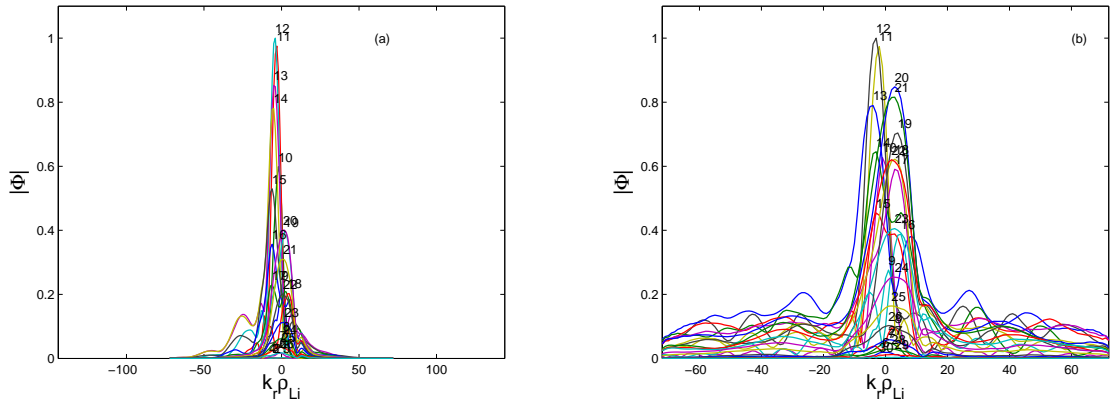


Figure 3.13: Right panel: Radial Fourier harmonics for each poloidal mode for the electrostatic mode shown in Fig. 3.10(a) for TEM without nonadiabatic passing electron response. Left panel: Radial Fourier harmonics for each poloidal mode for the electrostatic mode shown in Fig. 3.10(b) for TEM with nonadiabatic passing electron response.

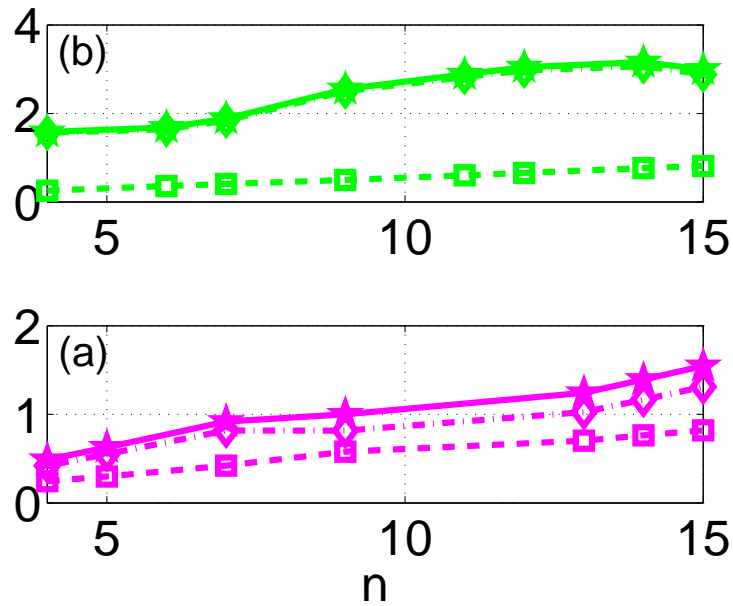


Figure 3.14: Eigenmode-averaged normalized mode numbers  $\langle k_{\theta}\rho_{Li} \rangle$  (squares),  $\langle k_r\rho_{Li} \rangle$  (diamonds), and  $\langle k_{\perp}\rho_{Li} \rangle$  (stars) as a function of  $k_{\theta}\rho_{Li}$  at  $\eta_i(s_0) = 2$ : (a) TEM without nonadiabatic passing electron response and (b) TEM with nonadiabatic passing electrons at  $\eta_e(s_0) = 2.0$ .

### Chapter 3: Trapped Electron Coupled Ion Temperature Gradient Mode And Trapped Electron Mode In The Presence Of Nonadiabatic Passing Electrons

adiabatic passing electrons have strong effect near these surfaces leading to a strong rise in the radial perturbed electric field. This breaks up the mode structure at these surfaces. Similar to the ITG-TEM case, the mode rotates toward the good-curvature region. The local rise in the perturbed radial electric field near mode rational surfaces becomes clear when one looks at the potential amplitude across minor radius, corresponding to different poloidal harmonics in Fig. 3.12, without and with nonadiabatic passing electrons. Strong poloidal coupling is well demonstrated in both cases where at each radial position the mode has contribution from several neighboring components. Figure 3.13 delineates the potential in the Fourier space for the two cases. Production of short scales in the eigenmode structure rises the effective averaged  $k_{\perp}$  from the adiabatic passing electron case to nonadiabatic passing electron case, as can be seen in Fig. 3.14. Estimation of transport via electron channel for which TEM is believed to be an obvious candidate is shown in Fig. 3.15 using simple mixing length estimation, where  $\mathcal{D}_{ML} = \gamma / \langle k_{\perp}^2 \rangle$  is plotted in gyro-Bohm units versus  $k_{\theta} \rho_{Li}$ . The transport coefficient decreases monotonically with increasing  $k_{\theta} \rho_{Li}$  for both cases. However,  $\mathcal{D}_{ML}$  is reduced when one introduces a nonadiabatic fraction of passing electrons to the adiabatically responding passing electron TEM. The reduction in the transport similar to the ITG-TEM case can be understood as due to decreased transport step size caused by the nonadiabaticity of passing electrons.

## 3.4 Conclusion

In the present chapter, we have investigated the effects of nonadiabaticity of passing electrons on ITG-TEM and TEM using the global gyrokinetic spectral code EM-GLOGYSTO. The model includes both passing and trapped particles, profile variations, true ion to electron mass ratio, arbitrary order FLR effects, transit/trapped particle resonances, and poloidal and radial coupling. A comprehensive description of ITG, ITG-TEM, and TEM including all relevant species is presented. The major findings are as follows.

- [1] For the low  $n$  or global modes, nonadiabatic passing electrons stabilize the ITG-TEM. However, it has deleterious effect on TEM leading to an increase

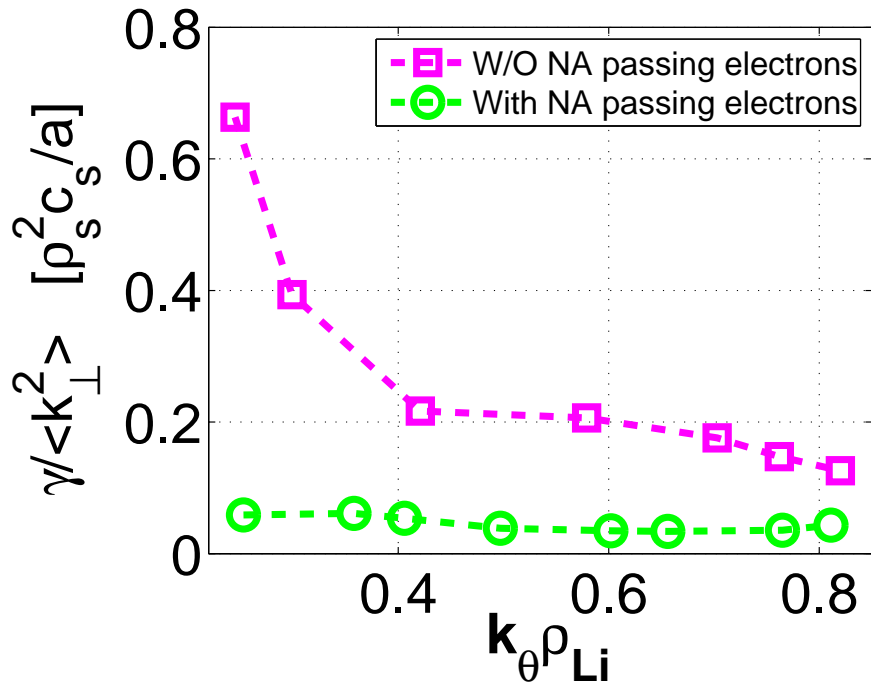


Figure 3.15: Mixing length estimate for transport coefficient  $D_{ML} = \gamma / \langle k_{\perp}^2 \rangle$  in gyro-Bohm units as a function of  $k_{\theta} \rho_{Li}$  with  $\eta_i(s_0) = 2.0$  for (a) TEM without nonadiabatic passing electron response (dashed line with squares) and (b) TEM with nonadiabatic passing electron response at  $\eta_e(s_0) = 2.0$  (dashed line with open circles).

### Chapter 3: Trapped Electron Coupled Ion Temperature Gradient Mode And Trapped Electron Mode In The Presence Of Nonadiabatic Passing Electrons

in the growth rate.

- [2] For both ITG-TEM and TEM, spatial mode structures exhibit multiscale feature. Because of the drastic rise in the phase velocity near the  $k_{\parallel} = 0$  surfaces, passing electrons fail to respond adiabatically near these surfaces, leaving open charge separation and pronounced  $E \times B$  drift. This breaks up the mode structure near the  $k_{\parallel} = 0$  surfaces.
- [3] The existence of multiscale features in the spatial mode structure makes effective  $k_{\perp}$  higher, which eventually reduces the mixing length based estimation of transport of the corresponding modes below the level predicted by their respective adiabatic electron models.

# Chapter 4

## Modes inherent to nonadiabatic/kinetic passing electrons

### 4.1 Introduction

Having elucidated the effect of kinetic/nonadiabatic electrons on temperature gradient driven modes of thermal ions and trapped electrons we now discuss the modes inherent to the nonadiabatic/kinetic passing electrons. A correct kinetic/nonadiabatic passing electron model should be able to produce modes that are inherent to the nonadiabaticity of passing electrons. Therefore, this chapter is dedicated to the study of temperature and density gradient driven modes of kinetic electrons, namely, the electron temperature gradient (ETG) mode and universal drift mode. We will study the linear ETG mode in the presence of completely kinetic ions and Debye Shielding effect. A comparison of the pure ion temperature gradient (ITG) mode with the pure ETG mode in the presence of fully gyro-kinetic second species (e.g., electrons for ITG and ions for ETG) will be carried out. One will see the breaking of isomorphy of ITG and ETG modes even in the electrostatic limit without incorporating the trapped electrons. A comparison of the electron flux by ETG mode in the presence of nonadiabatic ions with  $\eta_i$  above the ITG threshold and ion flux by ITG mode in the presence of nonadiabatic electrons with  $\eta_e$  above the ETG threshold reveals that these modes are not independent of each other. In

## Chapter 4: Modes inherent to nonadiabatic/kinetic passing electrons

fact, one mode tends to reduce the transport by the other and vice versa.

Regarding the other mode driven by the density gradient of nonadiabatic passing electron, i.e., the universal drift mode: although the studies have evolved from a simple slab model to the toroidal geometry, most of them, however, are based on the fluid or hybrid kinetic-fluid models. A few gyrokinetic models either exploited the ballooning formulation or a simple geometry. In this chapter we will present a global, fully gyrokinetic linear study of the toroidicity driven universal drift mode considering both ions and electrons to be nonadiabatic. The formulation retains toroidal coupling effects due to both electron and ion  $\nabla B$  and curvature drift with no assumption regarding the magnetic drift frequency of the ions and electrons compared to the mode frequency, thereby allowing full magnetic drift resonance by both species. The formulation also keeps the Landau damping term of both electrons and ions. The finite Larmor radius effects are kept up to all orders. More importantly, the present study retains the transit frequency resonance term in the nonadiabatic part of the density perturbation for both species as shown in Eqs. (2.8) and (2.9). It is to be noted that, we use a large aspect ratio, circular geometry for the tokamak, with no Shafranov shift. Though the universal toroidal mode is inherently due to the passing nonadiabatic electrons, effects of trapped electrons and trapped ions are also retained in the formulation. Furthermore, no collisional effect is considered in the formulation.

With this model, various parametric studies of the toroidal branch of universal mode have been carried out. We observe finite mode frequencies and growth rates beyond the critical  $\eta = L_n/L_T$  for Ion Temperature Gradient (ITG) and Electron Temperature Gradient (ETG) modes, where  $L_n$  and  $L_T$  are, respectively, the density and temperature scale lengths. A comparative study of the contribution of magnetic drift resonance as well as Landau resonance from both species toward the stability properties of the mode is performed by a systematic parametric scan. An electromagnetic study of the mode is also carried out that elucidates the effect of finite  $\beta$  on the universal drift mode driven by toroidicity. The effect of trapped electrons on the universal mode is studied and growth rates and real frequencies are compared with the ion temperature gradient mode and trapped electron mode.

## 4.2 Electron Temperature Gradient Driven Mode

Having unravelled the effect of the nonadiabatic passing electrons on the ITG mode [132] and trapped electron coupled ITG mode (ITG-TEM) [133] in the previous chapters, we now proceed to study the mode inherent to the nonadiabatic passing electrons, that is, the ETG mode.

With the formulation discussed in Chapters 2 and 3, the Poisson equation can be written as,

$$\nabla^2 \tilde{\varphi} = \frac{e}{\epsilon_0} \sum_{j=e,i} \tilde{n}_j(\mathbf{r}; \omega); \quad (4.1)$$

where,  $j$  stands for charge species, viz., electrons (e) and ions (i). For single charged passing ions and electrons we have

$$\sum_{\mathbf{k}'} \sum_{j=i} \hat{\mathcal{M}}_{\mathbf{k},\mathbf{k}'}^j \tilde{\varphi}_{\mathbf{k}'} + \sum_{\mathbf{k}'} \sum_{j=e} \hat{\mathcal{M}}_{\mathbf{k},\mathbf{k}'}^j \tilde{\varphi}_{\mathbf{k}'} = 0$$

### 4.2.1 Profiles and Parameters

For the purpose of our study, we consider following profiles and parameters.

Table 4.1: Profiles and parameters

Parameters:

- B-field :  $B_0 = 1.0$  Tesla
- Temperature :  $T_0 = T(s_0) = 7.5$  keV
- Major Radius :  $R = 2.0$  m
- Minor Radius :  $a = 0.5$  m
- radius :  $s = \rho/a$ ,  $0.01 < s < 1.0$ ,  $s_0 = 0.6$
- $L_{n0} = 0.4$  m,  $L_{T0} = 0.2$  m
- $\eta_{i,e}(s_0) = 2.0$ ,  $\epsilon_n = L_{n0}/R = 0.2$
- $\tau(s) = T_e(s)/T_i(s) = 1$ .

Equilibrium Profiles:

- N-profile and T-profile
- $\frac{N(s)}{N_0} = \exp\left(-\frac{a \delta s_n}{L_{n0}} \tanh\left(\frac{s-s_0}{\delta s_n}\right)\right)$
- $\frac{T_{i,e}(s)}{T_0} = \exp\left(-\frac{a \delta s_T}{L_{T0}} \tanh\left(\frac{s-s_0}{\delta s_T}\right)\right)$
- $\delta s_n = 0.35$ ,  $\delta s_T = 0.2$  at  $s = s_0$
- $q(s) = 1.25 + 0.67 s^2 + 2.38 s^3 - 0.06 s^4$
- such that  $q(s = s_0) = 2.0$ ;
- shear  $s = s_0$ ,  $\hat{s} = 1$ .

The chosen parameters lead to the value of  $\rho^* \equiv \rho_{Li}(s = s_0)/a \simeq 0.0175$ . Note

that  $\rho_e = 2.065 \times 10^{-4}\text{m}$  and  $\rho_i = 8.848 \times 10^{-3}\text{m}$ . Any change in the parameters will be stated wherever necessary.

### 4.2.2 Pure ETG Mode

At the outset, let us compare the ETG mode results with respect to some known works. To that end we have chosen the local, linear, electrostatic, and kinetic results of Horton *et al.* [21] for which  $k_\theta \rho_e \simeq 0.5$ ,  $\epsilon_n = L_n/R = 0.2$  and  $\tau = 1.0$ . From Figs.3 and 4 of Horton *et al.* [21] we have extracted manually some points and replotted with the results of our global, linear, electrostatic, and gyrokinetic model for nonadiabatic electrons in Fig. 4.1 for the same parameters. For the ease of comparison for the readers, we have also copied and pasted Figs. 3 and 4 of Horton *et al.* in Fig. 4.2. It is to be noted that  $r_n$  and  $v_{ei}$  in the latter case correspond to  $L_n$  and  $v_{the}$  in our case. Note that the differences in the real frequencies as well as growth rates in both cases can be ascribed to the differences in the two models, namely, local versus global and kinetic versus gyrokinetic.

### Effect of Debye Shielding

Now a days, fast wave electron heating (FWEH) experiments [69], to study specifically electron channel transport, use preferentially dominant electron heating such that  $T_e$  can take very high values. Furthermore, experiments dedicated to the ETG mode study require separation between the electron and ion channel of transport. This is achieved by reducing the energy exchange between the two species. The conducive environment is achieved with plasma of low density that ensures less amount of collisionality. Thus, the Debye length, which is proportional to  $\sqrt{(T_e/n)}$  can be expected to violate the condition  $k\lambda_{de} \ll 1$ . In such a situation, one requires to take in to account the space charge effect, and the Debye shielding effect inevitably comes into the picture.

The Debye shielding effect was taken into account in a number of previous works in the slab and sheared slab [20, 134, 135] geometry and toroidal geometry [22, 136]. In the present case, we produce a toroidal mode number  $n$  and  $k_\theta \rho_e$  scan with and without the Debye shielding effect for the ETG mode that contains no trapped particles and no effect of nonadiabatic ions. Figure. 4.3 presents the real frequency and growth rate versus  $k_\theta \rho_e$  with and without the Debye shielding.

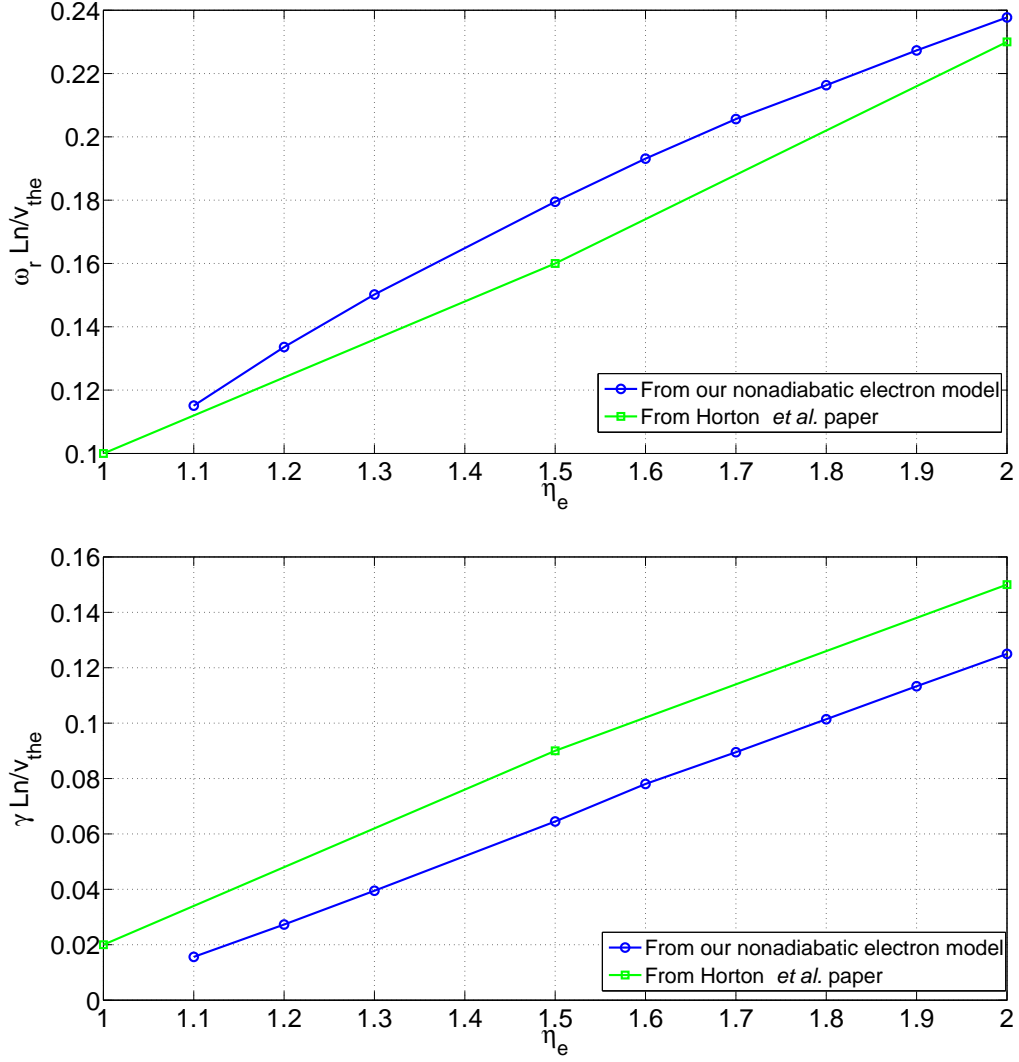
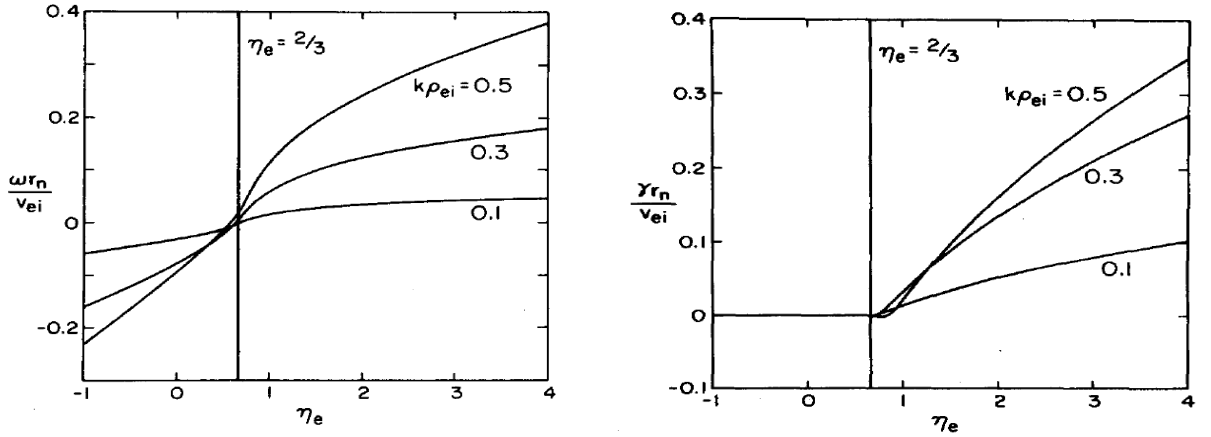


Figure 4.1: The normalized real frequency  $\omega_r$  (upper panel) and growth rate  $\gamma$  (lower panel) for the ETG mode as function of  $\eta_e$  for  $k_\theta \rho_e \simeq 0.5$ ,  $\epsilon_n = L_n/R = 0.2$ , and  $\tau = 1.0$ . The lines with squares represent manually extracted points from Horton *et al.* [21] which uses local kinetic formulation. The lines with open circles depict the results from our global linear gyrokinetic model.


 Figure 4.2: Figures 3 and 4 from Horton *et al.* [21]

The corresponding toroidal mode numbers  $n$  are shown in the upper axis for both frequency and growth rate of the mode. From the figure it is apparent that the mode frequency for the case without Debye shielding is being slightly higher than that in the case with the Debye shielding. Also, one can infer that the Debye shielding has strong stabilizing effect on the mode. One important point to be noted is that the Debye shielding effect removes the high  $k$  tail of the ETG mode. The observed effect of the Debye shielding on the real frequency of the mode is weak as compared to the effect of the same on the growth rate. The other purpose, these figures serve, is that they exhibit the dispersion diagram for the ETG mode with and without Debye shielding showing the dependence of the frequency and growth rate on  $k_{\theta}\rho_e$ . For the case with Debye shielding the growth rate peaks at  $k_{\theta}\rho_e = 0.34$  and for the case without Debye shielding the same peaks at  $k_{\theta}\rho_e = 0.5$ , and both decrease by substantial fraction as one goes both side from the respective peaks. The toroidal mode numbers corresponding to both cases are  $n = 250$  and  $n = 360$ , respectively. Thus, the Debye shielding not only reduces the growth rate of the mode but also shifts the maximum of the growth rate toward lower  $k$ , and wipes out the higher  $k$  tail. It is interesting to see whether Debye shielding has any effect on the threshold of the onset of the ETG mode; it may be important to take into account the Debye shielding effect while calculating precisely the threshold. Figure 4.4 displays the growth rate of the ETG mode against  $\eta_e$  for the two cases with and without the Debye shielding effect. The

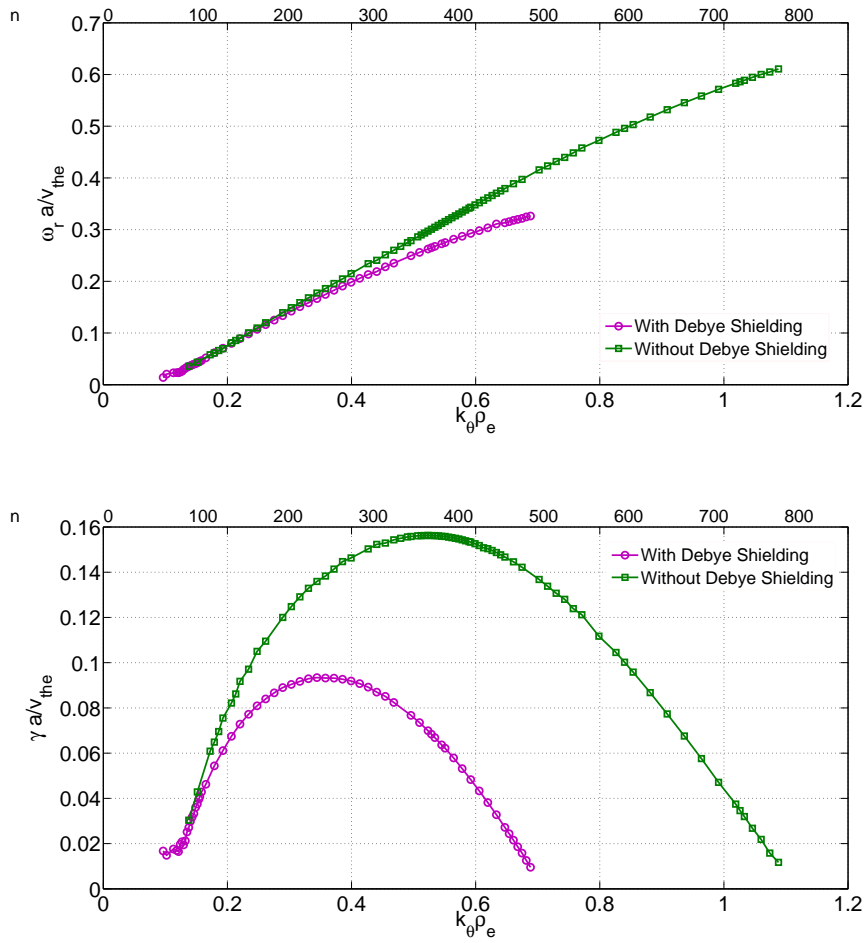


Figure 4.3: The normalized real frequency  $\omega_r$  (upper panel) and growth rate  $\gamma$  (lower panel) for the ETG with and without Debye shielding for  $\eta_e(s_0) = 2$ . Ions are considered adiabatic.

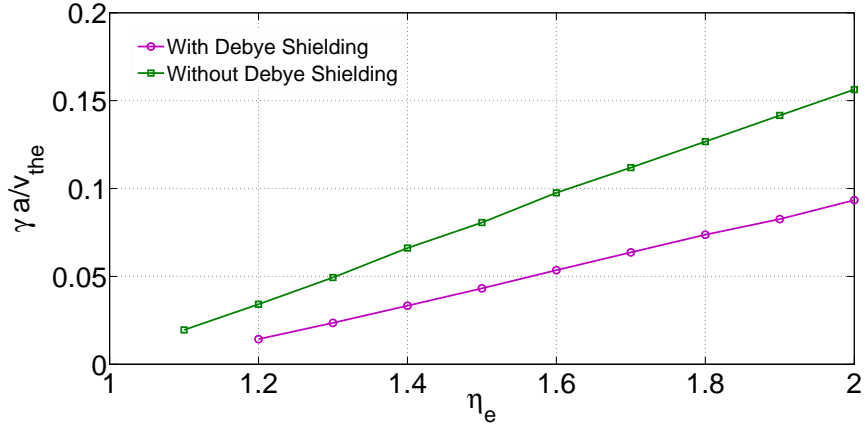


Figure 4.4:  $\eta_e(s_0)$  scan for the growth rate of the ETG mode with and without Debye shielding for  $n = 250$  and  $380$ , respectively.

Debye shielding enhances the threshold of the mode and the mode without the Debye shielding effect is more susceptible to the instability, lowering the threshold of the instability. Thus, one can conclude that Debye shielding affects significantly the ETG mode; it has stabilizing effect on the mode leading to enhanced threshold; shifts the maximum growth rate toward lower  $k_\theta \rho_e$  or  $n$ ; wipes out the high wave number tail of the mode.

### Effect of Nonadiabatic Ions: A Comparison With ITG Mode

The coupling of ITG mode with trapped electrons has been studied both theoretically, and also observed experimentally. Earlier studies of the ETG mode preferred to proceed with the adiabatic ion model, upon the basis of the assumption that the ions are adiabatic as their Larmor radii are larger than the scale-length of the ETG/streamer/zonal flow/geodesic acoustic mode.

The finite mass effect of ions, nonetheless, was studied earlier in Refs. [136, 137] and was found to have very weak effect on the mode. However, of late, nonlinear simulations [36, 37, 91, 92, 93, 94] have demonstrated the limitations of this adiabatic ion model. The nonadiabatic ions are found to be important for the development of low  $k$  tail of the ETG mode. Furthermore, the nonadiabatic ions help getting saturation in the simulation of the electron heat diffusivity. Here, we investigate the impact of the ions on the ETG mode if considered fully nonadia-

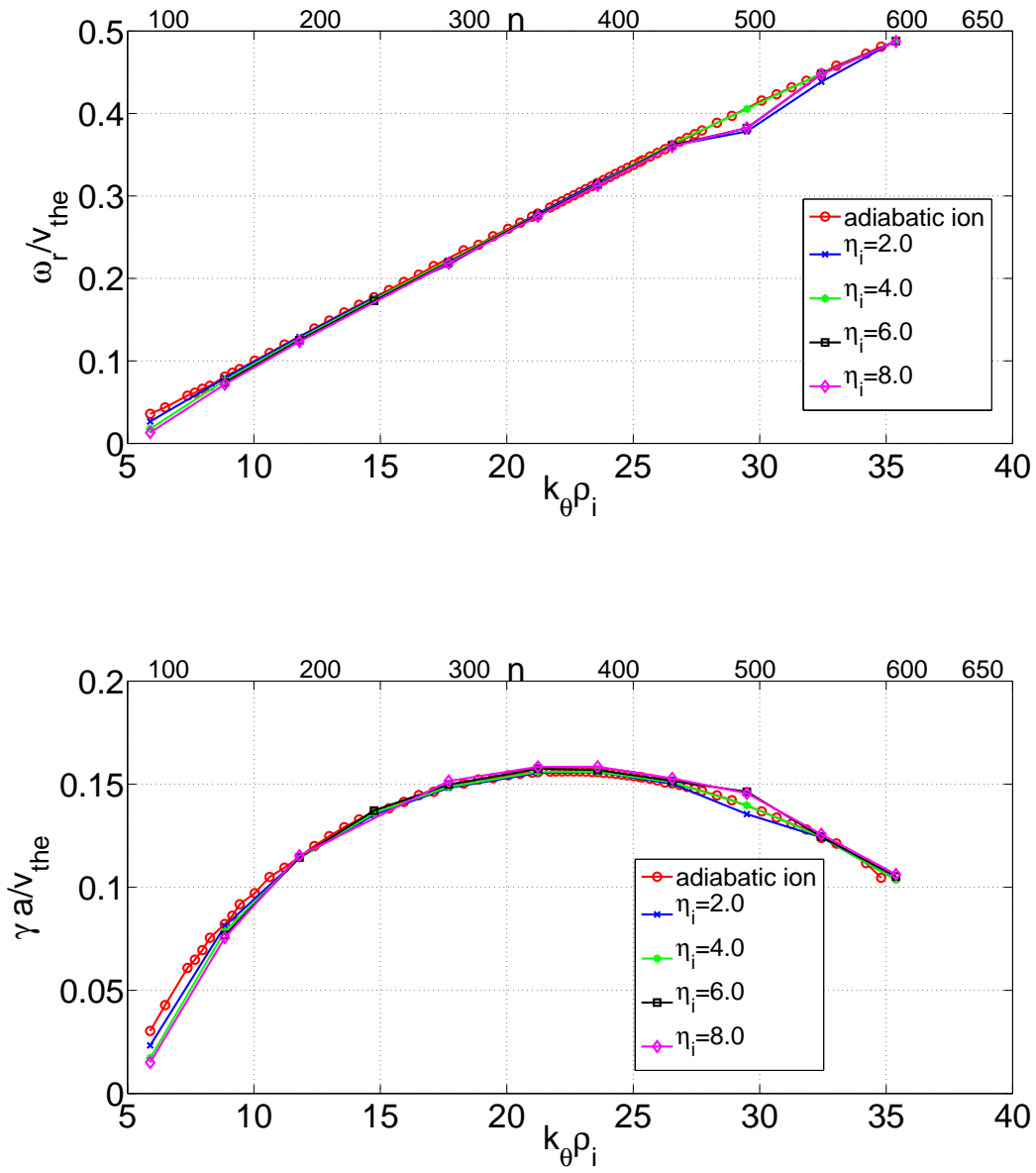


Figure 4.5: Upper panel: The normalized real frequency  $\omega_r$  for the ETG mode without Debye shielding  $\eta_e(s_0) = 2.0$  with adiabatic ions and nonadiabatic ions.  $\eta_i(s_0)$  takes values 2, 4, 6, 8 for nonadiabatic ions. Lower panel: The corresponding growth rates  $\gamma$ .

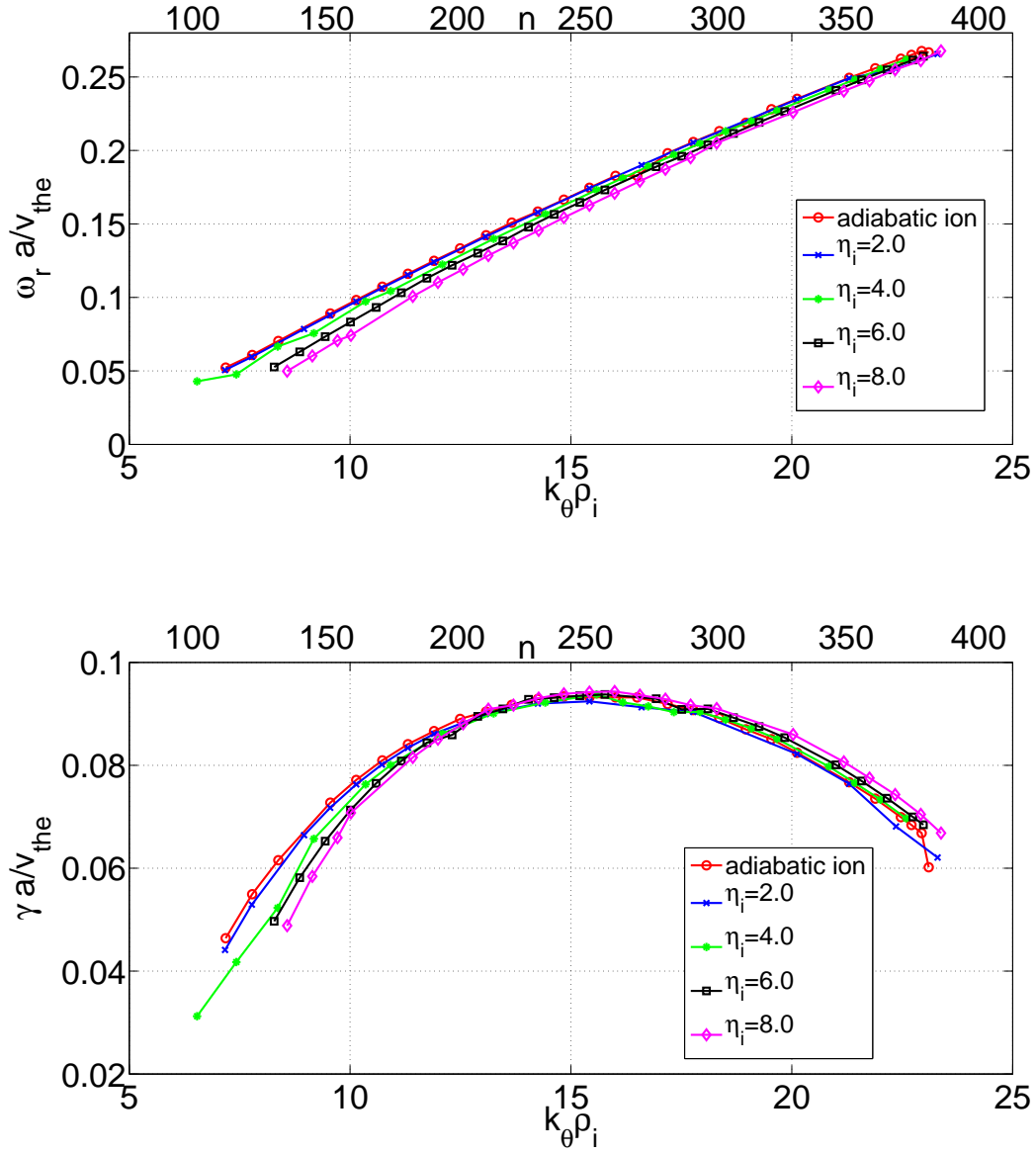


Figure 4.6: Upper panel: the normalized frequency  $\omega_r$  for the ETG mode with Debye shielding for  $\eta_e(s_0) = 2.0$  with adiabatic ions and nonadiabatic ions.  $\eta_i(s_0)$  takes values 2, 4, 6, 8 for nonadiabatic ions. Lower panel: the corresponding growth rates  $\gamma$ .

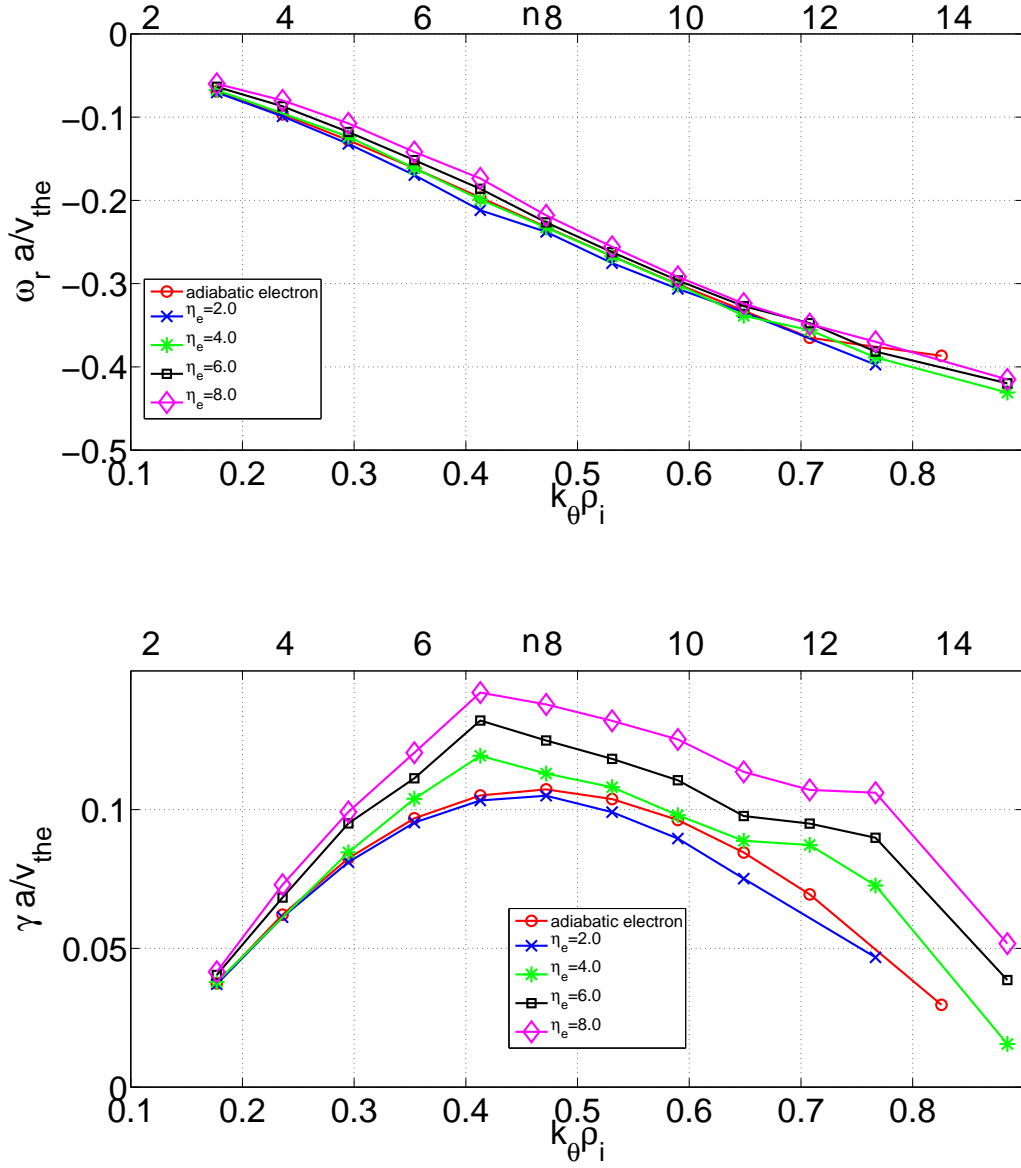


Figure 4.7: Upper panel: the normalized frequency  $\omega_r$  for the ITG mode for  $\eta_i(s_0) = 2.0$  with adiabatic and nonadiabatic electrons.  $\eta_e(s_0)$  takes values 2, 4, 6, 8 for nonadiabatic electrons. Debye shielding is not included for these runs. Lower panel: the corresponding normalized growth rates  $\gamma$ .

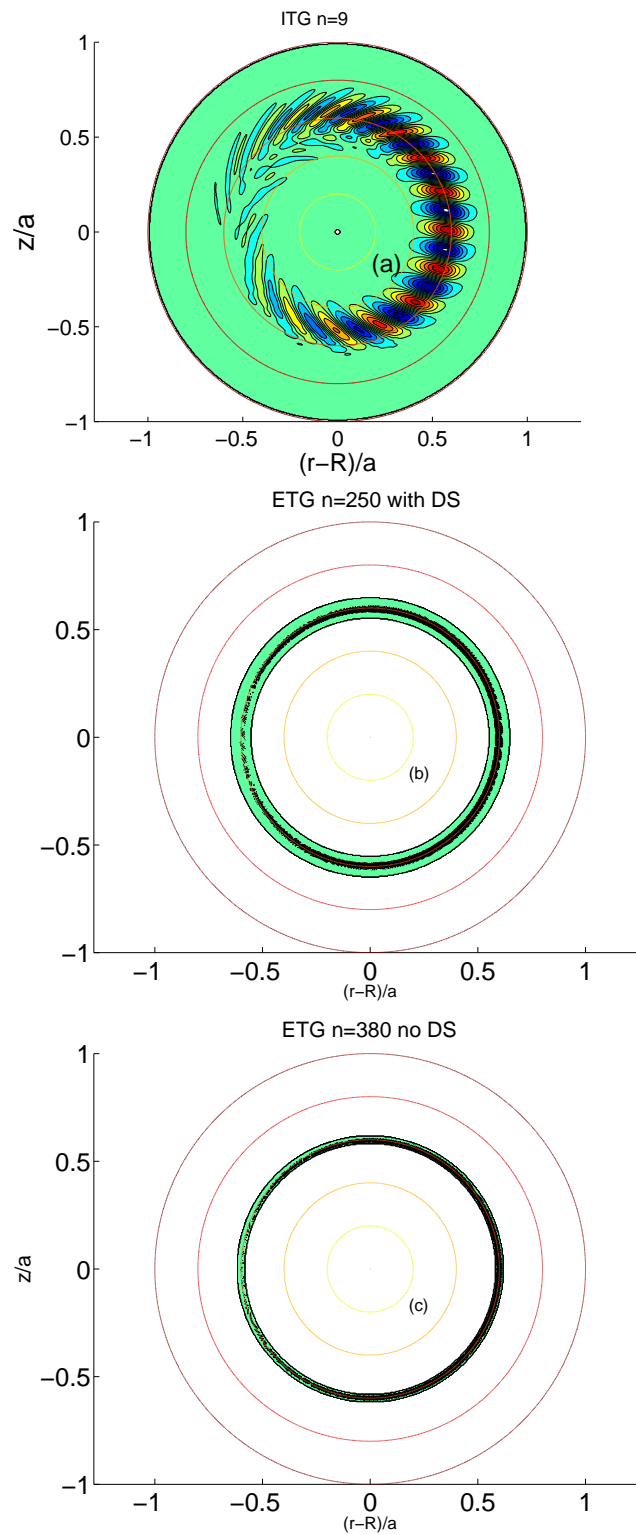


Figure 4.8: Mode structures for the ITG mode for  $\eta_i(s_0) = 2.0$  (left) and ETG mode for  $\eta_e(s_0) = 2.0$  with (middle) and without (right) Debye shielding on the poloidal cross section of a tokamak for the maximum growth rates. The other species (electron for ITG, ion for ETG) is considered adiabatic. 73

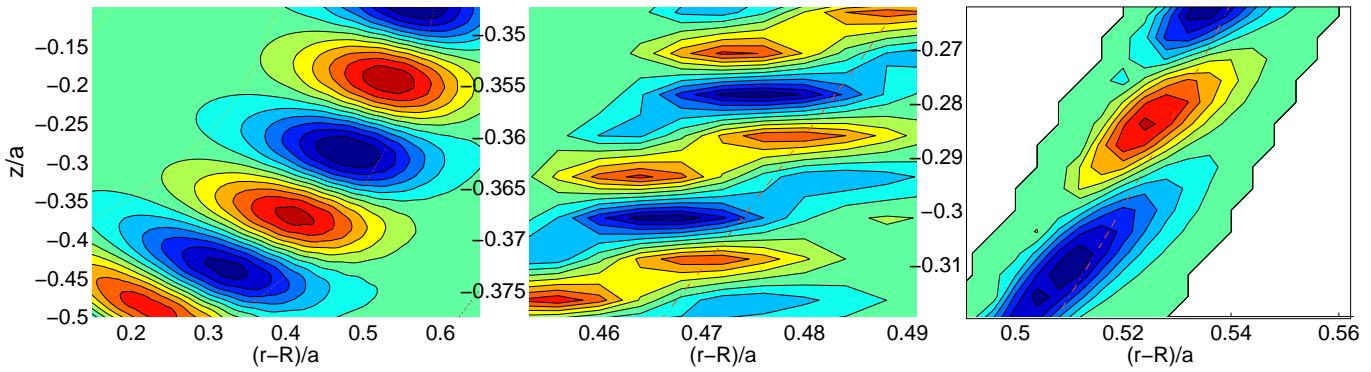


Figure 4.9: Closeup view of Fig. 4.8

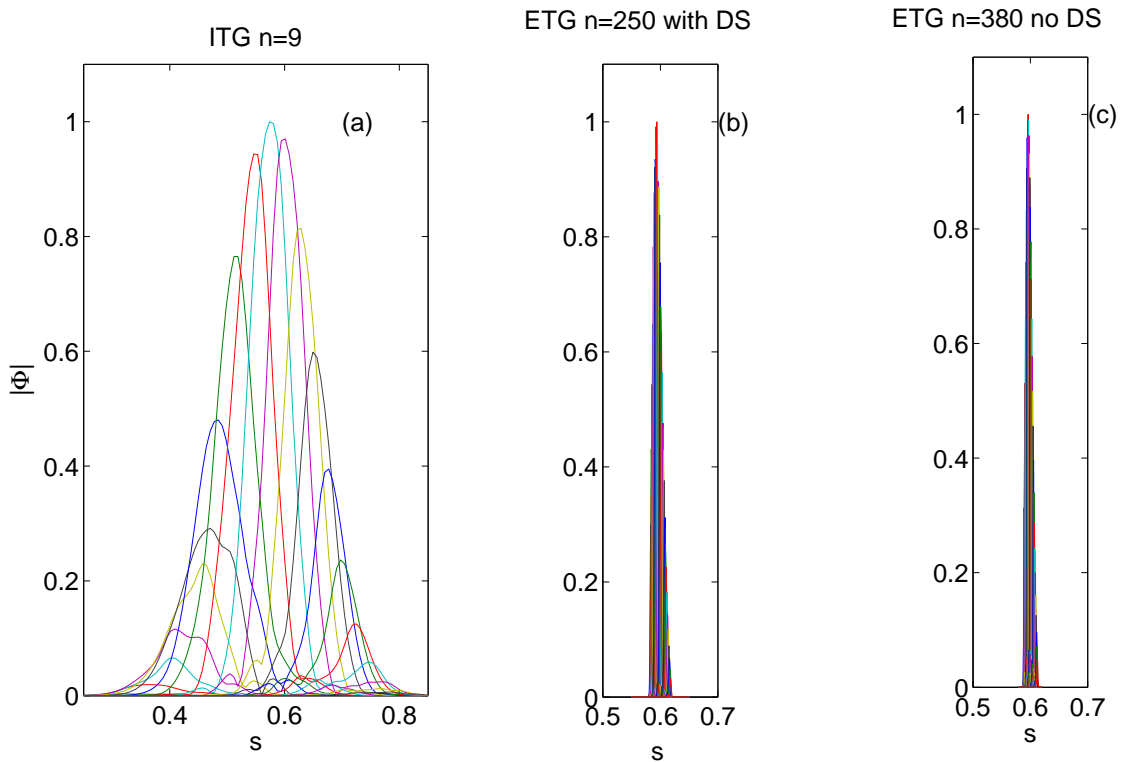


Figure 4.10: Poloidal Fourier harmonics for the modes shown in Fig. 4.8

## Chapter 4: Modes inherent to nonadiabatic/kinetic passing electrons

batically, i.e., taking into account all the kinetic effects of ions from FLR to various resonances and keeping  $\eta_i$  above the threshold of the ITG drive. Figure 4.5 depicts the mode frequency and growth rate of the ETG mode against  $k_\theta \rho_i$  (Note that  $k_\theta$  is normalized with  $\rho_i$  here.) with (i) adiabatic ions and (ii) nonadiabatic ions for increasing  $\eta_i$  for the case without Debye shielding. The corresponding toroidal mode numbers are displayed on the upper axis. It is observed that the nonadiabatic ions have very weak effect on the growth rates of the mode. In the second case, we have carried out same kind of scan but with Debye Shielding effect included. Figure 4.6 shows the real frequency and growth rate for the case of the ETG mode when Debye shielding is taken in to account. A comparison of the real frequency and growth rate with the case without Debye shielding reveals that the ion dynamics have visible albeit weak effect on the mode frequency as well as growth rate of the mode. The nonadiabatic ions tend to lower the growth rate of the ETG mode as one increases the ITG drive by increasing  $\eta_i$  of ions in the long wavelength side of the ETG mode corresponding to low  $k$  tail of the spectrum. For the purpose of comparison, we present a  $k_\theta \rho_i$  scan for the ITG mode (from Chapter 2) including the adiabatic and nonadiabatic electrons, with  $\eta_e$  increasing for the latter case. Figure 4.7 depicts the real frequency as well as corresponding growth rates for the ITG mode. While the ITG mode is influenced strongly by the nonadiabatic electrons with substantial change in the growth rate, the ETG mode, on the other hand, is weakly affected by the nonadiabatic ions. Thus, one can draw a conclusion that even within the electrostatic limit, without taking into account the trapped species, the isomorphism of the ITG and ETG mode breaks, when the other species (electrons for the ITG mode and ions for the ETG mode) is considered fully kinetically. The corresponding mode structures of the ITG and ETG mode with and without the Debye shielding effect are compared in the top panel of Fig. 4.8 for the maximum growth rates of the respective cases. The figure delineates the vast difference in the scale-lengths of the two modes. While the ITG mode prevails over a considerable fraction, ETG mode, on the other hand, is restricted to a small annular ring in the poloidal cross section of the tokamak. The middle panel shows a closeup view of the ITG and ETG mode structures. The poloidal Fourier components for the three cases are displayed in the bottom panel.

### 4.2.3 Mixing length estimate of flux

It would be interesting to see, how one mode's scale-dynamics have effect on the transport of the other or in other words how the ITG scale can affect the ETG scale and vice versa. For that purpose, simple mixing length estimate of transport has been evaluated. Before going to the results, we would like to add a line of caveat regarding the mixing-length based estimation of transport. The earlier results showed that the calculation of transport using mixing-length theory gives very low level of transport of electrons. Nonlinearly these modes generate streamers, by means of which, the ETG mode can give rise to experimentally relevant level of transport. Nonetheless, within our scope, we present a qualitative picture of the transport with the mixing-length calculation.

#### Pure ETG: a comparison with ITG

Figure 4.11 presents the heat diffusivity in the electron gyro-Bohm unit for the pure ETG mode without (top panel) and with (middle panel) the Debye shielding effect for the multiple cases of increasing  $\eta_i$  of nonadiabatic ions and with adiabatic ions. It is apparent from the figure that even though the nonadiabatic ions have very weak effect on the growth rate of the ETG mode, they can change the heat diffusivity of the electrons substantially. The diffusivity peaks toward the low  $k$  side of the spectrum but not at  $k$  where the growth rate peaks, and decreases as the  $\eta_i$  increases from 2 to 8, in steps of 2 which are all above the ITG threshold. One can hence conclude that the ion scale drive in the low  $k$  regime reduces the high  $k$  ETG drive, even if it has weaker effect on the mode frequency and growth rate of the ETG mode. The bottom panel displays the nonadiabatic electron effect on the ITG mode, where  $\eta_e$  of the electrons increases gradually from 2 to 8. This leads to the reduced ion diffusivity for the ITG case in the presence of an electron drive with  $\eta_e$  being above the ETG threshold. Thus, the comparison of the three cases depicted in Fig. 4.11, leads to the interesting conclusion that the ETG drive on the high  $k$  side tends to reduce the ion transport on the low  $k$  side, while the ITG drive on the low  $k$  side tends to reduce the electron transport on the high  $k$  side of the spectrum. One other conclusion is that in spite of exhibiting disparate scales, one mode can have effect on the other mode, putting a caveat to the tacit assumption that one mode is independent of the other because of the

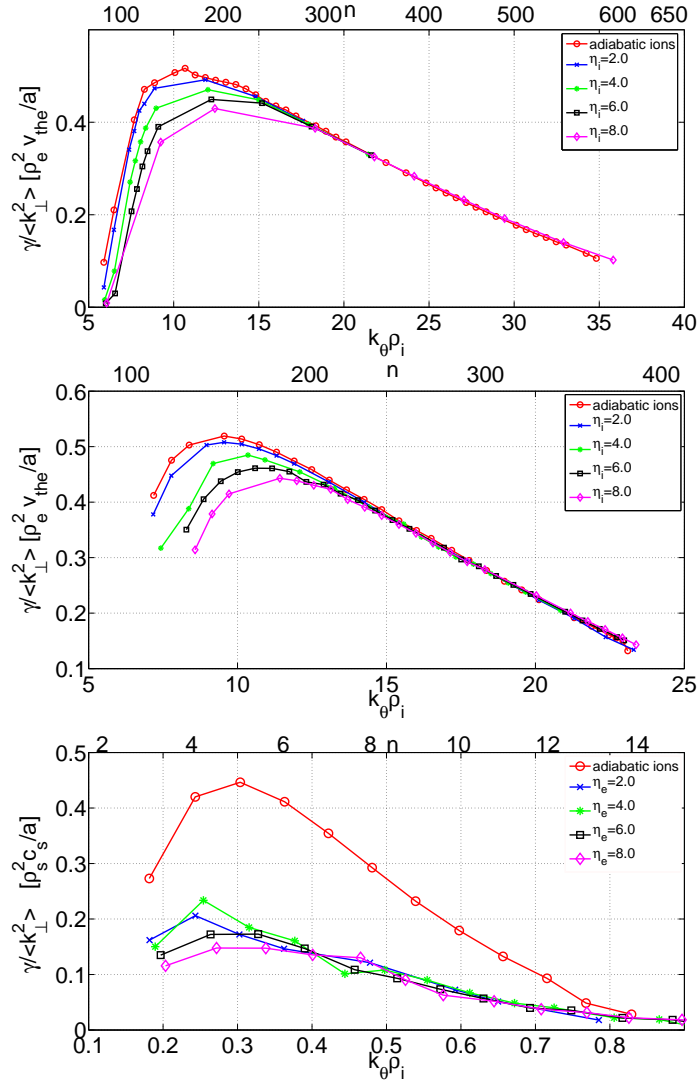


Figure 4.11: Top panel: mixing length estimate for transport coefficient  $D_{ML} = \gamma / \langle k_{\perp}^2 \rangle$  in electron gyro-Bohm units as a function of  $k_{\theta} \rho_{Li}$  for the ETG mode without Debye shielding at  $\eta_e(s_0) = 2$  with adiabatic ions and nonadiabatic ions for  $\eta_i(s_0) = 2, 4, 6, 8$ ; Middle panel: mixing length estimate for transport coefficient  $D_{ML} = \gamma / \langle k_{\perp}^2 \rangle$  in electron gyro-Bohm units as a function of  $k_{\theta} \rho_{Li}$  for the ETG mode with Debye shielding at  $\eta_e(s_0) = 2$  with adiabatic ions and nonadiabatic ions for  $\eta_i(s_0) = 2, 4, 6, 8$ ; Bottom panel: mixing length estimate for transport coefficient  $D_{ML} = \gamma / \langle k_{\perp}^2 \rangle$  in ion gyro-Bohm units as a function of  $k_{\theta} \rho_{Li}$ ;  $\eta_i(s_0) = 2$ , with adiabatic electrons and nonadiabatic electrons for  $\eta_e(s_0) = 2, 4, 6, 8$ .

## Chapter 4: Modes inherent to nonadiabatic/kinetic passing electrons

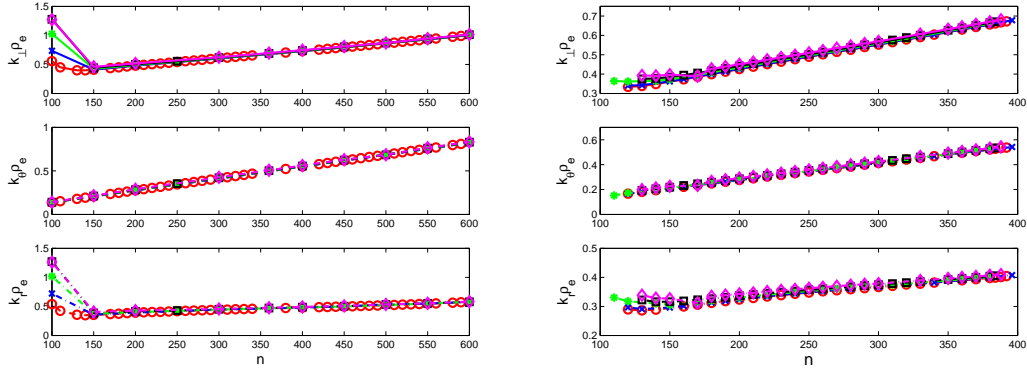


Figure 4.12: Left panel: normalized perpendicular wave numbers  $k_r$ ,  $k_\theta$ ,  $k_\perp$  vs toroidal mode number  $n$  for the ETG mode without Debye shielding. Right panel: normalized perpendicular wave numbers  $k_r$ ,  $k_\theta$ ,  $k_\perp$  vs toroidal mode number  $n$  for the ETG mode with Debye shielding.

vast spatio-temporal differences in their respective scales. The fact, in spite of the weak effect on the mode frequency and growth rate of the ETG mode by the nonadiabatic ions, that the mixing length estimates show a considerable reduction in the electron heat diffusivity has its origin in the change in the perpendicular scale lengths brought about by the nonadiabatic ions. Figure 4.12 plots the  $k_r \rho_e$ ,  $k_\theta \rho_e$  and  $k_\perp \rho_e$  against toroidal mode number  $n$ . It is apparent that  $k_r \rho_e$  of the ETG mode rises in the presence of the nonadiabatic ion dynamics, so does  $k_\perp \rho_e$ . This leads to the reduction in the mixing length estimates of electron transport.

## 4.3 Toroidal Universal Drift Instability: A Global Gyrokinetic Study

The confinement of electrons is marred not only by the temperature gradient driven instabilities such as ETG modes described in the preceding section but also by the density gradient driven instabilities. The density gradient also can equally be the source of free energy for instabilities in the case of no temperature gradient or very weak temperature gradient. These instabilities in tokamaks are called the toroidal universal drift instabilities. A brief review of earlier works on this topic can be found in the section 1.2 of Chapter 1.

In the present section, various parametric studies of the toroidal branch of the universal drift mode are carried out. We observe finite mode frequencies and growth rates beyond the critical  $\eta = L_n/L_T$  for the Ion Temperature Gradient (ITG) and Electron Temperature Gradient (ETG) modes, where  $L_n$  and  $L_T$  are respectively, the density and temperature scale lengths. A comparative study of the contribution of the magnetic drift resonance as well as of the Landau resonance from both species towards the stability properties of the mode is performed by a systematic parametric scan. An electromagnetic study of the mode is also carried out that elucidates the effect of finite  $\beta$  on the universal drift mode driven by toroidicity. The effect of trapped electrons on the universal mode is studied and growth rates and real frequencies are compared with the ion temperature gradient and trapped electron modes.

### 4.3.1 Model equations

The electrostatic formulation has been discussed in Chapters 2 and 3. Here we will elaborate the electromagnetic formulation only. For the electromagnetic case the perturbed density is modified as [48]

$$\tilde{n}_j(\mathbf{r}; \omega) = - \left( \frac{q_j N}{T_j} \right) \left[ \tilde{\varphi} + \int d\mathbf{k} \exp(i\mathbf{k} \cdot \mathbf{r}) \times \int d\mathbf{v} \frac{f_{Mj}}{N} (\omega - \omega_j^*) (\iota \mathcal{P}_j) [\tilde{\varphi}(\mathbf{k}; \omega) - v_{\parallel} \tilde{A}_{\parallel}(\mathbf{k}; \omega)] J_0^2(x_{Lj}) \right], \quad (4.2)$$

## Chapter 4: Modes inherent to nonadiabatic/kinetic passing electrons

where  $\tilde{A}_{\parallel}$  is the component parallel to the equilibrium magnetic field of the vector potential associated with the perturbation. The other terms are defined in Chapter 2 and 3. In addition to  $\tilde{n}_j$ , one has to consider the fluctuation of the parallel current density given by

$$\tilde{j}_{\parallel j}(\mathbf{r}; \omega) = - \left( \frac{q_j^2}{T_j} \right) \left[ \int d\mathbf{k} \exp(\iota \mathbf{k} \cdot \mathbf{r}) \times \int v_{\parallel} d\mathbf{v} f_{Mj}(\omega - \omega_j^*) (\iota \mathcal{P}_j) [\tilde{\varphi}(\mathbf{k};) - v_{\parallel} \tilde{A}_{\parallel}(\mathbf{k};)] J_0^2(x_{Lj}) \right] \quad (4.3)$$

Along with the quasineutrality condition Eq. (2.10), Ampere's law

$$\frac{1}{\mu_0} \nabla_{\perp}^2 \tilde{A}_{\parallel} = - \sum_j \tilde{j}_{\parallel j}$$

will finally close the set of equations, to give a linear system of equations of the form

$$\sum_{\mathbf{k}'} \sum_{j=i,e} \hat{\mathcal{M}}_{\mathbf{k},\mathbf{k}'}^j \begin{pmatrix} \tilde{\varphi}_{\mathbf{k}'} \\ \tilde{A}_{\parallel \mathbf{k}'} \end{pmatrix} = 0$$

Simple diagnostics for various physical quantities are computed as averages over the eigenmode. For example mode-averaged  $k_{\theta}^2$  for the electrostatic case is computed as

$$\langle k_{\theta}^2 \rangle = \frac{\int d\rho \sum_m \left| \frac{m}{\rho} \varphi_{(\rho,m)} \right|^2}{\int d\rho \sum_m \left| \varphi_{(\rho,m)} \right|^2}. \quad (4.4)$$

The above shown averaging procedure is suitably extended to the electromagnetic cases by including  $\tilde{A}_{\parallel}$  mode structure averaging as follows:

$$\langle k_{\theta}^2 \rangle = \frac{\int d\rho \sum_m \left| \frac{m}{\rho} \varphi_{(\rho,m)} \right|^2 + \int d\rho \sum_m \left| \frac{m}{\rho} A_{\parallel(\rho,m)} \right|^2}{\int d\rho \sum_m \left| \varphi_{(\rho,m)} \right|^2 + \int d\rho \sum_m \left| A_{\parallel(\rho,m)} \right|^2}. \quad (4.5)$$

### 4.3.2 Results and Discussion

In the present section, we will delineate the results from the global linear gyrokinetic numerical analysis. It is to be noted that the mode frequencies and growth rates are expressed in units of  $v_{thi}/a$  throughout the paper.

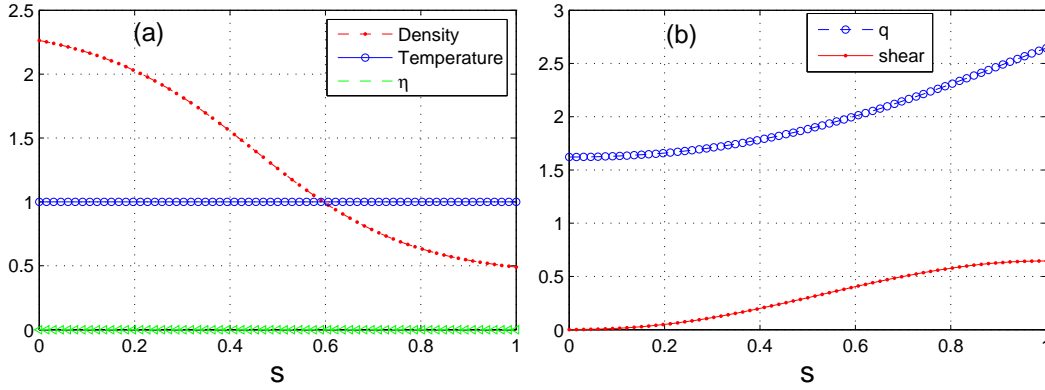


Figure 4.13: Equilibrium profiles to study the global toroidal universal drift instability mode (for parameters in Table I): (a) normalized density (dots), temperature (circle),  $\eta_{i,e}$  (triangle), (b) Safety factor  $q$  (circle) and magnetic shear  $\hat{s}$  (dots) profiles as functions of normalized radius  $s = r/a$ . Note that  $q(s_0) = 2.0$ ,  $\hat{s}(s_0) = 0.40$ ,  $\epsilon_n(s_0) = 0.1$ , and  $\tau(s_0) = 3.0$  for  $s_0 = 0.6$ .

#### Profiles and Parameters:

Let us consider the profiles and parameters as displayed in Table 4.2 for a plasma with single charged ions. The equilibrium profiles corresponding to these parameters are shown in Fig. 4.13.

#### Growth Rate $\gamma$ and Real Frequency $\omega_r$ vs $k_\theta \rho_{Li}$

The dispersion diagram for the toroidal universal drift instability with real frequency and growth rate plotted versus the normalized poloidal wave number  $k_\theta \rho_{Li}$ , is shown in Fig. 4.14. The upper axis presents the corresponding toroidal mode

Table 4.2: Profiles and parameters

Parameters:

- B-field :  $B_0 = 1.0$  Tesla
- Temperature :  $T_0 = T(s_0) = 7.5$  keV
- Major Radius :  $R = 2.0$  m
- Minor Radius :  $a = 0.5$  m
- radius :  $s = \rho/a$ ,  $0.01 < s < 1.0$ ,  $s_0 = 0.6$
- $L_{n0} = 0.2$  m
- $\eta_{i,e}(s_0) = 0.0$ ,  $\epsilon_n = L_{n0}/R = 0.1$
- $\tau(s) = T_e(s)/T_i(s) = 3$ .

Equilibrium Profiles:

- N-profile and T-profile
 
$$\frac{N(s)}{N_0} = \exp\left(-\frac{a \delta s_n}{L_{n0}} \tanh\left(\frac{s-s_0}{\delta s_n}\right)\right)$$

$$\frac{T_{i,e}(s)}{T_0} = \exp\left(-\frac{a \delta s_T}{L_{T0}} \tanh\left(\frac{s-s_0}{\delta s_T}\right)\right)$$

$$\delta s_n = 0.35, \delta s_T = 0 \text{ at } s = s_0$$
- $q(s) = 1.691 + 0.603 s^2 + 0.705 s^4$   
such that  $q(s = s_0) = 2.0$ ;  
shear  $s = s_0$ ,  $\hat{s} = 0.4$ .

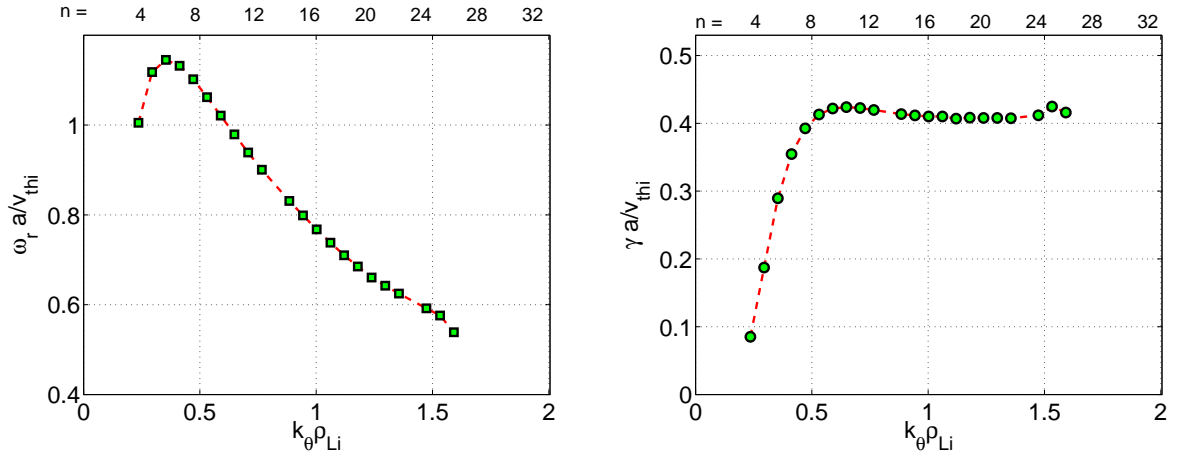


Figure 4.14: Real frequency and growth rate for the electrostatic case corresponding to the parameters in the Table I and profiles shown in Fig. 4.13.

## Chapter 4: Modes inherent to nonadiabatic/kinetic passing electrons

numbers. The real frequency is in the electron diamagnetic drift direction. The real frequency at very low  $k_{\theta}\rho_{Li}$  increases first and then peaks at the value of  $k_{\theta}\rho_{Li} = 0.4$  corresponding to  $n \simeq 6$ . After this point, it starts falling with  $k_{\theta}\rho_{Li}$  in a monotonic way. The growth rate, on the other hand, initially increases until the point  $k_{\theta}\rho_{Li} \simeq 0.58$  corresponding to the toroidal mode number  $n \simeq 10$  and is practically constant at larger value of  $k_{\theta}\rho_{Li}$ . It is apparent from this observation that the toroidal branch of the universal drift instability spans from the low wave number or longer wavelength regime, where ion dynamics are dominant, to higher wave number or shorter wavelength regime, where usually electron dynamics play the dominant role. This is in contrast to the observation in the slab case [99], which is marginally stable at high wave number regime and damped in the low wave number regime.

### Electrostatic mode structure

In the present section, we discuss the global electrostatic mode structure of the toroidal branch of the universal drift mode. Figure 4.15 displays the potential contours on a poloidal cross section of the tokamak in the upper left panel for  $k_{\theta}\rho_{Li} = 0.58$  corresponding to the toroidal mode number  $n = 10$ . The various poloidal components of the potential with coupling brought about by the toroidicity, both in Fourier and real space, are presented in the upper right panel for  $k_{\theta}\rho_{Li} = 0.58$  corresponding to the toroidal mode number  $n = 10$ . A few important points to be noted in this context are: (1) The mode structure is quite global passing through many mode rational surfaces. (2) It exhibits a weak ballooning character, with a finite amplitude observed at the favourable curvature side (high field side). In the upper right panel, coupling of poloidal components has been shown across the minor radius, with a maximum amplitude at  $s=\rho/a=0.6$ , where the density gradient peaks. The points in the upper axis, labelled by the corresponding poloidal mode numbers  $m$ , display the position of the mode rational surfaces where  $k_{\parallel}(m, n) = 0$ . Corresponding to each of these points, one can see a dip in the potential corresponding to each poloidal mode number. These dips correspond to  $k_{\parallel}(m, n) = 0$  surfaces where  $|\omega/k_{\parallel}| \gg v_{the}$ ,  $v_{the}$  being the electron thermal velocity. Thus, the strong effect of the off-resonant electrons is clearly visible from this figure. The convergence in the Fourier space for the considered

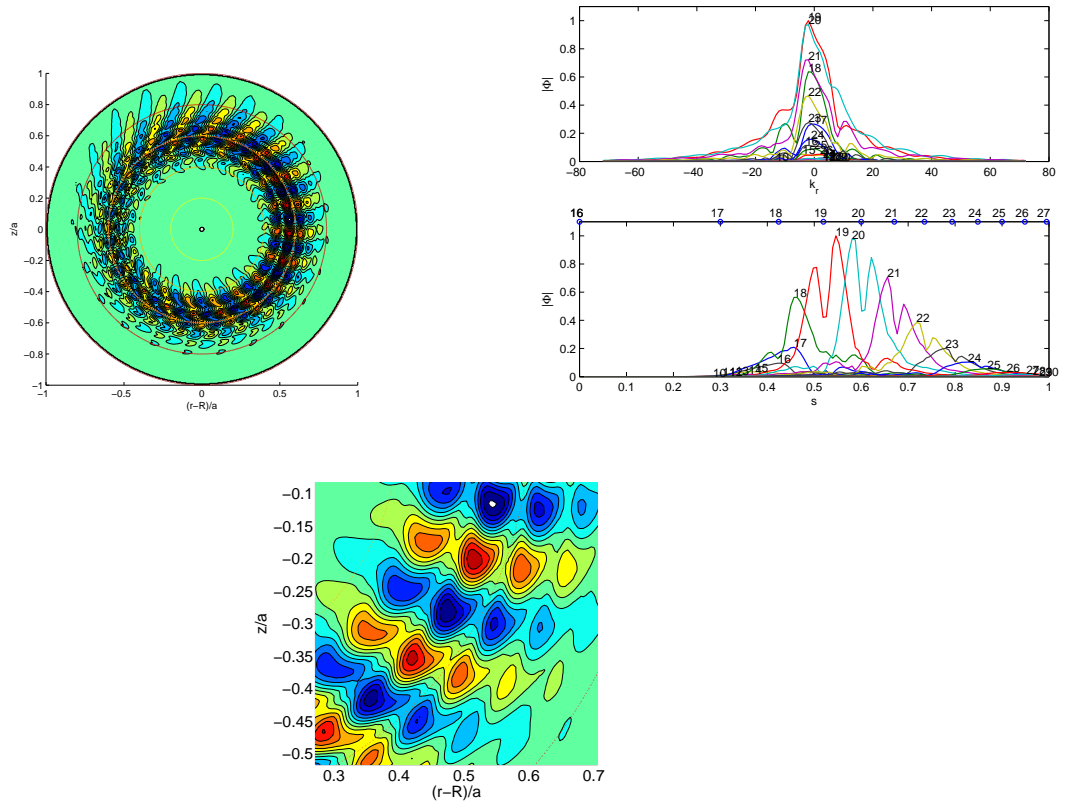


Figure 4.15: Upper panel: (Left) The electrostatic mode structure for toroidal mode number  $n = 10$ ,  $k_\theta \rho_{Li} = 0.58$ , corresponding to the parameters in the Table I and profiles shown in Fig. 4.13. (Right) poloidal component of  $\tilde{\phi}$  in (top) radial Fourier representation and (bottom) radial direct space. Lower panel: A closeup view of the mode structure.

mode is presented in the upper part of the upper right panel of Fig. 4.15. Lower panel presents a closeup view of the mode considered here.

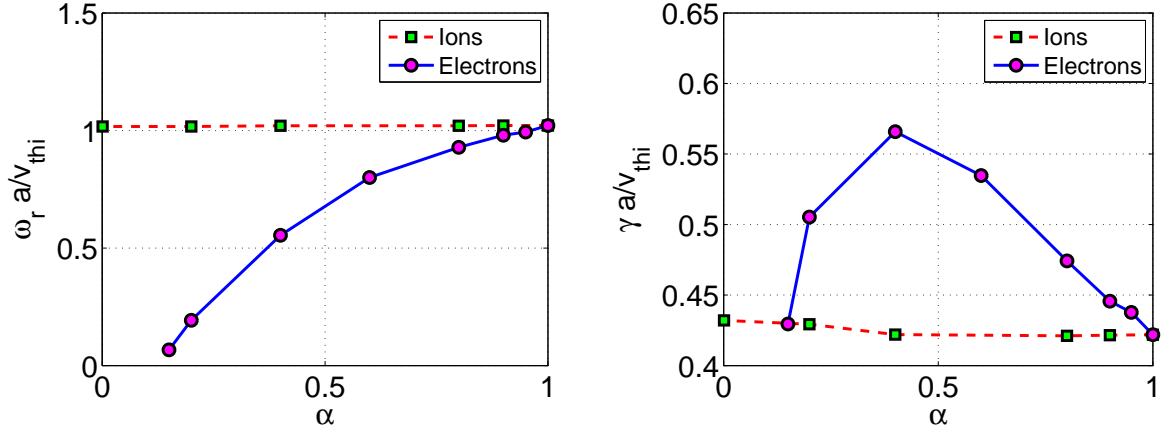


Figure 4.16: The effect of electron and ion Landau resonance for the mode  $n = 10$  corresponding to  $k_{\theta}\rho_{Li} = 0.58$ . This is done by weighting the Landau resonance term by  $\alpha$  and running it from 0 to 1 for one species, and keeping  $\alpha = 1.0$  for the other species and vice versa.

### Effect of Landau Resonance

To investigate the effect of the Landau resonance of electrons and ions on the toroidal universal drift instability, one can artificially put a multiplying factor, say  $\alpha$ , in front of the  $k_{\parallel}v_{\parallel}$  term in the denominator of the propagator for both species [see Eq. (2.8)] and decrease it gradually from 1 to 0, once for ions, keeping full electron Landau resonance effect, and vice versa. It is to be noted that only the values 0 and 1 of the artificial factor  $\alpha$  are physically meaningful. The other values of  $\alpha$  simply represent a fractional weight to the Landau resonance term in the propagator so as to enable us to track numerically the Landau effect continuously. Thus the value 1 will refer to the case of full Landau resonance term taken into account and 0 the complete omission of the Landau resonance term from the propagator. It is clear from Fig. 4.16 that the ion Landau resonance apparently has no significant effect on the growth rate as well as on the mode frequency compared to that of the electrons. For the electron Landau resonance, the growth rate exhibits

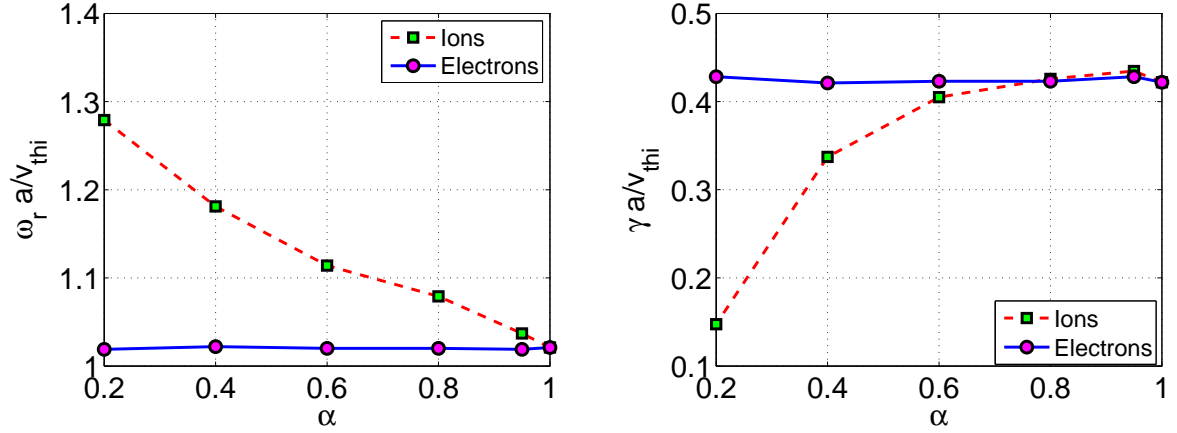


Figure 4.17: Effect of ion and electron magnetic drift resonance for the mode  $n=10$  corresponding to  $k_{\theta}\rho_{Li} = 0.58$ . This is done by weighting the magnetic drift term by  $\alpha$  and running it from 0 to 1, and keeping  $\alpha = 1.0$  for the other species and vice versa.

a nonmonotonic dependence on the electron Landau resonance weighting parameter  $\alpha$ . For example, at lower values of  $\alpha$  the growth rate increases and again falls at higher values. Regarding the mode frequency: in contrast to the growth rate, it increases monotonically with  $\alpha$  for the electrons, while it has little variation in the case of ions. Thus, with the complete omission of the electron Landau resonance, the mode may become nonexistent even if one keeps the other destabilizing factors intact.

### Effect of Magnetic Drift Resonance

In toroidal geometry, a mode will certainly have magnetic drift resonance if its frequency is of the same order as the magnetic drift frequency. We have looked at the effect of magnetic drift resonance for both species on the toroidal universal mode. This is done in a similar way as for the study of the previous section, by putting a multiplying factor  $\alpha$  in front of the magnetic drift resonance term,  $x_{tj}$  appearing as arguments of the Bessel functions in the numerator of the propagator in Eq. (2.8). To be noted again that, while doing the scan for one species, the full weight  $\alpha = 1$  is kept for the other species. One notes a destabilizing effect due to the magnetic drift resonance of ions when the multiplying factor  $\alpha$  increases. As shown in Fig. 4.17, the real frequency decreases with the increasing multiplying

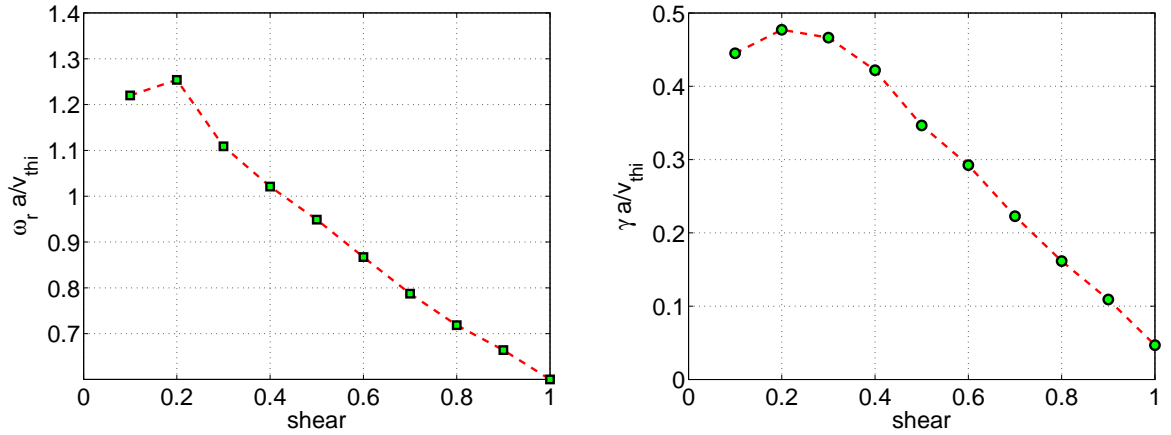


Figure 4.18: Shear scan for the mode  $n = 10$  corresponding to  $k_\theta \rho_{Li} = 0.58$  at position  $s = s_0 = 0.6$ , where the density gradient peaks. For these scans the safety factor at  $s = s_0$  is kept at the fixed value  $q = 2.0$ .

factor  $\alpha$ , while the growth rate increases and starts saturating as one approaches  $\alpha = 1$ , i.e., for the full magnetic drift resonance term in the ion propagator. Electron magnetic drift resonance however does not play a significant role for the universal drift instability, as is clear from Fig. 4.17.

### Shear Scan

Though magnetic shear has a strong stabilizing influence on the universal drift mode, in a slab model, the toroidal resonance effects, intrinsic to toroidal geometry, can reduce the shear damping of the mode. The shear scan is displayed in Fig. 4.18. It is clear that for the parameters chosen in this study, the critical value of shear, beyond which the mode gets stabilized, is of the order of 1. The growth rate and real frequency, however, do not decay monotonically with increasing shear. The growth rate rather increases weakly at low shear and then starts decreasing with increasing shear. Similarly the real frequency of the mode also decays with increasing shear. The stabilization of the mode by shear in the presence of finite toroidicity can be understood as follows. The shear damping of the universal drift mode in the slab geometry is basically due to the convection of energy away from the mode rational surfaces. In the presence of finite toroidicity, the toroidal coupling effect inhibits this convection of wave energy, and thus reduces the shear damping [101]. Similar effects of toroidicity on shear induced stabilization was also

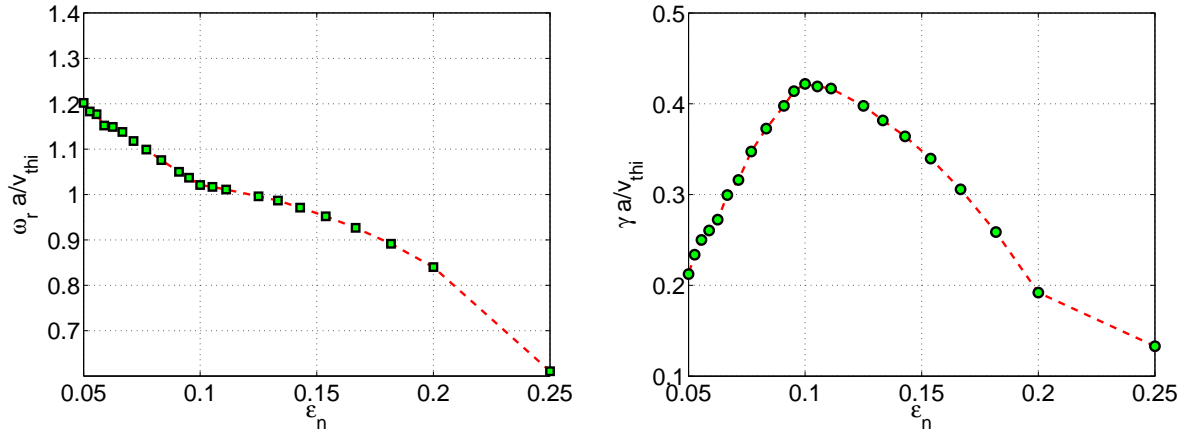


Figure 4.19: Real frequency and growth rate for  $\epsilon_n = L_n/R$  for the parameters and profiles as in the Table I and Fig. 4.13 in the case of mode  $n = 10$  corresponding to  $k_{\theta}\rho_{Li} = 0.58$ . Note that  $a$ ,  $L_n$ ,  $Rq$  and  $nq$  are kept constant in this scan.

observed for high- $n$  toroidal universal drift instabilities.

### Toroidicity Scan

The real frequency and growth rate of the mode versus  $\epsilon_n = L_n/R$  is presented in Fig. 4.19. The toroidicity scan is done by varying  $R$ , but keeping  $Rq$ ,  $L_n$ ,  $nq$ , and  $a$  constant. While the real frequency decreases almost monotonically, the growth rate, on the other hand increases first with toroidicity, peaks at around  $\epsilon_n \simeq 0.1$ , and then starts falling for larger values of  $\epsilon_n$ . Since,  $\epsilon_n \rightarrow 0$  implies  $R \rightarrow \infty$ , i.e., the cylindrical limit, the toroidal driving term becomes weak at low  $\epsilon_n$ . Since the mode is basically driven by the magnetic drift resonance, the growth rate increases with  $\epsilon_n$  for low values. However, for large enough values of  $\epsilon_n$  the mode becomes off-resonant with respect to the magnetic drift frequency, which increases with  $\epsilon_n$  and growth rate falls down. Also, increasing  $\epsilon_n$  implies decreasing  $R$ , which means reduced connection length  $\sim Rq$  between the favorable and unfavorable magnetic field. This nonmonotonic dependency of growth rate on  $\epsilon_n$  for toroidal universal drift modes has not been reported before.

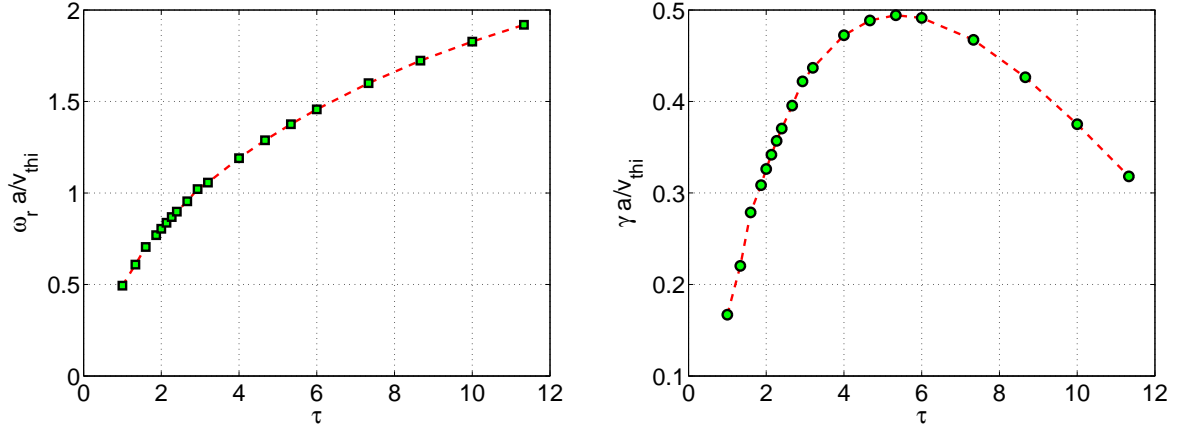


Figure 4.20: Real frequency and growth rate for  $\tau = T_e/T_i$  and for the parameters and profiles of Table I and Fig. 4.13 in the case of the mode  $n = 10$  corresponding to  $k_\theta \rho_{Li} = 0.58$ .

#### $\tau = T_e/T_i$ Scan

The dependence of the mode frequency and growth rate for the toroidal universal drift instability on the temperature of the species is elucidated in the present section. Figure 4.20 displays the plots of the mode frequency and growth rate corresponding to  $k_\theta \rho_{Li} = 0.58$  ( $n = 10$ ) as a function of the ratio of temperatures of electrons and ions, i.e.,  $T_e/T_i = \tau$ . To be noted that in this scan the ion temperature  $T_i$  is kept constant, while varying only the electron temperature  $T_e$ . The real frequency increases monotonically with the magnitude of  $\tau$ , i.e., with increasing electron temperature. The growth, on the other hand, exhibits a nonmonotonic character: increases at first with  $\tau$ , peaks at around  $\tau = 5.0$  and then starts decaying with increasing  $\tau$ . One may correlate this result with the role of electron Landau resonance on the universal mode, as the electron distribution in the vicinity of parallel resonant velocity, which is strongly dependent on the thermal velocity and so the temperature of the electrons, is the key factor in determining Landau damping or inverse Landau damping of the mode.

#### Effect of Temperature Gradient

Thus far, the entire analysis has been carried out considering flat temperature profiles, that is, zero temperature gradients by putting  $\delta s_T = 0$  in the profiles

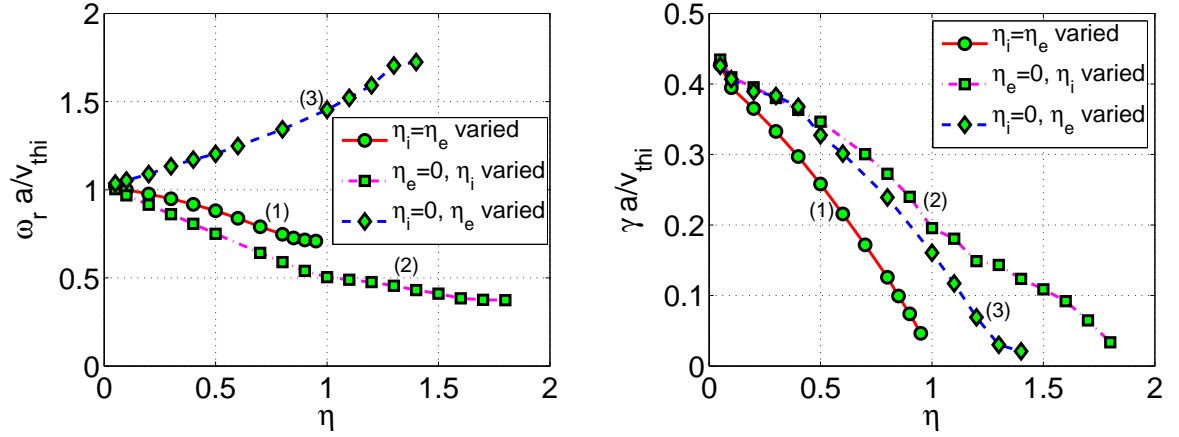


Figure 4.21: Real frequency and growth rate in the case of a temperature gradient scan for the parameters and profiles of Table I and Fig. 4.13 for the mode  $n = 10$  corresponding to  $k_{\theta}\rho_{Li} = 0.58$ . The flat temperature profile in Table I, has been replaced by one with  $\delta s_T = 0.2$  instead of 0 for the previous cases.

displayed in Table I. In the present section, we incorporate profile variation to the temperatures of both ions and electrons. This is achieved by using a finite value for  $\delta s_T$ , which is chosen as 0.2 in this case. Since most tokamaks contain temperature gradients in the pressure profile, it is thus necessary to look at the effect of the temperature gradient on the toroidal universal drift instability. This is done by evaluating the real frequency and growth rate against  $\eta_{i,e} = L_n/L_T$ , keeping  $L_n$  constant and varying  $L_T$ . Three cases are considered here: (1) the temperature gradient scale lengths for both electrons and ions are increased simultaneously, (2) the temperature gradient of only ions is increased, keeping that of the electrons zero, and (3) the temperature gradient of only electrons is increased, keeping that of the ions zero. The last two options may be relevant to experimental situations with preferential ion heating [e.g., ion cyclotron resonance heating (ICRH)] or electron heating [e.g., electron cyclotron resonance heating (ECRH)], respectively. The results for all the cases are presented in Fig. 4.21. The real frequency is reduced with increasing temperature gradient for the cases 1 and 2, while it increases in the case 3. The growth rate, on the other hand, decreases in all three cases. However, it decays more slowly when the electron temperature profile is flat, as apparent from case 2. It is clear from case 3 that the mode exhibits a finite growth rate for values of  $\eta_e$  beyond the critical value for ETG instability ( $\eta_e \simeq 1.0$ ). Thus,

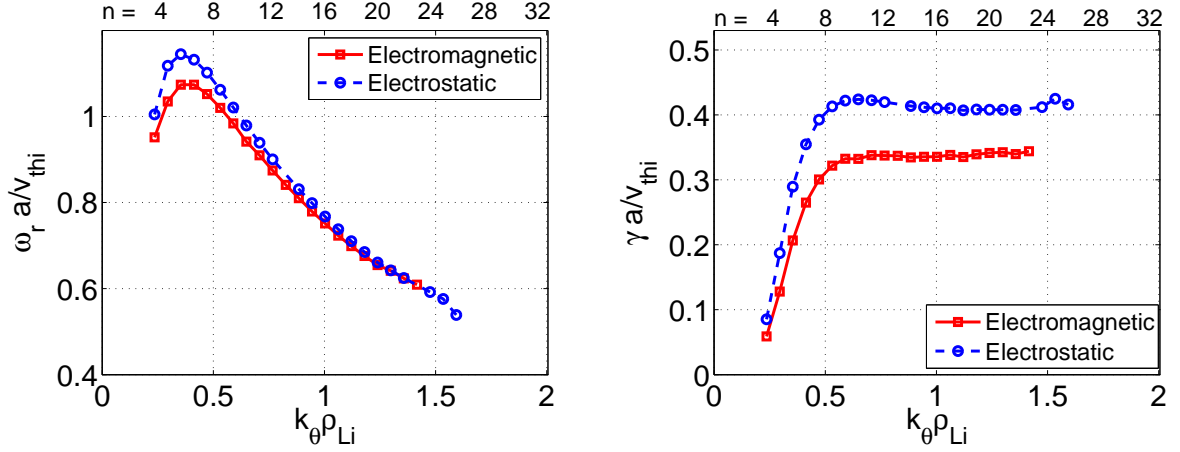


Figure 4.22: Real frequency and growth rate for the electrostatic (dashed curve) and electromagnetic case (solid curve) for the parameters in Table I and profiles as shown in Fig. 4.13. The value of  $\beta$  considered here is 0.001.

the point to be noted is that, even in the presence of finite  $\eta$  above the critical value for the temperature gradient driven modes to get destabilized, the universal drift instability preserves finite growth rate. It is observed from case 2 that the ion temperature gradient has weaker effect on the mode. It has finite growth rate even after the critical value of  $\eta_i$  for the ion temperature gradient driven mode ( $\eta_i \simeq 1.0$ ). Thus, one may conclude that, in some situations as delineated in the last two cases, temperature gradient driven modes and universal drift mode driven by the density gradient can coexist. One other important point to be noted here is that the toroidal universal drift mode is unstable in the  $\tau$  domain from 1 to more than 10, as evident from Fig. 4.20, while ETG modes are stable at higher values of  $\tau$  even with finite  $\eta_e$ . So electron transport at high  $k_\perp \rho_{Li} > 1$  with larger values of  $\tau$  may have contributions from the toroidal universal drift mode as well. Similarly, at low  $k_\perp \rho_{Li}$ , where ITG is dominant, the electron transport can be due to this mode, as it appears to be unstable in regions where ITG is pronounced.

## Electromagnetic Effects

### $k_\perp \rho_{Li}$ scan

The electrostatic assumption is justified in a low  $\beta$  plasma. However, considering the higher  $\beta$  environment in the present day devices, it is of interest to study the effect of the electromagnetic fluctuation on the toroidal branch of the universal

mode. In this section, we perform a  $k_{\theta}\rho_{Li}$  scan for the growth rate and mode frequency in the presence of transverse magnetic perturbations with  $\beta = 0.001$  in the **zero temperature gradient limit**. The corresponding results are plotted in Fig. 4.22, with the upper axis representing the respective toroidal mode numbers  $n$ . For the purpose of comparison, we also plot the purely electrostatic values for the real frequency and growth rate of the mode (same results as in Fig. 4.14).

At very low  $k_{\theta}\rho_{Li}$ , the real frequency increases first and then peaks at a value of  $k_{\theta}\rho_{Li} \simeq 0.4$  corresponding to  $n = 6$ . Beyond this point, the frequency starts falling monotonically with  $k_{\theta}\rho_{Li}$  (or  $n$ ). The growth rate however increases until  $k_{\theta}\rho_{Li} \simeq 0.58$  (or  $n = 10$ ) and then becomes practically constant. It is apparent from the figure for the real frequency that the effect of finite  $\beta$  is more pronounced at lower  $k_{\theta}\rho_{Li}$ , and the real frequency is reduced in this region. Going towards the higher  $k_{\theta}\rho_{Li}$  the effect of  $\beta$  seems to be weaker on the mode frequency. The growth rate, on the other hand, is substantially reduced by finite plasma  $\beta$ . A  $\beta$  of value 0.001 brings almost 20% reduction in the growth rate as compared to the electrostatic case. A complete  $\beta$  scan is presented in the following section clearly illustrating the stabilizing effect of  $\beta$ .

A global mode structure for the electromagnetic case for  $n = 10$  and  $\beta = 0.001$  corresponding to  $k_{\theta}\rho_{Li} \simeq 0.58$  is shown in Figs. 4.23 and 4.24. The electrostatic part  $\tilde{\phi}$  (Fig. 4.23) is very similar to the purely electrostatic mode in Fig. 4.15. The  $\tilde{A}_{\parallel}$  component (Fig. 4.24), on the contrary, apparently shows a weak anti-ballooning character, being weaker at the outboard side than the inboard side. The convergence in the radial and poloidal Fourier space for the mode has been depicted in the upper part of the right panel in Fig. 4.24. The lower panel presents the radial dependence of various poloidal mode numbers  $m$ . It retains the effect of nonresonant electrons at  $k_{\parallel}(m, n) = 0$  surfaces. The antiballooning character of the  $\tilde{A}_{\parallel}$  mode structure and the stabilization of the mode in the presence of finite  $\beta$  are all related to the inherent electrostatic nature of the toroidal universal drift instability.

### $\beta$ Scan

A complete  $\beta$  scan for the mode with  $k_{\theta}\rho_{Li} = 0.58$  ( $n = 10$ ) is displayed in Fig. 4.25. Both real frequency and growth rate are reduced with increasing  $\beta$ . The complete stabilization occurs at  $\beta \simeq 1.1\%$ . This is in contrast to earlier investigations in slab geometry, where the value of critical  $\beta$  was much higher

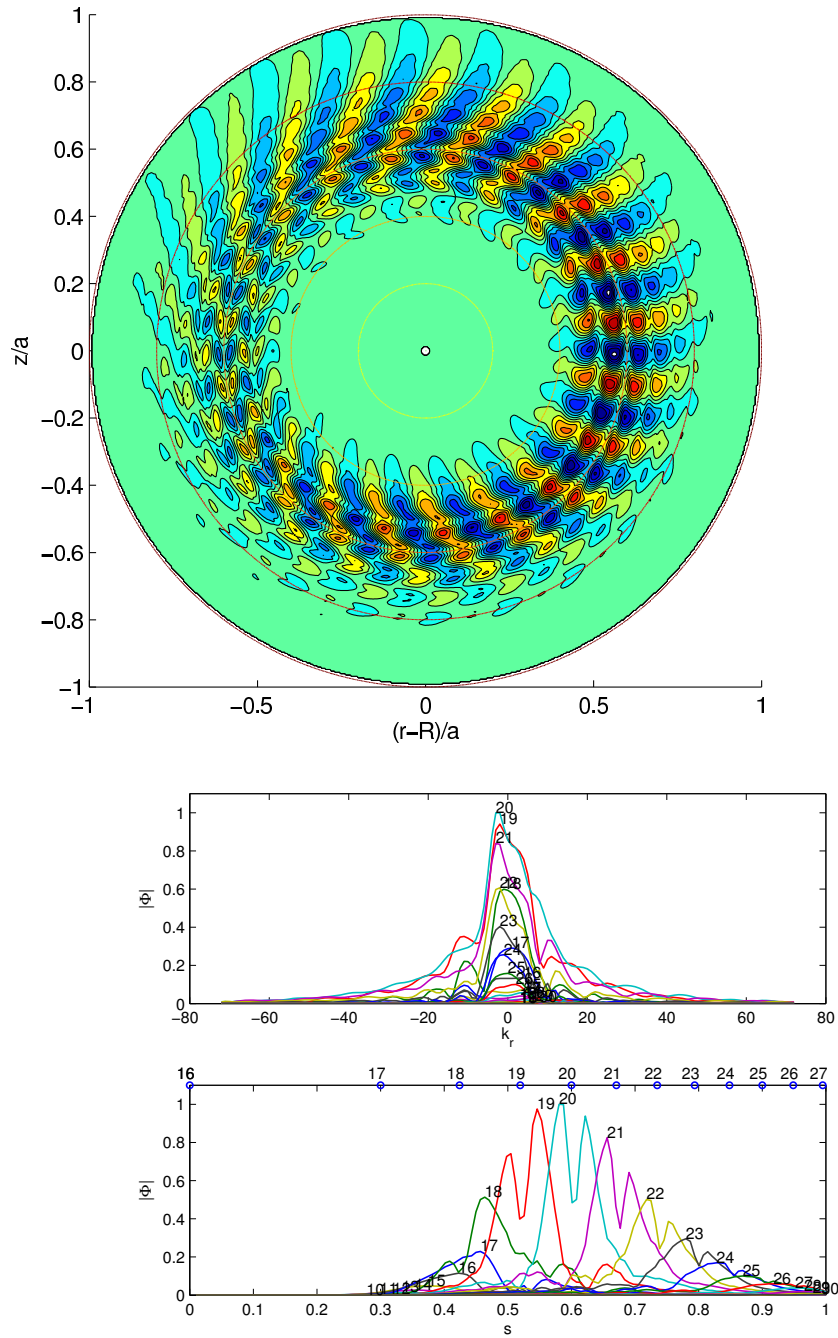


Figure 4.23: (Upper panel) The global mode structure for the  $\tilde{\phi}$  component in the poloidal cross section in the electromagnetic case for  $n = 10$ ,  $k_{\theta}\rho_{Li} = 0.58$ , and  $\beta = 0.001$ . (Lower panel) Poloidal component of  $\tilde{\phi}$  in (top) radial Fourier representation and (bottom) radial direct space.

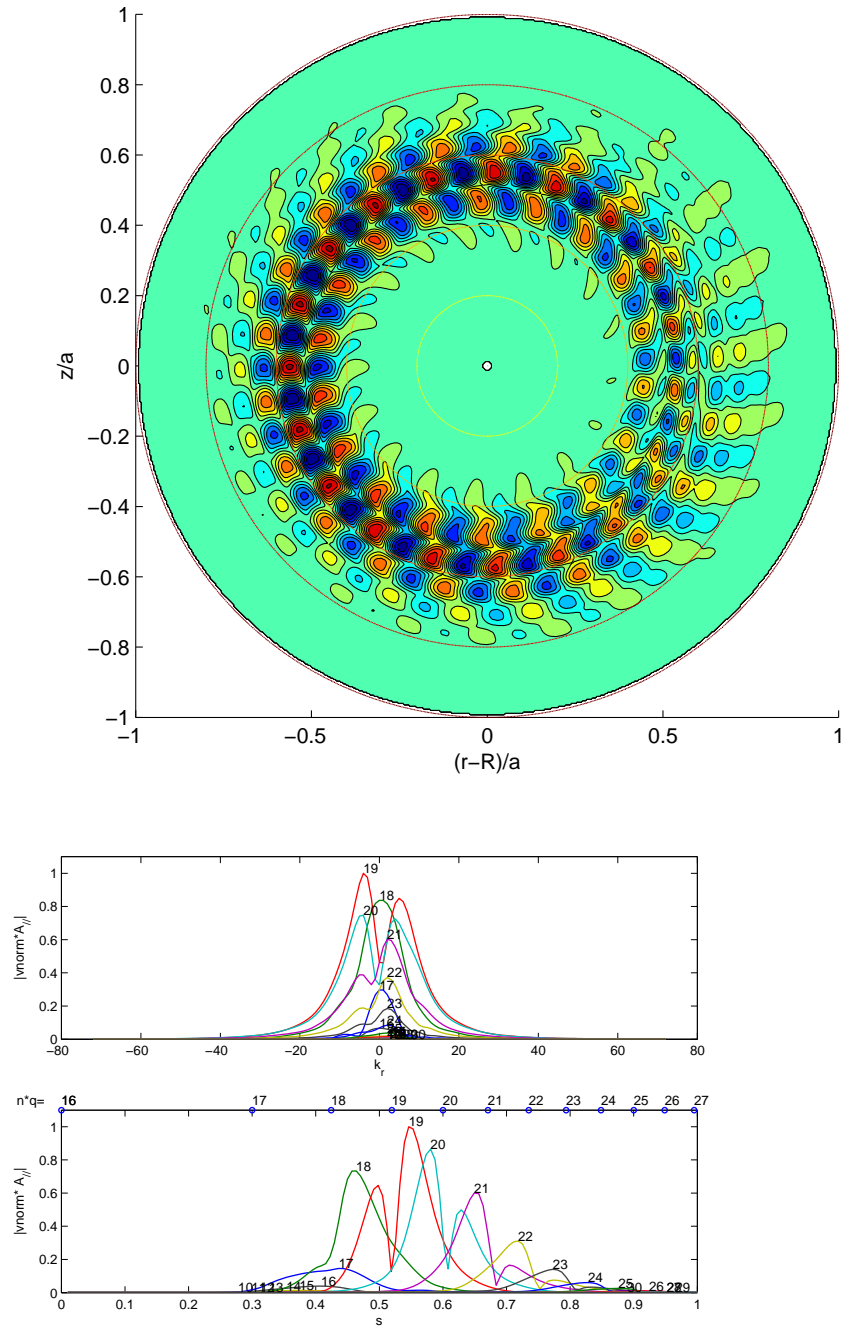


Figure 4.24: (Upper panel) The global mode structure for the  $\tilde{A}_{\parallel}$  component in the poloidal cross section in the electromagnetic case for  $n = 10$ ,  $k_{\theta}\rho_{Li} = 0.58$ , and  $\beta = 0.001$ . (Lower panel) Poloidal component of  $\tilde{\phi}$  in (top) radial Fourier representation and (bottom) radial direct space.

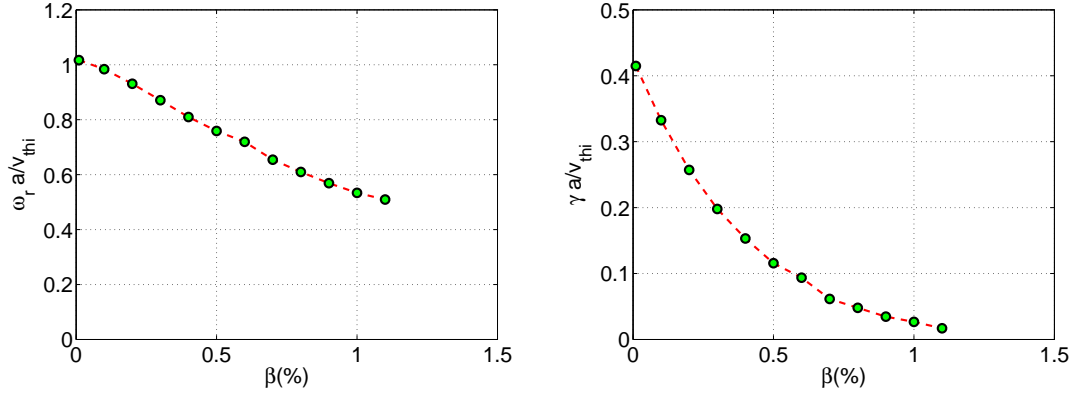


Figure 4.25:  $\beta$  scan for the mode frequency and growth rate for the parameters and profiles as in Table I and Fig. 4.13 for the mode  $n = 10$  corresponding to  $k_{\theta}\rho_{Li} = 0.58$  .

[105]. The observed stabilization is perhaps due to the coupling of the wave with the Alfvén perturbation.

The relative strength of the electromagnetic to the electrostatic character is shown

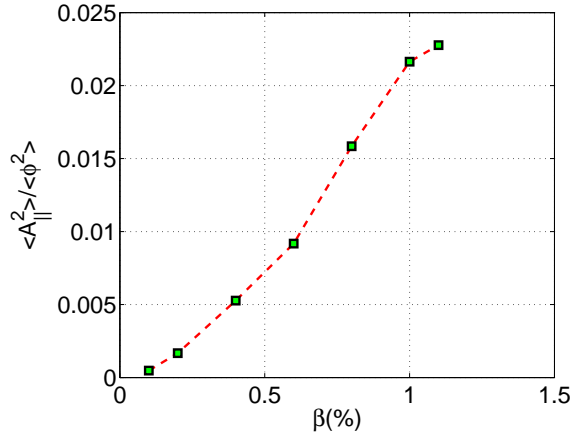


Figure 4.26: Electromagnetic ratio with increasing function of  $\beta$  for the parameters and profiles as in Table I and Fig. 4.13 for the mode  $n = 10$  corresponding to  $k_{\theta}\rho_{Li} = 0.58$  .

in Fig. 4.26, measured as the ratio of flux surface averaged squared  $\tilde{A}_{\parallel}$  to  $\tilde{\phi}$  with increasing value of  $\beta$  expressed in percentage. It is clear from this plot that the strength of the magnetic fluctuation in comparison to the electrostatic fluctuation

increases almost linearly with increasing plasma  $\beta$ .

### Effect of trapped electron on the electrostatic mode:

As clearly demonstrated by the above results, the global toroidal universal drift instability is triggered by purely passing electron dynamics. However, as a toroidal device is bound to have some fraction of trapped electrons, it would be interesting to obtain the effect of trapped electrons on the purely universal drift mode studied in the previous sections. To this end, an extensive  $\eta$  scan is performed with and without trapped electrons **for the electrostatic case**. To identify the most unstable mode, the other drift instabilities such as ITG with trapped electrons as well as the TEM branches are computed together with the universal mode. The combined data is plotted in Fig. 4.27. There are several interesting points to be noted: (1) The trapped electron coupled universal drift mode and pure universal drift mode have distinct real frequencies and growth rates. (2) In contrast to the pure universal drift mode studied in previous sections, whose growth rate was shown to decrease with increasing  $\eta$ , the trapped electron coupled universal drift mode appears to be more unstable with increasing  $\eta$ . This study indicates that in the presence of trapped electrons, the nature of the universal drift mode is predominantly “trapped electron like”. (3) To make a better quantitative comparison, growth rates and real frequencies of the pure trapped electron mode (TEM), the ion temperature gradient mode with trapped electrons (ITG-TE) for the same equilibrium parameters are also plotted. For the parameters studied here, it appears that the trapped electron coupled universal drift modes in the presence of  $\eta \geq 1$  have growth rates comparable to ITG-TE or TEMs and could contribute substantially to the overall transport.

## 4.4 Conclusions

In the present work, we have presented some features of the electron temperature gradient driven (ETG) mode using a linear gyrokinetic model in toroidal geometry that treats both species, namely, ions and electrons fully gyro-kinetically, taking into account all the kinetic effects. The effect of Debye Shielding, breaking of isomorphism of ITG and ETG modes even in the electrostatic limit when the

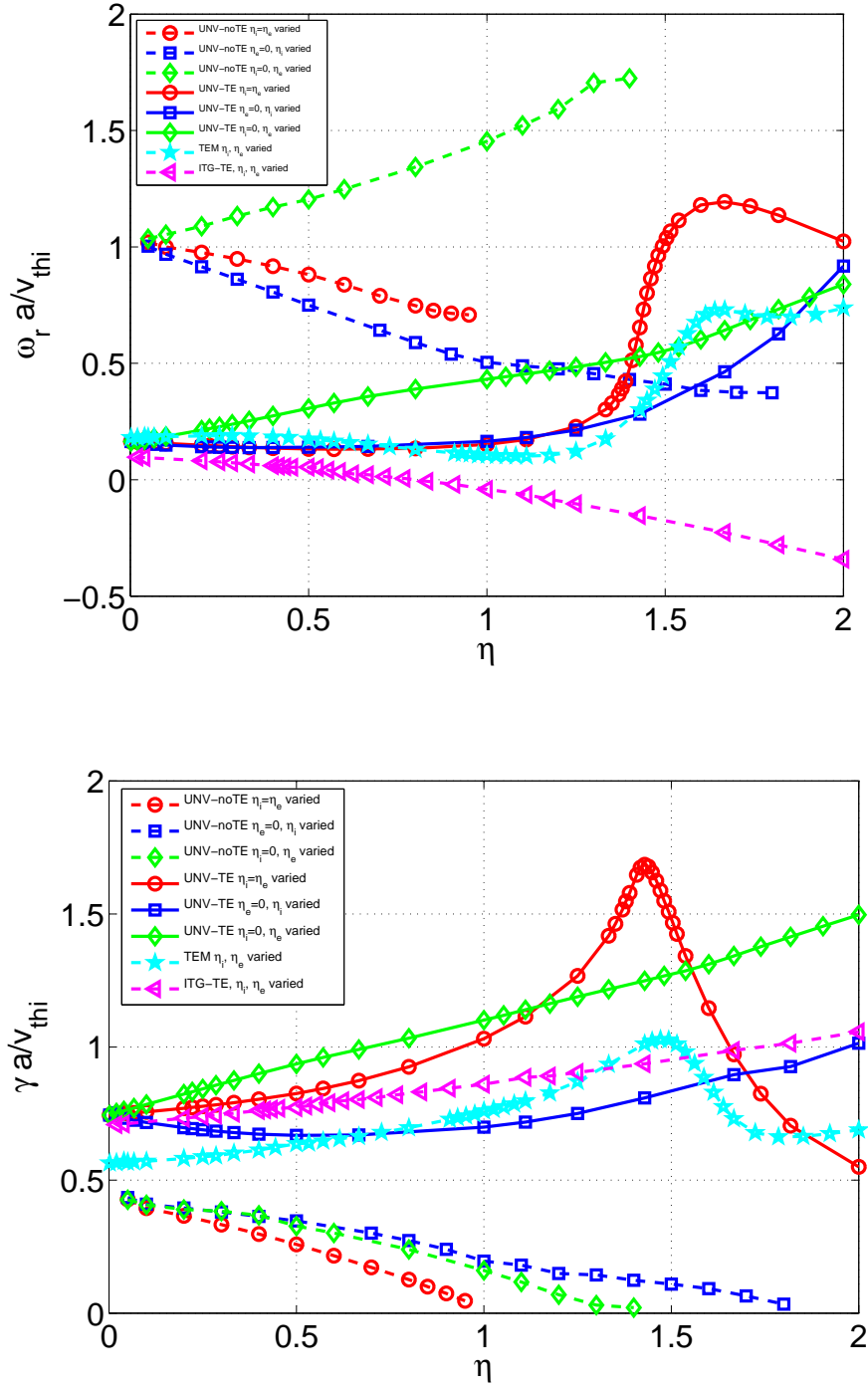


Figure 4.27: The real frequency and growth rate vs temperature gradient for different unstable modes in the presence of trapped electrons in the same regime defined by the parameters and profiles of Table I and Fig. 4.13 for the mode  $n = 10$  corresponding to  $k_{\theta} \rho_{Li} = 0.58$ . The flat temperature profile in Table I, has been replaced by one with  $\delta s_T = 0.2$  instead of 0 for the previous cases. The three dashed curves<sup>97</sup> (circle, square, diamond) are for universal mode without trapped electrons (same as Fig. 4.21), three solid lines (circle, square, diamond) are for universal mode in the presence of trapped electrons (UNV-TE), the dashed curve with triangles is for ion temperature gradient mode with trapped electrons (ITG-TE) and the solid curve with stars is for pure trapped electron mode (TEM).

## Chapter 4: Modes inherent to nonadiabatic/kinetic passing electrons

other species is considered fully gyrokinetically are revealed one by one. In the following we summarize the results obtained.

- Debye Shielding is stabilizing to the ETG mode, enhances the threshold in  $\eta_e$ , and wipes out the high  $k$  tail of the ETG spectrum.
- Nonadiabatic ions have very weak effect on the growth rate and mode frequency of the pure ETG modes. In contrast, nonadiabatic electrons affect the mode frequency and growth rate of the ITG mode strongly. It breaks the supposed isomorphy between the two modes even in the electrostatic limit.
- We have presented an estimation of the transport of ions and electrons on the basis of mixing length theory. Results reveal that, drive for the ion channel tends to reduce the transport via the electron channel and vice versa. This means that a low  $k$  mode can have strong effect on a high  $k$  mode and vice versa. The assumption of adiabatic particles fails to interpret this result.

Also, we have performed a global linear gyrokinetic study of the toroidal universal drift mode driven by the density gradient in the presence of finite toroidicity on the intermediate scale  $k_{\perp}\rho_{Li}$ . The model considers both passing electrons and ions to be fully nonadiabatic, incorporating toroidal coupling effects, magnetic drift resonances, Landau resonance effects, transit harmonic resonances, finite Larmor radius to all orders, and orbit width effect for both species. The effect of finite  $\beta$  is also studied in the frame of an electromagnetic model that retains the transverse magnetic perturbation. However, effects of collisions and Shafranov shift have been dropped. Furthermore, the model considers large aspect ratio circular cross section for the tokamak plasma. The major results are as follows

- The growth rate increases at lower  $k_{\theta}\rho_{Li}$  until  $k_{\theta}\rho_{Li} \simeq 0.58$  and starts saturating thereafter. The real frequency too increases at lower  $k_{\theta}\rho_{Li}$  and then decays monotonically with  $k_{\theta}\rho_{Li}$  at larger  $k_{\theta}\rho_{Li}$ .
- The electrostatic mode structure is global and exhibiting structure at mode rational surfaces.
- Studying the effect of Landau resonance for both electrons and ions shows weak dependence of the frequency and growth rate on ion Landau damp-

## Chapter 4: Modes inherent to nonadiabatic/kinetic passing electrons

ing and a strong dependence on electron Landau damping preserving finite growth rate in both cases.

- Both electron and ion magnetic drift resonance terms are considered in the formulation. The ion magnetic drift resonance does play a significant role in making the toroidal branch of the universal drift mode unstable, while electron magnetic drift resonance has a weak effect on the stability property of the mode.
- As reported in earlier works for high  $n$  modes ( $k_\theta \rho_{Li} \gg 1$ ), the toroidicity driven universal drift mode is found to be stable beyond a shear value  $\hat{s} \simeq 1$ , even for low  $n$  modes.
- The nonmonotonic dependency of the growth rate on  $\epsilon_n = L_n/R$  in a toroidicity scan (varying  $R$  and keeping  $L_n$ ,  $a$ ,  $Rq$  and  $nq$  constant) is demonstrated here for the first time.
- The mode is unstable in a fairly large domain of  $\tau = T_e/T_i$  ranging from 1 to more than 10, thus clearly showing that in regions of  $\tau$  where the electron temperature gradient (ETG) mode is believed to be stable, electron transport can be due to this toroidal universal drift mode.
- The  $\eta$  scan for both ions and electrons shows that the universal drift mode driven by toroidicity can coexist with the temperature gradient driven modes. Therefore, electron transport at low  $k_\theta \rho_{Li}$  may have contributions from the mode under investigation. Similarly at higher  $k_\theta \rho_{Li}$ , where ETG is thought to be the main driving mechanism for electron transport, this mode may also contribute.
- The electromagnetic effect is found to be strongly stabilizing in the present case. The  $\tilde{A}_\parallel$  component of the mode structure exhibits anti-ballooning character. The mode gets stabilized at  $\beta \simeq 1.1\%$ . The relative magnetic fluctuation amplitude  $\langle \tilde{A}_\parallel^2 \rangle / \langle \tilde{\phi}^2 \rangle$  varies almost linearly with the magnitude of  $\beta$ .
- Trapped electrons enhance the growth rate of the universal mode. However, the universal mode changes its character regarding its dependence on

#### Chapter 4: Modes inherent to nonadiabatic/kinetic passing electrons

the density and temperature gradients. While in the absence of trapped electrons the universal mode decays with the temperature gradient, trapped electrons, on the contrary, enhances the growth rate of the mode. The universal mode with trapped electrons exhibits, qualitatively, the same character as the trapped electron mode. Also, it has a comparable growth rate to the trapped electron coupled ion temperature gradient mode in the parameter range considered in this study.

# Chapter 5

## Short wavelength ion temperature gradient mode and coupling with trapped electrons

### 5.1 Introduction

The ion temperature gradient driven mode has hitherto been studied only in the region  $k_y \rho_i \leq 1.0$ . However, under steep density profiles, the ions can behave nonadiabatically at scales  $k_y \rho_i > 1.0$  giving rise to what is called the short wavelength ion temperature gradient (SWITG) driven modes. In all the earlier studies on SWITG modes (see section 1.2 of Chapter 1), the trapped electrons were ignored. However, in a toroidal device, the trapped electrons are inevitable, and as demonstrated in the present work, can play a paramount role in defining the stability properties of the mode. In the limit  $\omega_{be} > \omega$ , where  $\omega_{be}$  is the bounce frequency of the trapped electrons, the trapping of the electrons prevents thermalization along the magnetic field line and the wave field appears stationary during a bounce period. The trapped electrons, therefore, can alter the stability properties of the mode significantly.

The other lacuna of the earlier studies is that they were done either using a local kinetic theory or at the best kinetic theory based on ballooning formalism in the slab as well as toroidal geometry. A ballooning formalism is essentially an one dimensional model in  $\theta_b$ , the ballooning angle. Therefore, the estimation of the

## Chapter 5: Short wavelength ion temperature gradient mode and coupling with trapped electrons

characteristic radial scale length of the mode is not possible unless one uses the higher order ballooning theory. Thus, to understand the two dimensional mode structure in the presence of the trapped electrons, a global model becomes necessary. Also, an estimation of the radial scale length of the mode is not only required for completeness but help estimate the probable transport induced by the mode. In fact, for the first time, the two dimensional SWITG mode structure will be shown in the present work. For the parameters chosen, the SWITG mode is found to be quite global.

Thus, the purpose of the present work is twofold: first, to incorporate the trapped electrons to the SWITG mode and, second, to use a global linear electrostatic gyro-kinetic model, which enables one to evaluate the two dimensional mode structure of the SWITG mode.

The inclusion of the trapped electrons has drastic effect on the growth rate as well as real frequency of the SWITG mode, in contrast to the earlier speculation that the trapped electrons may not be important for the mode. The trapped electrons enhance the growth rate of the mode substantially because of the nonideal effects such as magnetic drift resonance and reduction in the adiabatic fraction of the electrons. The trapped electrons enhance the real frequency which may lead to weaker Landau damping of the wave by the ions. This perhaps is another reason of the mode getting unstable in the presence of trapped electrons. The parameter regime of existence of the mode, consequently, gets widened introducing new domain of instability. Also, the mode structure of the so-called short wavelength ion temperature gradient mode has been observed to be quite global, even though it exists at short wavelength compared to the ion Larmor radius. The mode structure spans over a substantial fraction of the tokamak poloidal cross section.

In this work, we use the electrostatic version of the code EM-GLOGYSTO. A local version of this gyro-kinetic formulation is also used for the purpose of comparison.

## 5.2 Linear SWITG

### 5.2.1 Model Equations

The global formulation has been elucidated in Chapter 2 and Chapter 3. Here we shall discuss the local formulation only.

Integrating the following local gyrokinetic equation, for which  $k_{\perp} \simeq k_{\theta}$  and  $k_{\parallel} = \text{constant}$ , to get the perturbed density

$$f_j = -\frac{q_j F_{Mj}}{T_j} \tilde{\phi} + \frac{q_j F_{Mi}}{T_j} (\omega - \omega_{*j}) (i\mathcal{P}_j) J_0^2(k_{\perp} \rho_j) \tilde{\phi}, \quad (5.1)$$

one can write  $\tilde{n}_j$  as

$$\tilde{n}_j(k) = -\frac{q_j N_j}{T_j} \left[ 1 - \frac{1}{\sqrt{2\pi} v_{thj}^3} \int dv_{\perp} dv_{\parallel} v_{\perp} e^{-\frac{v_{\perp}^2}{2v_{thj}^2}} (\omega - \omega_{*j}) (i\mathcal{P}_j) J_0^2(k_{\perp} \rho_{Lj}) \right] \tilde{\phi}, \quad (5.2)$$

where the propagator for the untrapped particles is given by  $i\mathcal{P}_j = \frac{1}{\omega - k_{\parallel} v_{\parallel} - \omega_{dj}}$ , which for trapped particles is replaced by  $i\mathcal{T}_j = \frac{1}{\omega - \omega_{dj}}$ . Using the quasineutrality condition and considering the passing electrons to be adiabatic and adding the trapped electrons, one would finally get

$$1 + \tau - \sqrt{(2\epsilon)} I_{00}^{tr-e} - \tau I_{00}^i = 0. \quad (5.3)$$

The trapped electron integral  $I_{00}^{tr-e}$  is weighted by the trapped fraction  $\sqrt{2\epsilon}$ ,  $\epsilon = r/a$ , and  $\tau = T_e/T_i$ . Here we put

$$\tilde{I}_{l,p}^j = \frac{1}{\sqrt{2\pi} v_{thj}^3} \int dv_{\perp} dv_{\parallel} v_{\perp} e^{-\frac{v_{\perp}^2}{2v_{thj}^2}} (\omega - \omega_{*j}) (i\mathcal{P}_j) \left( \frac{v_{\parallel}}{v_{thj}} \right)^l \left( \frac{v_{\perp}}{v_{thj}} \right)^p J_0^2(k_{\perp} \rho_{Lj}).$$

In the present section, we will delineate the results from the global and local gyrokinetic formulation and compare the cases of SWITG without the trapped electrons and with the trapped electrons. It is to be noted that the frequencies are normalized with  $v_{thi}/a$  throughout the chapter. Let us consider the following profiles and parameters.

## Chapter 5: Short wavelength ion temperature gradient mode and coupling with trapped electrons

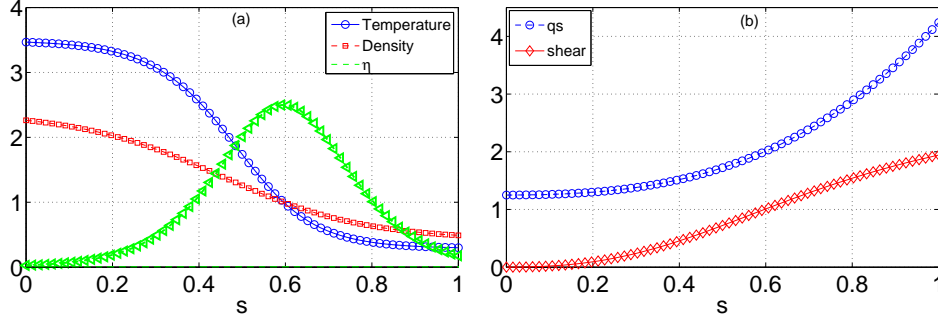


Figure 5.1: Equilibrium profiles to study the global SWITG mode (for parameters in Table I): (a) normalized density (square), temperature (circle),  $\eta_{i,e}$  (triangle), (b) Safety factor  $q$  (circle) and magnetic shear  $\hat{s}$  (diamond) profiles as functions of normalized radius  $s = r/a$ . Note that  $\eta$  peaks at  $s = \rho/a = s_0 = 0.6$  and is equal to 2.5. Also  $q(s_0 = 0.6) = 2.0$ ,  $\hat{s}(s_0 = 0.6) = 1.0$ ,  $\epsilon_n(s_0 = 0.6) = 0.1$ , and  $\tau(s_0 = 0.6) = 1.0$ .

Table 5.1: Profiles and parameters

### Parameters:

- B-field :  $B_0 = 1.0$  Tesla
- Temperature :  $T_0 = T(s_0) = 7.5$  keV
- Major Radius :  $R = 2.0$  m
- Minor Radius :  $a = 0.5$  m
- radius :  $s = \rho/a$ ,  $0.01 < s < 1.0$ ,  $s_0 = 0.6$
- $L_{n0} = 0.2$  m,  $L_{T0} = 0.08$  m
- $\eta_{i,e}(s_0) = 2.5$ ,  $\epsilon_n = L_{n0}/R = 0.1$
- $\tau(s) = T_e(s)/T_i(s) = 1$ .

### Equilibrium Profiles:

- N-profile and T-profile
 
$$\frac{N(s)}{N_0} = \exp\left(-\frac{a \delta s_n}{L_{n0}} \tanh\left(\frac{s-s_0}{\delta s_n}\right)\right)$$

$$\frac{T_{i,e}(s)}{T_0} = \exp\left(-\frac{a \delta s_T}{L_{T0}} \tanh\left(\frac{s-s_0}{\delta s_T}\right)\right)$$

$$\delta s_n = 0.35, \delta s_T = 0.2 \text{ at } s = s_0$$
- $q(s) = 1.25 + 0.67 s^2 + 2.38 s^3 - 0.06 s^4$   
such that  $q(s = s_0) = 2.0$ ;  
shear  $s = s_0$ ,  $\hat{s} = 1$ .

The equilibrium profiles corresponding to these parameters are shown in Fig. 5.1. The chosen parameters lead to the value of  $\rho^* \equiv \rho_{Li}(s = s_0)/a \simeq 0.0175$ . Note that for the local results all the input parameters are given at  $s = s_0$ .

### 5.2.2 $k_{\theta}\rho_{Li}$ Scan

Figure 5.2 shows the growth rates of the SWITG mode with respect to  $k_{\theta}\rho_{Li}$  for the cases (1) without the trapped electrons and (2) with the trapped electrons as obtained with the global as well as local gyrokinetic model. The upper axis displays the corresponding toroidal mode numbers  $n$ . Let us first consider the curve with solid line and open circles. This presents the growth rate from the global model versus  $k_{\theta}\rho_{Li}$  for the SWITG mode without the trapped electrons. The growth rate

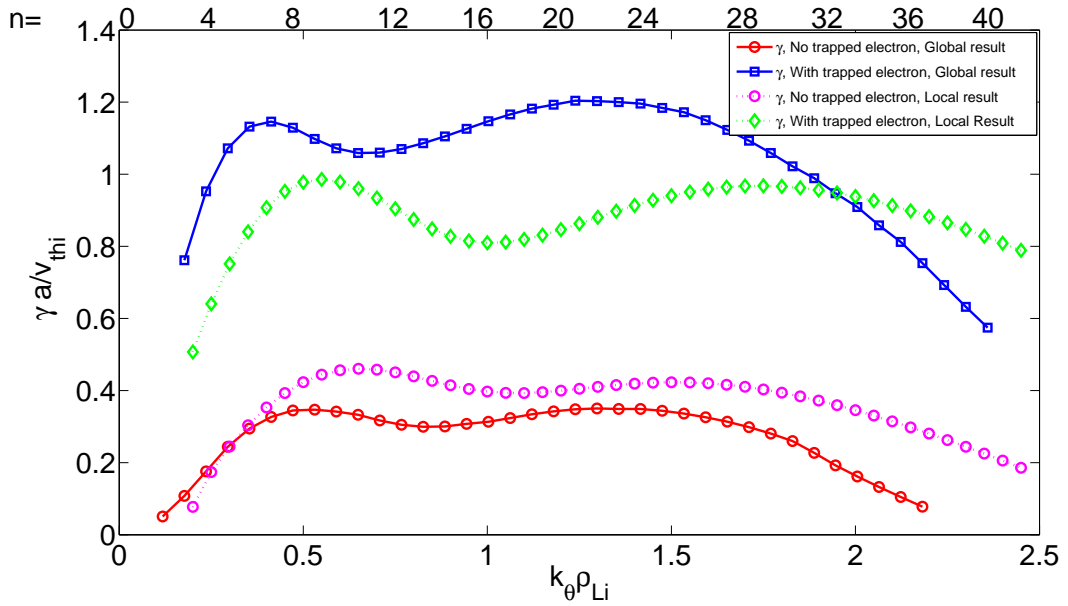


Figure 5.2: The normalized growth rate  $\tilde{\gamma}$  of the ITG (first peak) and of the SWITG (second peak) mode with (solid line+square) and without (solid line + circle) the trapped electrons from the global as well as local formulation (dotted line + diamond, for the case with the trapped electrons and dotted line + circle, for the case without the trapped electrons.)  $\eta_{e,i}(s_0) = 2.5$ ,  $q(s_0) = 2.0$ ,  $\hat{s}(s_0) = 1.0$ ,  $\tau = 1.0$ , and  $\epsilon_n = 0.1$ . Upper axis shows the corresponding toroidal mode numbers.

increases at lower  $k_{\theta}\rho_{Li}$ , peaks at  $k_{\theta}\rho_{Li} \approx 0.5$ ,  $n = 9$ , and then starts falling again, with a minimum at  $k_{\theta}\rho_{Li} \approx 0.8$ ,  $n = 14$ . After this point, the growth rate exhibits a similar trend as the first hump and peaks at  $k_{\theta}\rho_{Li} \approx 1.3$ ,  $n = 21$ . The dotted line with open circles is the similar curve obtained from the local model without the trapped electrons. The peaks for both conventional ITG and SWITG modes are

## Chapter 5: Short wavelength ion temperature gradient mode and coupling with trapped electrons

shifted toward higher  $k_\theta \rho_{Li}$  in comparison with the global results. The first peak appears at  $k_\theta \rho_{Li} \approx 0.65$  and the second peak appears at  $k_\theta \rho_{Li} \approx 1.5$  corresponding, respectively, to the ITG and SWITG mode. The growth rates are slightly higher in the case of the local results than those obtained in the case of the global results. The real frequency as shown in Fig. 5.3 (solid line with open circle for the global model and dotted line with open circle for the local model), on the other hand, increases with  $k_\theta \rho_{Li}$  upto the point  $k_\theta \rho_{Li} \approx 0.8$  and  $k_\theta \rho_{Li} \approx 1.3$ , respectively, for the global and local models. Beyond this point, the frequency starts to behave nonmonotonically with  $k_\theta \rho_{Li}$ . For both cases, the first hump corresponds to the conventional ITG mode. In this region, the mode frequency being proportional to the  $k_\theta \rho_{Li}$  increases almost linearly with  $k_\theta \rho_{Li}$ . The ITG mode then smoothly changes to the high  $k$  SWITG mode. The nonmonotonic part can be considered as one of the characteristics of the SWITG mode. From Fig. 5.2, it is clear that the SWITG mode also suffers FLR stabilization like the conventional ITG; the mode growth rate increases initially then peaks at  $k_\theta \rho_{Li} \approx 1.3$  ( $k_\theta \rho_{Li} \approx 1.5$ ) for the global (local) mode and then starts falling. Following the formulation of Gao *et al.*[107, 108], the nonmonotonic behavior of the real frequency and the double humped growth rate can be explained qualitatively using the local gyrokinetic model for which  $k_\perp \simeq k_\theta$ . Let us rewrite the perturbed distribution function  $\tilde{f}_i$  for the ions as

$$f_i = -\frac{q_i F_{Mi}}{T_i} \tilde{\phi} + \frac{q_i F_{Mi}}{T_i} \left( \frac{\omega - \omega_{*i}}{\omega - \omega_{di} - k_\parallel v_\parallel} \right) J_o^2(k_\perp \rho_{Li}) \tilde{\phi}. \quad (5.4)$$

The first part corresponds to the adiabatic response while the second part corresponds to the non-adiabatic response of the ions. Integrating over velocity, to get the perturbed density for the ions in the limit  $\omega_n > \omega > (\omega_{di} + k_\parallel v_\parallel)$ , one can write

$$\tilde{n}_i = -\frac{q_i n_o}{T_i} \tilde{\phi} + \frac{q_i}{T_i} \tilde{\phi} \frac{\omega_{ni}(\eta_i/2 - 1)}{\omega} I_o(k_\perp^2 \rho_{Li}^2) \exp(-k_\perp^2 \rho_{Li}^2), \quad (5.5)$$

where  $I_o$  is the modified Bessel function of order zero. Since the SWITG mode can exist even with the adiabatic electrons and retains its basic characters, we for simplicity drop the non-adiabatic part of the electrons and consider them to be adiabatic, i.e.,  $\tilde{n}_e/n_o = q_e \tilde{\phi}/T_e$ . The quasineutrality condition will then give

Chapter 5: Short wavelength ion temperature gradient mode and coupling with trapped electrons

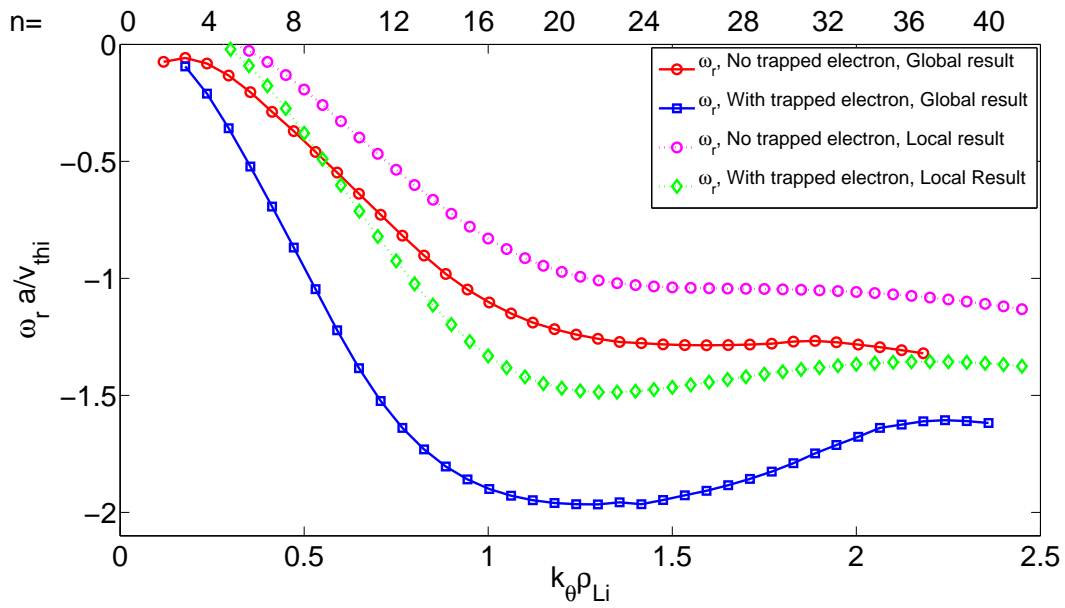


Figure 5.3: The normalized real frequency  $\tilde{\omega}_r$  of the ITG and of the SWITG mode with (solid line+square) and without (solid line+circle) the trapped electrons from the global as well as local formulation (dotted line+diamond, for the case with the trapped electrons and dotted line + circle, for the case without the trapped electrons.)  $\eta_{e,i}(s_0) = 2.5$ ,  $q(s_0) = 2.0$ ,  $\hat{s}(s_0) = 1.0$ ,  $\tau = 1.0$ , and  $\epsilon_n = 0.1$ . Upper axis shows the corresponding toroidal mode numbers.

**Chapter 5: Short wavelength ion temperature gradient mode and coupling with trapped electrons**

$$\omega = \left( \frac{\tau}{\tau + 1} \right) \left( \frac{\eta_i}{2} - 1 \right) \omega_{ni} I_o(k_{\perp}^2 \rho_{Li}^2) \exp(-k_{\perp}^2 \rho_{Li}^2), \quad (5.6)$$

where  $\omega_{ni} = -(v_{thi}/L_n)(k_{\perp} \rho_{Li})$ . Thus, it is clear from the expression that the mode frequency  $\omega$  behaves as  $\omega_{ni} I_o(k_{\perp}^2 \rho_{Li}^2) \exp(-k_{\perp}^2 \rho_{Li}^2)$  which for small  $k_{\perp}^2 \rho_{Li}^2$  scales as  $k_{\perp} \rho_{Li}$  and for larger  $k_{\perp}^2 \rho_{Li}^2$  scales as almost a constant. It is because, from the property of the scaled modified Bessel function, one finds that

$$I_o(k_{\perp}^2 \rho_{Li}^2) \exp(-k_{\perp}^2 \rho_{Li}^2) \rightarrow 1/\sqrt{2\pi(k_{\perp}^2 \rho_{Li}^2)} = 1/\sqrt{2\pi}(k_{\perp} \rho_{Li}),$$

for large  $k_{\perp}^2 \rho_{Li}^2$  and  $\omega_{ni} \propto k_{\perp} \rho_{Li}$ . This explains the nonmonotonic part of the real frequency. Regarding the growth rate, in the toroidal geometry, it is the toroidal magnetic drift term  $\omega_{di}$  of the ions, the resonance of which with the mode frequency gives rise to the the double hump behavior. It is to be noted that  $\omega_{di} \sim (L_n/R)\omega_{ni}$  and thus scales as  $k_{\perp} \rho_{Li}$ . Therefore, the ratio  $\omega/\omega_{di}$  at first increases for small  $k_{\perp} \rho_{Li}$  and then decreases as the numerator saturates but the denominator still grows as  $k_{\perp} \rho_{Li}$ .

The finite Larmor stabilization (FLR) of the SWITG mode can be inferred from the nonadiabatic part of ion density response. At very high  $k_{\perp} \rho_{Li}$ ,  $\omega_{di}$  surpasses  $\omega$  and the nonadiabatic part of the perturbed ion density can be reduced to, for  $\omega_{di} \gg \omega$

$$\tilde{n}_i^{na} = \frac{q_i}{T_i} \tilde{\phi} \frac{\omega_{ni}(\eta_i/2 - 1)}{\omega_{di}} I_o(k_{\perp}^2 \rho_{Li}^2) \exp(-k_{\perp}^2 \rho_{Li}^2), \quad (5.7)$$

which for large  $k_{\perp} \rho_{Li}$  will decrease according to

$$\frac{\omega_{ni}}{\omega_{di}} I_o(k_{\perp}^2 \rho_{Li}^2) \exp(-k_{\perp}^2 \rho_{Li}^2) \sim \frac{R}{L_n} I_o(k_{\perp}^2 \rho_{Li}^2) \exp(-k_{\perp}^2 \rho_{Li}^2), \quad (5.8)$$

as  $k_{\perp}^2 \rho_{Li}^2$  increases.

Having elucidated the basic characters of the SWITG mode, let us now see what happens to the mode when trapped electrons are included. In Fig. 5.2 the solid line with squares represents the growth rates from the global model and the dotted line with diamonds represents the growth rates from the local model with trapped electrons present in both cases. Similar curves in Fig. 5.3 represent the corre-

## Chapter 5: Short wavelength ion temperature gradient mode and coupling with trapped electrons

sponding real frequencies. It is clear that for both cases, the growth rate rises substantially in the presence of the trapped electrons. The mode frequencies also increase as compared to their counterparts with no trapped electrons. The global curve for growth rates peaks at  $k_{\theta}\rho_i \approx 0.4$ ,  $n = 7$ , while the local curve peaks at  $k_{\theta}\rho_i \approx 0.55$  for the conventional ITG. For the SWITG mode, the growth rate peaks at  $k_{\theta}\rho_i \approx 1.3$ ,  $n = 21$ , for the global result while it peaks at  $k_{\theta}\rho_i \approx 1.7$  for the local result. It is to be noted that the local growth rates stay below the global growth rates for most of the part of the  $k$  spectrum. Beyond  $k_{\theta}\rho_i \approx 2.0$ , the global growth rates fall faster than the local growth rates.

The strong rise in the the growth rate of the SWITG mode in the presence of trapped electrons can be explained, similar to the conventional ITG mode, as follows. In a toroidal plasma with ion temperature gradient, a pressure perturbation in the outboard side creates hotter and colder regions locally. The magnetic drift velocity  $v_d$  of the ions, which depends on the temperature, is therefore different in regions of different temperatures. This produces variations in the local concentration of the ion density giving rise to a potential perturbation and concurrently a poloidal electric field. The SWITG instability arises because of the radial  $E \times B$  drift produced by this electric field in the presence of the applied magnetic field. When one considers electrons to be adiabatic, the moment charge separation is produced, these electrons move to the regions of charge separation and wipe out the space charge, thus denying the possibility of building up of  $E \times B$  advection or reducing it. However, in a toroidal geometry, because of  $1/R$  dependence of the magnetic field, some electrons are "trapped" on the weaker magnetic field region and fail to behave adiabatically, in the sense that their motion is restricted to a limited region of the magnetic field lines. Trapped electrons, therefore, can not respond adiabatically to reach the region of  $E \times B$  advection and participate in canceling the charge separations, thereby allowing finite time for the mode to grow. The SWITG growth rate thus gets enhanced, when one considers the fraction of the trapped electrons.

The presence of the trapped electrons increases the real frequency and hence the phase velocity of the wave. This can perhaps make the wave off resonant with the ions and leads to weaker Landau damping of the wave by the ions with the concomitant enhancement in the growth rate. The SWITG growth rate, therefore, increases with the inclusion of the trapped electrons.

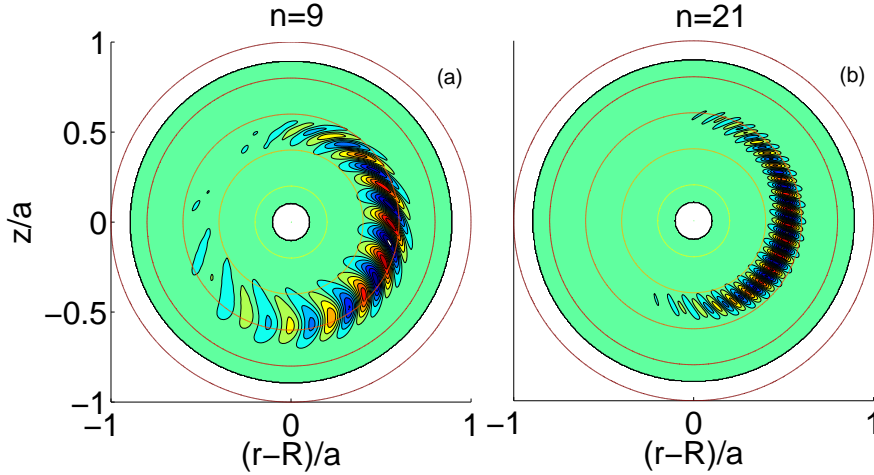


Figure 5.4: Two dimensional eigenmode structures of (a) the ITG mode at  $k_{\theta}\rho_{Li} \approx 0.5$ ,  $n = 9$ , (b) the SWITG mode at  $k_{\theta}\rho_{Li} \approx 1.3$ ,  $n = 21$  without the trapped electrons both corresponding to the maximum growth rate. The mode structure of the SWITG mode is finer than the ITG mode but yet global enough.

Figure 5.4 presents the mode structures of (a) the conventional ITG at  $n = 9$  and (b) the SWITG at  $n = 21$ , both corresponding to the maximum growth rate without the trapped electrons. The eigenmode-averaged radial wave numbers for the two cases are  $\langle k_r\rho_{Li} \rangle = 0.687$  and  $\langle k_r\rho_{Li} \rangle = 0.702$  respectively. These figures show clearly that though the mode is termed as short wavelength ITG, its mode structure is quite global albeit lesser than the conventional ITG mode. The mode structure spans over a considerable fraction of the poloidal cross section of a tokamak. It corroborates the necessity of a global model to study the SWITG mode. Figure 5.5 then displays the mode structures, respectively, of the (a) conventional ITG mode with the trapped electrons at  $n = 7$  and (b) SWITG mode with the trapped electrons at  $n = 21$ , both corresponding to the maximum growth rate of the mode. It is to be noted that the corresponding eigenmode-averaged radial wave numbers in these cases are  $\langle k_r\rho_{Li} \rangle = 0.489$  and  $\langle k_r\rho_{Li} \rangle = 1.132$ , respectively. For clarity, we present a closeup view of the mode structures in Fig. 5.6 for the case without the trapped electrons for the conventional ITG mode and SWITG mode and in Fig. 5.7 for the case with the trapped electrons.

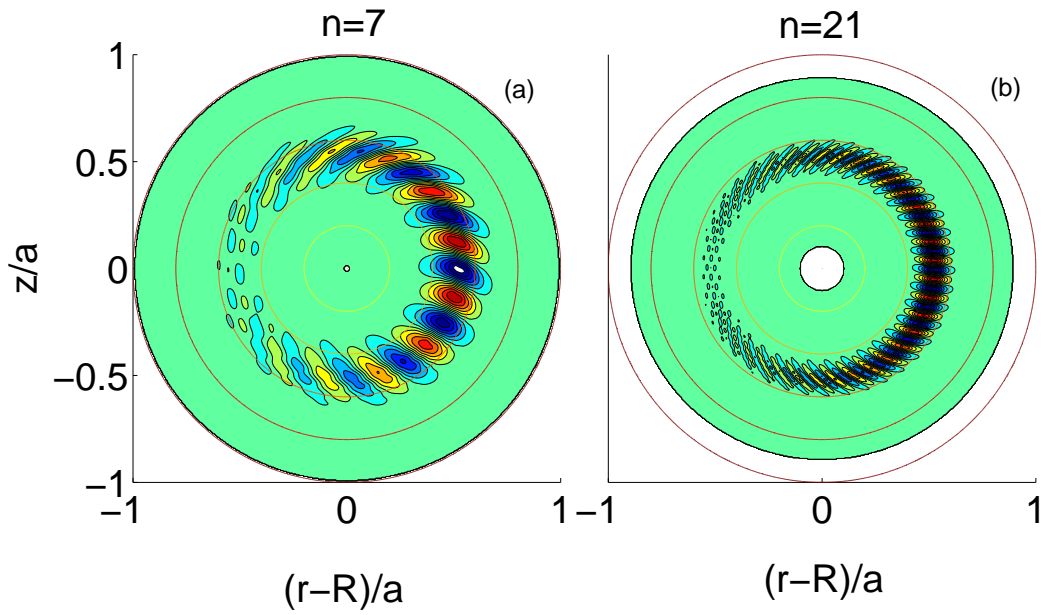


Figure 5.5: Two dimensional eigenmode structures of (a) the ITG mode at  $k_{\theta}\rho_{Li} \approx 0.4$ ,  $n = 7$ , (b) the SWITG mode at  $k_{\theta}\rho_{Li} \approx 1.3$ ,  $n = 21$  with the trapped electrons, both for the maximum growth rates respectively. The mode structure of the SWITG mode is finer than the ITG mode but still global enough.

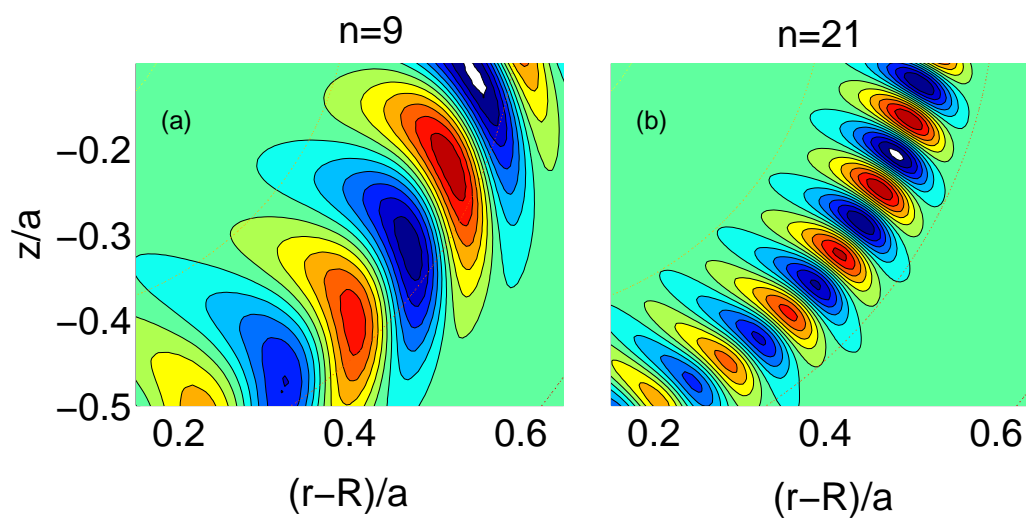


Figure 5.6: A closeup view of the eigenmode structures of (a) the ITG mode at  $k_{\theta}\rho_{Li} \approx 0.5$ ,  $n = 9$ , (b) the SWITG mode at  $k_{\theta}\rho_{Li} \approx 1.3$ ,  $n = 21$  without the trapped electrons shown in Fig. 5.4.

## Chapter 5: Short wavelength ion temperature gradient mode and coupling with trapped electrons

Figure 5.8 portrays the poloidal Fourier components for the cases of (a) the ITG mode at  $n = 9$ , (b) the SWITG mode at  $n = 21$  without the trapped electrons, (c) the ITG mode at  $n = 7$ , and (d) the SWITG mode at  $n = 21$  with the trapped electrons. The strong poloidal coupling of the mode brought about by the cross field drift of the particles is quite apparent from these figures. Figure 5.9 shows the radial Fourier harmonics for the modes displayed in Figs. 5.4 and 5.5.

### 5.2.3 $\epsilon_n$ Scan

The  $L_n/R$  scan is performed by varying  $R$  but keeping  $Rq$ ,  $n/R$ ,  $a$ , and  $L_n$  constant. Figure 5.10 presents the growth rates for the two cases: (a) without the trapped electrons (circle) and (b) with the trapped electrons (square) from the global gyrokinetic formulation. Local results are not shown here. It is clear that the SWITG mode subsides more rapidly with  $\epsilon_n$  and vanishes at around  $\epsilon_n \sim 1.7$ . It is argued, therefore, in the earlier literature that the SWITG mode is preferentially a slab mode which decays with increasing toroidicity. The decrease in the growth rate with  $L_n/R$  can again be attributed to the reduction in the non-adiabatic fraction of the ion's perturbed density response with  $L_n/R$ , as it scales as inverse of  $L_n/R$  as apparent from Eq. (5.7). Inclusion of the trapped electrons, however, widens the  $L_n/R$  window. The mode sustains to a higher value of  $L_n/R$ . Thus, one concludes that the trapped electrons have deleterious effect on the SWITG mode enhancing not only its growth rate but also widening its parameter regime of existence. The fact is that, with increasing toroidicity, the fraction of the trapped particles which is proportional to  $\sqrt{r/R}$  also increases. Therefore, in contrast to the previous case of the SWITG where toroidicity has strong stabilizing effect, making the mode vanish beyond  $L_n/R \sim 0.15$ , the SWITG in the presence of trapped electrons can exist above this limit, as the stabilizing effect of the toroidicity is compensated by the destabilizing effect of the trapped electrons. In Fig. 5.11, the corresponding real frequencies are shown. Solid line with circles presents the case without the trapped electrons and solid line with squares presents the case with the trapped electrons. While, with toroidicity the growth rates decay, real frequencies on the other hand increase with the toroidicity. Thus, though earlier SWITG was thought to be stable beyond some specific value of  $\epsilon_n$ , the trapped electrons can make it

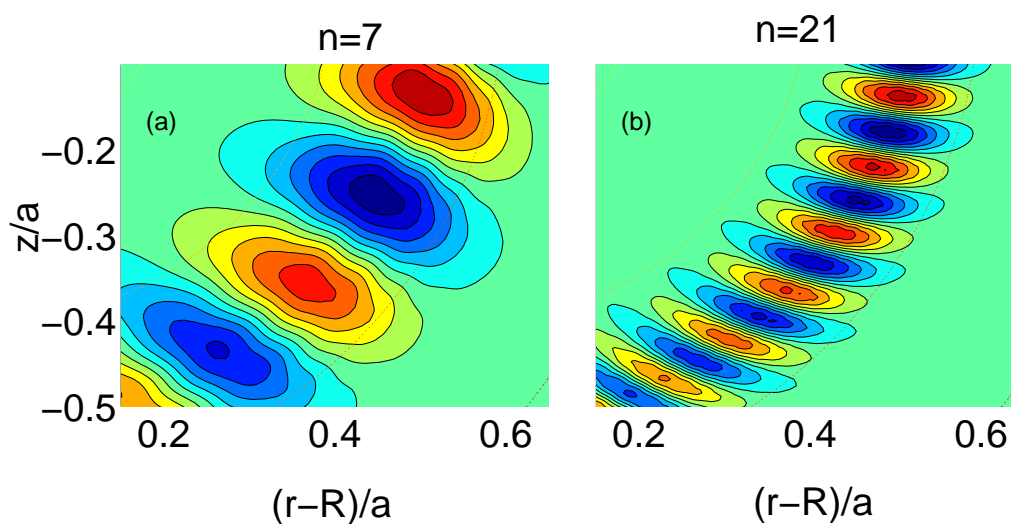


Figure 5.7: A closeup of the two dimensional eigenmode structures of (a) the ITG mode at  $k_{\theta}\rho_{Li} \approx 0.4$ ,  $n = 7$ , (b) the SWITG mode at  $k_{\theta}\rho_{Li} \approx 1.3$ ,  $n = 21$  with the trapped electrons shown in Fig. 5.5.

Chapter 5: Short wavelength ion temperature gradient mode and coupling with trapped electrons

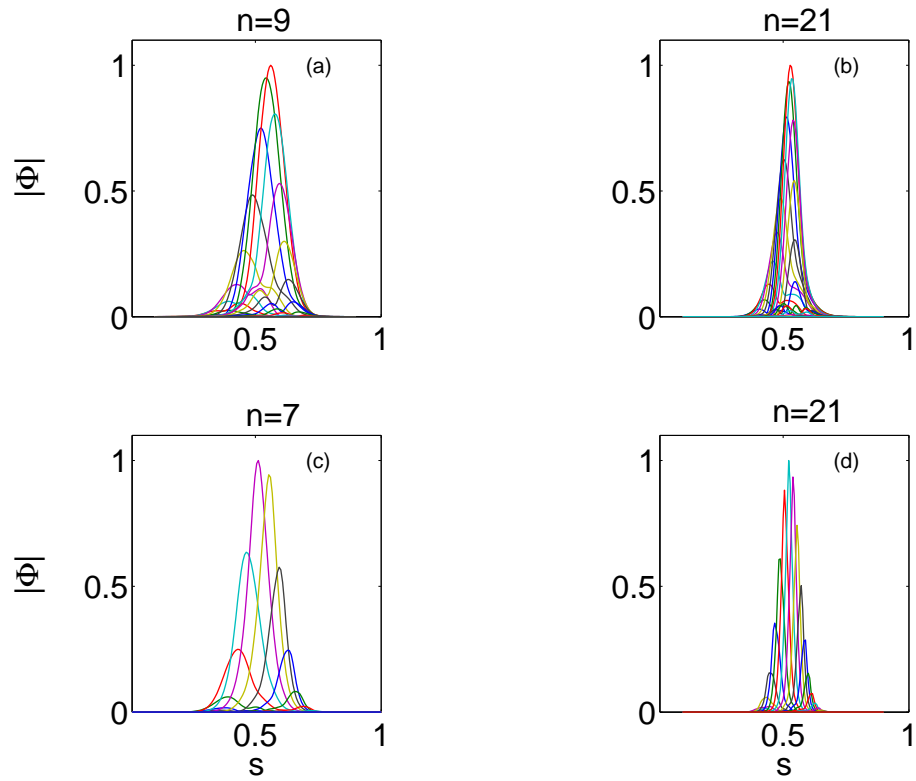


Figure 5.8: Poloidal Fourier components for electrostatic modes shown in Figs. 5.4 and 5.5, (a) the ITG mode at  $k_{\theta\rho_{Li}} \approx 0.5$ ,  $n = 9$ , (b) the SWITG mode at  $k_{\theta\rho_{Li}} \approx 1.3$ ,  $n = 21$ , both without the trapped electrons, (c) the ITG mode at  $k_{\theta\rho_{Li}} \approx 0.4$ ,  $n = 7$ , and (d) the SWITG mode at  $k_{\theta\rho_{Li}} \approx 1.3$ ,  $n = 21$ , both with the trapped electrons.

Chapter 5: Short wavelength ion temperature gradient mode and coupling with trapped electrons

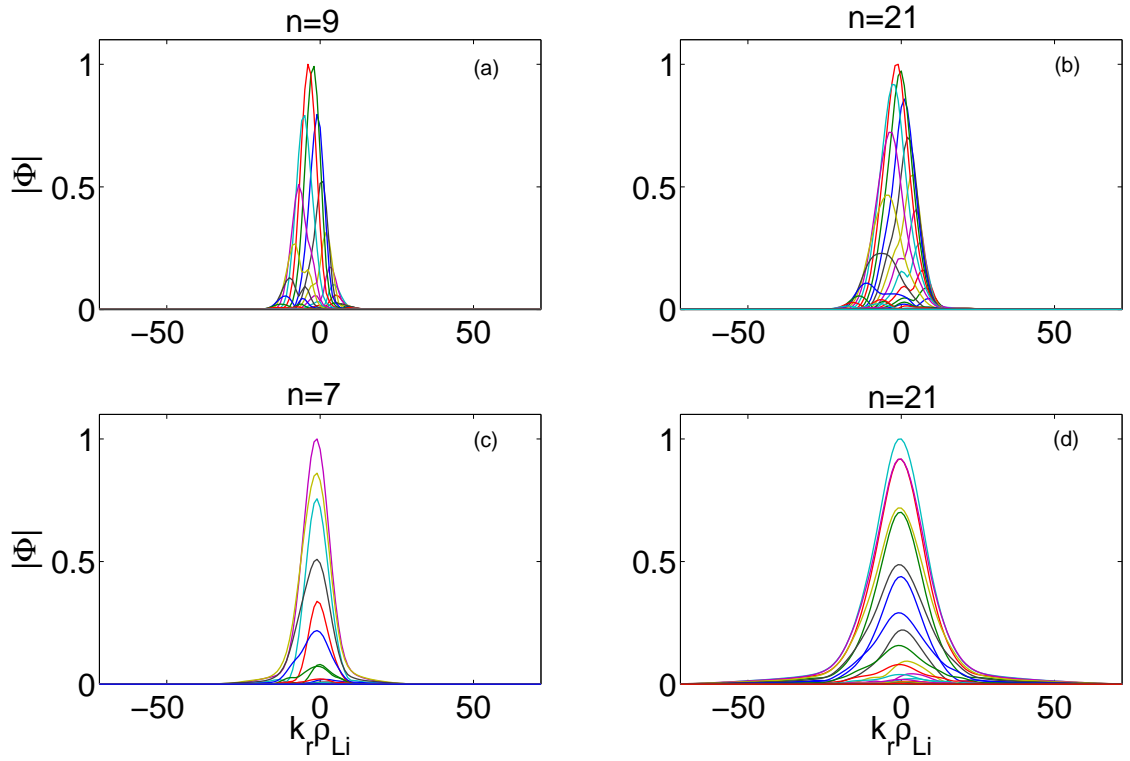


Figure 5.9: Radial Fourier components for electrostatic modes shown in Fig. 5.4 and 5.5, (a) the ITG mode at  $k_{\theta}\rho_{Li} \approx 0.5$ ,  $n = 9$ , (b) the SWITG mode at  $k_{\theta}\rho_{Li} \approx 1.3$ ,  $n = 21$ , both without the trapped electrons, (c) the ITG mode at  $k_{\theta}\rho_{Li} \approx 0.4$ ,  $n = 7$ , and (d) the SWITG mode at  $k_{\theta}\rho_{Li} \approx 1.3$ ,  $n = 21$ , both with the trapped electrons.

## Chapter 5: Short wavelength ion temperature gradient mode and coupling with trapped electrons

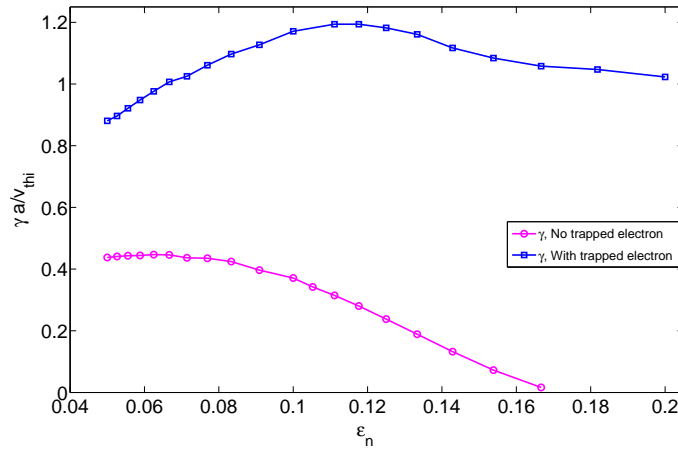


Figure 5.10: Normalized growth rates  $\tilde{\gamma}$  vs.  $\epsilon_n$  scan for the SWITG mode at  $k_{\theta}\rho_{Li} \approx 1.3$  with (solid line + square) and without (solid line + circles) the trapped electrons (from the global gyrokinetic model).  $\eta_{e,i}(s_0) = 2.5$ ,  $q(s_0) = 2.0$ ,  $\hat{s}(s_0) = 1.0$ ,  $\tau = 1.0$ ,  $L_n = 0.2$ , and  $a = 0.5$ .

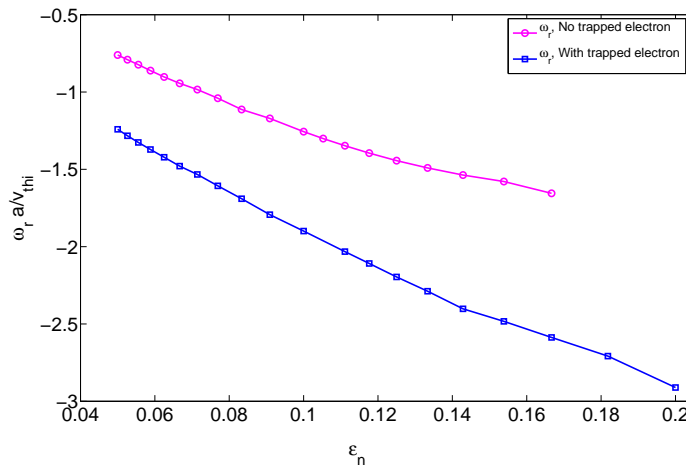


Figure 5.11: Normalized real frequency  $\tilde{\omega}_r$  vs.  $\epsilon_n$  scan for the SWITG mode at  $k_{\theta}\rho_{Li} \approx 1.3$  with (solid line + square) and without (solid line + circles) the trapped electrons (from the global gyrokinetic model).  $\eta_{e,i}(s_0) = 2.5$ ,  $q(s_0) = 2.0$ ,  $\hat{s}(s_0) = 1.0$ ,  $\tau = 1.0$ ,  $L_n = 0.2$ , and  $a = 0.5$ .

## Chapter 5: Short wavelength ion temperature gradient mode and coupling with trapped electrons

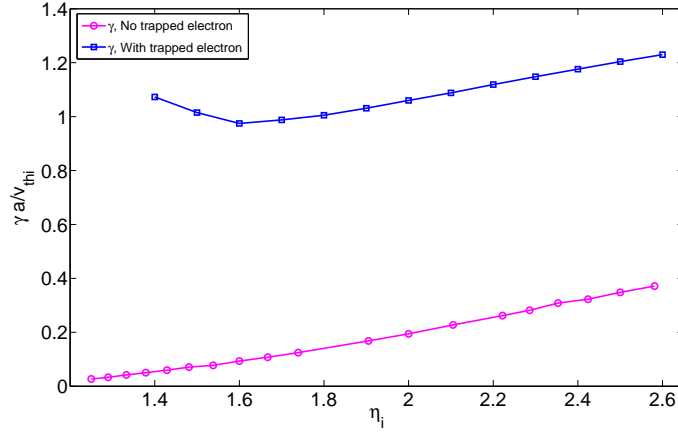


Figure 5.12: Normalized growth rates  $\tilde{\gamma}$  vs.  $\eta_i$  scan for the SWITG mode at  $k_{\theta}\rho_{Li} \approx 1.3$  with (solid line + square) and without (solid line + circles) the trapped electrons (from the global gyrokinetic model).  $\eta_e(s_0) = 2.5$ ,  $q(s_0) = 2.0$ ,  $\hat{s}(s_0) = 1.0$ ,  $\tau = 1.0$ , and  $\epsilon_n = 0.1$ .

unstable for a general set of parameters. Therefore, the theories for experimentally observed anomalous transport, explained with the conventional ITG mode coupled with trapped electrons and trapped electron mode as plausible candidates, should be revisited. It is perhaps worth noting at this point that experimentally Wong *et al.* [112] reported the observation of such a short wavelength fluctuation in the context of electron transport. The mode has frequency lower than the ion diamagnetic drift frequency and propagates in the ion diamagnetic direction as the SWITG mode studied here. However,  $k_{\perp}\rho_{Li}$  measured is higher ( $\sim 5$ ) than the one found in our simulation.

### 5.2.4 $\eta_i$ Scan

To demonstrate the temperature gradient dependence of the SWITG mode, an  $\eta_i$  scan for the maximum growth rates is shown in Fig. 5.12 without (circles) and with (squares) the trapped electrons using the global gyrokinetic model. It is clear from the figure that the SWITG mode without the trapped electrons is inherently an ion mode, requiring no finite  $\eta_e$  and solely depends on the temperature gradient of the ions. The dependence of the mode growth rate on  $\eta_i$  is quite similar to the conventional ITG which decays with decreased  $\eta_i$ . The SWITG mode decays as

## Chapter 5: Short wavelength ion temperature gradient mode and coupling with trapped electrons

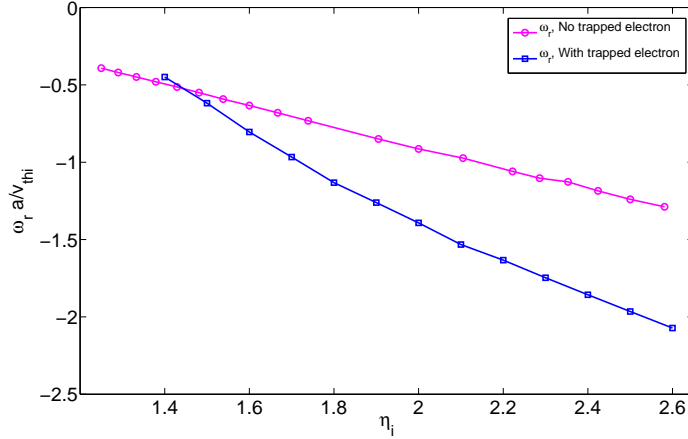


Figure 5.13: Normalized real frequency  $\tilde{\omega}_r$  vs.  $\eta_i$  scan for the SWITG mode at  $k_{\theta}\rho_{Li} \approx 1.3$  with (solid line + square) and without (solid line + circles) the trapped electrons (from the global gyrokinetic model).  $\eta_e(s_0) = 2.5$ ,  $q(s_0) = 2.0$ ,  $\hat{s}(s_0) = 1.0$ ,  $\tau = 1.0$ , and  $\epsilon_n = 0.1$ .

one reduces  $\eta_i$  and vanishes completely around  $\eta_{ic} \sim 1.2$ . Inclusion of the trapped electrons, on the other hand, restricts the mode to vanish, rather the mode transforms from the ion temperature gradient driven mode to the trapped electrons driven mode. When the ion drive is reduced by reducing  $\eta_i$ , the growth rate decreases, but since the mode now includes the trapped electrons with finite  $\eta_e$ , mode inherent to the trapped electrons takes over the ion temperature gradient driven mode. Thus, the SWITG mode transforms from dominantly ion temperature gradient driven mode to dominantly electron temperature gradient driven mode as the  $\eta_i$  of the ions is reduced keeping  $\eta_e$  fixed. The transition takes place at around  $\eta_i \sim 1.6$ . The corresponding real frequencies without (circle) and with (squares) the trapped electrons are shown in Fig. 5.13. Both reduce almost linearly with  $\eta_i$ , but because of the presence of the trapped electrons the later reduces faster than the former and tend to move in the electron diamagnetic direction. It is because of the fact that the mode inherent to the trapped electrons with finite  $\eta_e$  starts to dominate over ion temperature gradient driven mode as one reduces  $\eta_i$ .

## Chapter 5: Short wavelength ion temperature gradient mode and coupling with trapped electrons

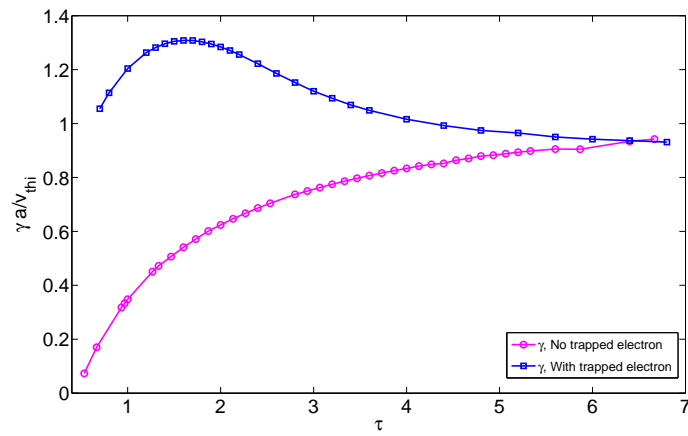


Figure 5.14: Normalized growth rates  $\tilde{\gamma}$  vs.  $\tau$  scan for the SWITG mode at  $k_{\theta}\rho_{Li} \approx 1.3$  with (solid line + square) and without (solid line + circles) the trapped electrons (from the global gyrokinetic model).  $\eta_{e,i}(s_0) = 2.5$ ,  $q(s_0) = 2.0$ ,  $\hat{s}(s_0) = 1.0$ , and  $\epsilon_n = 0.1$ .

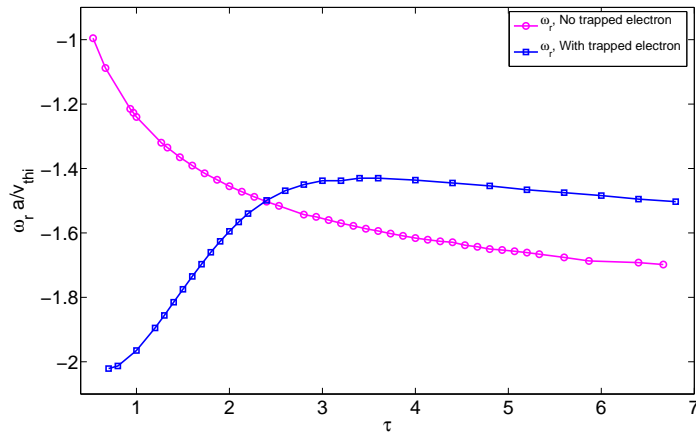


Figure 5.15: Normalized real frequency  $\tilde{\omega}_r$  vs.  $\tau$  scan for the SWITG mode at  $k_{\theta}\rho_{Li} \approx 1.3$  with (solid line + square) and without (solid line + circles) the trapped electrons (from the global gyrokinetic model).  $\eta_{e,i}(s_0) = 2.5$ ,  $q(s_0) = 2.0$ ,  $\hat{s}(s_0) = 1.0$ , and  $\epsilon_n = 0.1$ .

## Chapter 5: Short wavelength ion temperature gradient mode and coupling with trapped electrons

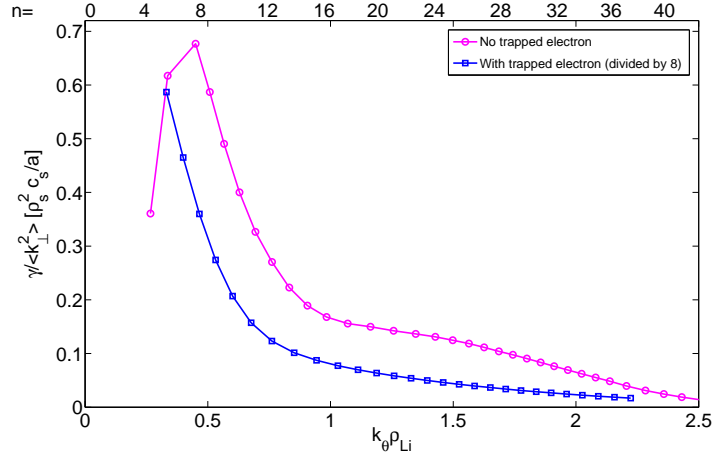


Figure 5.16: Mixing length estimate for transport coefficient  $D_{ML} = \gamma / \langle k_{\perp}^2 \rangle$  of the ions in the ion gyro-Bohm units as a function of  $k_{\theta} \rho_{Li}$ ; (a) the ITG and the SWITG mode without the trapped electrons (solid line + circle) (b) the ITG and the SWITG mode with the trapped electrons (solid line + square) (from the global gyrokinetic model). Note that this curve is scaled down by a factor of 8. The upper axis presents the corresponding toroidal mode numbers.

### 5.2.5 $\tau$ Scan

To look at the temperature dependence of the mode, a  $\tau = T_e/T_i$  scan is shown in Figs. 5.14 and 5.15 for the growth rate and real frequency, respectively, using the global gyrokinetic model. The growth rate in Fig. 5.14 for the SWITG mode without the trapped electrons (circles) increases gradually with  $\tau$  and at higher value of the latter it starts saturating. For the case with the trapped electrons (square), on the other hand, it increases initially and becomes maximum in the region  $\tau \approx 1 - 2$ . It then falls and finally saturates. This can be explained from the fact that in the first case electrons are considered adiabatic, while the trapped electrons are included in the second case. So, at  $\tau \gg 1$ ,  $T_e \gg T_i$ , the electron drive appears to be stronger reducing the growth rate in the later case. This is apparent from Fig. 5.15 where the real frequencies are plotted against  $\tau$ . For the case with the trapped electrons, as  $\tau$  increases the dominant electron drive pulls the real frequency toward the electron diamagnetic direction. Therefore, the real frequency decreases with increasing  $\tau$  going toward more positive value, and then saturates. For the case without the trapped electrons, however, the real frequency

## Chapter 5: Short wavelength ion temperature gradient mode and coupling with trapped electrons

rises initially with  $\tau$  and then starts saturating in line with its corresponding growth rates.

### 5.2.6 Mixing Length Estimation

It will be interesting to calculate the heat diffusivity of the ions in the presence of the SWITG mode, over and above the conventional ITG mode. Within our linear model, we do this by using the mixing length estimation where  $\gamma / \langle k_{\perp}^2 \rangle$ , with  $k_{\perp} = \sqrt{k_r^2 + k_{\theta}^2}$ ,  $k_r$  and  $k_{\theta}$  being, respectively, the radial and poloidal wave numbers of the mode, is plotted with respect to  $k_{\theta} \rho_{Li}$ . Thus, the heat diffusivity  $\gamma / \langle k_{\perp}^2 \rangle$  of the ions in the gyro-Bohm unit is depicted in Fig. 5.16 for the SWITG mode without (circle) and with (square) the trapped electrons. The diffusivity increases initially with  $k_{\theta} \rho_{Li}$ , peaks at  $k_{\theta} \rho_{Li} \approx 0.5$ , and then starts falling for the first case, but decreases monotonically for the second case. The maximum diffusivity shifts toward lower  $k$  for both cases with and without the trapped electrons. It is to be noted that the values of the heat diffusivity for the case with the trapped electrons have been scaled down, dividing the actual values by 8, to show both curves in the same scale. Thus, one can conclude that the trapped electrons enhance the heat diffusivity substantially. One important point to be noted is that there is no peak specific to the  $k_{\perp} \rho_{Li}$  of the SWITG mode, the whole spectrum of the heat diffusivity tends to peak at lower  $k_{\perp} \rho_{Li} \leq 0.5$  despite the fact that the SWITG mode peaks at around  $k_{\perp} \rho_{Li} \sim 1.5$ .

## 5.3 Nonlinear SWITG

Although detailed studies have been pursued in the linear behaviour, there are very few nonlinear studies available on the SWITG mode. It is therefore of interest to investigate how this mode behaves nonlinearly and if there is any significant contribution of this mode to the net ion transport in the core of the system. To this end, we carry out a systematic nonlinear study of the mode using the flux tube version of the well benchmarked, massively parallel, nonlinear, gyrokinetic code GENE [32, 84], however, **without considering the trapped electrons**. We have found that although the  $k$  spectrum bears signature of the SWITG mode, there is practically no contribution to the net ion thermal transport from the SWITG mode.

In the following we describe the nonlinear simulation model and then the results and conclusions.

### 5.3.1 The Model

**Coordinate System:** The set of equations for the electrostatic case are cast in the Clebsch-type field aligned coordinate system  $(x, y, z)$ , such that  $(x, y)$  represents the plane perpendicular to the magnetic field given by  $\mathbf{B} = B_0 \nabla x \times \nabla y$ , where  $x$  stands for the flux surface label, simply the radial coordinate in units of length,  $y$  is the binormal direction in units of length that labels the field line on a given flux surface and  $z$  is the straight field line poloidal angle that labels the position along a field line and thus represents the parallel direction.  $B_0$  is the reference magnetic field on axis. The velocity space is represented by  $(v_{\parallel}, \mu)$ , where,  $v_{\parallel}$  is the velocity component parallel to  $\vec{B}$  and  $\mu = mv_{\perp}^2/2B$  stands for the magnetic moment.

As the present nonlinear simulation uses the flux tube version of GENE, the system considered is therefore a flux tube, where system size is a box of dimension  $L_x \times L_y \times L_z$  in configuration space as well as  $L_{v_{\parallel}} \times L_{\mu}$  in velocity space. In the perpendicular direction i.e., radial  $x$  and binormal  $y$  directions, periodic boundary conditions are applied. The discretization scheme used is based on the so-called "method of lines", that is, the phase space operators are discretized first, and then the resulting ordinary differential equations are solved as an initial value problem using the fourth order Runge-Kutta scheme. The differential operators related to

## Chapter 5: Short wavelength ion temperature gradient mode and coupling with trapped electrons

the field-line following coordinate  $z$  or the parallel velocity  $v_{\parallel}$  are discretized using the fourth-order finite difference scheme. The periodic boundary conditions in the perpendicular  $x$  and  $y$  directions allow one to treat  $x$  and  $y$  in the framework of a pseudo-spectral approach, that is, all linear terms as well as spatial derivatives are evaluated in  $k_x$ - $k_y$  space, while the nonlinearities are computed in real space with the help of Fourier transform and a proper dealiasing method. The velocity space integrations are performed using Gauss and trapezoidal rules in  $\mu$  and  $v_{\parallel}$  space, respectively. For the time stepping, the fourth-order explicit Runge-Kutta method is used.

**$\delta f$  splitting:** In order to separate the macroscopic evolution of the plasma from the microturbulence, the full distribution function is considered to be composed of two parts, namely, the static background distribution function  $f_0$  and a perturbed part  $f_1$  of the order of  $|f_1/f_0| \sim \epsilon = \rho_{ref}/L_{ref}$ , where  $\rho_{ref}$  and  $L_{ref}$ , respectively, stand for a reference Larmor radius and equilibrium scale length. We consider

$$f_{0i}(v_{\parallel}, \mu) = \frac{n_0}{(2\pi T_i/m_i)^{3/2}} \exp\left[-\frac{m_i v_{\parallel}^2/2 + \mu B}{T_i}\right],$$

to be a local Maxwellian distribution function,  $n_0$  and  $T_i$  being the background density and temperature. The perturbed distribution function  $f_1$  is, on the other hand, a function of 5 phase space coordinates  $(x, y, z, v_{\parallel}, \mu)$  and time  $t$ .

**Normalization:** The formal normalization of the various equilibrium and fluctuating quantities are displayed in the following tables, where  $v_{T_i} = \sqrt{2T_i/m_i}$  and  $c_s = \sqrt{Z_i T_e/m_i}$  stand, respectively, for the ion thermal velocity and sound speed,  $\rho_s = c_s/\Omega_i$  is the ion Larmor radius at the sound speed and  $\Phi_1$  is the electrostatic potential related to the fluctuations. Also,  $L_{ref}$  is a reference macroscopic length scale.

$\hat{f}_{j0}$	$\hat{f}_{j1}$	$\hat{\Phi}_1$
$\frac{f_{j0} v_{T_j}^3}{n_0}$	$\left(\frac{f_{j1} v_{T_j}^3}{n_0}\right) \left(\frac{L_{ref}}{\rho_s}\right)$	$\frac{e\Phi_1}{T_e} \left(\frac{L_{ref}}{\rho_s}\right)$

Table 5.2: Normalization of dependent variables.

## Chapter 5: Short wavelength ion temperature gradient mode and coupling with trapped electrons

The spirit behind the choice of the normalization is to make each normalized quantity of order unity. Furthermore, all gradient scale lengths of the equilibrium quantities, *viz.*,  $n_0$ ,  $T_i$ ,  $B$ , are normalized to  $L_{ref}$ .

$\hat{t}$	$\hat{x}$	$\hat{y}$	$\hat{z}$	$\hat{v}_{\parallel}$	$\hat{\mu}$
$c_s t / L_{ref}$	$x / \rho_s$	$y / \rho_s$	$z$	$v_{\parallel} / v_{thi}$	$\mu B_0 / T_i$

Table 5.3: Normalization of independent variables.

**Model Equations:** With the above defined coordinate system and normalizations, and with the suffix defining particle type and the hat for normalized quantities being dropped to ease the notation, the gyrokinetic equation for ions can formally be written as

$$\frac{\partial f_1}{\partial t} + \left[ \frac{1}{L_n} + \frac{1}{L_T} (v_{\parallel}^2 + \mu B - 3/2) \right] f_0 \frac{\partial \bar{\Phi}_1}{\partial y} + \left[ \frac{\partial \bar{\Phi}_1}{\partial x} \frac{\partial f_1}{\partial y} - \frac{\partial \bar{\Phi}_1}{\partial y} \frac{\partial f_1}{\partial x} \right] +$$

$$\frac{1}{B} \frac{\mu B + 2v_{\parallel}^2}{\sigma} (K_x G_x + K_y G_y) + \frac{v_{\parallel}^2 \beta}{\sigma B} \frac{dp}{dx} G_y + \alpha \frac{v_{\parallel}}{JB} G_z - \frac{\mu \alpha}{2JB} \frac{\partial f_1}{\partial v_{\parallel}} \frac{\partial B}{\partial z} = 0, \quad (5.9)$$

where  $G_j = \partial_j f_1 - (\sigma/v_{\parallel}) \partial_j \bar{\Phi}_1 \partial f_0 / \partial v_{\parallel}$  for  $j = x, y, z$ ,  $\alpha_i = v_{Ti}/c_s$  and  $\sigma_i = Z_i T_e / T_i$  and  $\bar{\Phi}_1 = J_0(\lambda) \Phi_1$  is the gyroaveraged potential with  $\lambda^2 = k_{\perp}^2 (2\mu/B)$  and  $J_0$  being the Bessel function of order zero. Also,  $1/L_T = -d(\ln T)/dx$  and  $1/L_n = -d(\ln n)/dx$  are the inverse gradient scale lengths of temperature and density, respectively. The second term in Eq. (5.9) thus represents the equilibrium gradients that drive the instability. The third term is the nonlinear  $E \times B$  drift term. The fourth and fifth terms contain the effect of magnetic curvature and  $\nabla B$ , with

$$K_x = - \frac{g^{xx} g^{yz} - g^{yx} g^{xz}}{B^2} \frac{\partial B}{\partial z},$$

and

$$K_y = \frac{\partial B}{\partial x} - \frac{g^{xy} g^{yz} - g^{yy} g^{xz}}{B^2} \frac{\partial B}{\partial z},$$

where  $g$ 's are the metric tensor elements defined as  $g^{ij} = \nabla u^i \cdot \nabla u^j$ ,  $u^i, u^j = x, y, z$ .

## Chapter 5: Short wavelength ion temperature gradient mode and coupling with trapped electrons

The total plasma pressure appearing with a radial derivative in the fifth term is normalized to  $\hat{p} = p/p_{ref} = n_0 T_e$ , and  $\beta = 2p_{ref}\mu_0/B^2$ ,  $p_{ref}$  is the reference pressure (at the center of the flux tube) and  $\mu_0$  is the permeability in vacuum. Finally, the last two terms take into account the effect of particle trapping in the low magnetic field side of the tokamak and include the Jacobian  $J = J^{xyz} = [(\nabla x \times \nabla y) \cdot \nabla z]^{-1}$ . Integrating over velocity the perturbed distribution  $f_1$ , solution to Eq. (5.9), provides the perturbed ion density, which can be inserted in the quasineutrality condition with adiabatic electrons, thus leading to the following equation

$$Z^2\tau[1 - \Gamma_0(b)]\Phi_1 = \pi ZB \int J_0(\lambda) f_1 dv_{\parallel} d\mu - (\Phi_1 - \langle \Phi_1 \rangle), \quad (5.10)$$

which can then be solved numerically, to get the self consistent electrostatic potential. Note that in Eq. (5.10), one defines  $\tau = T_e/T_i$ ,  $b = [1/(Z_i^2\tau B^2)]k_{\perp}^2$ ,  $k_{\perp}^2 = g^{xx}k_x^2 + g^{yy}k_y^2 + g^{xy}k_xk_y$  and  $\Gamma_0(b) = \exp(-b)I_0(b)$  is the scaled modified Bessel function. The term  $\langle \Phi_1 \rangle$  represents the flux surface averaged value of  $\Phi_1$ . Note that in a flux-tube simulations, the  $x$ -dependence of all equilibrium quantities across the simulation domain is neglected. Thus, all coefficients relative to the magnetic equilibrium ( $B(z), J(z), K_x(z), K_y(z), g^{ij}(z)$ ) as well as equilibrium profiles and their gradients ( $1/L_n, 1/L_T$ ) are independent of  $x$  and represent values at the flux tube center defined by  $x = x_0$ .

**Geometry:** The GENE code is capable to interface with the general geometry MHD equilibrium obtained from the numerical solution of the Grad-Shafranov equation. It can, in addition, also be run using an *ad hoc* analytical model which is an approximate solution of the Grad-Shafranov equation in the limit of axisymmetric, circular, concentric flux surfaces. In the present investigation we use this *ad hoc* equilibrium, which is defined in the  $(r, \theta, \phi)$  (radial, poloidal and toroidal) coordinate system, related to the cylindrical coordinate system  $(R, z, \phi)$  by the relations  $R = R_0 + r \cos\theta = R_0(1 + \epsilon \cos\theta)$  and  $Z = r \sin\theta$  with  $R_0$  being the major radius of the toroidal coordinate system and  $\epsilon = r/R_0$  being the inverse aspect ratio. The axisymmetric magnetic field can in any case be written as  $B = \nabla\phi \times \nabla\psi + RB_{\phi}\nabla\phi$ , where in the *ad hoc* model  $B_{\phi} = R_0B_0/R$ ,  $\Psi = \Psi(r)$  and  $d\Psi/dr = rB_0/\bar{q}$ . The

## Chapter 5: Short wavelength ion temperature gradient mode and coupling with trapped electrons

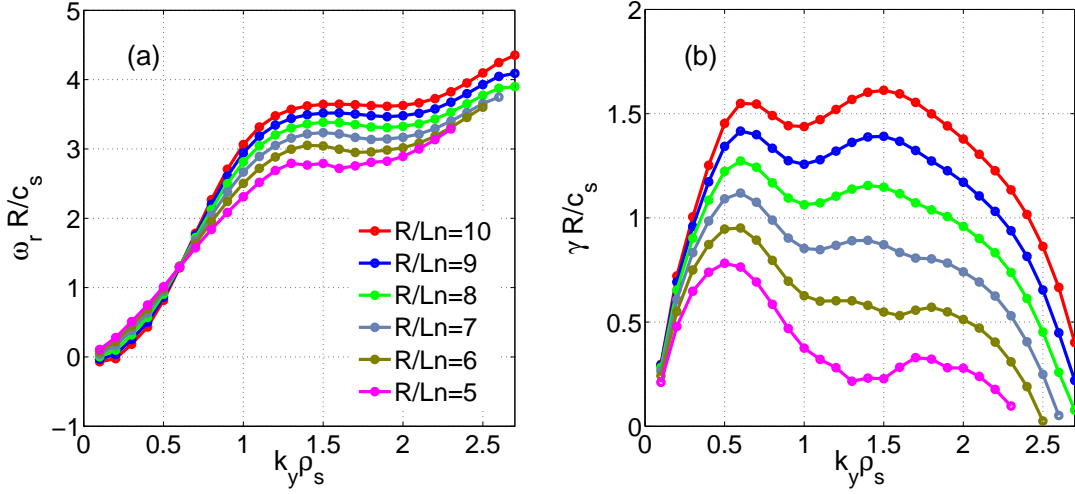


Figure 5.17: (a) Real frequency  $\omega_r$ , and (b) growth rate  $\gamma$  versus wave number  $k_y \rho_s$  of the linear short wavelength ion temperature gradient mode (SWITG) for different values of  $R/L_n$ . Here  $\eta_i = 2.5$ ,  $q = 2.0$ ,  $\hat{s} = 1.0$ ,  $\tau = 1.0$  in these simulations.

function  $\bar{q}(r)$  is related to the true safety factor  $q$  by the relation

$$q(r) = \frac{1}{2\pi} \int_0^{2\pi} \frac{B \cdot \nabla \phi}{B \cdot \nabla \theta} d\theta = \frac{\bar{q}(r)}{\sqrt{1 - \epsilon^2}}.$$

More details related to this *ad hoc* model are found in Ref [65].

**Physical Parameters:** Our main focus is to study the nonlinear short wavelength ion temperature gradient mode using the flux tube version of GENE. Note that a detailed parametric study of the linear SWITG mode has been carried out in Ref. [66] considering  $\rho^* = \rho_s/a = 0.017$ , inverse aspect ratio  $a/R_0 = 0.25$  where steepest gradients are at  $s = r/a = 0.6$ . Inspired by that linear study we have chosen flux tube aspect ratio  $r_0/R_0 = 0.15$  in the present nonlinear flux tube simulations where  $\rho^* \rightarrow 0$ . Also in the present simulation we have considered  $\tau = T_e/T_i = 1$ ,  $q = 2.0$ ,  $\hat{s} = 1.0$  and  $\eta_i = L_n/L_{T_i} = 2.5$  where  $L_n$  and  $L_{T_i}$  are, respectively, the density and temperature gradient scale lengths. Also, the parameters considered here are relevant to small size tokamaks and hence atypical for ITER grade machines.

## Chapter 5: Short wavelength ion temperature gradient mode and coupling with trapped electrons

Numerical parameters: The simulation is carried out in a box of size  $L_x \times L_y =$

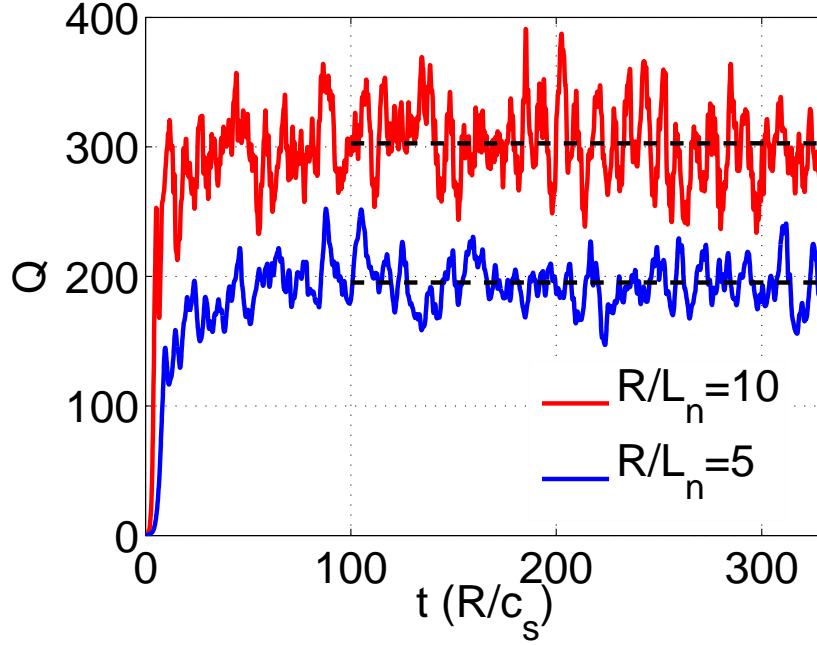


Figure 5.18: Time (in units of  $R/c_s$ ) evolution of ion heat flux  $Q$  normalized by  $Q_{norm} = p_{ref} c_s \rho_s^2 / R^2$  for SWITG simulation, with  $R/L_n = 5$  and  $R/L_n = 10$ . The black dashed lines represent the time average of the heat flux between  $t = 100 R/c_s$  and  $t = 330 R/c_s$ . For  $R/L_n = 5$  the average  $Q = 195 Q_{norm}$  and for  $R/L_n = 10$  the average  $Q = 302 Q_{norm}$ .

$133.3\rho_s \times 209.4\rho_s$  in the perpendicular direction. One connection length of  $2\pi Rq$  is considered in the parallel direction. This 3-dimensional spatial domain is resolved by using  $200 \times 120 \times 16$  grid points, respectively, in the  $x$ ,  $y$ , and  $z$  directions. The velocity space, on the other hand, is resolved with  $32 \times 16$  grid points, respectively, for  $v_{\parallel}$  and  $\mu$  with the limit for  $v_{\parallel}$  from  $-3$  to  $+3$ , and  $0$  to  $9$  for  $\mu$  in normalized units (see Table 5.3). Also, throughout the paper we have chosen  $L_{ref} = R$ , the major radius.

### 5.3.2 Results

In this section we will delineate our results for linear and nonlinear runs for the physical and numerical parameters introduced above using the flux tube version of

## Chapter 5: Short wavelength ion temperature gradient mode and coupling with trapped electrons

GENE. Note that since higher resolution runs are computationally very expensive, the nonlinear results presented in this section are somewhat preliminary.

### Linear spectrum

We start with a linear simulation with parameters considered above. Figure 5.17(a) shows the real frequency versus  $k_y \rho_s$  for different values of  $R/L_n$  ranging from 5 to 10. The real frequency rises monotonically with  $k_y \rho_s$  for  $k_y \rho_s \leq 1$  and remains virtually constant at higher  $k_y \rho_s$ . It is clear from the expression of the dispersion relation, Eq. (5.6), that the mode frequency  $\omega$  behaves as  $\omega_{ni} I_0(k_{\perp}^2 \rho_s^2) \exp(-k_{\perp}^2 \rho_s^2)$  which for small  $k_{\perp}^2 \rho_s^2$  scales as  $k_{\perp} \rho_s$  and for larger  $k_{\perp}^2 \rho_s^2$  scales almost as a constant as  $I_0(k_{\perp}^2 \rho_s^2) \exp(-k_{\perp}^2 \rho_s^2) \rightarrow 1/\sqrt{2\pi(k_{\perp}^2 \rho_s^2)} = 1/(\sqrt{2\pi} k_{\perp} \rho_s)$  for  $k_{\perp} \rho_s \gg 1$  (recall that  $\omega_{ni} \sim k_{\perp} \rho_s$ ). Figure 5.17(b) displays the growth rate for the same scan. It exhibits two peaks for all considered values of  $R/L_n$  in contrast to the single peak around  $k_y \rho_s \simeq 0.5$  routinely observed in the linear analysis of the standard ITG modes. The second peak appears around  $k_y \rho_s \simeq 1.5$  and is characteristic of the SWITG mode. Regarding the growth rate in toroidal geometry, it is the toroidal magnetic drift term  $\omega_{di}$  of the ions, resonating with the mode frequency  $\omega$ , which gives rise to the double hump behavior. It is to be noted that  $\omega_{di} \sim (L_n/R)\omega_{ni}$  and thus scales as  $k_{\perp} \rho_s$ . Therefore, both  $\omega$  and  $\omega_{di}$ , at first increase for small  $k_{\perp} \rho_s$  and then  $\omega$  saturates while  $\omega_{di}$  still grows as  $k_{\perp} \rho_s$  increases. It is important to note that the SWITG mode is also subject to finite Larmor radius effects. The finite Larmor radius stabilization (FLR) of the SWITG mode can be inferred from the nonadiabatic part of the ion density response. At very high  $k_{\perp} \rho_s$ ,  $|\omega_{di}| \gg |\omega|$  and the nonadiabatic part of the perturbed ion density can be reduced to

$$\tilde{n}_i^{na} = \frac{q_i}{T_i} \tilde{\phi} \frac{\omega_{ni}(\eta_i/2 - 1)}{\omega_{di}} I_0(k_{\perp}^2 \rho_s^2) \exp(-k_{\perp}^2 \rho_s^2),$$

which for large  $k_{\perp} \rho_s$  will decrease according to

$$\frac{\omega_{ni}}{\omega_{di}} I_0(k_{\perp}^2 \rho_s^2) \exp(-k_{\perp}^2 \rho_s^2) \sim \frac{R}{L_n} I_0(k_{\perp}^2 \rho_s^2) \exp(-k_{\perp}^2 \rho_s^2) \sim \frac{R}{L_n} \frac{1}{\sqrt{2\pi} k_{\perp} \rho_s},$$

as  $k_{\perp}^2 \rho_s^2$  increases. It is apparent that the second hump is equally strong as the first hump for higher value of  $R/L_n$  or even slightly more dominant for  $R/L_n \geq 10$ . It

## Chapter 5: Short wavelength ion temperature gradient mode and coupling with trapped electrons

also is present for lower values of  $R/L_n$  albeit less pronounced and finally vanishes at values of  $R/L_n$  typical of the standard ITG mode ( $R/L_n < 5$ ).

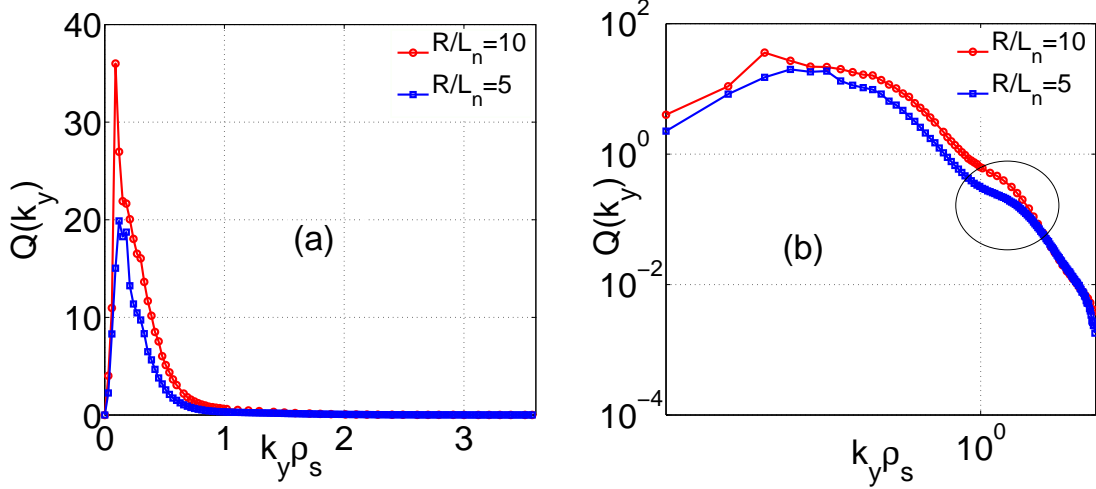


Figure 5.19: (a) Time averaged ion heat flux versus normalized wavenumber  $k_y$  for  $R/L_n = 5$  and  $R/L_n = 10$  in lin-lin plot. (b) Time averaged ion heat flux as a function of normalized wavenumber  $k_y$  for  $R/L_n = 5$  and  $R/L_n = 10$  in log-log plot.  $Q$  is normalized with respect to  $Q_{norm} = p_{ref} c_s \rho_s^2 / R^2$ .

### Nonlinear Spectra

Till date, there have been very few nonlinear studies of the SWITG mode. The study of the SWITG mode turbulence and its contribution to the net thermal ion heat transport is thus of prime interest. Here we try to address this issue. We have adopted two cases in the present nonlinear study: case (I)  $R/L_n = 10$ , where the peak in the linear growth rate corresponding to the SWITG (at  $k_y \rho_s \sim 1.5$ ) mode is as pronounced as that at lower  $k_y$  ( $k_y \rho_s \sim 0.45$ ) corresponding to the standard ITG mode, case (II)  $R/L_n = 5$ , where the linear growth rate of SWITG at  $k_y \rho_s > 1$  is much weaker than that of the standard ITG mode at  $k_y \rho_s < 1$ . The time evolution of the nonlinear ion heat flux given by the relation  $Q = \left\langle \int (1/2) m v^2 v_E \cdot \nabla x f_1 d^3 v \right\rangle$ , normalized with respect to  $Q_{norm} = p_{ref} c_s \rho_s^2 / R^2$ , where  $p_{ref}$  is the equilibrium pressure, is shown in Fig. 5.18 for the parameters described in the previous section for the two cases of the parameter

## Chapter 5: Short wavelength ion temperature gradient mode and coupling with trapped electrons

$R/L_n$ . Note that  $\langle A \rangle_z = \int J^{xyz}(z)A(z)dz / \int J^{xyz}(z)dz$  is the definition of flux-averaged quantity  $A$ , where  $J^{xyz}$  is the Jacobian relative to the coordinate system  $(x, y, z)$ . Also,  $v$  and  $v_E$ , respectively, are particle velocity and radial component of the gyroaveraged  $E \times B$  drift velocity, and  $f_1$  is the perturbed distribution function. It is clear that the heat flux in the case of  $R/L_n = 10$  is higher than that in the case of  $R/L_n = 5$ . This is in conformity with the linear results where the SWITG mode with  $R/L_n = 10$  exhibits the highest growth rate compared to  $R/L_n = 5$  at both scales i.e.,  $k_y \rho_s < 1$  and  $k_y \rho_s > 1$  corresponding, respectively, to the standard ITG and SWITG mode. The ratio of growth rates for  $R/L_n = 5$  compared to  $R/L_n = 10$  is even weaker for the SWITG scales than for the ITG scales. The time averaged heat flux between  $t = 100 R/c_s$  and  $t = 330 R/c_s$  is estimated at  $302 Q_{norm}$  and  $195 Q_{norm}$ , respectively, for the nonlinear simulations with  $R/L_n = 10$  and  $R/L_n = 5$ . Figure 5.19(a) depicts the time averaged (from  $t = 0$  to  $t = 330 R/c_s$ ) spectrum  $Q(k_y)$  of the heat flux for the  $R/L_n = 10$  case, normalized with respect to  $Q_{norm}$ , over the entire  $k_y \rho_s$  spectrum considered in the simulation. For the purpose of comparison, we also plot in the same figure the time averaged (from  $t = 0$  to  $t = 330 R/c_s$ ) spectrum of the heat flux  $Q(k_y)$  measured from the simulation with  $R/L_n = 5$ . The corresponding log-log plots for both simulations are shown in Fig. 5.19(b). It is quite clear that the  $Q(k_y)$  spectrum exhibits a strong peak around  $k_y \rho_s \simeq 0.3$  for both values of  $R/L_n$ . However, the peak corresponding to  $R/L_n = 5$  is significantly lower than the one corresponding to  $R/L_n = 10$ , in conformity with the observed heat flux displayed in Fig. 5.18. The figure also implies that, on the higher side of the  $k_y$  spectrum corresponding to the SWITG mode, the contribution to the net ion heat flux is very low compared to the contribution from the standard ITG mode on the lower side of the  $k_y$  spectrum. The characteristic of the SWITG mode, though weak, is nevertheless still visible from Fig. 5.19(b), which is the corresponding log-log plot of Fig. 5.19(a). The hump corresponding to the SWITG mode (encircled in Fig. 5.19(b)) centers around  $k_y \rho_s = 1.5$ , reflecting that there is another source of instability in this region of the spectrum. For completeness, it is important to comment here that the mixing length estimate of transport from the linear growth rate and wavenumber is expected to be much higher than that measured from the nonlinear simulation. In this context, the reader may be referred to Ref. [66].

It is evident from Fig. 5.17 that the SWITG mode has growth rate comparable to

Chapter 5: Short wavelength ion temperature gradient mode and coupling with trapped electrons

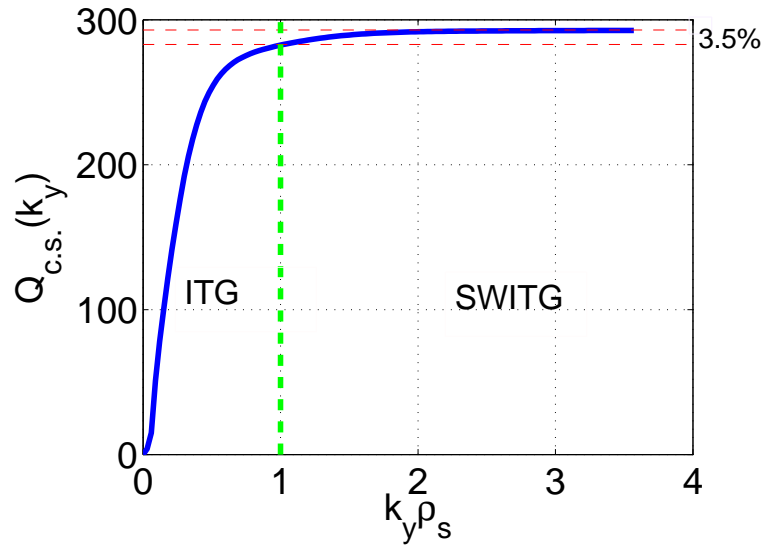


Figure 5.20: Cumulative sum of heat flux for  $R/L_n = 10$ . The standard ITG contribution to the heat flux is for  $k_y \rho_s \leq 1$  and SWITG contribution to the heat flux is for  $k_y \rho_s \geq 1$ .  $Q_{c.s.}$  is normalized with respect to  $Q_{norm} = p_{ref} c_s \rho_s^2 / R^2$ .

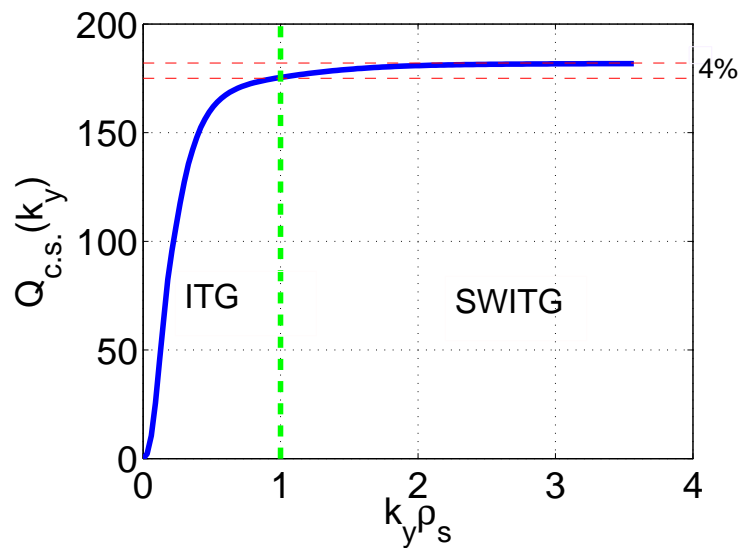


Figure 5.21: Cumulative sum of heat flux for  $R/L_n = 5$ . The standard ITG contribution to the heat flux is for  $k_y \rho_s \leq 1$  and SWITG contribution to the heat flux is for  $k_y \rho_s \geq 1$ .  $Q_{c.s.}$  is normalized with respect to  $Q_{norm} = p_{ref} c_s \rho_s^2 / R^2$ .

## Chapter 5: Short wavelength ion temperature gradient mode and coupling with trapped electrons

the standard ITG mode for  $R/L_n = 10$  in the linear regime. On the other hand, for  $R/L_n = 5$  both humps become weaker, with the second hump corresponding to the SWITG mode being even weaker than the first hump corresponding to the standard ITG mode. Therefore, it is interesting to nonetheless estimate from the nonlinear simulation results the (small) contribution of the SWITG part of the  $k_y$  spectrum to the net thermal ion transport. To estimate the relative contribution of the SWITG mode to the thermal ion heat flux compared to the standard ITG mode, we have calculated the cumulative sum of the time averaged (from  $t = 0$  to  $t = 330 R/c_s$ ) heat flux  $Q(k_y)$  given by

$$Q_{c.s.}(k_{y1}) = \sum_{k_y=k_{ymin}}^{k_{y1}} Q(k_y).$$

It has been plotted versus  $k_y\rho_s$  for the two cases  $R/L_n = 10$  and  $R/L_n = 5$  in Figs. 5.20 and 5.21, respectively. It is apparent from the figures that  $Q_{c.s.}$  increases rapidly for  $k_y\rho_s \leq 1$  and then tends to saturate for  $k_y\rho_s \geq 1$  in both cases. The cumulative heat flux in the case of  $R/L_n = 10$  appears to be higher than the case of  $R/L_n = 5$ . It is obvious from Figs. 5.18 and 5.19(a) that heat flux in the case of  $R/L_n = 10$  is much higher than that of  $R/L_n = 5$  leading to higher value of  $Q_{c.s.}$ . To evaluate the relative contribution to the net ion heat transport, of the higher  $k_y$  tail,  $k_y\rho_s \geq 1$ , corresponding to the SWITG mode compared to the lower  $k_y$  part,  $k_y\rho_s \leq 1$ , relevant to the standard ITG, one may compute

$$\frac{Q_{c.s.}(k_y\rho_s)_{max} - Q_{c.s.}(k_y\rho_s = 1)}{Q_{c.s.}(k_y\rho_s = 1)},$$

where  $(k_y\rho_s)_{max}$  is the maximum wavenumber. One thus obtains that the net contribution of the SWITG part of the  $k_y$  spectrum to the total ion heat flux is less than 4% in both cases in spite of the fact that linearly the SWITG mode with  $R/L_n = 10$  has growth rate more than double that with  $R/L_n = 5$  and comparable to the ITG growth rate. Thus, even in the strongest case of linear SWITG, for example,  $R/L_n = 10$  in the present case, the thermal ion heat flux is predominantly determined by the lower  $k_y$  components of the fluctuation relevant to the standard ITG mode.

Snapshots of the electrostatic potential  $\Phi_1(x, y)$  and  $n_1(x, y)$  measured at

Chapter 5: Short wavelength ion temperature gradient mode and coupling with trapped electrons

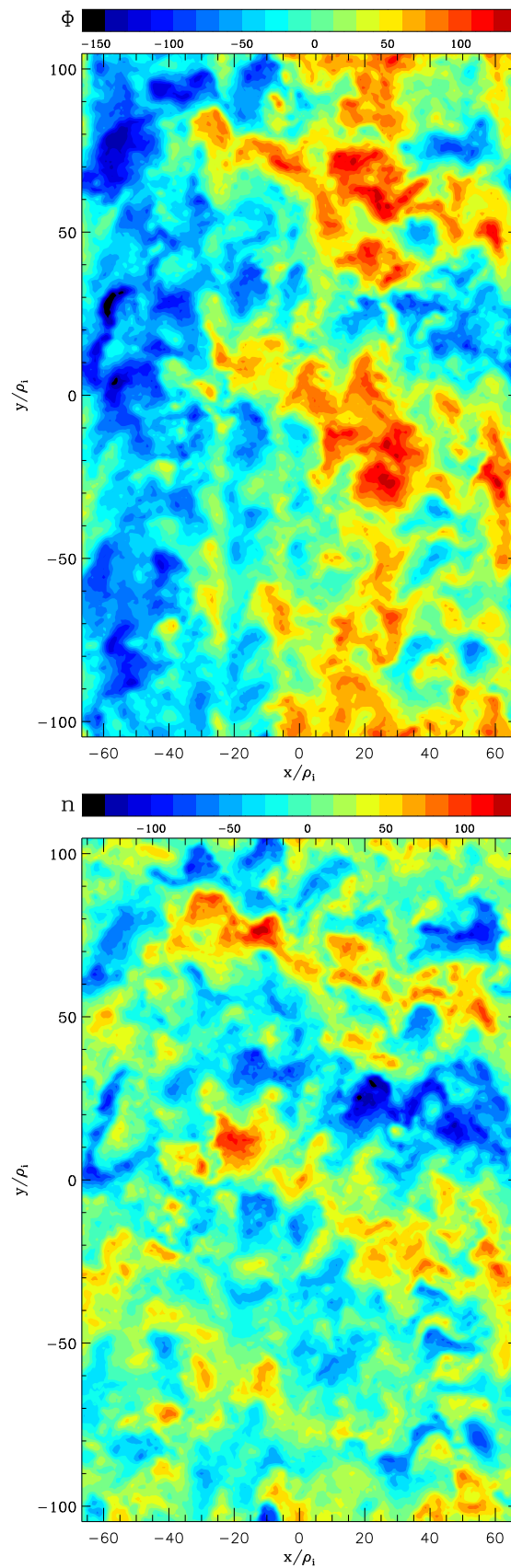


Figure 5.22: Snapshots of the potential (top) and perturbed density (bottom) of the SWITG mode for  $R/L_n = 5$  taken at  $t = 330 R/c_s$ .

Chapter 5: Short wavelength ion temperature gradient mode and coupling with trapped electrons

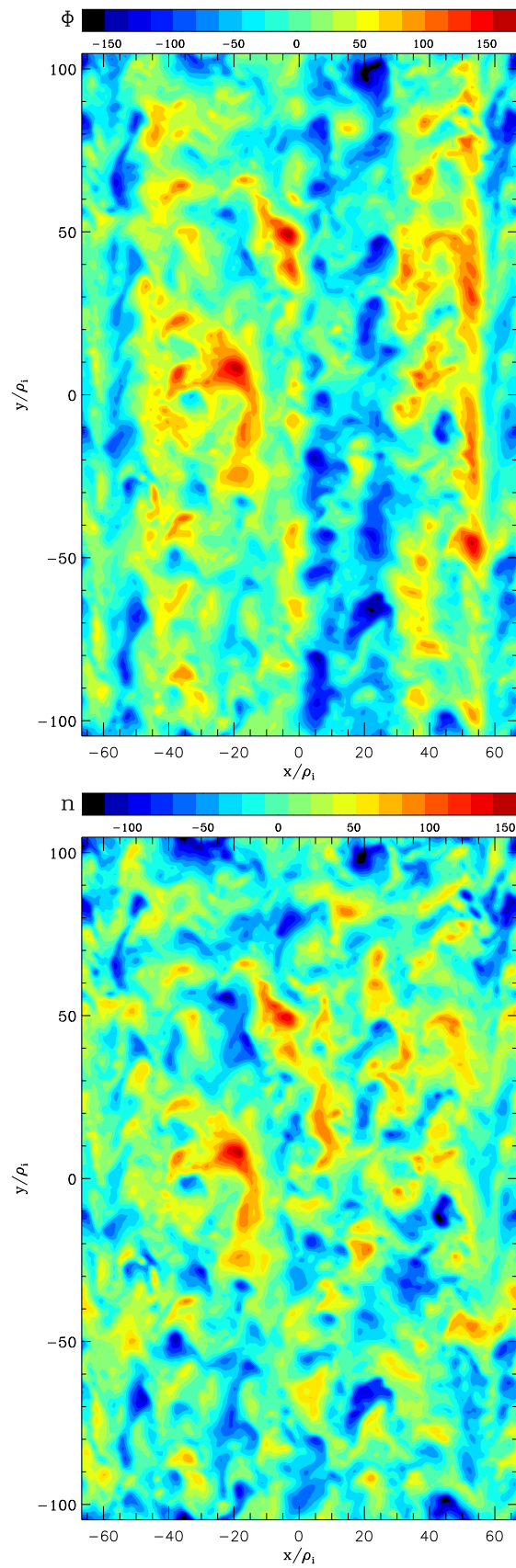


Figure 5.23: Snapshots of the potential (top) and perturbed density (bottom) of the SWITG mode for  $R/L_n = 10$  taken at  $t = 330 R/c_s$ .

## Chapter 5: Short wavelength ion temperature gradient mode and coupling with trapped electrons

$t = 330 R/c_s$  on the low field side ( $z = 0$ ) of the tokamak during the nonlinear simulations with  $R/L_n = 5$  and  $R/L_n = 10$  are displayed in Figs. 5.22 and 5.23, respectively. It is clear from the figures that in the case of  $R/L_n = 5$ , where SWITG is weak in the linear spectrum, the quantities  $\Phi_1(x, y)$  and  $n_1(x, y)$  exhibit elongated structures along the  $x$  direction. The same quantities, in contrast, exhibit fine structures in the case of the nonlinear simulation with  $R/L_n = 10$ , which has the highest growth rate in the linear phase. Given the elongated radial structures observed for  $R/L_n = 5$ , which appear to be essentially broken up for  $R/L_n = 10$ , one is motivated to investigate the zonal flow [113, 114] shearing rate in both cases. For that purpose we have measured the zonal flow shearing rate in both simulations  $R/L_n = 5$  and  $R/L_n = 10$ , respectively. The time evolution of the shearing rate is presented in Fig. 8 for the two nonlinear simulations. The time average of the shearing rate  $\omega_E = dv_{Ey}/dx$  is estimated  $2.4 c_s/R$  for  $R/L_n = 5$  and  $4.36 c_s/R$  for  $R/L_n = 10$ , respectively. This means that the zonal flow shearing rate for the SWITG mode with  $R/L_n = 10$  is almost double that with  $R/L_n = 5$ . That is why the SWITG mode with  $R/L_n = 10$  exhibits fine structures, while that with  $R/L_n = 5$  bears elongated structures in all perturbed quantities. In both cases, the shearing rate is much higher than the linear growth rate implying that zonal flows are the dominant saturation mechanism for the SWITG mode turbulence. The higher shearing rate of zonal flows in the case of nonlinear SWITG mode with  $R/L_n = 10$  could be a reason for very low contribution of the higher  $k_y \rho_s$  part of the spectrum corresponding to the SWITG mode to the total thermal ion heat flux, in spite of being the mode with highest growth rate linearly. This contribution is almost comparable to the contribution of the higher  $k_y \rho_s$  part of the spectrum in the case of the nonlinear SWITG mode with  $R/L_n = 5$ , which has the weakest growth rate among all values of  $R/L_n$  considered in the linear simulation.

### 5.4 Conclusion

In the first part of the present work, we have presented the features of the short wavelength ion temperature gradient (SWITG) mode in the presence of trapped electrons using a linear, global, gyrokinetic model in the toroidal geometry, that

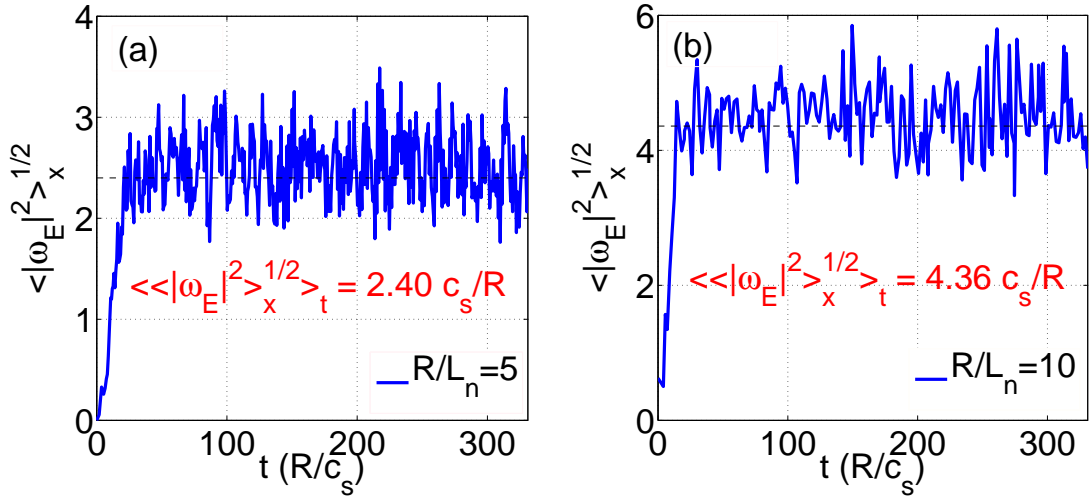


Figure 5.24: Time traces of the zonal flow shearing rate  $\omega_E = dv_{E,y}/dx$ , in units of  $c_s/R$  for the SWITG modes with (a)  $R/L_n = 5$  and (b)  $R/L_n = 10$ .

treats both species, namely, ions and electrons fully gyro-kinetically, taking into account all the kinetic effects. A comparison of parametric dependencies for the two cases of SWITG mode with and without the trapped electrons is presented. In line with the global model, we also compare the results from a local gyro-kinetic model for the two cases, with and without the trapped electrons. This is for the first time where the SWITG mode is studied (1) in the presence of trapped electrons and (2) in the frame of a global gyrokinetic model. The major findings of the present work are the following.

- The trapped electrons have strong effect on the SWITG modes, raising the growth rate substantially. This is in contrast to the earlier conjecture that the trapped electrons may not be important for the SWITG mode.
- Although defined as short wavelength ITG, the two dimensional mode structure of the SWITG mode has been found to be quite global occupying a considerable fraction of the tokamak cross-section for the chosen set of parameters. This establishes the necessity of a global model to study such a phenomenon.
- The most important observation is that, in the presence of trapped elec-

## Chapter 5: Short wavelength ion temperature gradient mode and coupling with trapped electrons

trons, the  $L_n/R$  window for the existence of the SWITG mode gets widened. The toroidicity has strong stabilizing effect on the SWITG mode in the absence of trapped electrons. Inclusion of the trapped electrons, however, has been found to make the mode stronger against the stabilizing effect of the toroidicity. Thus, the inference from this result is that the mode acquires toroidal-like nature in the presence of trapped electrons in contrast to the slab-like nature in the absence of trapped electrons. The increased fraction of the trapped electrons with increased toroidicity is the main factor behind this flipping of the mode from slab nature to toroidal nature. The increased trapped fraction of the electrons with toroidicity reduces the adiabatic response of the electrons, which in turn enhances the formation of the space charge leading to a higher growth rate of the mode and hence the mode can withstand the effect of increased toroidicity.

- The SWITG mode is an ion temperature gradient driven mode in the higher  $k_{\perp}\rho_{Li}$  regime exhibiting a threshold in  $\eta_i$ . The mode persists even if the electrons are considered adiabatic. In the absence of trapped electrons the mode vanishes below a critical  $\eta_i$ . But, in the presence of trapped electrons, with the decreasing value of  $\eta_i$ , the mode does not vanish, rather it transforms itself from the dominantly ion mode to the dominantly trapped electron mode.
- The growth rate increases for lower values of  $\tau$  but starts saturating at higher values of it. In the presence of trapped electrons, the growth rate increases initially, but at higher values of  $\tau$ , where the electrons become hotter than the ions the growth rate falls and then saturates with the mode frequency tending to move toward the electron diamagnetic direction.
- An estimation of the ion transport based on the mixing length theory is carried out. The trapped electrons rise the heat diffusivity significantly. It is found that the ion heat diffusivity peaks at lower  $k_{\perp}\rho_{Li}$ . No significant diffusivity is observed at higher  $k_{\theta}\rho_{Li}$  where the SWITG mode is strongest for both cases with and without the trapped electrons.

In the second part of the present work, the short wavelength ion temperature gradient mode has been studied linearly and nonlinearly using the flux tube version

## Chapter 5: Short wavelength ion temperature gradient mode and coupling with trapped electrons

of the massively parallel, gyrokinetic code GENE using only the adiabatic electrons. The trapped electrons are ignored for the sake of ease in computations as our sole focus is to study the nonlinear behaviour of the mode.

Linearly the mode appears to be as dominant as the standard ITG mode for high  $R/L_n \sim 10$ . However, the growth rate decreases with decreasing  $R/L_n$ , and below  $R/L_n = 5$  the SWITG mode vanishes, i.e., only the standard ITG mode remains unstable. Nonlinear simulations show higher heat flux for higher value of  $R/L_n$  in conformity with the trend in the linear growth rate with respect to  $R/L_n$ . The nonlinear heat flux spectrum is peaked at lower  $k_y \rho_s \simeq 0.3$ . The estimate of relative contribution of the higher  $k_y \rho_s$  part of heat flux spectrum corresponding to the SWITG mode reveals that the contribution of the SWITG mode to the total heat flux is very low (less than 4%) compared to the contribution from the lower  $k_y$  part of the spectrum typically belonging to the standard ITG mode. The zonal flow shearing rate has been found to be much higher than the linear mode frequency and growth rate of the SWITG mode suggesting that the zonal flows are the main saturation mechanisms of the SWITG turbulence. Also, the zonal flow shearing rate is found to be higher for the SWITG modes with higher  $R/L_n$  which also exhibit higher growth rate linearly compared to the shearing rate for those with lower  $R/L_n$  and lower growth rate linearly. The higher shearing rate appears to compensate for the higher growth rate of the mode leading to a minimal contribution to the thermal ion heat flux from the higher  $k_y \rho_s$  part of the spectrum relevant to the SWITG mode, irrespective of the density scale length which determines the strength of the SWITG mode with respect to the standard ITG linearly.

# Chapter 6

## Interaction of microturbulence with energetic ions

### 6.1 Introduction

Thus far, we have studied the various linear properties of the temperature and density gradient driven modes in the category of microinstabilities using the global, linear, gyrokinetic code EM-GLOGYSTO. In addition, the short wavelength ion temperature gradient driven mode is studied nonlinearly using the flux tube version of the nonlinear, gyrokinetic, electromagnetic code GENE. It is now well understood that these instabilities are the cause of anomalous transport of thermal ions and electrons.

Recently, some experiments show that these microinstabilities transport not only the thermal ions and electrons out of the system but also the energetic ions produced by the auxiliary heating schemes and  $\alpha$  particles of energy in the MeV range produced as fusion product. These energetic particles constitute a considerable fraction of the total plasma, and thus a sound understanding of the impact of these energetic ions on the plasma confinement through the interaction with the background instabilities is very much required. The various magnetohydrodynamics (MHD) events are observed to transport and redistribute the energetic ion population via resonant and nonresonant phenomena [115, 116]. For example, resonant MHD activities such as fishbone, toroidal Alfvén mode (TAE), etc., can cause large transport of the energetic ions. Similarly, high  $\beta$  sawteeth can also pro-

## Chapter 6: Interaction of microturbulence with energetic ions

duce loss of the energetic ions. The low frequency MHD modes such as neoclassical tearing modes (NTM) are equally capable to drive both passing and trapped energetic ion loss [117, 118]. The toroidal field ripples and stochastic magnetic field are also among the other mechanism of fast ion losses. The energetic ions can in turn also alter the stability of the plasma by exciting and sometimes suppressing the MHD events. One may, for example, note the observed stabilization of sawteeth by perpendicular energetic ion population, the destabilization of internal kink mode, TAE, fishbone, etc. The energetic ions also can give rise to modes on their own which are generally named as energetic particle modes (EPM) [119].

Though much understanding and confidence have been gained in the case of the interplay between the MHD events and energetic ions via theory and experiments, little attention is paid toward the interaction of these energetic ions with microturbulence induced by the ITG mode, TEM, ETG mode, etc. One partial reason could perhaps be the observation of very weak diffusivities of the energetic ions and  $\alpha$  particles in comparison with the thermal ions experimentally [115, 116, 120] as well as theoretically [121]. The reason for it, as speculated, is that the energetic ions do not stay in resonance with these microturbulence driven fluctuations as their drift orbit radii are far higher than the radial correlation length of these fluctuations, and therefore average over the fluctuation spectrum temporally and spatially. These phenomena are generally defined as the drift averaging and gyro-radius averaging [115]. On the contrary, recent numerical experiments [122] have shown that  $\alpha$  particle and energy loss could be higher than the corresponding losses of thermal ions and large orbit averaging is not strong enough to ignore the interaction of the  $\alpha$  particles with ITG turbulence. However, it is a recent experiment [123] reporting evidence of correlation between microturbulence and redistribution of energetic ions that has spurred a fresh interest among the researchers in the subject. Even in the absence of any MHD activity, fast radial broadening of the current profile driven by the off axis neutral beam injection (NBI) has been observed supporting the fact that there must indeed be some correlation between redistribution of energetic ions and background microturbulence. This has been further studied in Refs. [124, 125]. Following this, numerical analysis [126] on the interaction of energetic ions with ITG turbulence observes  $1/E$  dependence for the passing energetic ion diffusion, where,  $E$  is the energy of the energetic ions and  $1/E^2$  dependence for the trapped energetic ion diffusion. Similar study [127]

## Chapter 6: Interaction of microturbulence with energetic ions

found  $1/E$  dependence of diffusion for the beam energetic ions in the presence of electrostatic fluctuation. In contrast, the diffusion of the energetic ions in the presence of magnetic fluctuations [127] has been found to be independent of the particle energy, and therefore, may play more important role than the electrostatic fluctuations in redistributing the energetic ions. The reciprocal dependence of diffusivity on the particle energy of the energetic ions could be one of the reasons for the superficial effect of microturbulence on the energetic ions observed in the earlier experiments. The difference in the born energy of the energetic ions between the earlier and recent experiments can be a likely explanation of the difference in the observations regarding the effect of microturbulence on these energetic ions. Note that such phenomena of redistribution of hot ions by microturbulence is not confined to only toroidal devices like tokamaks; experiments on linear system also confirm the interaction of hot ions with density gradient driven turbulence [172]. Astrophysical plasmas also encounter similar phenomena resulting from interaction of the energetic ions with turbulent field [129].

Coming back to the back reaction of energetic ions on microturbulence, one may cite latest experiments [130] that has reported signature of internal transport barrier (ITB) in the ion channel even in the absence of reverse shear. The formation of the ITB has been observed to have correlation with the transport suppression mechanism by the injected energetic ions with a lifetime of the order of slowing down time of the beam ions. Similar observation of the ITG mode suppression by the energetic ions produced by ion cyclotron resonance heating (ICRH) and concurrent formation of the ITB triggered by these energetic ions in a plasma with monotonic safety factor profile has been reported in Ref. [131].

Following the recent theoretical, numerical and experimental studies regarding the prospective interaction of the energetic ions with the background microturbulence, we, in the present chapter, present the results from (1) a linear study on the effect of the energetic ions on the stability properties of the ITG mode using the linear numerical code EM-GLOGYSTO (2) a nonlinear passive tracer study on the effect of the ion temperature gradient (ITG) mode microturbulence on energetic ions using the nonlinear global gyrokinetic code Gyrokinetic Tokamak Simulation (GTS) [139, 140] based on particle in cell simulation, and (3) a nonlinear passive tracer study on the effect of the trapped electron mode (TEM) microturbulence on energetic ions using the nonlinear global gyrokinetic code Gyrokinetic Tokamak

Simulation (GTS).

The results are discussed in tandem in the following sections.

## 6.2 Effect of energetic ions on the stability of temperature gradient driven mode of thermal ions.

We incorporate the energetic ions in the model of EM-GLOGYSTO nonperturbatively as an active component that would modify the quasineutrality condition. It is to be noted that, in the past, the effect of the fast particle pressure on the MHD modes, for example, TAEs and its family of modes, kinetic ballooning mode or Alfvén ion temperature gradient mode, has been investigated extensively using perturbative methods by considering the fast particle effects as corrections to the underlying “equilibrium” in the limit  $\beta_f/\beta_p \ll 1$ . Nonperturbative treatments [119] wherein bulk electrons, ions and fast particles, all are treated on the same physics footing have been very few. In all these studies, an unstable MHD equilibrium with  $E_{\parallel} = 0$  is assumed. Either perturbative ( $\beta_f/\beta_p \ll 1$ ) or nonperturbative ordering ( $\beta_f \simeq \beta_p \epsilon$ ,  $\epsilon = a/R$ ) is invoked; the fast particle distribution function is calculated drift-kinetically and finally the instability problem is solved using standard  $\delta W$  method distinguishing the “fluid” part and “kinetic part”. Closure is obtained by taking moments of the fast particle distribution function and using Maxwell’s equations. In such formulations, the bulk electrons/ions constituting the MHD equilibrium naturally do not contribute to any kinetic effects such as Landau damping, transit/trapped particle effects orbit width effects or finite Larmor radius (FLR) corrections.

With respect to these earlier studies, the present work treats electrons, ions and fast particles on equal footing; all the three “species” are fully “gyrokinetic”, fully “nonadiabatic”, thus including the above said effects automatically. The formulation retains all the kinetic effects, namely, the Landau resonance, transit resonance, magnetic drift resonance and finite Larmor radius effect to all orders. However, we do not include the effect of the trapped particles and magnetic perturbation. Thus the treatment is purely electrostatic in the present study. The energetic particles enter the quasineutrality equation as a third species in the plasma, but with higher energy. To be noted that we consider three different  $\eta = L_n/L_T$  ( $L_n$  and  $L_T$  are

## Chapter 6: Interaction of microturbulence with energetic ions

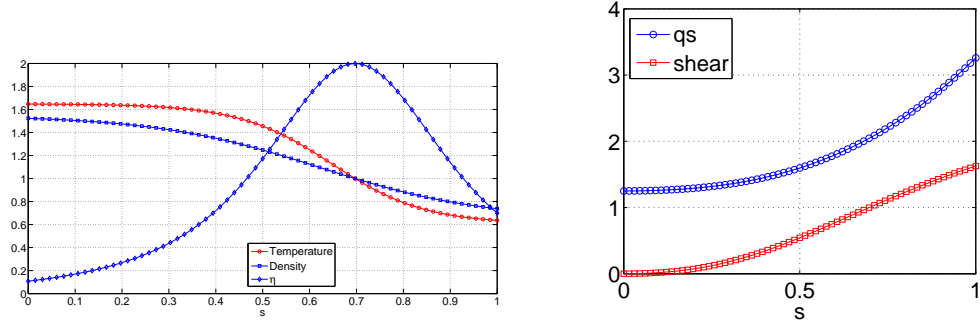


Figure 6.1: Left panel: the equilibrium density and temperature profiles along with the  $\eta$  profile of the thermal ions and electrons. Right panel: the safety factor profile and shear profile. The  $\eta$  profile peaks at  $s_0 = 0.7$  with the magnitude  $\eta = 2.0$ . The safety factor  $q$  and shear value  $\hat{s}$  at this point, respectively, are 2.0 and 1.0.

scales (lengths for density and temperature) profiles for the energetic ions with respect to the thermal ions and electrons to look if there is any effect at all of the energetic ions'  $\eta$  on the ITG mode. Effects of energetic ions' density and temperature on the ITG mode are discussed along with a mixing length estimate for the prospective thermal ion transport by the ITG mode in the presence of energetic ions.

### 6.2.1 Model equations

Starting from Eq. (2.9) and reformulating it for the energetic ions, one can modify the quasineutrality condition to accommodate the energetic ions as a third active species as follows.

$$\tilde{n}_i + Z_f \tilde{n}_f = \tilde{n}_e \quad (6.1)$$

where,  $Z_f$  and  $\tilde{n}_f$ , respectively, are charge and perturbed density of the energetic ions. This equation can further be written following Eq. (2.13) as,

$$\sum_{\mathbf{k}'} \sum_{j=i,e,f} \hat{\mathcal{M}}_{\mathbf{k},\mathbf{k}'}^j \tilde{\varphi}_{\mathbf{k}'} = 0 \quad (6.2)$$

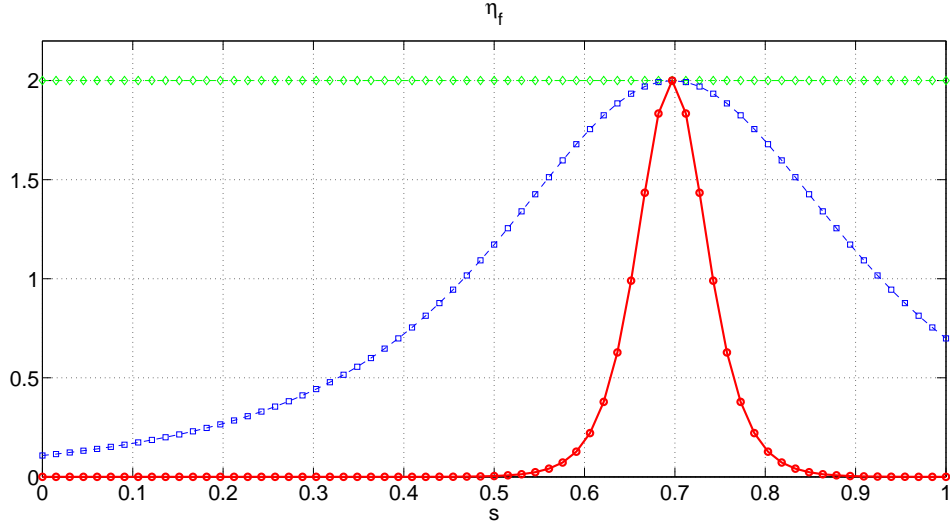


Figure 6.2: The  $\eta$  profiles considered for the energetic ions with respect to the background profiles of the thermal ions and electrons. While the thermal ion and electron  $\eta$  profiles are kept the same, energetic ion profiles are considered for three different cases, namely, flat  $\eta$  profile (green curve), peaked  $\eta$  profile (red curve) and same  $\eta$  profile (blue curve) as the thermal ions.

Note again that we have considered 3 species here: passing ions ( $i$ ), passing electrons ( $e$ ) comprising the thermal background plasma and energetic ion species ( $f$ ) with charge  $Z_f e$ .

### 6.2.2 Profiles and Parameters:

In the following sections, we will elucidate the results regarding the effect of the energetic ions on the stability of the ITG mode using the global linear gyrokinetic code EM-GLOGYSTO.

For the purpose we consider profiles and parameters as given in Table 6.1. Note that all our results in the present section are only for one  $a/\rho_i = 57$ . The equilibrium profiles for density, temperature,  $\eta$ , safety factor, and shear are displayed in Fig. 6.1 according to the parameters charted in Table 6.1. However, for the case of energetic ions we consider three different  $\eta$  profiles as presented in Fig. 6.2: (1) a flat  $\eta$  profile (green line), same throughout the minor radius of the tokamak, (2) a

Table 6.1: Profiles and parameters

Parameters:	Equilibrium Profiles:
<ul style="list-style-type: none"> <li>• B-field : <math>B_0 = 1.0</math> Tesla</li> <li>• Temperature : <math>T_0 = T(s_0) = 7.5</math> keV</li> <li>• Major Radius : <math>R = 2.0</math> m</li> <li>• Minor Radius : <math>a = 0.5</math> m</li> <li>• radius : <math>s = \rho/a</math>, <math>0.01 &lt; s &lt; 1.0</math>, <math>s_0 = 0.7</math></li> <li>• <math>L_{n0} = 0.4</math> m, <math>L_{T0} = 0.2</math> m</li> <li>• <math>\eta_{i,e}(s_0) = 2.0</math>, <math>\epsilon_n = L_{n0}/R = 0.2</math></li> <li>• <math>\tau(s) = T_e(s)/T_i(s) = 1</math>.</li> </ul>	<ul style="list-style-type: none"> <li>• N-profile and T-profile</li> <li><math>\frac{N(s)}{N_0} = \exp\left(-\frac{a \delta s_n}{L_{n0}} \tanh\left(\frac{s-s_0}{\delta s_n}\right)\right)</math></li> <li><math>\frac{T_{i,e}(s)}{T_0} = \exp\left(-\frac{a \delta s_T}{L_{T0}} \tanh\left(\frac{s-s_0}{\delta s_T}\right)\right)</math></li> <li><math>\delta s_n = 0.35</math>, <math>\delta s_T = 0.2</math> at <math>s = s_0</math></li> <li>• <math>q(s) = 1.25 + 0.67 s^2 + 2.38 s^3 - 0.06 s^4</math></li> <li>such that <math>q(s = s_0) = 2.0</math>;</li> <li>shear <math>s = s_0</math>, <math>\hat{s} = 1</math>.</li> </ul>

$\eta$  profile (blue line) same as the background thermal ions and electrons, and (3) a steeper  $\eta$  profile (red line) compared to the background ions and electrons. These are achieved by considering  $\delta s_T$  equal to 0.35, 0.2, 0.05, respectively, for the three cases keeping  $\delta s_n = 0.35$  same as that listed in Table 6.1 for the thermal ions and electrons. Also note that  $m_f/m_i = 1.0$ ,  $Z_f = 1$ , where  $m_i$  and  $m_f$  are masses for the thermal ions and fast ions. We also carry out similar studies considering He ions as the energetic species, with the  $\eta$  profile same as the thermal ions and electrons. All the parameters are kept same except considering  $m_f/m_i = 2.0$  and  $Z_f = 2.0$  for the He ions.

### 6.2.3 Wave number scan for the mode frequency and growth rate

In the present section, we carry out a  $k_\theta \rho_{Li}$  scan for the ITG mode by varying the toroidal mode number  $n$ . Thus we display the mode frequency  $\omega_r$  and growth rate  $\gamma$  of the ITG mode with respect to  $k_\theta \rho_{Li}$  for the cases with and without the energetic species in Fig. 6.3. We here consider three cases, namely, (i) ITG mode without the energetic species (the magenta line), (ii) ITG mode with singly charged energetic ions, with flat  $\eta$  profile (green line), steeper  $\eta$  profile (red line) and  $\eta$  profile (blue line) same as the thermal ions and electrons as shown in Fig. 6.2, all with  $m_f/m_i = 1$ ,  $Z_f = 1$ , and (iii) ITG mode with He ions for  $m_f/m_i = 2$ ,

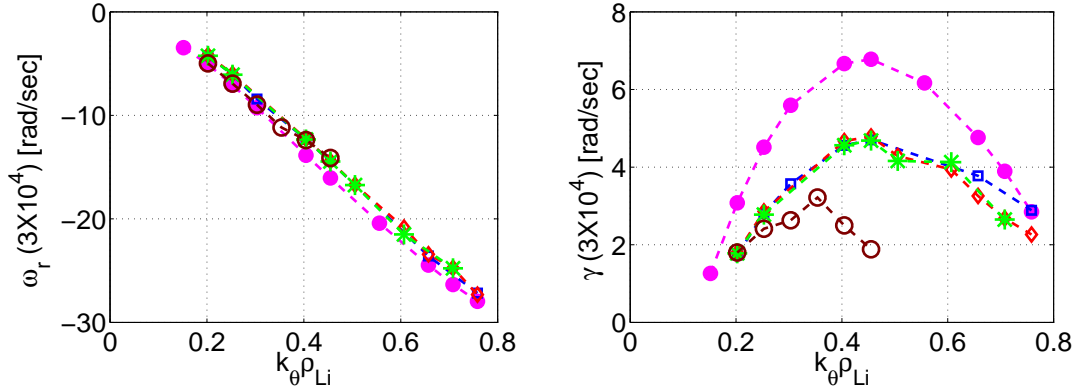


Figure 6.3: The wavenumber scan for the mode frequency  $\omega_r$  (left panel) and growth rate  $\gamma$  (right panel) of the ITG mode is presented for the cases, viz., (i) without energetic ions (magenta line), (ii) with singly charged energetic ions with flat  $\eta$  profile (green line), steeper  $\eta$  profile (red line), same  $\eta$  profile (blue line) as the thermal ions and (iii) with energetic He ions (brown line).

$Z_f = 2$ . The other parameters, apart from tabulated in table 6.1, are  $n_f/n_e = 0.1$  for the singly charged energetic ions, and  $n_f/n_e = 0.06$  for the He ions. The ratio  $T_f/T_e = 20$  and  $\tau = T_e/T_i = 1$  are same for all the cases. It is clear from the picture that the energetic ions strongly stabilize the ITG mode. For the parameters considered, the growth rate of the ITG mode is reduced by about 30% when one considers the energetic ions. It is apparent from Fig. 6.3 that the stabilization by the energetic ions is almost independent of the energetic ions'  $\eta$  profile. For He ions the stabilization is far stronger than the singly charged ions for the parameters chosen. A typical mode structure of the linear ITG in the presence of nonadiabatic passing electrons and nonadiabatic passing energetic ions is shown in Fig. 6.4

Regarding the mode frequency of the ITG mode (left panel of Fig. 6.3), the effect of the energetic ions is not significant. The effect of these energetic ions on the mode frequency of the ion temperature gradient driven mode is to reduce it slightly as is apparent from Fig. 6.3. Similar to the growth rate, the mode frequency also seems as well to be almost independent of the energetic particles'  $\eta$  profile.

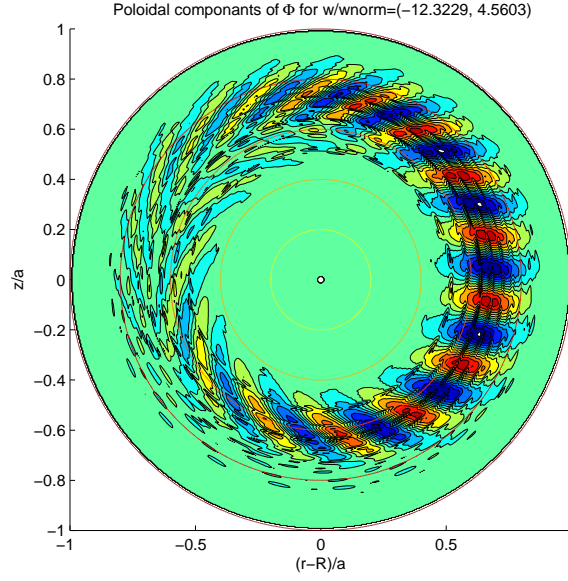


Figure 6.4: A typical electrostatic mode structure for  $n = 8$ ,  $k_{\theta}\rho_{Li} = 0.4$  corresponding to the maximum growth rate of the ITG mode with nonadiabatic electrons and energetic ions.

#### 6.2.4 Effect of density fraction of energetic ions

Next, we consider the effect of the population of the energetic ions on the ITG mode. The real frequency  $\omega_r$  (left panel) and growth rate  $\gamma$  (right panel) are plotted in Fig. 6.5 for the various cases described in the above section. The toroidal mode number  $n$  and  $k_{\theta}\rho_{Li}$  in the present section correspond to the mode with the highest growth rate in the toroidal mode number or  $k_{\theta}\rho_{Li}$  scan in the above section, that is, we choose  $n = 8$  corresponding to  $k_{\theta}\rho_{Li} \simeq 0.43$ . The scan is performed by increasing the ratio  $n_f/n_e$  gradually and finding out the corresponding mode frequency and growth rate of the  $n = 8$  or  $k_{\theta}\rho_{Li} \simeq 0.43$  mode. The other parameter that is kept fixed is the ratio  $T_f/T_e$ , which is set 20 in the scan. It is clear from the figure that the growth rate decreases almost linearly with the increase in the parameter  $n_f/n_e$ . For all the three cases of different  $\eta$  for the singly charged energetic ions, the growth rate finally subsides completely at around  $n_f/n_e \simeq 0.35$ . The mode frequency in contrast to the growth rate, decreases weakly with the increasing fraction of  $n_f/n_e$ . Thus, with the enhancement in the energetic ion

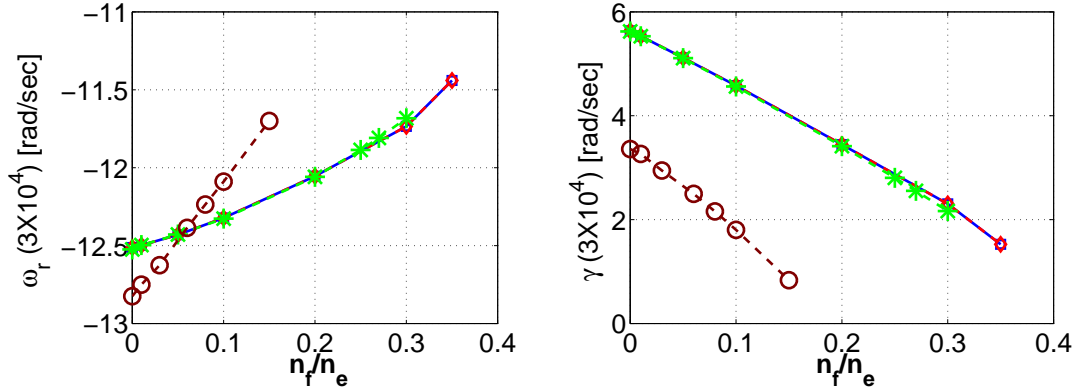


Figure 6.5: The mode frequency  $\omega_r$  and growth rate  $\gamma$  are plotted as a function of density fraction of the energetic ions compared to background density of electron for the mode with  $n = 8$ ,  $k_\theta \rho_{Li} = 0.4$  for the cases, viz., (i) with singly charged energetic ions with flat  $\eta$  profile (green line), steeper  $\eta$  profile (red line), same  $\eta$  profile (blue line) as the thermal ions and (ii) with energetic He ions (brown line).

population ITG mode becomes weaker gradually and at one stage it is suppressed completely. In the case of He ions, the stabilization is stronger than the cases discussed earlier. The mode frequency also falls faster than the cases of the singly charged energetic ions. It apparently conforms to the experimental observation of reduction in the ITG mode intensity with the fast ion population. The explanation is based upon the dilution of the thermal ion population by the energetic ions, which weakens the ion temperature gradient drive of the thermal ions, leading to stabilization of the mode. It also states the necessity of a nonperturbative model that treats the energetic ions on the same physics footing as the thermal ions and electrons, and that they need to be considered as an active element contributing to the quasineutrality constraint of the plasma. The increase in the energetic ion population dilutes the thermal ion population and thus the modes inherent to the thermal ions get stabilized. Looking at the curve for the He ions, one can understand that the He ions can ameliorate the confinement by further reducing the thermal ion temperature gradient mode, the prime cause of energy and particle loss from the confining device. Thus, over and above the ignition, He ions, especially those with lower energy can provide a mean to suppress the ITG mode efficiently thereby keeping the density and energy well preserved in the system, and at the

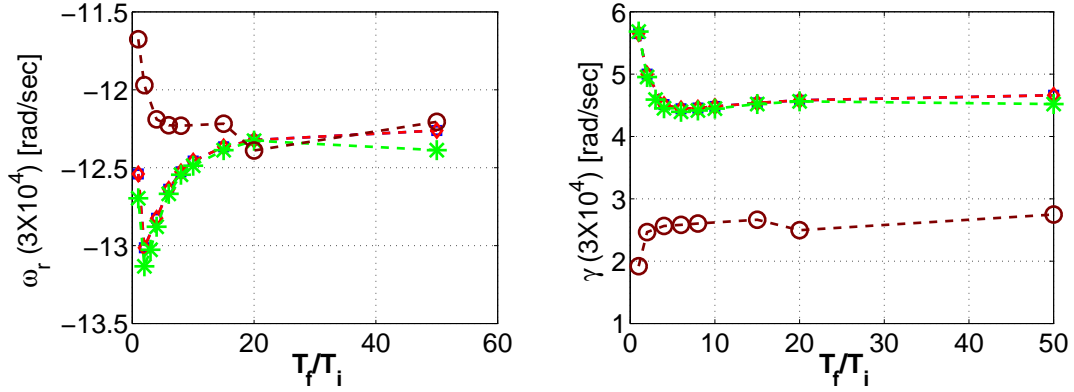


Figure 6.6: The mode frequency  $\omega_r$  and growth rate  $\gamma$  are plotted as a function of temperature fraction of the energetic ions compared to the temperature of the thermal ions for the mode characterized by the toroidal mode number  $n = 8$ , corresponding to  $k_\theta \rho_{Li} = 0.4$  for the cases, viz., (i) with singly charged energetic ions with flat  $\eta$  profile (green line), steeper  $\eta$  profile (red line), same  $\eta$  profile (blue line) as the thermal ions and (ii) with energetic He ions (brown line).

same time, continuing the energy transfer cycle, viz., from He ions to the electrons and finally to the ions. The argument for the observed stabilization of the ITG mode of the thermal ions by the energetic ions based upon thermal ion dilution, is further corroborated by the fact that the He ion (which is doubly charged) is more stabilizing than the singly charged energetic ions for the same parameters considered. The mode subsides completely at around  $n_f/n_e \simeq 0.15$  for He ions in comparison to the  $n_f/n_e \simeq 0.35$  of the singly charged energetic ions.

### 6.2.5 Effect of temperature of the energetic ions

In this section, we study the effect of the energetic ion temperature on the ITG mode of the thermal ions. This is performed by doing a temperature ratio scan  $T_f/T_i$  for the ITG mode keeping  $T_i$  intact and increasing only the energetic ion temperature. The other parameters are kept same as given in Table 6.1. The values of  $n_f/n_e$  are considered to be 0.1 for singly charged ions and 0.06 for He ions. The results are displayed in Fig. 6.6. It is clear from the scan that the energetic ion effect on the stabilization of the ITG mode is effective mainly in the low temperature region of the energetic ions. The variations in the the growth

## Chapter 6: Interaction of microturbulence with energetic ions

rate with the energetic ion temperature is more pronounced in the the region  $T_f/T_i \leq 10$ . This again conforms to the experimental observation where the effect of energetic ions has been found to be significant for  $T_f/T_i \leq 10$ . The growth rate of the thermal ion ITG mode decreases with the temperature and hence energy of the energetic ions upto  $T_f \simeq 10T_i$ , and saturates thereafter. Thus, the dilution effect is also related to the temperature of the energetic ions. When the energetic ion velocity is around the thermal ion velocity, the dilution is the most effective and so does the stabilization. Beyond  $T_f/T_i > 10$  the growth rate is insensitive to the temperature of the energetic ions. However, the overall stabilization by these energetic ions is always there irrespective of the energetic ion temperature. In the case of the He ions the trend of the growth rate with the temperature of the energetic ions is different than the singly charged energetic ions. It shows a weak increase in the growth rate with temperature of the He ions in the region  $T_f/T_i \leq 10$ . Thus, one may conclude that the He ash in the fusion will play an important role determining the stability properties of the ITG mode than the newly born He ions during the course of the fusion process. Coming to the mode frequency of the ITG mode, it increases slightly with the temperature of the energetic ions and at  $T_f/T_i \simeq 2$  it turns around for the singly charged energetic ions. Similar to the growth rate, the variation in the mode frequency is also visible only at lower value of  $T_f/T_i$ . It remains unaltered by the energetic ions beyond  $T_f/T_i > 10$ . Until  $T_f/T_i \leq 10$  the mode frequency continues decaying, and then onward, ceases to vary with the energetic ion temperature. One may mention here the findings of Ref. [126, 127] on the influence of the ITG turbulence on the energetic ions, which show that the effect of the ITG turbulence on the energetic ions is significant only in the lower temperature regime of the energetic ions. The influence is the strongest at  $T_f \simeq 2T_i$  [126]. Following the present results one may conclude that the vis-a-vis interaction of the ITG mode and energetic ions, and consequent redistribution of the energetic ions and stabilization of the ITG mode, all happen only in the lower energy regime of the energetic ions. Similar to the results in other sections, the stabilization is independent of the parameter  $\eta$  of the energetic ions.

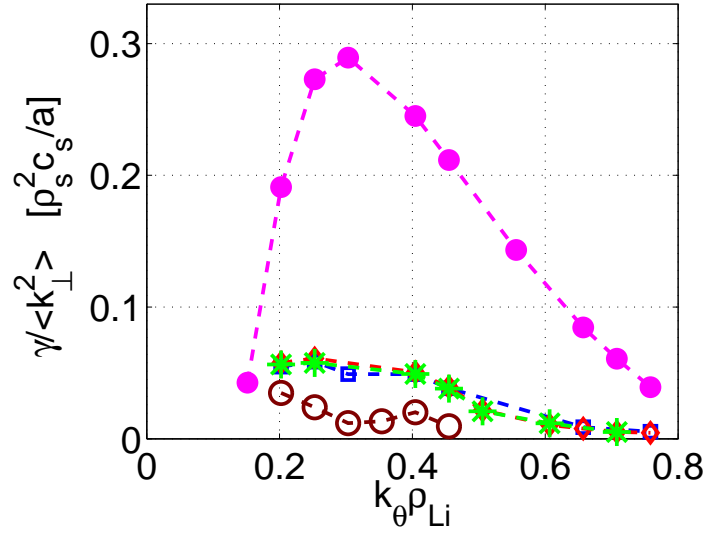


Figure 6.7: A mixing length based estimation of transport in gyroBohm units is presented for the cases, viz., (i) without energetic ions (magenta line), (ii) with singly charged energetic ions with flat  $\eta$  profile (green line), steeper  $\eta$  profile (red line), same  $\eta$  profile (blue line) as the thermal ions and (iii) with energetic He ions (brown line).

### 6.2.6 Mixing length estimate of transport

In the frame of linear theory, the transport can be estimated at the best using the mixing length estimation, where the diffusivity is calculated from the highest growth rate divided by the corresponding averaged squared wave number. Thus, in the present section we discuss the mixing length estimated transport for the various cases considered in this analysis. In Fig. 6.7 the mixing length based diffusivity expressed in gyro-Bohm unit is plotted as a function of the perpendicular wave number  $k_{\theta} \rho_{Li}$ . The magenta curve depicts the diffusivity calculated for the pure ITG mode without the energetic ions. The diffusivity initially increases, then at  $k_{\theta} \rho_{Li} \simeq 0.35$  becomes maximum and starts decreasing monotonically thereafter. Such a trend can be understood from Fig. 6.3 where growth rate variation is shown versus  $k_{\theta} \rho_{Li}$ . It is clear from Fig. 6.7 that the diffusivity is significantly decreased in the presence of the energetic ions. The diffusivity, however, is not strongly dependent on the respective  $\eta$  profiles of the energetic ions. It remains same for

## Chapter 6: Interaction of microturbulence with energetic ions

all the three cases of different  $\eta$  profiles. In the case of the He ions the effect, as expected, is the strongest on the observed diffusivity.

### 6.3 Size and energy scaling of hot ion transport in the presence of ion temperature gradient driven turbulence.

Motivated by the recent developments discussed in the Section 6.1, a study on the influence of the ITG mode turbulence on the hot/energetic ions is carried out in the present work with a passive tracer method using the massively parallel, global nonlinear gyrokinetic code named Gyrokinetic Tokamak Simulation (GTS) [139, 140], based on particle in cell method.

The passive tracer has proved to be a robust tool in the atmospheric and oceanographic turbulence studies [141, 142] and been fruitfully implemented in the plasma turbulence studies. In recent years, it has garnered much popularity because of its simplicity; a slew of studies on plasma turbulence are now based upon this passive tracer method [121, 143, 144, 145, 146, 147, 148], and sometimes the latter can be used to predict the nature of turbulence much like passive diagnostics [121]. Thus, such a tool can be quite useful to model hot species in tokamak, for example,  $\alpha$  particles, beam ions which have very low concentration compared to the thermal ions and electrons.

We adopt the same method to study the dispersion and energy scaling of the hot ions in the presence of turbulent field produced by the nonlinear ITG mode and predict their nature of transport. Note that the transport of the hot ions is a complex process; a whole lot of factors are there that can influence it. Among them poloidal drift, zonal flows, finite Larmor radius effect, gyro-averaging, orbit averaging can play critical role [149].

The purpose of the present work is to elucidate the system size effect in the ratio of plasma minor radius ( $a$ ) to the thermal ion Larmor radius ( $\rho_i$ ) on the transport of the hot ions. It is to be noted that the size scaling of hot ion transport is a crucial issue in view of the future fusion devices of larger size, for example, ITER [3].

In the present work, the hot ion transport has been observed to increase initially with system size and then to remain virtually independent of system size at larger system size; a behavior analogous to the Bohm to gyro-Bohm transition of thermal

ion transport [151, 152, 153]. Also, the nature of transport has been found to exhibit subdiffusive character for smaller system size, which continuously changes toward diffusive process as the system size increases.

Before discussing the details of the simulation model and results, we briefly explain, in the following, the anomalous transport and its importance in a complex medium such as tokamak plasmas.

It is obvious that complex systems are all pervading from exact to life sciences, embracing a variety of systems such as plasmas, glasses, liquid crystals, polymers, proteins, biopolymers, organisms or even ecosystems [169]. The mean physical quantities, in such systems have been known to be anomalous. With increasing sophistication in experimental and numerical techniques these anomalies have been brought out with more confidence. A particularly interesting and yet simple to measure physical process is particle diffusion and corresponding diffusion coefficient. Diffusion processes in various complex systems are found to exhibit non-Gaussian statistics. In such cases, the Fick's law of diffusion can not be applied to describe the transport behaviour. The mean squared displacement in these cases is no longer linear with respect to time, i.e.,  $\lim_{t \rightarrow \text{large}} \langle \sigma^2 \rangle = A t^p$ ,  $A$  being a constant, with  $p \neq 1$ . This is called anomalous diffusion and present in wide variety of systems. The main characteristics of such systems is the nonlinear growth of the mean squared displacement with respect to time which is, in general, caused by broad distributions and long range correlations [169]. These anomalous diffusion comprises of different domains, defined through the MSD equation  $\langle \sigma^2 \rangle = A t^p$  and parameterized by the anomalous diffusion exponent  $p$ . These domains are (a) subdiffusion, (b) superdiffusion and (c) normal diffusion on the threshold between sub and super diffusion [167, 168, 169]. Another special case is ballistic motion with  $p = 2$ . These are shown in Fig. 6.8. The generalized diffusion coefficient  $A$  in the above equation has the dimension  $[A] = L^2 T^{-p}$ .

Complex systems such as plasmas have been studied extensively for such anomalous behaviour. Nondiffusive transport has been observed [171] in numerical studies of three-dimensional, resistive pressure-gradient-driven plasma turbulence. It has been found that the probability density function of tracer particles' radial displacements is strongly non-Gaussian and exhibits algebraic decaying tails incorporating in a unified way space-time non locality (non-Fickian transport), non-Gaussianity,

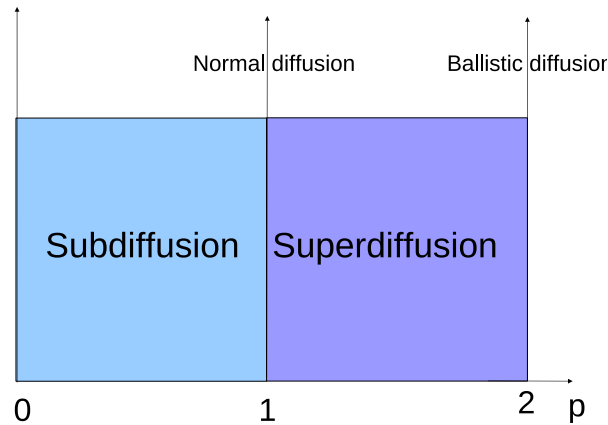


Figure 6.8: Different domains of anomalous diffusion, defined through the mean squared displacement  $\langle \sigma^2 \rangle = A t^p$ , and parameterized by the anomalous diffusion exponent  $p$ : (a) subdiffusion for  $0 < p < 1$ , (b) superdiffusion for  $1 < p < 2$ . On the threshold between sub- and superdiffusion is the normal Brownian diffusion located. Another special case is ballistic motion  $p = 2$  [169].

and nondiffusive scaling. [171]

Some examples from experiments indicating nondiffusive transport are [173]: the dependence of transport on the system size in low confinement mode plasmas [159], the observation of rapid propagation of an induced perturbation [160, 161], the measurement of long range temporal and radial correlations in the plasma edge [162, 163, 164], etc.

Nondiffusive transport in confined plasma is not only relevant to tokamaks [158]. Particle transport in a reversed field pinch (RFP) device is shown to be nondiffusive when magnetic chaos is present. A phenomenological fit to density profiles gives a diffusion constant and also a pinch velocity directed up the density gradient [158]. It has been shown in Ref. [158] that the combination of diffusion and pinch is actually an expression of the nonlocal, subdiffusive nature of the transport. Nondiffusive transport is also observed in the Large Plasma Device [172] in density gradients driven turbulence in the case of energetic ions. The energetic ion transport decreases rapidly with increasing gyroradius of the energetic ions. The turbulent transport is found to be nondiffusive in contrast to the diffusive transport caused by the Coulomb collisions.

## Chapter 6: Interaction of microturbulence with energetic ions

Coming back to tokamak, by means of toroidal gyrokinetic simulations of electrostatic, collisionless ion-temperature-gradient turbulence [154], it is shown that the nature of the transport is anticorrelated and subdiffusive. Additionally, whenever the flows are self-consistently driven by turbulence, the transport gains an additional non-Gaussian character. Similarly, several tracer particle studies in Hasegawa-Mima and Hasegawa-Wakatani models show nondiffusive character for the tracer particles. This kind of subdiffusive nature of transport, in particular, for radial transport in the presence of drift wave turbulence is sometimes referred to as *strange kinetics* [147]. Zonal flows are found to play critical role in determining the nature of transport [147, 121, 143, 144, 145, 146, 173] for the tracer particles.

### 6.3.1 Simulation Model

The particle dynamics is determined on the basis of the gyrokinetic formalism, where we follow the time evolution of the perturbed part  $\delta f$  of the particle distribution function  $f$  expressed as the sum of an equilibrium part  $f_0$  and a perturbed part  $\delta f$ . Thus, for the collisionless case, the gyrokinetic equation for ions can be written as [150]

$$\begin{aligned} \frac{\partial \delta f_i}{\partial t} + (v_{\parallel} \hat{b} + v_{E_0} + v_E + v_d) \cdot \nabla \delta f_i - \hat{b}^* \cdot \nabla (\mu B + \frac{e}{m_i} \Phi_0 + \frac{e}{m_i} \bar{\phi}) \frac{\partial \delta f_i}{\partial v_{\parallel}} = \\ -v_E \cdot \nabla f_0 + \hat{b}^* \cdot \nabla (\frac{e}{m_i} \bar{\phi}) \frac{\partial f_0}{\partial v_{\parallel}}. \end{aligned} \quad (6.3)$$

Here  $\vec{v}_{E_0}$ ,  $\vec{v}_E$  are  $\mathbf{E} \times \mathbf{B}$  drifts resulting, respectively, from the equilibrium potential  $\Phi_0$  and turbulent potential  $\bar{\phi}$ ,  $\vec{v}_d$  is the  $\nabla B$  drift,  $\hat{b}^* = \hat{b} + \rho_{\parallel} \hat{b} \times (\hat{b} \cdot \nabla \hat{b})$ , with  $\hat{b} = \mathbf{B}/B$  and  $\rho_{\parallel} = v_{\parallel}/B$ . This equation along with the equation for adiabatic electrons are solved numerically in the code GTS with particle in simulation method.

In contrast, the hot ion (*hi*) species is pushed according to the equation

$$\frac{\partial f_{hi}}{\partial t} + (v_{\parallel} \hat{b} + v_{E_0} + v_E + v_d) \cdot \nabla f_{hi} - \hat{b}^* \cdot \nabla (\mu B + \frac{e}{m_i} \Phi_0 + \frac{e}{m_i} \bar{\phi}) \frac{\partial f_{hi}}{\partial v_{\parallel}} = 0. \quad (6.4)$$

This equation has been added additionally to govern the evolution of the passive tracers incorporated as energetic ions. Note again that these passive tracers do not affect the turbulent field, and hence do not enter the gyrokinetic Poisson equation.

Although, the code GTS is equipped with the capability to treat general geometry tokamak, for simplicity, we consider circular geometry for the plasma cross-section.

### 6.3.2 Parameters and profiles

For the study of size scaling of hot ion transport we consider the following profiles and parameters. The average aspect ratio is  $R_0/a = 2.86$ , while three different values of system size are considered; (1) average  $a/\rho_i = 157$ , (2) average  $a/\rho_i = 315$ , and (3) average  $a/\rho_i = 500$ . Note that here  $\rho_i = v_{thi}/\omega_{ci}$  is the thermal ion gyroradius,  $c_s = \sqrt{T_e/m_i}$  is the sound speed and  $\omega_{ci} = eB/m_i$  is the gyrofrequency. The parameters  $e$ ,  $B$ ,  $m_i$ ,  $T_e$  are electric charge, magnetic field, mass of thermal ion, and electron temperature, respectively. The thermal ion temperature profile, density profile and safety factor profile considered are  $R_0/L_T = 8.0 \exp\{-(r/a - 0.5)/0.28\}^6$ ,  $R_0/L_n = 2.0 \exp\{-(r/a - 0.5)/0.28\}^6$  and  $q = 0.854 + 2.184(r/a)^2$  respectively, with electron to ion temperature ratio  $T_e/T_i = 1$ . This implies that at  $r = 0.5a$ ,  $q = 1.4$ , shear  $\hat{s} = (r/q)dq/dr = 0.78$ ,  $R_0/L_T = 8.0$ ,  $R_0/L_n = 2.0$ . We consider thermal ions and electrons both being equal to  $1.2 \times 10^8$  in number. The radial simulation domain chosen spans from  $r = 0.1a$  to  $r = 0.9a$ . Regarding the incorporation of hot ions, we consider monoenergetic ions with temperature  $T_h = nT_i$ ,  $n$  being an integer, with uniform distribution in pitch angle, defined as the angle between the particle velocity and magnetic field applied. The mass and charge of these hot ions are kept the same as the background thermal hydrogen-like ions. With these specifications, they are inserted on a single flux surface at  $\Psi_0 = 0.5a$ , where the gradients peak, and distributed uniformly in the poloidal and toroidal direction.

### 6.3.3 Heat flux of thermal ions

Figure 6.9 depicts the time history of thermal ion heat flux, measured at  $r = 0.5a$ , arising from the ITG turbulence for three values of system size, namely,  $a/\rho_i = 157$ ,  $a/\rho_i = 315$  and  $a/\rho_i = 500$ . The heat flux is calculated using the relation  $Q_i = \int d^3v \frac{1}{2} v^2 v_E \delta f$ , where  $v$  is the particle velocity,  $v_E$  is the radial component of gyro-averaged  $E \times B$  drift and  $\delta f$  is the perturbed distribution function, and recorded at  $r = 0.5a$  at every time step. The typical snapshots of perturbed potential are

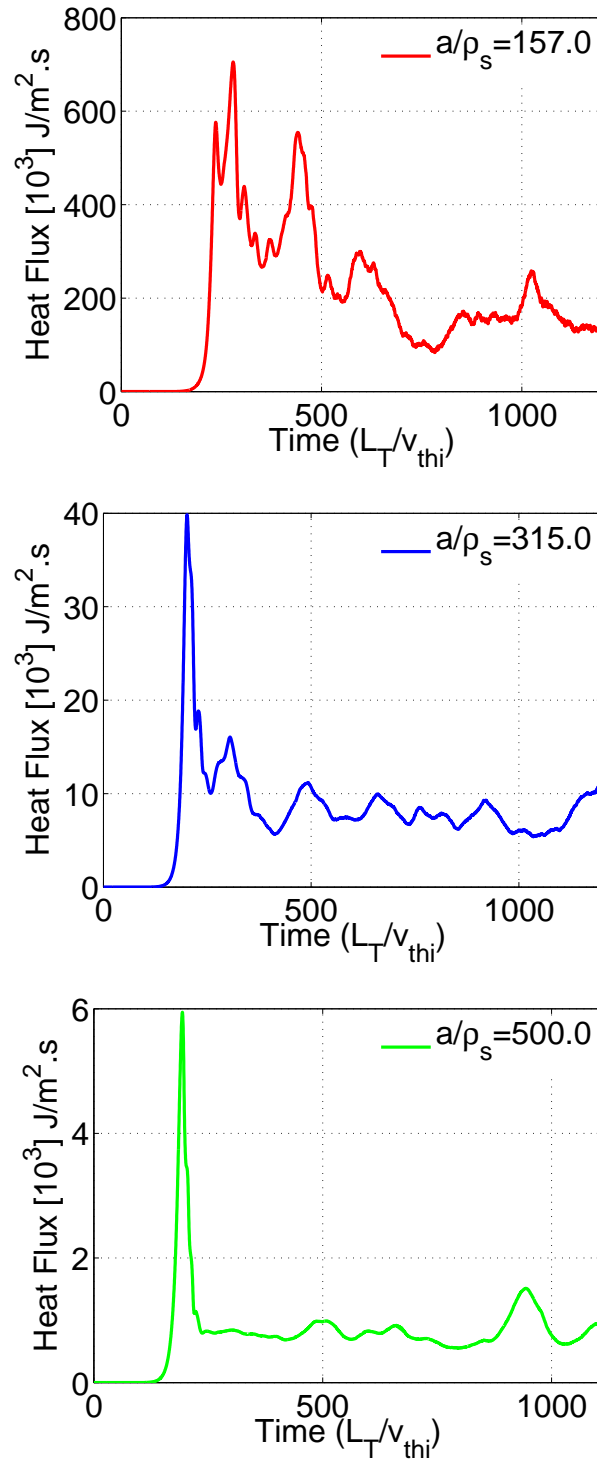


Figure 6.9: Time evolution of heat flux, measured at  $r = 0.5a$ , for system size (a)  $a/\rho_i = 157$ , (b)  $a/\rho_i = 315$ , and (c)  $a/\rho_i = 500$ .

## Chapter 6: Interaction of microturbulence with energetic ions

shown in the following figures for the three different system sizes considered here.

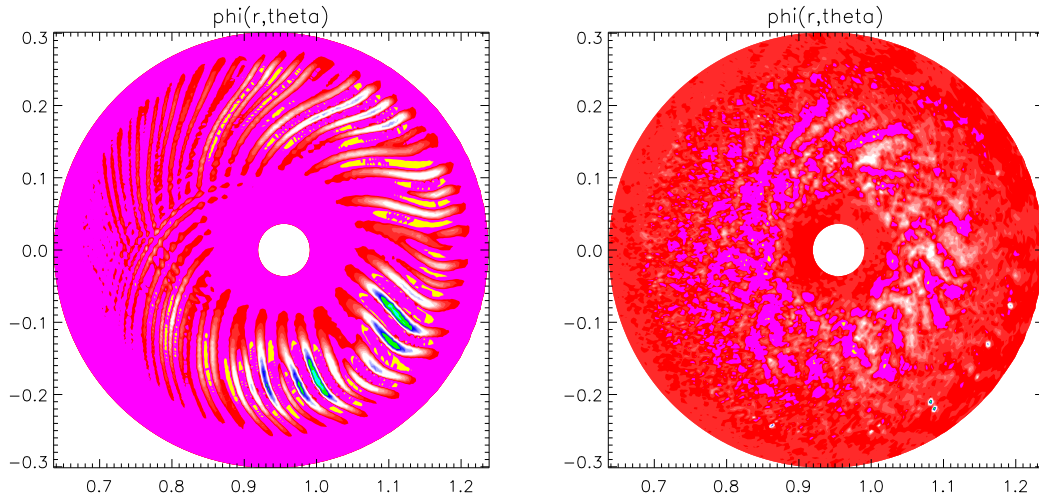


Figure 6.10: The typical snapshots of mode structure in the linear (left panel) and nonlinear (right panel) regime of the ITG turbulence for the system size  $a/\rho_i = 157$ .

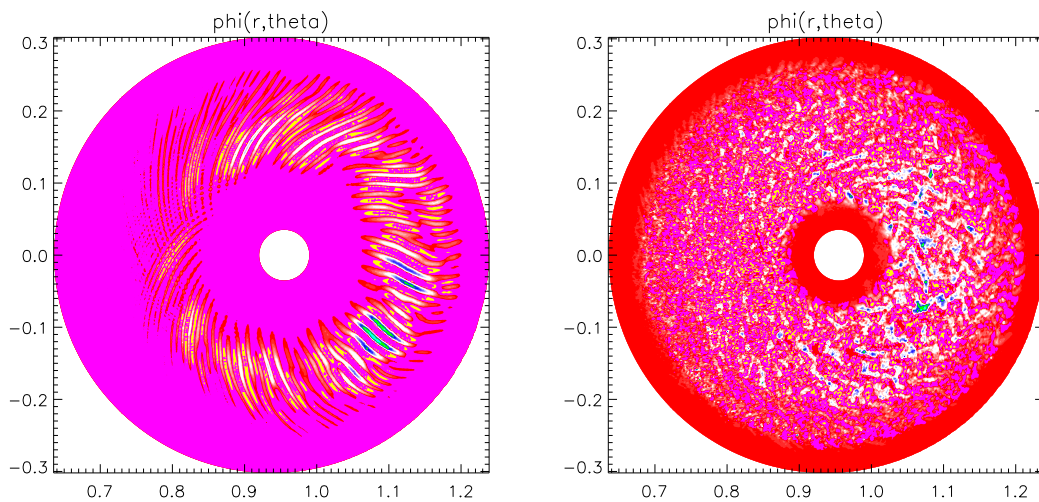


Figure 6.11: The typical snapshots of mode structure in the linear (left panel) and nonlinear (right panel) regime of the ITG turbulence for the system size  $a/\rho_i = 315$ .

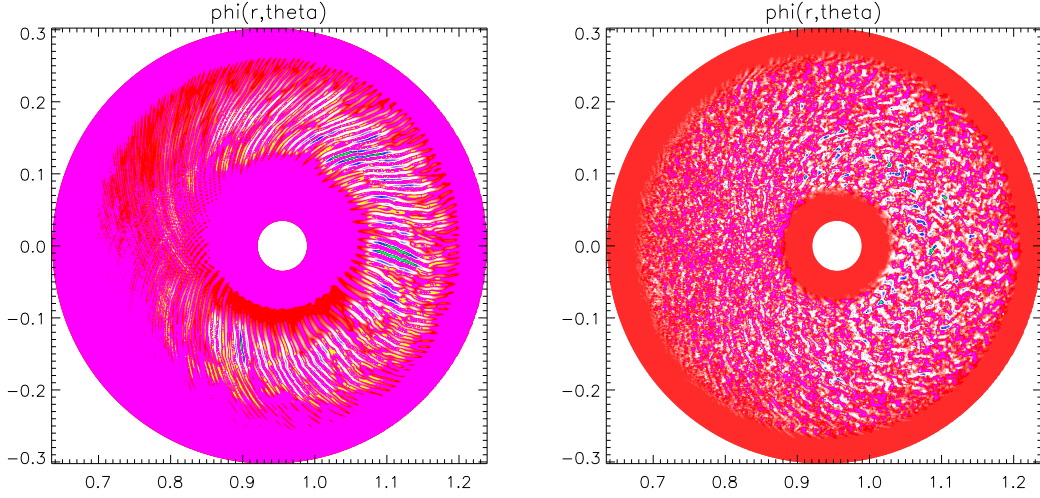


Figure 6.12: The typical snapshots of mode structure in the linear (left panel) and nonlinear (right panel) regime of the ITG turbulence for the system size  $a/\rho_i = 500$ .

### 6.3.4 Mean Squared Displacement of hot ions

The hot ions are incorporated at time  $t = 0$ , that is, before the turbulence sets in, on a single flux surface at  $\Psi_0 = 0.5a$  and are distributed uniformly in the poloidal and toroidal direction. The spirit of inserting the hot ions on  $\Psi_0 = 0.5a$  surface follows from the fact that the density and temperature gradients of the thermal ions peak on this surface and hence is the most unstable region. As described earlier, the hot ions in different energy groups are pushed according to the gyrokinetic Eq. (6.4) and the resulting mean squared displacement (MSD) is recorded at every instant of time using the following relation

$$\langle \sigma^2(\varepsilon, t) \rangle = \frac{1}{N} \sum_{i=1}^{i=N} (r_i(\varepsilon, t) - r_i(\varepsilon, 0))^2$$

where,  $N$  is the total number of particles of hot ions with energy  $\varepsilon$ ,  $r_i(\varepsilon, t)$  and  $r_i(\varepsilon, 0)$  are, respectively, the radial positions of the  $i^{\text{th}}$  hot ion with energy  $\varepsilon$  at time  $t$  and  $t = 0$ . Note that the number of hot ions inserted from each energy group is roughly  $6.7 \times 10^5$ . Figure 6.13 displays the time evolution of running MSD defined above for the hot ions with energy  $T_h = T_i, 2T_i, 4T_i, 8T_i, 16T_i$  for the three values of system size considered in the simulation. One can observe that

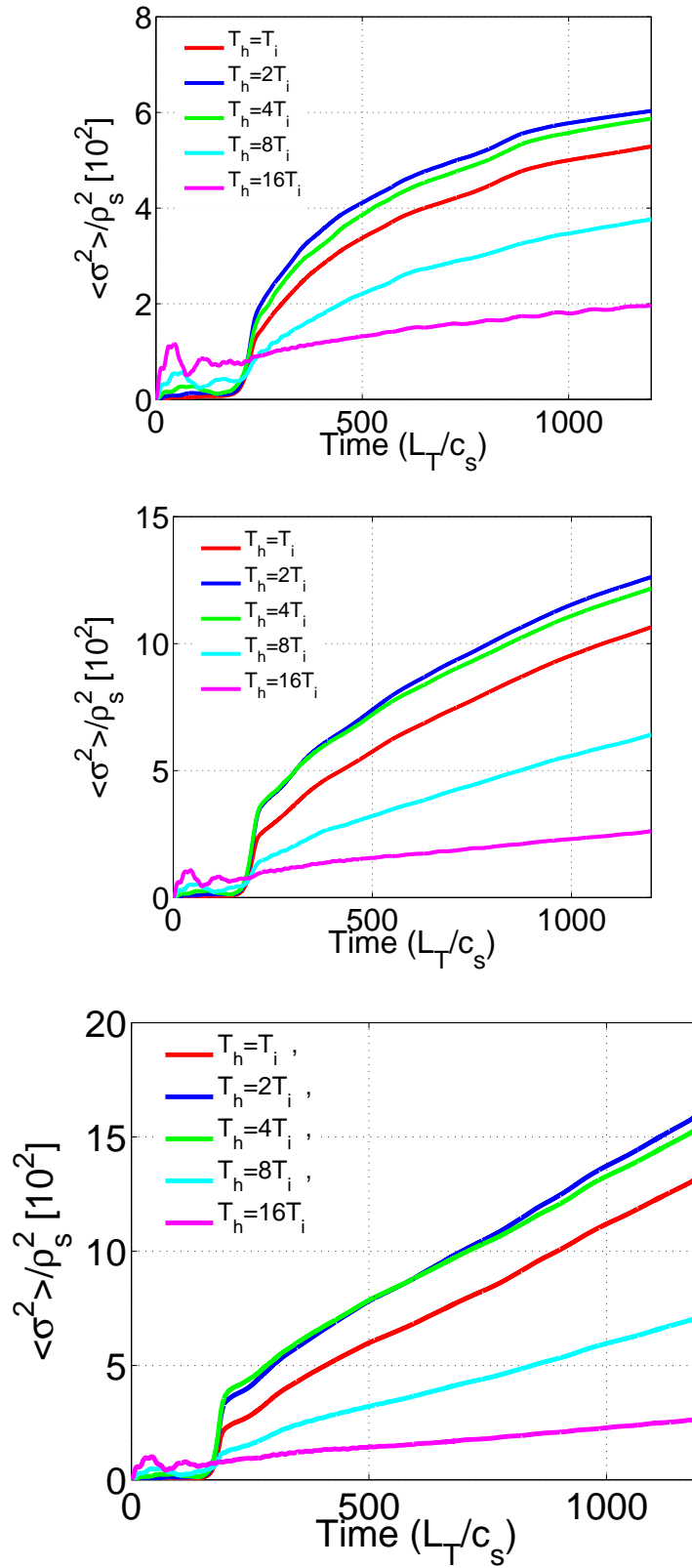


Figure 6.13: Mean squared displacement of the hot ions for system size a)  $a/\rho_i = 162$  157 (upper left panel), b)  $a/\rho_i = 315$  (upper right panel), c)  $a/\rho_i = 500$  (lower panel).

## Chapter 6: Interaction of microturbulence with energetic ions

till  $t = 200L_T/v_{thi}$  the hot ions undergo drift motion as the mode amplitude of the ITG mode during this time interval is too weak (see Fig. 6.9) to produce any effect on the hot ions. Their motion is thus governed by the equilibrium gradient and curvature of the magnetic field and therefore, the magnitude of the mean squared displacement is determined merely by the energy associated with the hot ions. The bounce period being inversely proportional to the particle velocity, hot ions with higher energy undergo more bounce cycles than the hot ions with lower energy for a given interval of time as depicted in the figure. It is clear from Fig. 6.9 that from time  $t = 200L_T/v_{thi}$  the ITG turbulence starts showing its signature with its exponential linear phase. Consequently, the hot ions also come under the influence of the electric field of the ITG mode and MSD rises abruptly at this point. Note that the MSD is maximum for  $T_h = 2T_i$  and gradually decreases with increase in the hot ion energy. There are important differences in the measured MSD for the three cases of different system size: first, the MSD for a given group of hot ions characterized by a given temperature increases with the increment in the system size; second, the MSD for all groups of energy of hot ions shows signature of saturation for  $a/\rho_i = 157$ , increases linearly at first, then weak tendency to saturate for  $a/\rho_i = 315$  and increases almost linearly for  $a/\rho_i = 500$  after the initial abrupt rise for all the three cases with respect to time; third, the MSDs of the hot ions with temperature  $T_h = 2T_i$  and  $T_h = 4T_i$  tend to be almost the same as the system size increases.

### 6.3.5 Nature of transport: Energy Scaling

In order to evaluate the dependence of the energetic ion transport on their energy and system size, one can calculate the net displacement in the interval, from time  $t_1 = 160L_T/v_{thi}$ , where the MSD in the presence and absence (not shown here) of ITG turbulence remains the same, to time  $t_2 = 1200L_T/v_{thi}$ , the end point of simulation and define a quantity,  $D_h = \delta \langle \sigma^2 \rangle / \delta t = (\langle \sigma^2(t_2) \rangle - \langle \sigma^2(t_1) \rangle) / (t_2 - t_1)$ . In the present case, the hot ions are introduced at  $r = 0.5a$  initially, and therefore, it can be shown that MSD and standard deviation remain almost the same. For a diffusive process, the parameter  $D_h$  can therefore represent the diffusion coefficient at late time when the system is in steady state. (A discussion on the issue regarding steady state and the diffusion coefficient is introduced in Section

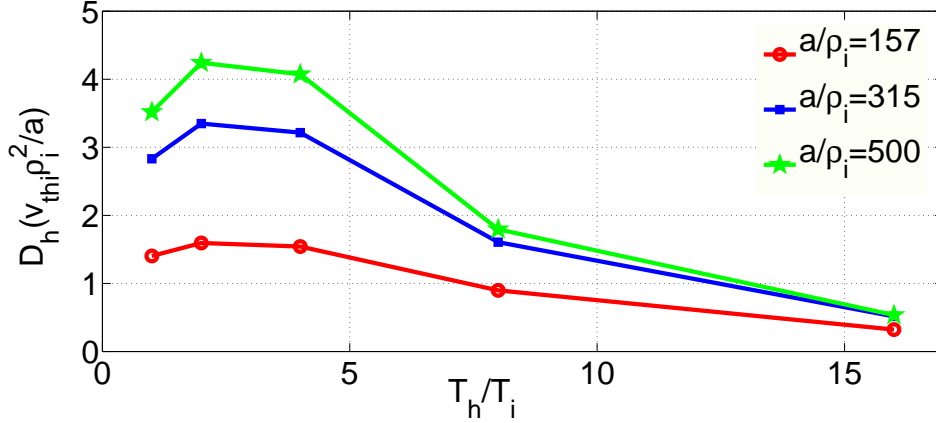
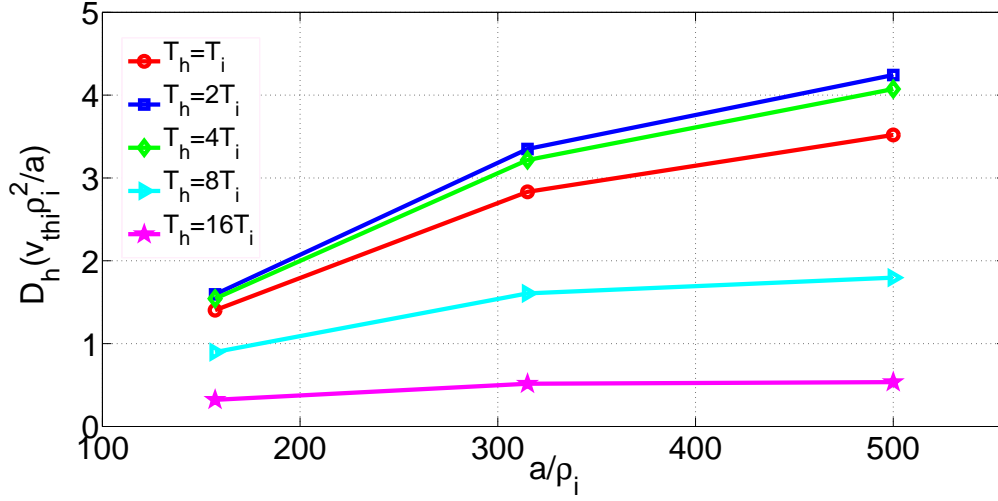


Figure 6.14:  $D_h = \delta \langle \sigma^2 \rangle / \delta t$  versus energy of hot ions.

6.3.7.) The parameter  $D_h$  is plotted versus energy of the hot ions in Fig. 6.14 for different values of system size, namely,  $a/\rho_i = 157, 315, 500$ . It is clear that for all the cases  $D_h$  is maximum for  $T_h = 2T_i$  and decreases monotonically with increasing energy with a tendency of saturation at higher value of hot ion energy for the chosen parameters. For energy below  $T_h = 16T_i$ , the quantity  $D_h$  exhibits significant dependence on the system size; it is maximum for  $a/\rho_i = 500$  and decreases with decreasing system size. However, at  $T_h = 16T_i$  the value of  $D_h$  is nearly the same for all the three values of system size. One expects that it converges to the same value for the hot ions with energy beyond  $T_h = 16T_i$ . Thus, it implies that while transport of hot ions with lower energy depends strongly on the system size, for hot ions with higher energy, in contrast, transport remains practically independent of the system size.

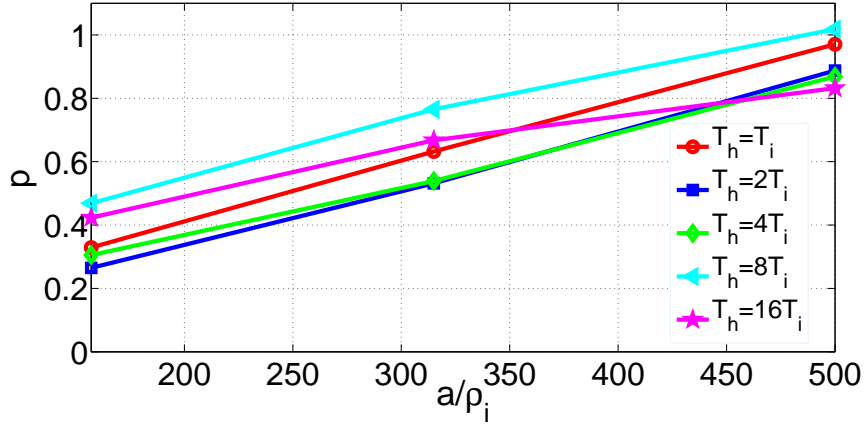
### 6.3.6 Nature of Transport: Size scaling

Next, we look at the dependence of hot ion transport on system size. Figure 6.15 presents the plot of  $D_h$  versus system size expressed in terms of the ratio  $a/\rho_i$ . It is evident that as the system size increases till  $a/\rho_i = 315$ ,  $D_h$  increases linearly, while the increment is very minor beyond that point showing a tendency of saturation at higher value of the system size. Thus, with increasing system size, the transport of hot ions for all groups of energy starts increasing initially and shows trend of


 Figure 6.15:  $D_h$  versus  $a/\rho_i$ .

saturation for larger system size. The trend reminds one the case of Bohm to gyro-Bohm transition of thermal ion transport [151, 152, 153].

Concerning the nature of transport let us consider the relation between MSD and time, given by  $\langle \sigma^2 \rangle = At^p$ , where  $A$  is an arbitrary constant and  $t$  is time. The value of the exponent parameter  $p$  determines whether the transport process undergoes a normal diffusion or anomalous diffusion. When  $p = 1$ , the transport is characterized by the diffusive process and said to be normal, while for values  $0 < p < 1$  and  $1 < p < 2$  the transport is characterized, respectively, by subdiffusive and superdiffusive processes and defined as anomalous. The value  $p = 2$  implies a ballistic motion where the velocity remains constant. The value of  $p$ , calculated from the slope of  $\log \langle \sigma^2 \rangle$  versus  $\log t$  between time  $t = 900L_T/v_{thi}$  to  $t = 1200L_T/v_{thi}$  is plotted in Fig. 6.16 versus system size  $a/\rho_i$  for the MSDs of hot ions delineated in Fig. 6.13 for various groups of energy. The figure shows that for smaller system size the hot ion transport is characterized by a subdiffusive process as  $p < 1$ . Due to this nature, one observes a trend of saturation in the measured MSD for  $a/\rho_i = 157$  as displayed in the first panel of Fig. 6.13. The exponent parameter  $p$  increases further for  $a/\rho_i = 315$  and the subdiffusivity becomes weaker. At even larger system size  $a/\rho_i = 500$ ,  $p$  approaches unity, thus showing the characteristics of a diffusive process. This means that


 Figure 6.16: Exponent  $p$  in  $\langle \sigma^2 \rangle \propto t^p$  versus  $a/\rho_i$ .

the hot ions exhibit subdiffusive transport for lower system size, which however, gradually becomes weaker and finally appears to be diffusive for larger system size. An extensive discussion on robustness of the exponent  $p$  can be found in Section 6.3.7. In that section, the simulation time is doubled and the calculation is repeated. This effort demonstrates that the transport is subdiffusive for  $a/\rho_i = 157$  and 315.

In the following, we have measured the probability density function (PDF) of radial displacement for the hot ions for all the device sizes considered here. We have also measured the standard deviation  $\sigma$ , skewness  $s$  and kurtosis  $k$  defined, respectively, as

$$\sigma^2 = \frac{1}{N} \sum_{i=1}^N (x_i - \bar{x})^2$$

,

$$s = \sqrt{N} \frac{\sum_{i=1}^N (x_i - \bar{x})^3}{\left\{ \sum_{i=1}^N (x_i - \bar{x})^2 \right\}^{3/2}}$$

and

$$k = N \frac{\sum_{i=1}^N (x_i - \bar{x})^4}{\left\{ \sum_{i=1}^N (x_i - \bar{x})^2 \right\}^2} - 3$$

from the simulation data. One may note that for a distribution kurtosis estimates the relative peakedness or flatness compared to the normal distribution, while

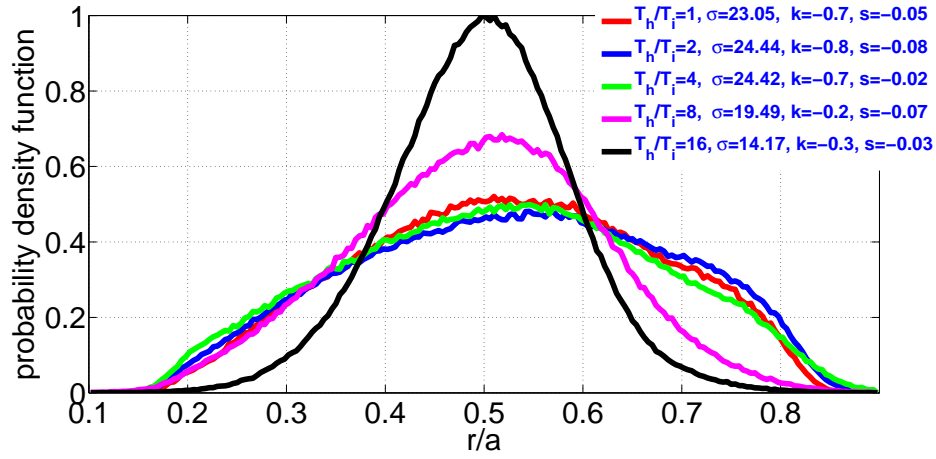
## Chapter 6: Interaction of microturbulence with energetic ions

skewness is a measure of symmetry about the mean. In the case of Gaussian distribution, both kurtosis and skewness as defined above become zero and infer a normal diffusion. Divergence of these quantities from zero, therefore, can be considered as the signature of a non-Gaussian distribution. A positive kurtosis characterizes a relatively peaked distribution while a negative kurtosis characterizes a relatively flat distribution. On the other hand, a positive skewness (right-skewed) represents a distribution with longer tail on the right side, while a negative skewness (left-skewed) represents a distribution with longer tail on the left side of the distribution. Creating 200 bins in the radial direction between  $0.1a$  and  $0.9a$  the probability density function for the test particles has been evaluated. The upper panel of Fig. 6.17 depicts plots of the PDFs for system size  $a/\rho_i = 157$ . Corresponding values of  $\sigma$ ,  $s$  and  $k$  are also displayed in the legend of the figure. Note that  $\sigma$  is normalized to corresponding  $\rho_i/a$ . It is clear from the figure that the PDFs are substantially deviated from the normal distribution. The lower panel of the same figure displays the plot of  $\langle \sigma^2 \rangle / t^p$  versus  $t$ . It remains virtually constant for the measured values of  $p$  in the given temporal window evincing the robustness of the quantity  $p$

The upper panel of Fig. 6.18 presents plots of the PDFs for system size  $a/\rho_i = 315$ . The legend shows the values of  $\sigma$ ,  $s$  and  $k$  extracted from the simulation data. The lower panel of the same figure displays the plot of  $\langle \sigma^2 \rangle / t^p$  versus  $t$ . It is clear that the quantity  $\langle \sigma^2 \rangle / t^p$  remains virtually constant for the measured values of  $p$  in the given temporal window. That means that though weak, the transport of the hot ions is still subdiffusive.

The upper panel of Fig. 6.19 presents plots of the PDFs for system size  $a/\rho_i = 500$ . In the legend the values of  $\sigma$ ,  $s$  and  $k$  are displayed. The lower panel of the same figure displays the plot of  $\langle \sigma^2 \rangle / t^p$  versus  $t$ . Both figures demonstrate that the transport of the hot ions in a bigger system exhibits diffusive nature.

Thus, from the Figs. 6.17, 6.18 and 6.19, one can conclude that for lower system size, hot ions' PDF exhibits deviation from Gaussian implying anomalous diffusion. As system size increases, the subdiffusion becomes weaker and at  $a/\rho_i = 500$  it gives qualitatively similar results of Zhang *et al.* [126] which has system dimension  $500\rho_i$ . Using first principle simulation in our work, we have shown, for the first time, a continuous transition of transport from subdiffusion for smaller device size to normal diffusion for larger device size.



$a/\rho_i=157$

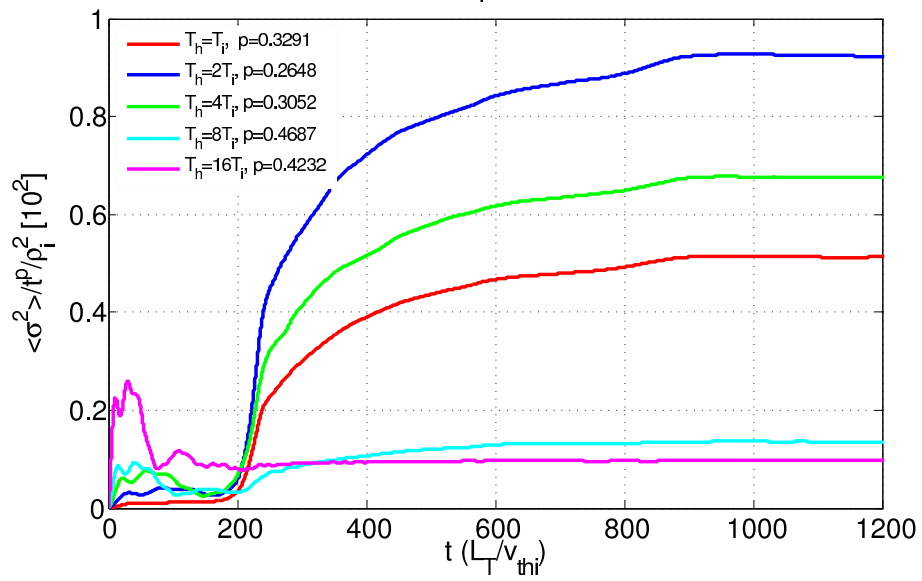


Figure 6.17: Upper panel: PDF for hot ions for  $a/\rho_i = 157$ . Lower panel:  $\langle \sigma^2 \rangle / t^p$  as a function of  $t$  for  $a/\rho_i = 157$ .

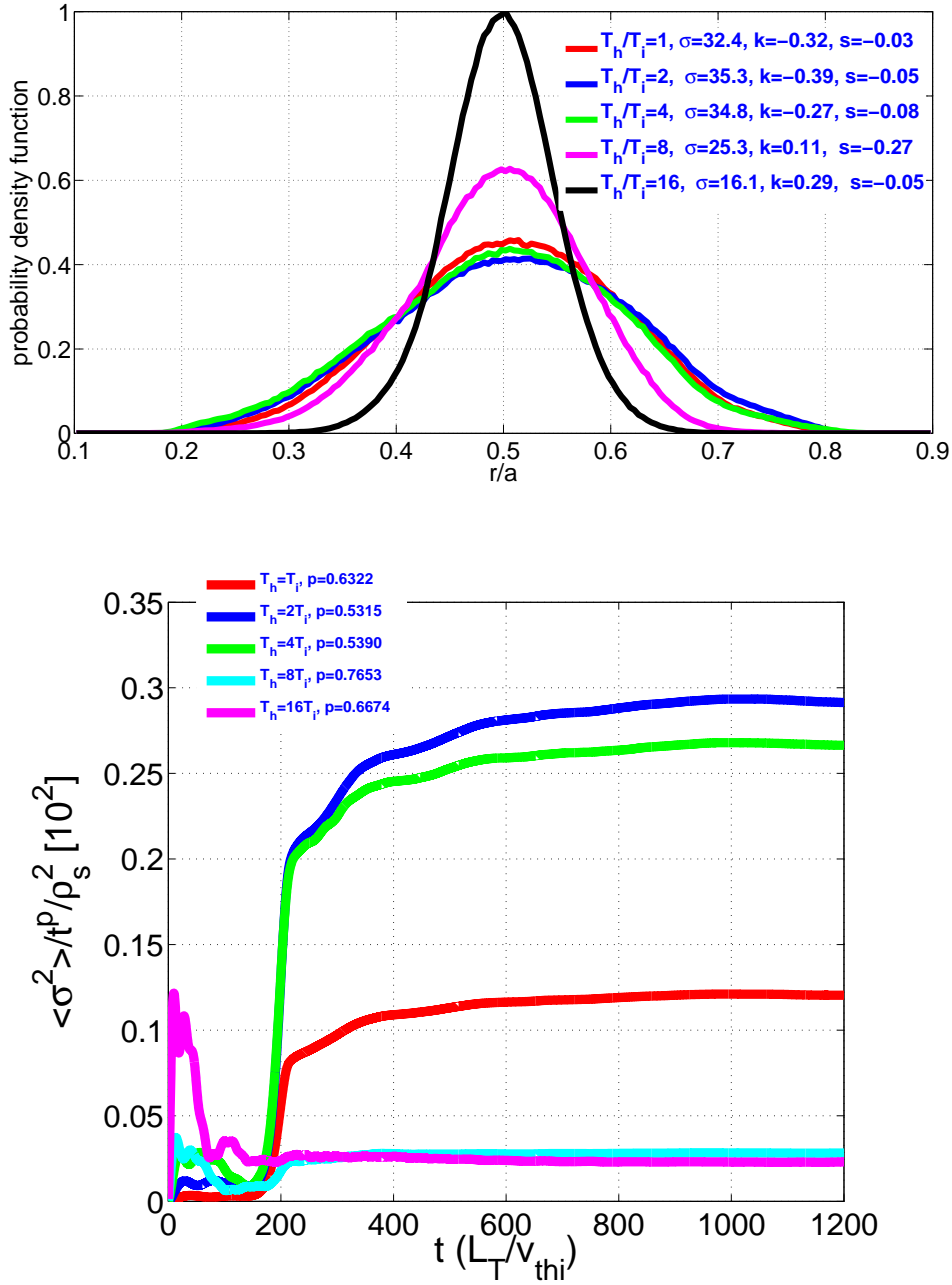


Figure 6.18: Upper panel: PDF for hot ions for  $a/\rho_i = 315$ . Lower panel:  $\langle \sigma^2 \rangle / t^p$  as a function of  $t$  for  $a/\rho_i = 315$ .

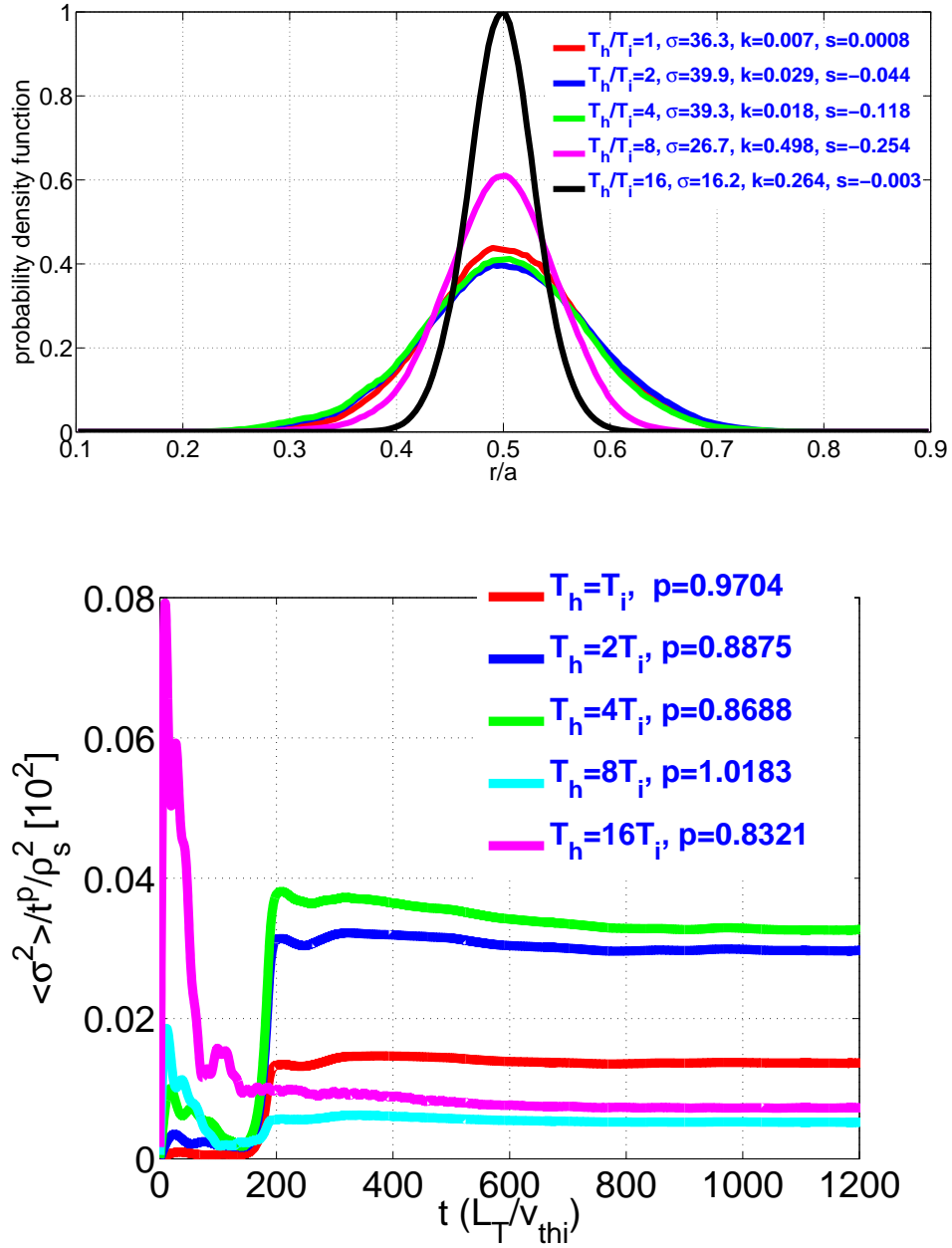


Figure 6.19: Upper panel: PDF for hot ions for  $a/\rho_i = 500$ . Lower panel:  $\langle \sigma^2 \rangle / t^p$  as a function of  $t$  for  $a/\rho_i = 500$ .

## Chapter 6: Interaction of microturbulence with energetic ions

It is interesting to point out here that similar subdiffusive nature of transport for thermal ions has also been reported by R. Sánchez *et al.* [154, 155] for smaller device size  $a/\rho_i = 200$  for ion temperature gradient driven turbulence. Exhibition of subdiffusive behavior of radial transport in smaller device is further corroborated by the results reported by Dewhurst *et al.* [143] which uses a modified Hasegawa-Wakatani model for drift wave turbulence, for system size  $L = 40\rho_i$ . Note that the particles with  $T_h = T_i$  considered in our work are similar to the thermal ions, considered passively and correspond to those in the aforementioned works.

The present work thus brings two different opinion (whether subdiffusive or diffusive) regarding radial transport of ions into the same frame. While on one hand, it observes subdiffusion like that of Sánchez *et al.* [154, 155] for lower system size, on the other hand, observes diffusion like Z. Lin *et al.* and Zhang *et al.* for larger system size [126, 151].

We, therefore, believe that the present first principle based simulation resolves a fundamental issue of whether the radial transport of thermal and hot ions is subdiffusive or otherwise. It has been demonstrated that the radial transport of thermal and hot ions is subdiffusive for lower system size, which eventually becomes diffusive for larger system size, exhibiting a segue from subdiffusion to normal diffusion with increasing system size.

### 6.3.7 Check for quasisteady state and robustness of the results

In the following we perform several reruns for longer duration to study the robustness of the exponent  $p$  and to demonstrate that diffusion remains anomalous in the quasisteady state. It is well known that the finite size effects and non-stationary state of numerical simulation may affect the conclusions as diffusion is meaningful only at steady state conditions. Interpretation in terms of standard versus anomalous diffusion could be difficult when simulations do not attain steady state. Therefore, we have rerun the cases of ITG mode and energetic particles for system sizes  $a/\rho_i = 157$  and 315 and doubled the simulation time, i.e, the total simulation time has been increased from 1200 to  $2500L_T/v_{thi}$ . It is clear from Fig. 6.20 that quasi-steady state is attained at late time for both system sizes.

The global mean squared displacement as a function of time is calculated and

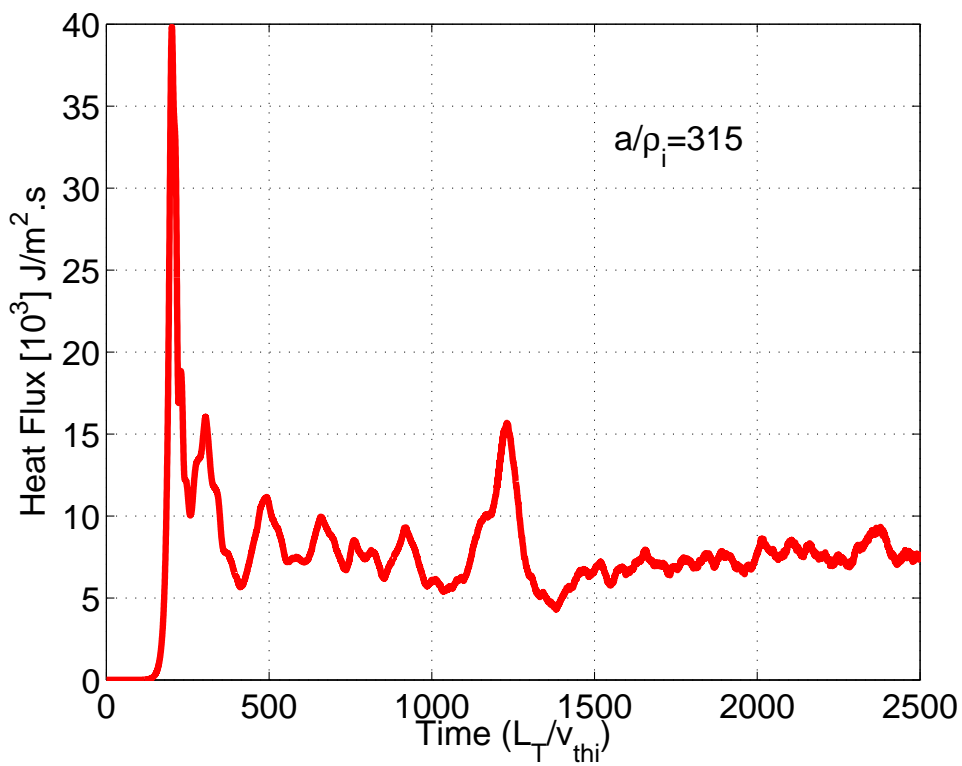
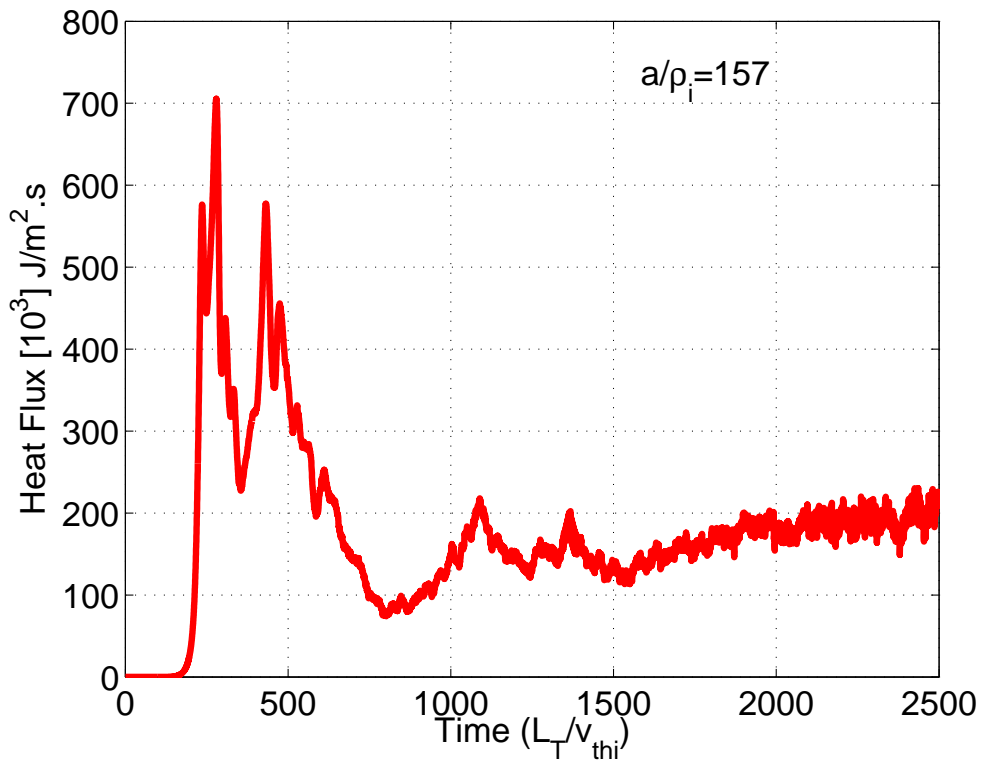


Figure 6.20: Heat flux for  $a/\rho_i = 157$  and 315

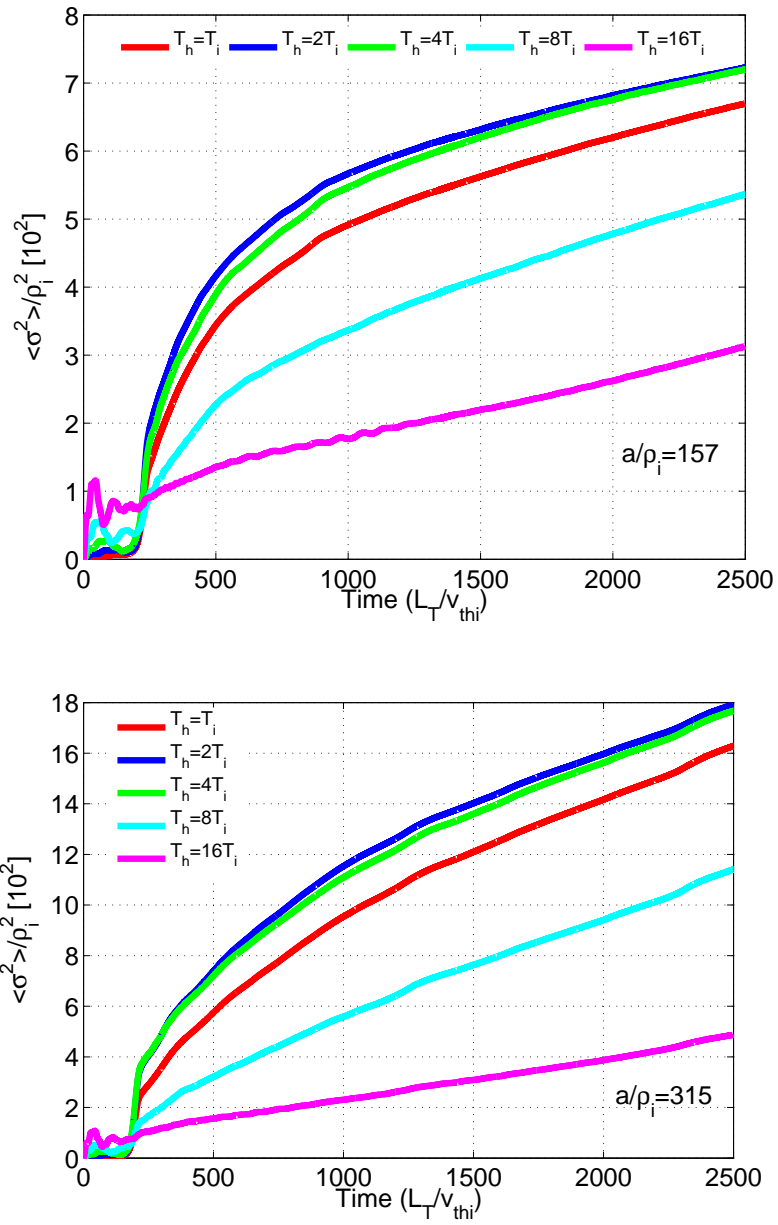


Figure 6.21: Mean squared displacement for  $a/\rho_i = 157$  and 315

## Chapter 6: Interaction of microturbulence with energetic ions

depicted in Fig. 6.21. Similarly, the PDFs are measured during the quasi-steady state for  $a/\rho_i = 157$  and 315 and displayed in Figs. 6.22 and 6.23. We find that the results remain the same qualitatively. Two cases are shown; one for earlier case of  $t = 1200L_T/v_{thi}$  and other, for  $t = 2500L_T/v_{thi}$ . It is clear from the figures that late time PDFs do not change much between these two times. If one considers occurrence of subdiffusion as merely a manifestation of the finite (small) size of the system (as the particles will fill up the system quickly), the  $p$  values in the case of  $a/\rho_i = 315$  should have reduced or in other words the transport should have been more subdiffusive (marked by smaller values of  $p$ ) when the simulation time is doubled. The PDFs in the case of  $a/\rho_i = 315$  clearly show that PDFs do not change much between  $t = 1200L_T/v_{thi}$  and  $t = 2500L_T/v_{thi}$  and are far away from the boundary throughout the simulation period. A comparison of  $p$  values

$T_h/T_i$	Mean $p$	standard deviation	$p$ from Section 6.3.6
1	0.3461	0.0032	0.3291
2	0.2675	0.0052	0.2648
4	0.2865	0.0031	0.3052
8	0.5153	0.0043	0.4687
16	0.7994	0.0099	0.4232

Table 6.2: New values of mean  $p$  and values measured in Section 6.3.6 (see Fig. 6.16) for  $a/\rho_i = 157$

from old (small time) simulation and new (long time simulation) for both systems reveals (please see Tables 6.2 and 6.3) that the  $p$  values do not change much except for  $T_h/T_i = 16$  which anyway is least affected by the turbulent field.

In the new runs, the mean value of  $p$  is evaluated taking the average of several temporal windows spanning from  $t = 2000L_T/v_{thi}$  to  $t = 2500L_T/v_{thi}$ . The robustness is reflected in the small values of standard deviation in the measurements of mean  $p$ . Note that the spirit behind taking the various temporal window is to rule out any doubt regarding the dependence of the value of  $p$  on the time span chosen for determining  $p$ . It is a standard procedure to determine the nature of transport from the calculated value of  $p$  [167, 168, 169]. A number of studies on nondiffusive transport, for example, Refs. [143, 147] rely upon the determination of the exponent  $p$  and is considered to be a robust method. As discussed earlier, for  $p = 1$  the transport is characterized by the diffusive process and said to be normal, while

## Chapter 6: Interaction of microturbulence with energetic ions

$T_h/T_i$	Mean $p$	standard deviation	$p$ from Section 6.3.6
1	0.6499	0.0350	0.6322
2	0.5390	0.0296	0.5315
4	0.5661	0.0331	0.5390
8	0.8785	0.0562	0.7653
16	1.0347	0.0748	0.6674

Table 6.3: New values of mean  $p$  and values measured in Section 6.3.6 (see Fig. 6.16) for  $a/\rho_i = 315$

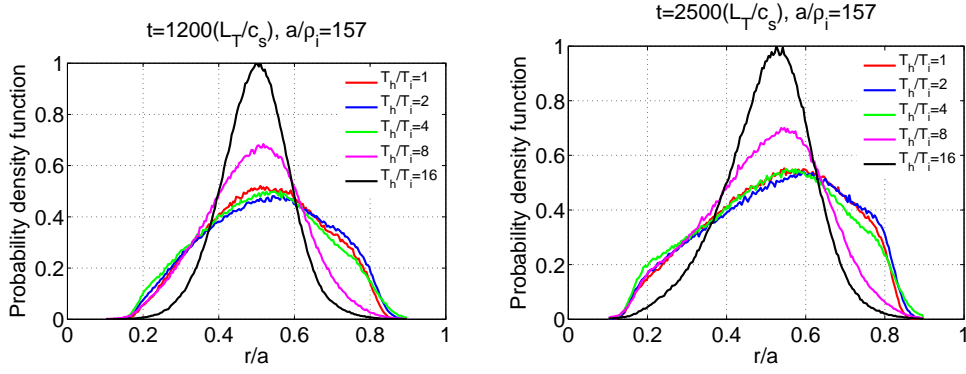


Figure 6.22: Probability distribution function for  $a/\rho_i = 157$

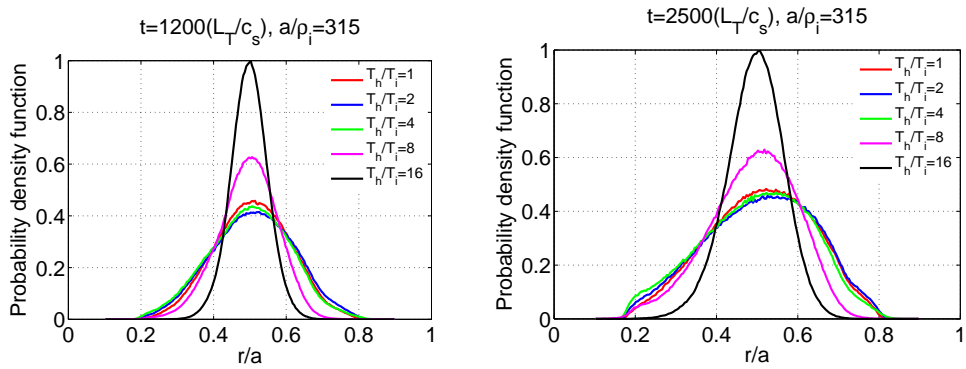


Figure 6.23: Probability distribution function for  $a/\rho_i = 315$

## Chapter 6: Interaction of microturbulence with energetic ions

for values  $0 < p < 1$  and  $1 < p < 2$  the transport is characterized, respectively, by subdiffusive and superdiffusive process and defined as anomalous [167, 168, 169]. The value  $p = 2$  implies a ballistic motion where the velocity remains constant.

The generalized diffusion coefficient defined by,  $A = \lim_{t \rightarrow \text{large}} \frac{\langle \sigma^2 \rangle}{t^p}$ , should be independent of time in the time window using which mean  $p$  is determined. The flat nature of  $\langle \sigma^2 \rangle / t^p$  with respect to time indeed demonstrates the robustness of the calculated values of mean  $p$ . This procedure has been extensively adopted in the past literature, for example, [143, 147]. Some authors determine mean squared displacement first and then compute  $\langle \sigma^2 \rangle / t^p$  with  $p$  chosen in such a way that it gives best fit to a constant curve  $\langle \sigma^2 \rangle / t^p$  at late time [143, 147]. In our work, to check the robustness and correctness of  $p$  we have performed the reverse procedure, i.e., first, the mean  $p$  values have been evaluated from the mean squared displacement versus time measurements at late time followed by the determination of mean  $p$  and then  $\langle \sigma^2 \rangle / t^p$  has been plotted to see whether it is constant or not with respect to time at late time. It is clear from the figures of  $\langle \sigma^2 \rangle / t^p$  versus  $t$  that the predicted values are indeed robust and accurate. The prediction over the nature of transport by the calculated values of  $p$ , is further corroborated by the evaluation of probability density function for the radial displacement of the energetic particles [Figs. 6.22 and 6.23]. We have plotted  $\langle \sigma^2 \rangle / t^p$  for the new values of  $p$  again as shown in Fig. 6.24. At late time, the curves remain virtually constant with respect to time showing the correctness of the values  $p$ . It can be expected that the effect of initial strong burst of turbulence, if any, on the energetic particles may not be considered to be responsible for the late time exhibition of subdiffusion. As mentioned above we have doubled the simulation time for the cases  $a/\rho_i = 157$  and 315. However the nature of the test energetic particle transport yet remains the same.

A related important issue is the inward particle pinch of energetic and thermal particles observed in several tokamaks and other systems such as RFP. For example, for electrostatic turbulence in a tokamak geometry, using nonlinear gyrokinetic formulation in GENE flux tube code, Jenko *et al.* [157] have addressed the particle pinch effect for thermal particles. A similar study was also performed in Ref. [156]. Both studies demonstrate that in the case of electrostatic ITG turbulence, the dynamics of nonadiabatic passing electrons (kinetic electrons) is necessary for pinch

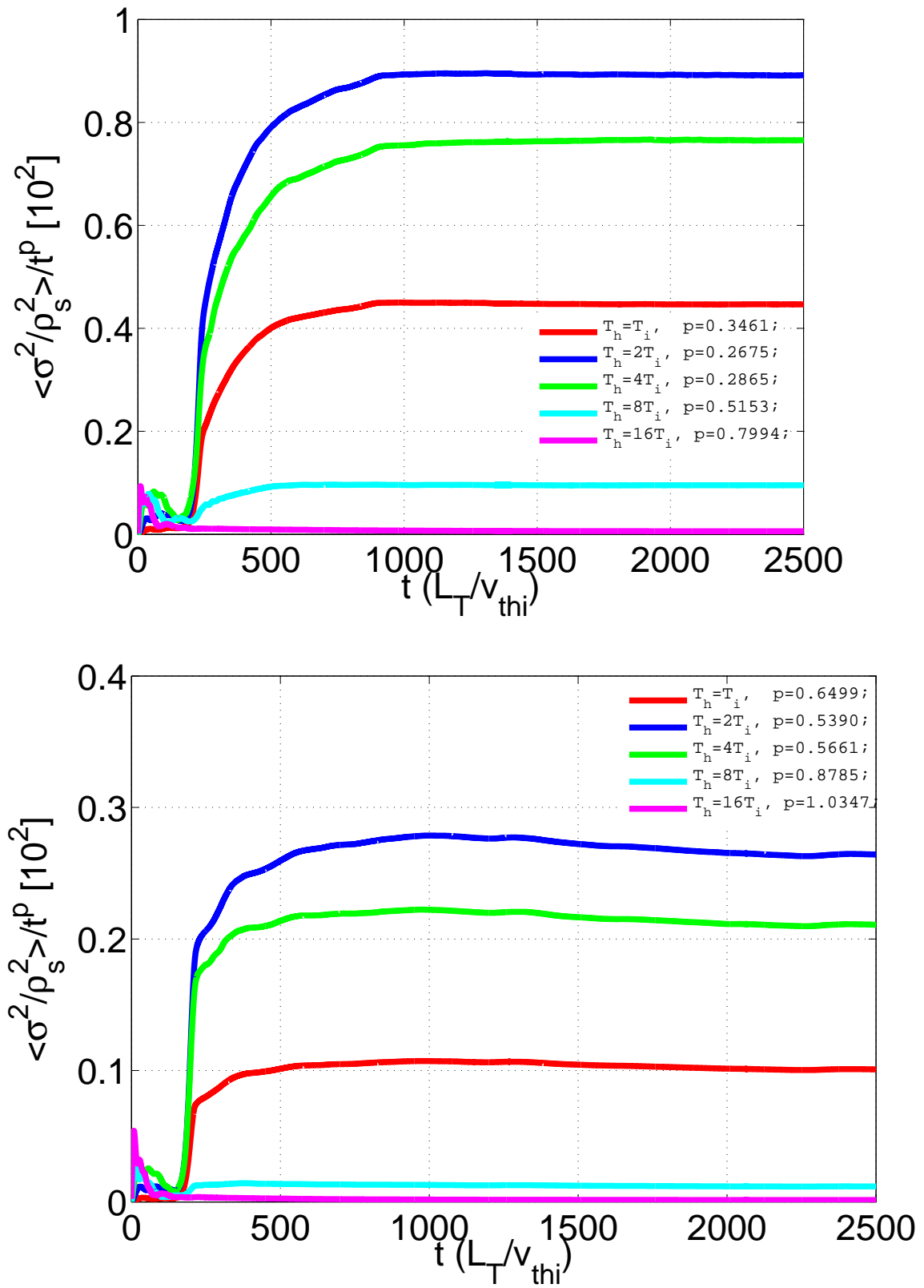


Figure 6.24: Upper panel:  $\langle \sigma^2 \rangle / t^p$  as a function of  $t$  for  $a/\rho_i = 157$ . Lower panel:  $\langle \sigma^2 \rangle / t^p$  as a function of  $t$  for  $a/\rho_i = 315$ . 177

## Chapter 6: Interaction of microturbulence with energetic ions

effect. In the case of TEM turbulence, a particle pinch can exist if and only if the inward flux of passing electrons is able to overcompensate the outward flux of trapped electrons [157].

For magnetic turbulence in an RFP, Spizzo *et al.* [158] show that one may split the particle flux in a diffusive and a pinch (convective) term

$$\Gamma = -D\nabla n + v.n,$$

where  $D$  and  $v$  are fit to the observed transport in tokamaks or reversed field pinches. A phenomenological fit to density profiles gives a diffusion constant and also a pinch velocity directed up the density gradient. It is shown [158] that the combination of diffusion and pinch is actually an expression of the nonlocal, subdiffusive nature of the transport.

As discussed earlier, our ITG model has adiabatic electrons. Moreover, our main focus is to elucidate the nature of redistribution of energetic passive particles in global electrostatic ITG/TEM turbulence by means of a global diffusion coefficient. Thus we believe that although of fundamental interest, a study relating the local diffusion coefficient and local pinch velocity of energetic test particles is beyond the scope of the present work. This has been indicated in the Section 7.2 for future work. In the following, we give a plausible explanation for the transition in nature of transport from subdiffusion to diffusion with increasing system size in tokamaks.

### 6.3.8 Plausible explanation for subdiffusion

It is now widely accepted that the correlation function for ITG perturbation is self-similar irrespective of the system size which suggests that the turbulent eddies due to ITG turbulence have the same size independent of the size of the tokamaks. The typical size is  $\sim 7\rho_i$ , where  $\rho_i$  is the ion Larmor radius [151]. So in a larger device of size like  $500\rho_i$  one would expect far larger number of eddies compared to that in a smaller device like  $157\rho_i$  as is apparent from Figs. 6.10, 6.11 and 6.12. Test particles are trapped in these eddies and move along them. They become detrapped when two such eddies interact strongly. Since in a smaller device, there are fewer eddies, probability of eddy-eddy interaction and detrapping a particle is

## Chapter 6: Interaction of microturbulence with energetic ions

small. In contrast, in a larger device with larger number of eddies, though particles are trapped, they are frequently detrapped because of the higher probability of eddy-eddy interaction giving the particles' transport a diffusive character. If one considers this trapping and subsequent detrapping as scattering or collision, for a smaller device, say  $157\rho_i$ , the aggregate number of scattering or collisions that a test particle suffers in the course of its radial excursion will be much less than that in a larger device, say  $500\rho_i$ . In other words, one can say that the test particles in the system with  $500\rho_i$  undergo more frequent random walks than in the system of size  $157\rho_i$ . Thus, for a test particle, randomization is much higher in the system with size  $500\rho_i$  than that with size  $157\rho_i$ . This explains qualitatively why hot ions' transport attains diffusive character in a larger device in contrast to subdiffusivity in a smaller device. Note that the Larmor radii of the hot ions in terms of thermal ion Larmor radius are  $\rho_i$ ,  $1.4\rho_i$ ,  $2\rho_i$ ,  $2.8\rho_i$ ,  $4\rho_i$ , and the typical size of a eddy is  $7\rho_i$ . So there is always a definite probability of the hot ions even with the highest energy in our simulation to interact strongly with the turbulent eddies. However, a mathematical model to actually verify the above said idea is beyond the scope of the present thesis.

## 6.4 Radial transport of energetic ions in the presence of trapped electron mode turbulence.

Inspired by recent results on interaction between the ITG mode turbulence and hot ions, a study on the influence of the trapped electron mode turbulence on the hot ions is carried out in the present section with the same passive tracer method using the massively parallel, global nonlinear gyrokinetic code named Gyrokinetic Tokamak Simulation (GTS) [139, 140], with the kinetic electrons included this time.

In the present study, we have considered three different types of hot ions, namely isotropic (in pitch angle), purely passing and purely trapped hot ions. We have observed that the nature of transport exhibits nondiffusive character, demonstrating subdiffusion for all the types of hot ions mentioned above. Corresponding energy scaling has also been estimated. It has been observed that isotropic and passing hot ions obey inverse energy scaling while purely trapped hot ions decay as inverse square of energy.

The trapped electron mode has different origin and saturation mechanism propagating in the electron diamagnetic direction in contrast to the ion diamagnetic direction of propagation for ITG modes. The mode is generated by the density or temperature gradient of the trapped electrons. In the present work, we study the nature of transport of hot ions in the presence of TEM turbulence. We report results for three different distributions of hot ions. Firstly, we consider hot ions having isotropic distribution in pitch angle (angle between particle velocity and magnetic field applied); thus, it contains effect of both passing and trapped population of hot ions. Secondly, we consider hot ions entirely in the loss cone, thus containing purely passing particles and finally, purely trapped hot ions. We investigate if there is any difference at all by incorporating hot ions before the turbulence sets in, and when the turbulence is well developed and attains the saturation phase. Energy scaling of the radial transport of the hot ions of different distributions is also studied. It is found that the transport decreases rapidly with energy for the hot ions with lower energy, and slowly as the energy of the hot ions increases further.

### 6.4.1 Simulation Model

The particle dynamics is determined on the basis of the gyrokinetic formalism, where we follow the time evolution of the perturbed part  $\delta f$  of the particle distribution function  $f$  expressed as the sum of an equilibrium part  $f_0$  and a perturbed part  $\delta f$ . Thus, for the collisionless case, the gyrokinetic equation for ions can be written as [150]

$$\begin{aligned} \frac{\partial \delta f_i}{\partial t} + (v_{\parallel} \hat{b} + v_{E_0} + v_E + v_d) \cdot \nabla \delta f_i - \hat{b}^* \cdot \nabla (\mu B + \frac{e}{m_i} \Phi_0 + \frac{e}{m_i} \bar{\phi}) \frac{\partial \delta f_i}{\partial v_{\parallel}} = \\ -v_E \cdot \nabla f_0 + \hat{b}^* \cdot \nabla (\frac{e}{m_i} \bar{\phi}) \frac{\partial f_0}{\partial v_{\parallel}} \end{aligned} \quad (6.5)$$

Here  $\vec{v}_{E_0}$ ,  $\vec{v}_E$  are  $\mathbf{E} \times \mathbf{B}$  drifts resulting, respectively, from the equilibrium potential  $\Phi_0$  and turbulent potential  $\bar{\phi}$ ,  $\vec{v}_d$  is the  $\nabla B$  drift,  $\hat{b}^* = \hat{b} + \rho_{\parallel} \hat{b} \times (\hat{b} \cdot \nabla \hat{b})$ , with  $\hat{b} = \mathbf{B}/B$  and  $\rho_{\parallel} = v_{\parallel}/B$ .

The drift kinetic equation is used for the electrons, thereby eliminating the finite Larmor radius effect. Thus the electron  $\delta f_e$  equation for collisionless case is given by [150]

$$\begin{aligned} \frac{\partial \delta f_e}{\partial t} + (v_{\parallel} \hat{b} + v_{E_0} + v_E + v_d) \cdot \nabla \delta f_e - \hat{b}^* \cdot \nabla (\mu B + \frac{e}{m_e} \Phi_0 + \frac{e}{m_e} \bar{\phi}) \frac{\partial \delta f_e}{\partial v_{\parallel}} = \\ -v_E \cdot \nabla f_{e0} + \hat{b}^* \cdot \nabla (\frac{e}{m_e} \bar{\phi}) \frac{\partial f_{e0}}{\partial v_{\parallel}} \end{aligned} \quad (6.6)$$

In contrast, the hot ion species is pushed according to Eq. (6.4).

### 6.4.2 Parameters and Profiles

With the set of equations described in the earlier section, the numerical experiment is carried out using the PIC based, massively parallel global nonlinear gyrokinetic code Gyrokinetic Tokamak Simulation (GTS). Although the code is equipped with the capability to treat general geometry tokamak, however, circular geometry is considered for the plasma cross-section. The average aspect ratio  $R_0/a = 2.86$  and average  $a/\rho_i = 157$ . The profiles considered for the thermal ions and electrons are  $R_0/L_{Te} = 6.0\{ -[(r/a - 0.5)/0.28]^6 \}$ ,  $R_0/L_{Ti} = 1.0 \exp\{ -[(r/a - 0.5)/0.28]^6 \}$ ,  $R_0/L_n = 6.0 \exp\{ -[(r/a - 0.5)/0.28]^6 \}$ ,  $T_e/T_i = 3$ ,  $q = 0.854 + 2.184(r/a)^2$ . This

## Chapter 6: Interaction of microturbulence with energetic ions

implies that at  $r = 0.5a$ :  $R_0/L_{Te} = 6.0$ ,  $R_0/L_{Ti} = 1.0$ ,  $R_0/L_n = 6.0$ ,  $T_e/T_i = 3.0$ ,  $q = 1.4$ , and  $\hat{s} = (r/q)dq/dr = 0.78$ . The total number of marker ions and electrons is  $1.9 \times 10^8$ . The radial simulation domain chosen spans from  $r = 0.1a$  to  $r = 0.9a$ . Regarding the incorporation of the hot ions, we consider monoenergetic ions with energy in integral multiples of the thermal ions' energy, with a careful choice of the distribution in pitch angle, in order to assure isotropic, passing and trapped population, respectively, for the three cases undertaken. The mass and charge of these hot ions are kept the same as the background thermal ions. With these specification, they are inserted on a single flux surface at  $\Psi_0 = 0.5a$ , where the density gradient peaks, distributed uniformly in the poloidal and toroidal direction. It may be noted that the NBI generated hot ions are passing, rf heated ions are mostly trapped, and the  $\alpha$  particles are isotropic in the pitch angle. Thus, the present study is relevant to all the types of hot ions prevalent in the fusion grade plasma in a tokamak.

### 6.4.3 Isotropic hot ions

Figure 6.25 depicts the time history of the particles flux for electrons arising from the TEM turbulence. The particle flux is calculated using the relation  $\Gamma_e = \int d^3v v_E \delta f_e$  and recorded at  $r = 0.5a$  at every time step. The various convergence tests for such a simulation with the same parameters mentioned above is discussed elaborately in Ref. [140]. It is clear from the figure that initially the mode amplitude of TEM remains very weak. Then, after the exponential growth of the linear phase of TEM instability around  $t = 20L_n/c_s$ , the particle flux (and associated fluctuations) starts saturating. We calculate the spatio-temporal evolution of the turbulent field intensity over the entire radial domain of simulation as shown in Fig. 6.27. This is important because it is the turbulent field, that incurs the radial transport under study over and above the usual drift motion of the hot ions in the presence of equilibrium drifts such as  $\nabla B$  and curvature drift, typical of a curved magnetic field geometry. The typical mode structures in the linear and nonlinear regime of TEM is depicted in Fig. 6.26. Groups of monoenergetic hot ions with energy given by  $T_h = T_i, 2T_i, 4T_i, 8T_i, 16T_i, 32T_i, 64T_i, 128T_i$  are loaded on the flux surface  $\Psi_0 = 0.5a$  where the gradients are maximum, with a isotropic pitch angle distribution. The poloidal and toroidal angles, namely,  $\theta$  and

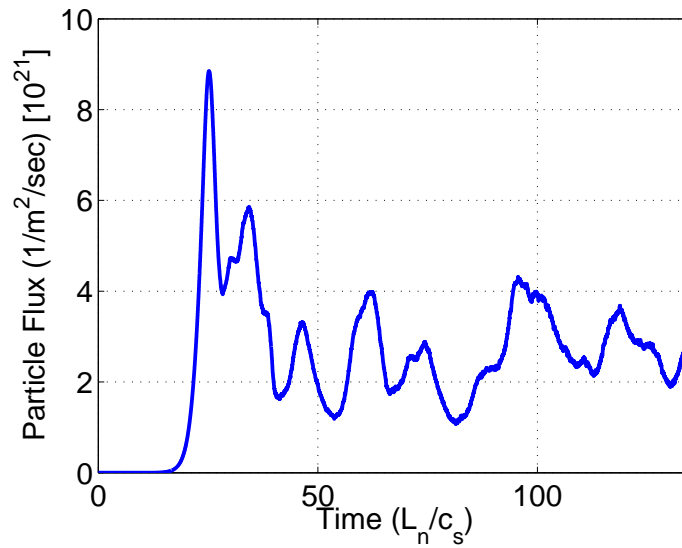


Figure 6.25: Time history of electron particle flux

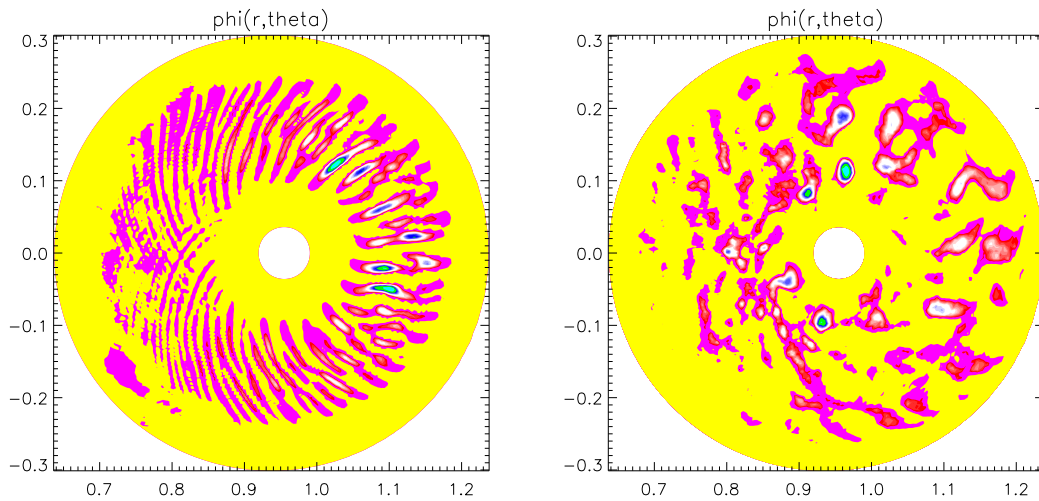


Figure 6.26: The typical snapshots of mode structure in the linear (left panel) and nonlinear (right panel) regime of the TEM turbulence for the system size  $a/\rho_i = 157$ .

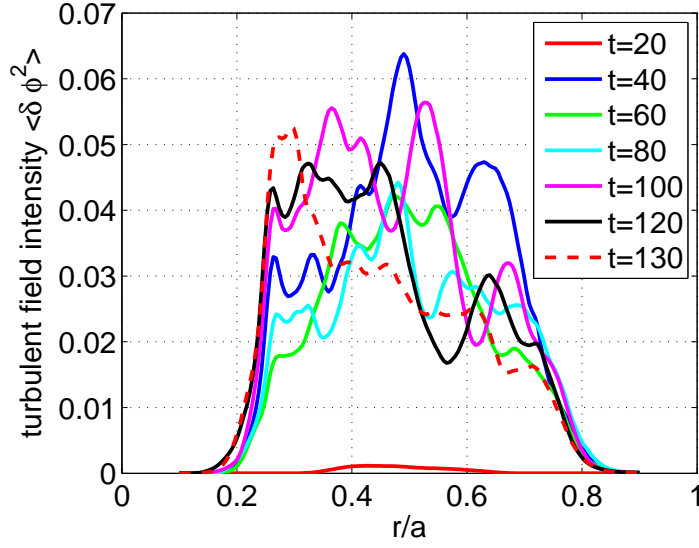


Figure 6.27: The spatio-temporal evolution of turbulent field intensity due to TEM turbulence

$\zeta$  are chosen uniformly on the entire flux surface. With the gyrokinetic equation Eq. (6.4) described in the previous subsection we push the hot ions of various energies and evaluate their positions and velocities at every instant. We calculate the mean squared displacement (MSD) for all the energy groups of hot ions, defined as

$$\langle \sigma^2(\varepsilon, t) \rangle = \frac{1}{N} \sum_{i=1}^{i=N} (r_i(\varepsilon, t) - r_i(\varepsilon, 0))^2$$

where,  $N$  is the total number of hot ions with energy  $\varepsilon$ ,  $r_i(\varepsilon, t)$  and  $r_i(\varepsilon, 0)$  are, respectively, the radial positions of the  $i^{\text{th}}$  hot ion with energy  $\varepsilon$  at time  $t$  and  $t = 0$ . Note that the number of hot ions loaded from each energy group is roughly  $6.7 \times 10^5$ . We carry out the simulation for two situations. First, we infuse the hot ions to the system when there is no TEM instability present and calculate the MSD for each group of hot ions with different energy. In the second case, the same experiment is performed but in the presence of TEM turbulence. In Fig. 6.28, left panel depicts the evolution of MSD of hot ions of different energy groups in the absence of TEM turbulence. It is clear from that figure that the hot ions undergo regular drift motion; their motion is governed by the equilibrium gradient

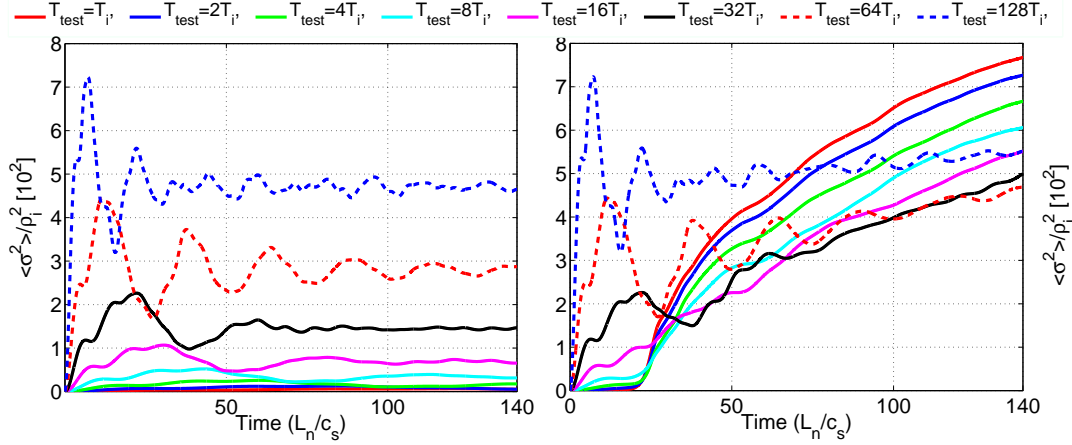


Figure 6.28: Hot ions are inserted at  $t = 0L_n/c_s$ , (a) when there is no TEM activity (left panel) and (b) when TEM turbulence is ON (right panel).

and curvature in the magnetic field and therefore the magnitude of displacement is determined merely by the energy associated with the hot ions. The bounce period being inversely proportional to the particle velocity, higher energy hot ions undergo more bounce cycles than the lower energy hot ions for a given span of time. The MSD of the hot ions, eventually, becomes constant with respect to time as there is no transport in the absence of turbulence and collisions. The right panel of Fig. 6.28, on the other hand, displays the time evolution of MSD for the hot ions when they are inserted into the system with environment conducive for TEM turbulence set by the above chosen parameters and profiles. To be noted that the moment of insertion of hot ions in both cases is  $t = 0$ . It is implied from the right panel of the figure that the hot ions undergo equilibrium drift motion till  $t = 20L_n/c_s$ , as the mode amplitude is too weak to influence the hot ion dynamics during this time interval (see Fig. 6.25). Their motion is simply governed by the equilibrium gradient and curvature in the magnetic field and therefore, the magnitude of displacement is determined by the energy associated with the hot ions. Their motion thus appears to be exactly similar to those in the absence of TEM turbulence shown in the left panel, till the moment  $t = 20L_n/c_s$ . From time  $t = 20L_n/c_s$  the energetic ions start to get affected by the electric field of TEM corresponding to the exponential growth of the linear phase of the mode. The

## Chapter 6: Interaction of microturbulence with energetic ions

least energetic hot ions are appeared to be the worst affected leading to higher value of MSD. The value of MSD decreases monotonically as the energy of the hot ions increases. This is in contrast with the case of the hot ions in the presence of ITG turbulence where the hot ions with  $T_h = 2T_i$  are observed to suffer maximum displacement among all energy groups. It is also apparent from Fig. 6.28 that highly energetic groups of hot ions such as  $T_h = 64T_i$  and  $T_h = 128T_i$  respond to the turbulent field later than the hot ions with comparatively lower energy and are least affected by the turbulent field. One may compare these results with

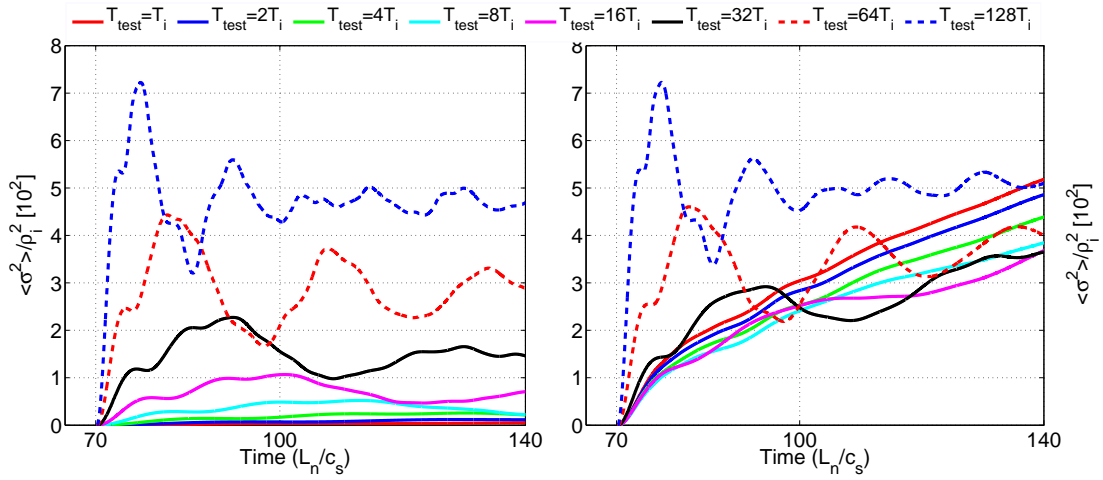


Figure 6.29: Hot ions are inserted at  $t = 70L_n/c_s$  (a) without TEM turbulence (left panel) and (b) in the presence of TEM turbulence (right panel).

that where hot ions are incorporated in the nonlinear saturation phase when the TEM turbulence is fully developed. Such a case is relevant to a situation where one has to pump hot ions in a later phase to maintain the plasma temperature propitious for fusion. The left panel of Fig. 6.29 displays the measured MSD at every instant of time for the hot ions without the presence of TEM turbulence, while, the right panel of same, presents the evolution of MSD for hot ions in the presence of TEM turbulence when inserted at an instant  $t = 70L_n/c_s$  where the turbulence attains statistical steady state reflected in Fig. 6.25. Regarding the left panel displaying MSD of hot ions in the absence of TEM, the MSD suffers only a dc shift of  $t = 70L_n/c_s$  compared to that in Fig. 6.28 without TEM turbulence. A comparison clarifies that the evolution of MSD in the present case resembles that

## Chapter 6: Interaction of microturbulence with energetic ions

of the left panel of Fig. 6.28 during first  $t = 70L_n/c_s$ . Regarding the right panel of Fig. 6.29, few important points to be noted here are: first, the measured MSD

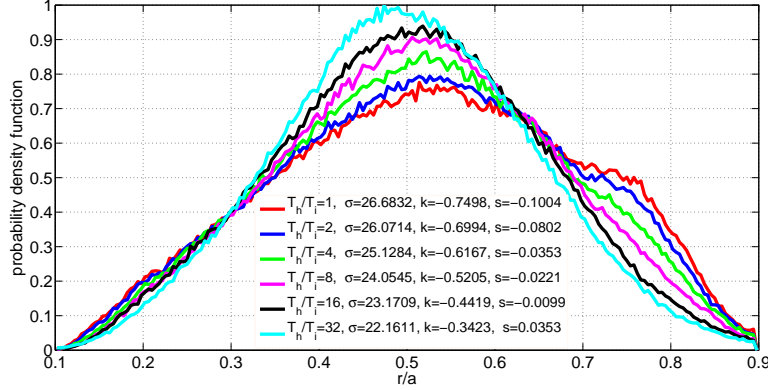


Figure 6.30: Probability distribution function of hot ions for isotropic distribution

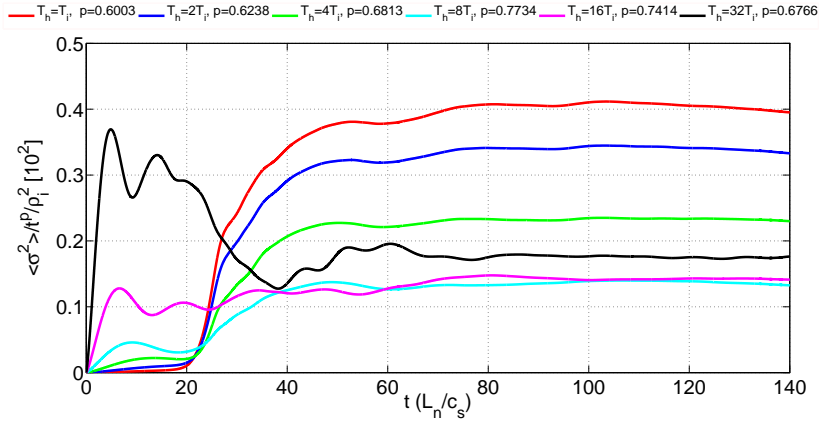


Figure 6.31:  $\langle \sigma^2 \rangle / t^p$  as a function of  $t$  for isotropic hot ions.

is quite smaller compared to the earlier case of Fig. 6.28 (right panel); second, the usual equilibrium drift motion of the hot ions with lower energy is absent and third, the higher energy hot ions, for example,  $T_h = 64T_i$  and  $T_h = 128T_i$  continue drift motion as they are weakly affected by the turbulent field. The lower energy hot ions are redistributed the very moment they fall into the turbulent field and therefore do not find time to undergo the equilibrium drift motion.

## Chapter 6: Interaction of microturbulence with energetic ions

The nature of the radial transport can be understood from the probability density function (PDF) of radial displacement of the hot ions in various energy groups under consideration. We have created 200 bins across the minor radius between  $0.1a$  and  $0.9a$  and constructed the PDF by calculating the number of hot ions in each bin for the case depicted in the right panel of Fig. 6.28, i.e., where the hot ions are inserted to the system at  $t = 0$ . The PDFs of the hot ions of various energy groups with a isotropic distribution in their pitch angle are plotted in Fig. 6.30 for radial displacements measured at  $t = 140L_n/c_s$ . At the same instant, we have also calculated the standard deviation  $\sigma$ , skewness  $s$  and kurtosis  $k$  from the simulation data using the relations  $\sigma^2 = \frac{1}{N} \sum_{i=1}^N (x_i - \bar{x})^2$ ,  $s = \sqrt{N} \frac{\sum_{i=1}^N (x_i - \bar{x})^3}{\{\sum_{i=1}^N (x_i - \bar{x})^2\}^{3/2}}$  and  $k = N \frac{\sum_{i=1}^N (x_i - \bar{x})^4}{\{\sum_{i=1}^N (x_i - \bar{x})^2\}^2} - 3$ , where standard deviation  $\sigma$  is normalized to  $a/\rho_i = 157$ . One may note that for a distribution kurtosis estimates the relative peakedness or flatness compared to the normal distribution, while skewness is a measure of symmetry about the mean. In the case of Gaussian distribution, both kurtosis and

$T_h/T_i$	$\sigma$	k	s	p
1	26.6832	-0.7498	-0.1004	0.6003
2	26.0714	-0.6994	-0.0802	0.6238
4	25.1284	-0.6167	-0.0353	0.6813
8	24.0545	-0.5205	-0.0221	0.7734
16	23.1709	-0.4419	-0.0099	0.7414
32	22.1611	-0.3423	0.0353	0.6766

Table 6.4: Energy, standard deviation, kurtosis, skewness, exponent  $p$  for isotropic hot ions

skewness as defined above become zero and infer a normal diffusion. Divergence of these quantities from zero, therefore, can be considered as the signature of a non-Gaussian distribution. A positive kurtosis characterizes a relatively peaked distribution while a negative kurtosis characterizes a relatively flat distribution. On the other hand, a positive skewness (right-skewed) represents a distribution with longer tail on the right side, while a negative skewness (left-skewed) represents a distribution with longer tail on the left side of the distribution. The standard deviation, kurtosis and skewness extracted from the simulation data at  $t = 140L_n/c_s$  are also displayed in Fig. 6.30 and separately in Table 6.4. It is apparent that the measured distributions for hot ions in all energy groups exhibit non

## Chapter 6: Interaction of microturbulence with energetic ions

Gaussian character implying an anomalous diffusion. Then question remains over whether the transport as prescribed by the non Gaussian character of distribution is subdiffusive or superdiffusive or ballistic one. This can be concluded by measuring the exponent  $p$  in the relation  $\langle \sigma^2 \rangle = \text{const.}t^p$ . For subdiffusion one has  $0 < p < 1$ , while for superdiffusion,  $1 < p < 2$ . The value  $p = 2$  implies a ballistic motion where the velocity remains constant. To evaluate  $p$  we have considered the portion of MSD between  $t = 70L_n/c_s$  and  $t = 140L_n/c_s$  where the simulation attains statistical steady state (Fig. 6.25) and determined  $p$  from log-log relation between  $\langle \sigma^2 \rangle$  and  $t^p$ . The values of  $p$  so calculated are also included in Table 6.4. It is apparent that the values of  $p$  come out to be less than 1 for all the energy groups of hot ions suggesting a subdiffusive radial transport for the hot ions under consideration. Figure 6.31 displays the plots for  $\langle \sigma^2 \rangle / t^p$  as a function of time  $t$  for the hot ions, with  $p$  determined in a way as delineated above. The values of  $p$  are displayed in the legend along with the corresponding energies of hot ions. It is clear from the figure that for the values of  $p$  extracted,  $\langle \sigma^2 \rangle / t^p$  remains virtually constant within the temporal window between  $t = 70L_n/c_s$  and  $t = 140L_n/c_s$ . This exhibition of subdiffusion could perhaps be ascribed to the presence of zonal flows. The hot ions in their radial excursion might become trapped in the vortices generated by the interplay between turbulence and zonal flows. Poloidal drift could be another plausible reason for this subdiffusive character. This kind of subdiffusive nature of transport, in particular, for radial transport in the presence of drift wave turbulence is sometimes referred to as *strange kinetics* [147]. Note that the values for various parameters listed in Table 6.4 are not universal.

The energy dependence of the observed transport of the hot ions can be estimated by calculating the quantity  $D_h = \delta \langle \sigma^2 \rangle / \delta t = (\langle \sigma_{TEM}^2(t = 140) \rangle - \langle \sigma_{noTEM}^2(t = 140) \rangle) / (t_2 - t_1)$ , with  $t_2 = 140$  and  $t_1 = 0$ . The significance of this parameter is that it characterizes the diffusion coefficient for a diffusive process. Though the diffusion coefficient is defined in terms of the standard deviation instead of MSD, it can be shown here that the result is same with standard deviation replaced by MSD. As we start from a single flux surface  $\Psi_0 = 0.5a$ , the middle of the simulation domain, the mean value of particles' position required to determine standard deviation always remains close to the the initial position which is  $r_i(\varepsilon, 0)$  and therefore the MSD and standard deviation give nearly the same result. Figure 6.32 plots  $D_h$  for the two cases discussed above, i.e., for hot ions inserted at

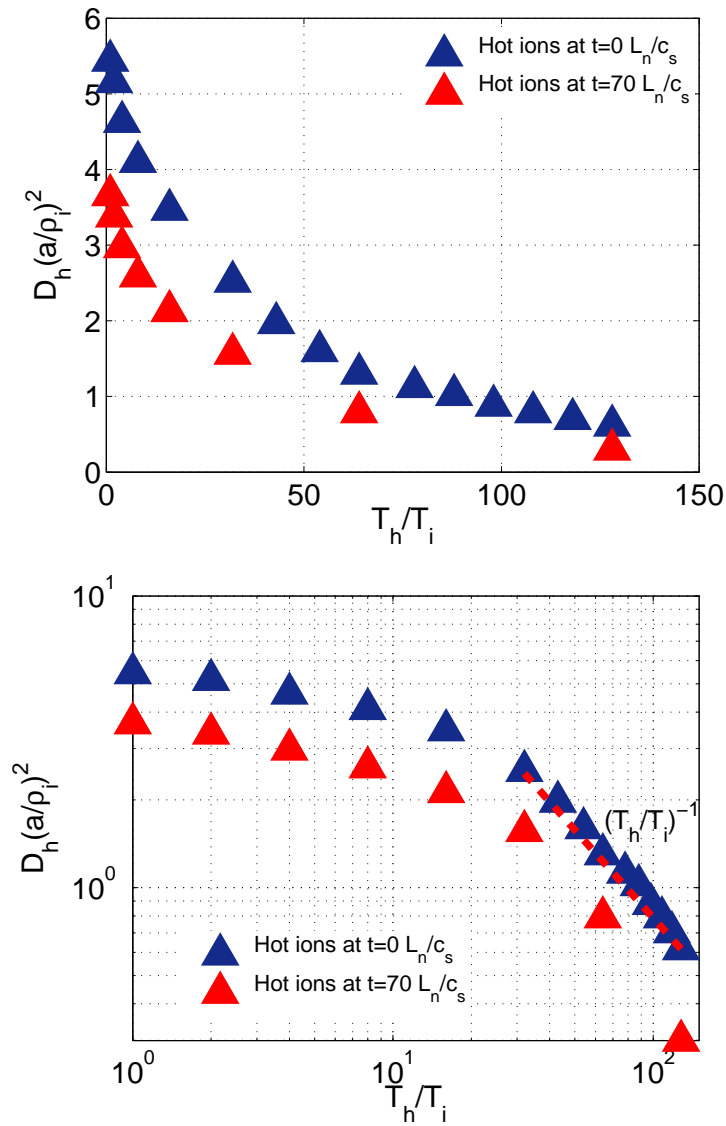


Figure 6.32:  $D_h$  versus energy of the hot ions for isotropic distribution; (a) in linear scale (upper panel) and (b) in log-log scale (lower panel).

## Chapter 6: Interaction of microturbulence with energetic ions

$t = 0$  and at  $t = 70L_n/c_s$  in linear as well as log-log plots. It is clear from the figure that in both cases  $D_h$  varies in the same way with respect to the energy of the hot ions in units of the thermal ion energy. The quantity  $D_h$  falls off faster with the energy of hot ions for lower energy but a bit slower for the hot ions with higher energy. The energy dependence, as shown in the log-log plot, appears to be inverse of the energy of the hot ions *i.e.*  $(T_h/T_i)^{-1}$  in the higher energy tail.

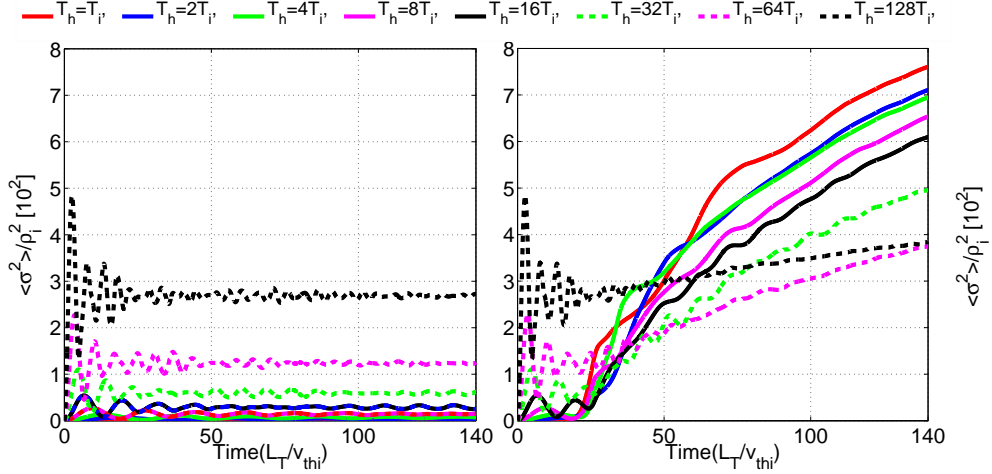


Figure 6.33: Passing hot ions are inserted at  $t = 0L_n/c_s$  (a) without TEM turbulence (left panel) and (b) in the presence of TEM turbulence (right panel).

### 6.4.4 Passing Hot Ions

Next we look at the passing hot ions. Hot ions with their pitch angle satisfying the loss cone condition  $v_{\parallel}/v > \sqrt{(1 - B_{min}/B_{max})}$  [174] where,  $B_{max}$  and  $B_{min}$ , respectively, are the maximum and minimum values of the magnetic field, are invoked in the flux surface  $\Psi_0$  at  $t = 0$ , and similar to the case of isotropic hot ions we note the MSD at every instant of time for the hot ions with energy  $T_h = T_i, 2T_i, 4T_i, 8T_i, 16T_i, 32T_i, 64T_i, 128T_i$ . We follow the same procedure as for the isotropic hot ions; once push them in the absence of TEM turbulence and measure MSD and then do the same in the presence of TEM turbulence. The left panel of Fig. 6.33 plots MSD in the absence of TEM turbulence, while the right

panel plots the same in the presence of TEM turbulence. It is clear that when the mode amplitude of TEM is very low, the particles simply move in the equilibrium fields in the same way they do in the absence of TEM turbulence. Comparison with Fig. 6.28 reveals that the amplitudes of the average squared displacement in equilibrium is less than those in Fig. 6.28. It is because of the fact that the passing particles' perpendicular velocity is very low compared to those with isotropic pitch distribution carrying a mixture of both passing and trapped particles.

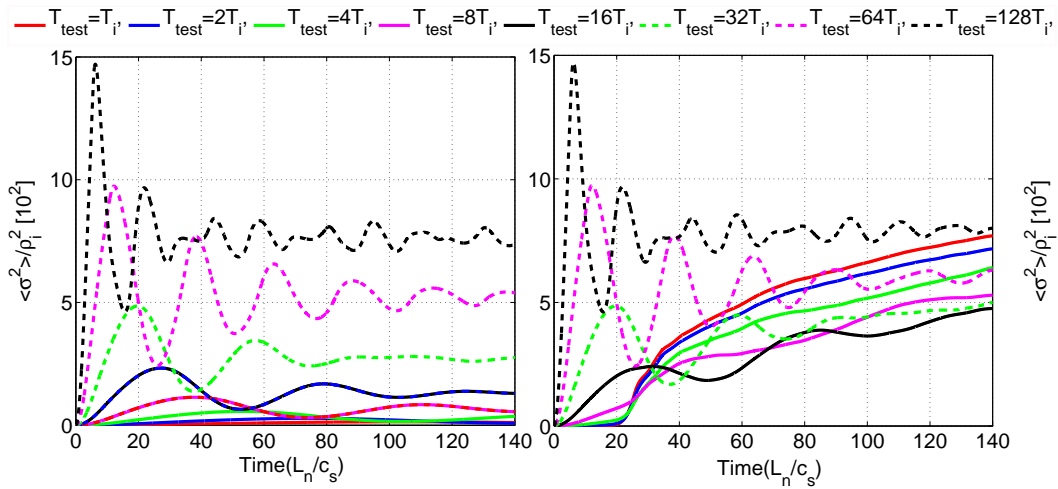


Figure 6.34: Trapped hot ions are inserted at  $t = 0L_n/c_s$  (a) without TEM turbulence (left panel) and (b) in the presence of TEM turbulence (right panel).

### 6.4.5 Trapped Hot Ions

The same experiment has been carried out for the trapped hot ions also. We incorporate hot ions into the system at  $t = 0$  with pitch angle chosen in such a way that they are in the trapped cone dictated by the condition  $v_{\parallel}/v < \sqrt{(1 - B_{\min}/B_{\max})}$  [174]. The energies of the hot ions chosen are  $T_h = T_i, 2T_i, 4T_i, 8T_i, 16T_i, 32T_i, 64T_i, 128T_i$ . This set of particles are having a large perpendicular velocity and hence stronger finite Larmor radius effect. Figure 6.34 depicts the motion of these purely trapped hot ions in the absence (left panel) and presence (right panel) of TEM turbulence. Compared to the earlier cases of hot ions with isotropic and

passing distribution, the amplitude of the trapped hot ions' MSD during the equilibrium drift motion is the highest. This is because of the large perpendicular velocity of the trapped hot ions; their mobility is restricted along the field direction and most of the movement is only in the poloidal and radial directions. That is why, we record the highest MSD in the case of trapped particles when there is no TEM turbulence or mode amplitude is very weak. Like the other two cases discussed above, these trapped hot ions also exhibit similar motion during the initial period when either the system is free of TEM turbulence or amplitude of the mode is very low.

### 6.4.6 Nature of Transport

To characterize the nature of radial transport of the passing and trapped hot ions we have again evaluated the PDFs for the two cases independently, following the same procedure elaborated in the earlier case of isotropic hot ions. These PDFs for all energy groups of hot ions under discussion, are portrayed in Fig. 6.35 for the passing (upper panel) and trapped (lower panel) hot ions. The corresponding values of the standard deviation  $\sigma$ , kurtosis  $k$  and skewness  $s$ , as extracted from the simulation data at  $t = 140L_n/c_s$  are also displayed in the legend for each group of hot ions. It is clear that the PDFs are substantially deviated from Gaussian implying non-diffusive transport again. We have estimated the exponent  $p$  from the relation  $\langle \sigma^2 \rangle = \text{const.}t^p$  in a similar fashion as in the case of isotropic

$T_h/T_i$	$\sigma$	k	s	p
1	26.2631	-0.7460	-0.1456	0.5638
2	25.5805	-0.7043	-0.1165	0.7048
4	25.4547	-0.6699	-0.0809	0.6453
8	24.8399	-0.5989	-0.0492	0.7285
16	24.3184	-0.5637	-0.0240	0.7543
32	22.1076	-0.4623	-0.0100	0.7517

Table 6.5: Energy, standard deviation  $\sigma$ , kurtosis  $k$ , skewness  $s$  and exponent  $p$  in  $\langle \sigma^2 \rangle \propto t^p$  for the passing hot ions

hot ions. All the values of  $p$  are found to be well below 1 evincing subdiffusive radial transport. We plot  $\langle \sigma^2 \rangle / t^p$  as a function of  $t$ , for different values of  $p$  in

## Chapter 6: Interaction of microturbulence with energetic ions

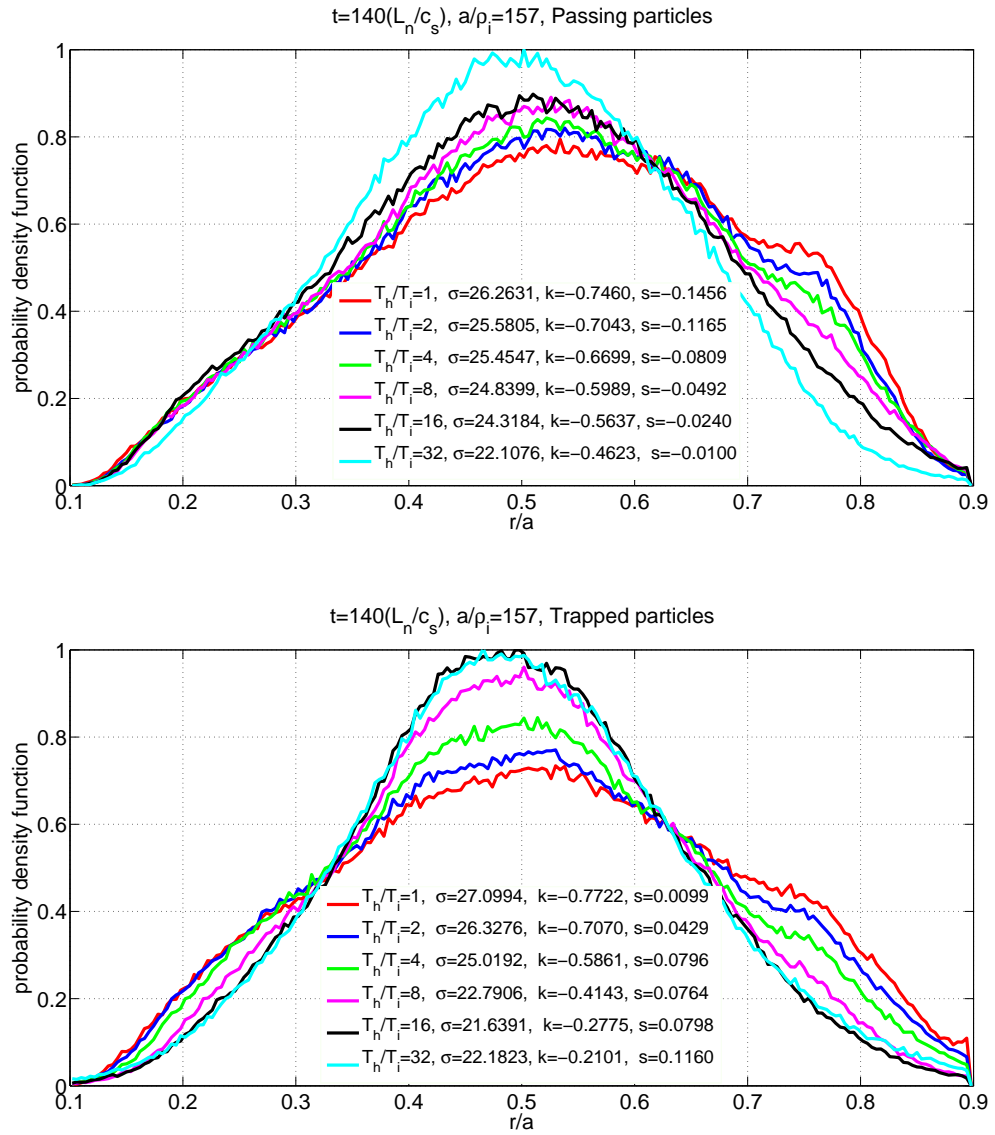


Figure 6.35: (a) Upper panel: PDFs for hot ions with passing distribution, (b) lower panel: PDFs for hot ions with trapped distribution

## Chapter 6: Interaction of microturbulence with energetic ions

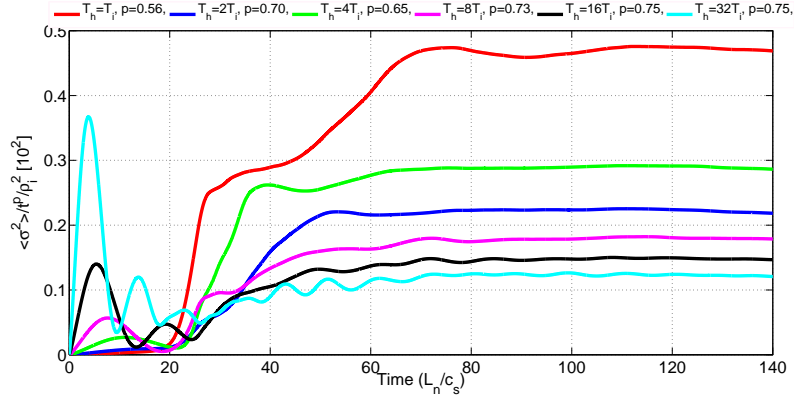


Figure 6.36:  $\langle \sigma^2 \rangle / t^p$  as a function of  $t$  for passing hot ions.

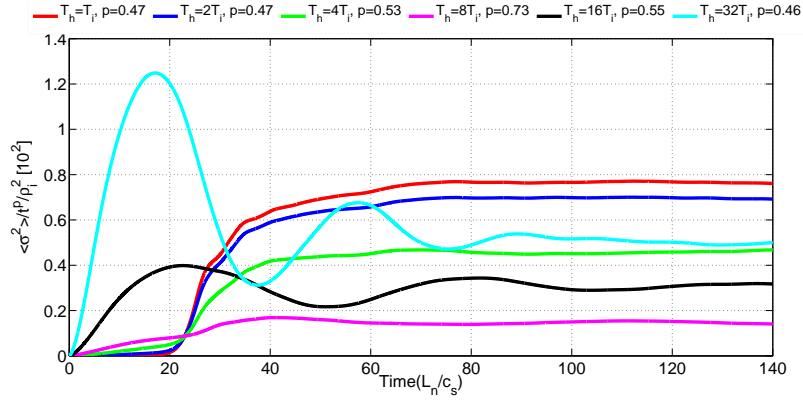


Figure 6.37:  $\langle \sigma^2 \rangle / t^p$  as a function of  $t$  for trapped hot ions.

$T_h/T_i$	$\sigma$	$k$	$s$	$p$
1	27.0994	-0.7722	0.0099	0.4683
2	26.3276	-0.7070	0.0429	0.4731
4	25.0192	-0.5861	0.0796	0.5296
8	22.7906	-0.4143	0.0764	0.7340
16	21.6391	-0.2775	0.0798	0.5478
32	22.1823	-0.2101	0.1160	0.4659

Table 6.6: Energy, standard deviation  $\sigma$ , kurtosis  $k$ , skewness  $s$  and exponent  $p$  in  $\langle \sigma^2 \rangle \propto t^p$  for the trapped hot ions

Figs. 6.36 and 6.37 for the passing and trapped hot ions respectively. It is evident from both figures that  $\langle \sigma^2 \rangle / t^p$  remains roughly constant for the extracted values of the exponent  $p$  corroborating the fact that the hot ions, whether passing or trapped exhibit subdiffusive nature. The values of standard deviation, kurtosis, skewness, and exponent  $p$ , extracted from the simulation data are displayed in Tables 6.5 and 6.6 for the passing and trapped particles respectively. Again, we want to comment that these values are not universal.

### 6.4.7 Energy Scaling of Hot Ions

Next we evaluate the energy dependence for the radial transport of passing and trapped hot ions. The energy dependence of net MSD, normalized by the time interval from  $t = 0$  to  $t = 140L_n/c_s$  is presented in Fig. 6.38 for the passing (upper panel) and trapped particle (lower panel), respectively, in linear plot. The corresponding log-log plots are displayed in Fig. 6.39. The quantity  $D_h = \delta \langle \sigma^2 \rangle / \delta t = (\langle \sigma_{TEM}^2(t = 140) \rangle - \langle \sigma_{noTEM}^2(t = 140) \rangle) / (t_2 - t_1)$ , with  $t_2 = 140$  and  $t_1 = 0$  is plotted as a function of  $T_h/T_i$  in the figures. It is clear that  $D_h$  falls very rapidly in the lower energy range of the hot ions, while decays slowly for the higher energy of the hot ions (Fig. 6.38). This implies that TEM turbulence is more dominant on the hot ions with lower energy but weakly affects those with higher energy. From the power law  $D_h = const.(T_h/T_i)^a$ , it appears that transport scales as  $(T_h/T_i)^{-1}$  for purely passing hot ions, while it falls as  $(T_h/T_i)^{-2}$  for purely trapped hot ions in the higher energy limit of the hot ions (Fig. 6.39). The gyroaveraging and orbit averaging along with wave particle resonance are the factors accounting for this type of power law for the hot ions transport. For passing hot ions only orbit averaging ( $\sim (T_h/T_i)^{-1/2}$ ) and wave particle resonance in the parallel direction ( $\sim (T_h/T_i)^{-1/2}$ ) contribute to the energy scaling giving it a  $(T_h/T_i)^{-1}$  dependence. In contrast, gyroaveraging is the extra parameter that contributes to the trapped hot ions' energy scaling. Thus, gyroaveraging ( $\sim (T_h/T_i)^{-1/2}$ ), drift orbit averaging ( $\sim (T_h/T_i)^{-1/2}$ ) and drift bounce resonance [175] ( $\sim (T_h/T_i)^{-1}$ ) altogether give a  $((T_h/T_i)^{-2})$  scaling for the trapped hot ions. The observed  $(T_h/T_i)^{-1}$  scaling of the isotropic hot ions suggests (Fig. 6.32) that the transport of these hot ions is perhaps dominated by the passing hot ions.

It is to be noted that very long time simulations are computationally very expen-

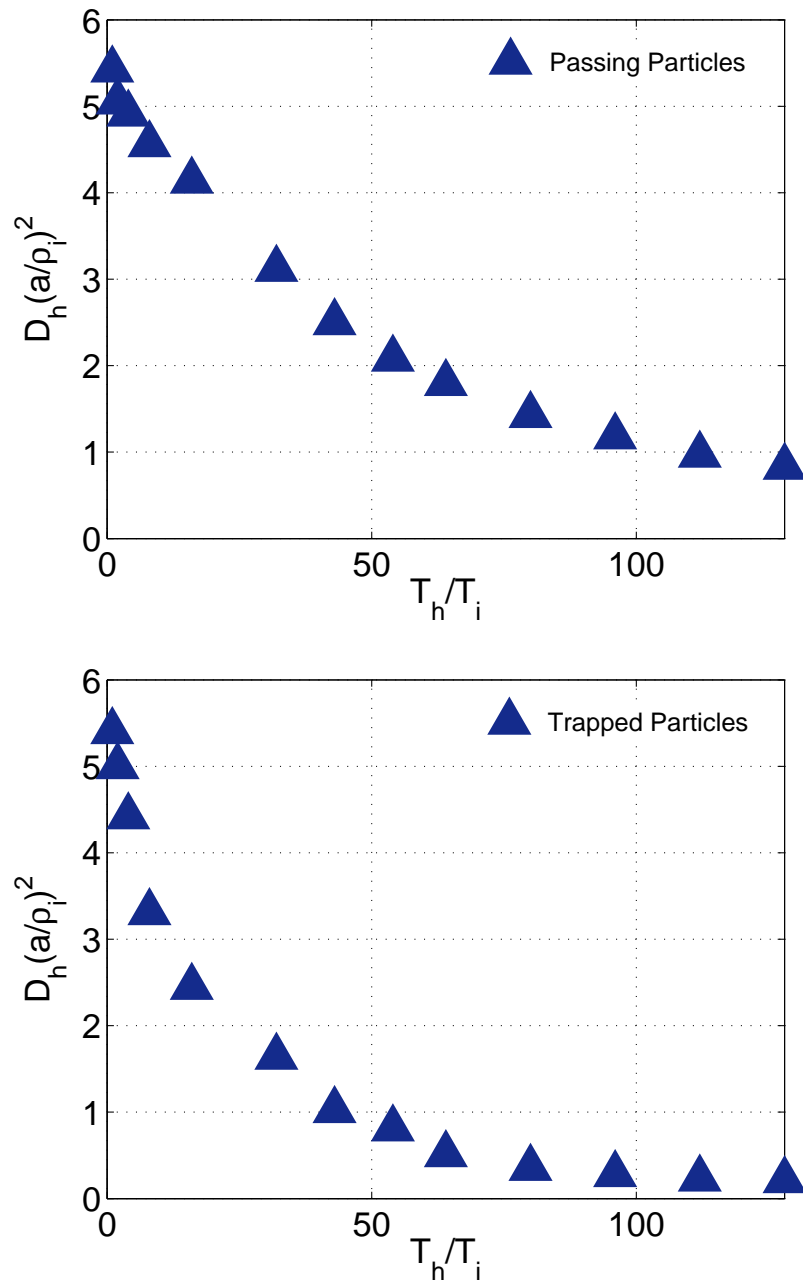


Figure 6.38: (a) Upper panel:  $D_h$  versus energy of the hot ions for passing distribution, (b) Lower panel:  $D_h$  versus energy of the hot ions for trapped distribution in linear scale.

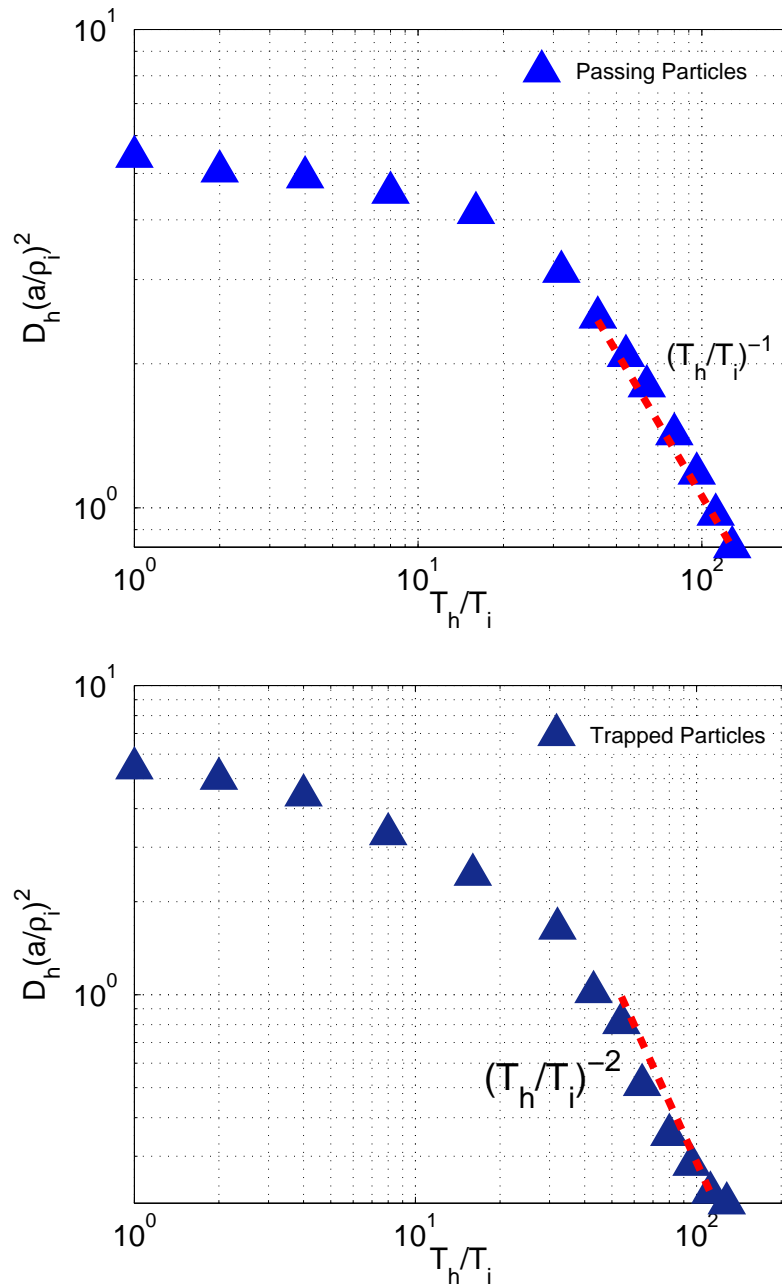


Figure 6.39: (a) Upper panel:  $D_h$  versus energy of the hot ions for passing distribution, (b) Lower panel:  $D_h$  versus energy of the hot ions for trapped distribution in log-log scale.

sive in the case of TEM turbulence as one has to resolve the electron time scales along with that of the ions. However, on the basis of the cross checks carried out in ITG mode simulation of the previous section by doubling the simulation time, we believe that the results of the present section will remain qualitatively same even if we wait for our simulation to attain strict quasisteady state by lengthening the simulation time.

### 6.5 Conclusion

In the first part of the present work we have elucidated the effect of the energetic ions on the thermal ion temperature gradient mode. For the purpose we use a global linear gyrokinetic code EM-GLOGYSTO, where the energetic particles are added nonperturbatively. We consider all the three species namely, thermal ions, electrons and energetic ions nonadiabatically, where the density perturbation of the respective species contains all the kinetic effects, such as, Landau resonance, magnetic drift resonance, transit resonance, finite Larmor radius effect, etc. However, for simplicity we neglect the trapped particles and magnetic fluctuation in the present analysis. We believe that the inclusion of these would not change the effect of energetic ions on the ion temperature gradient mode of the thermal ions qualitatively. We consider different  $\eta$  profiles for the energetic ions compared to the background thermal ions, to see if at all there is any effect of the energetic ions'  $\eta$  profile on the ion temperature gradient mode. However, all the three cases of different  $\eta$  profiles show the same result qualitatively and quantitatively. Thus, we find that the energetic ions irrespective of the  $\eta$  profile are stabilizing for the ion temperature gradient driven mode. In the case of He ions the stabilization is further enhanced. The stabilization is thought to be brought about by the dilution of the background thermal ions that drive the ion temperature gradient mode. Usually, the ion temperature gradient mode is observed to be stabilized by variety of factors, e.g., increasing fraction of  $T_i/T_e$ , impurity, electromagnetic effect, ion transit term,  $k_{\parallel}v_{\parallel}$ , etc. Thus, one may add another stabilizing factor to the list, that is, the presence of the energetic ions in the system. This kind of stabilization is experimentally observed [130, 131]. The stabilization is strongly dependent on the energetic ion population with respect to the thermal ions. The growth rate of the

## Chapter 6: Interaction of microturbulence with energetic ions

ITG mode decreases almost linearly with the increasing fraction of the energetic ions' population. The complete stabilization occurs at  $n_f/n_e \geq 0.35$  for the singly charged energetic ions. He ions on the other hand, have stronger effect on the ITG mode. The stabilization shows the same trend as the singly charged ions but falls more rapidly and one observes complete stabilization at  $n_f/n_e \geq 0.15$ . The stabilization incurred by these energetic ions however is pronounced only at the lower energy region of the energetic ions. The strong change in the growth rate as well as the mode frequency of the ITG mode is observed only in the region  $T_f/T_e \leq 10$  beyond which, the mode frequency and growth rate, both remain insensitive to the temperature variation of the energetic ions. This can be understood as that only in the low energy region of these energetic ions, the ion temperature gradient mode and energetic ions can interact efficiently and therefore the effect of each other on their respective properties is reasonable only in this regime of lower temperature or lower energy of the energetic ions. Thus, one may anticipate that the He ash in the fusion plasma can play a significant role in the stabilization of the ITG mode and thus in the reduction of ion energy and particle loss from the core of the tokamak. An estimation of the transport is carried out by calculating the thermal diffusivity on the basis of mixing length theory. The diffusivity is found to be reduced significantly in the presence of the energetic ions. The He ions are found to have stronger effect on the thermal ion diffusivity.

In the second part, the transport of hot ions induced by the ion temperature gradient driven turbulence is studied using the global nonlinear gyrokinetic code GTS, and with the aid of passive tracer method. The hot ions, treated as passive particles are pushed in the turbulent field using the gyrokinetic equations. At every instant of time the mean squared displacement and standard deviation for the hot ions are recorded. The probability distribution function for radial displacement is also estimated along with corresponding kurtosis and skewness. The nature of transport is determined by evaluating the exponent  $p$  from the relation  $\langle \sigma^2 \rangle \propto t^p$ . The major results can be itemized as follows.

- The MSD for a given group of hot ions characterized by a given energy increases with the increment in the system size.
- The MSD for all groups of energy of hot ions shows signature of saturation for  $a/\rho_i = 157$ , increases linearly at first, then shows a weak tendency to

## Chapter 6: Interaction of microturbulence with energetic ions

saturate for  $a/\rho_i = 315$  and increases almost linearly for  $a/\rho_i = 500$  after the initial abrupt rise for all the three cases with respect to time.

- For all the cases of system size under consideration, hot ions transport is maximum for  $T_h = 2T_i$  and decreases monotonically with increasing energy, with a tendency of saturation at higher value of hot ion energy for the chosen parameters.
- For energy below  $T_h = 16T_i$ , the transport of hot ions exhibits significant dependence on the system size; it is maximum for  $a/\rho_i = 500$  and decreases with the decreasing system size. However, at  $T_h = 16T_i$  transport is nearly the same for all the three values of system size. One expects that it converges to the same value for the hot ions with energy beyond  $T_h = 16T_i$ . Thus, one can conclude that while transport of hot ions with lower energy depends strongly on the system size, for hot ions with higher energy, in contrast, it remains practically independent of the system size.
- It is evident that as the system size increases till  $a/\rho_i = 315$ ,  $D_h$  increases linearly, while the increment is very minor beyond this point showing a tendency of saturation at higher value of the system size. Thus, with increasing system size, transport of hot ions for all groups of energy starts increasing initially and shows trend of saturation for larger system size.
- The exponent  $p$  in  $\langle \sigma^2 \rangle \propto t^p$  is found to be smaller than 1 for smaller device size, which gradually increases with increasing system size and finally approaches unity for larger system size. This indicates that the transport process, in the smaller machine size is subdiffusive for thermal as well as hot ions, which however becomes diffusive for larger device size. The measurement of PDF, kurtosis and skewness corroborate the conclusion derived from the values of  $p$
- The check for quasisteady state and robustness of  $p$  reveals that the results remain qualitatively the same. For the purpose, we have doubled the simulation time ( $t = 2500L_T/v_{thi}$ ) such that the simulations are well in a quasisteady state. We have evaluated the mean  $p$  again and observed that

## Chapter 6: Interaction of microturbulence with energetic ions

the values of  $p$  remain nearly same as the old  $p$  values evaluated in the short time simulations ( $t = 1200L_T/v_{thi}$ ).

The effect of TEM turbulence on the hot ion radial transport in tokamaks is studied in the last part of the present work. Results are demonstrated for three cases, differing in the pitch angle distribution; case (1) isotropic hot ions, case (2) purely passing hot ions, and case (3) purely trapped hot ions. For isotropic distribution, we have illustrated the results for two cases. In the first case, hot ions are inserted at  $t = 0$  before the trapped electron mode turbulence comes into existence, while in the second case, hot ions are introduced at a later time at  $t = 70L_n/c_s$ , that is, in the nonlinear saturation phase when TEM turbulence is fully developed. The probability density function (PDF) of radial displacement is constructed for each case for all the energy groups of hot ions. Also the energy dependence of hot ions' radial transport is evaluated in the present study. The major findings are given in the following.

- The mean squared displacement is the highest for the hot ion species with energy equal to the thermal ions' energy and decreases monotonically with the energy of the hot ions for all the cases encapsulated in the present study.
- The transport process exhibits anomalous character. The PDFs of the hot ions show deviation from Gaussian irrespective of energy and pitch angle distribution. Evaluation of kurtosis, skewness and the exponent  $p$  in the power law  $\langle \sigma^2 \rangle \propto t^p$  suggests subdiffusion for radial transport in small to medium size machines.
- Radial transport of the isotropic and purely passing hot ions manifests an inverse dependence on their energy, while that of the purely trapped hot ions demonstrates an inverse square dependence on energy. This means that the higher energy trapped hot ions are less likely to be redistributed by the turbulent field than the passing and isotropic hot ions.

# Chapter 7

## Conclusion and Future Direction

### 7.1 Conclusions

In Chapters 2 and 3, we have focused on the effect of treating the electrons on the same physics footing as the ions, i.e., fully nonadiabatic/kinetic electrons using EM-GLOGYSTO based on a 2-D linear, global, gyrokinetic model. The model includes both passing and trapped particles, profile variations, true ion to electron mass ratio, arbitrary order FLR effects, transit/trapped particle resonances, poloidal and radial coupling. A comprehensive description of ion temperature gradient (ITG) mode, trapped electron coupled ion temperature gradient driven mode (ITG-TEM), and trapped electron mode (TEM) in the presence of the passing nonadiabatic electrons has been provided.

We have observed rise in the linear growth rate of the ITG mode, ITG-TEM, and TEM in the presence of kinetic/nonadiabatic electrons. The linear, global mode structures are broken apart near the mode rational surfaces where the parallel wave vector ( $k_{\parallel}$ ) is zero. The phase lag between potential and density perturbations introduced by the kinetic electrons near the mode rational surfaces makes these modes further unstable. The perpendicular wave vectors rise because of the production of the short scales near the mode rational surfaces. This, eventually, results in the reduction of the mixing length estimate of the transport of thermal ions below the adiabatic electron model. However, nonlinear global simulations

## Chapter 7: Conclusion and Future Direction

will be necessary to confirm this fact, considering that there are situations where nonlinear effects tend to introduce larger scales, e.g., in the case of inverse cascades, and where mixing length estimates have proven wrong. It is perhaps worth noting that a flux-tube model with correct implementation of magnetic shear and boundary conditions along the magnetic field line should also be able to reproduce the fine radial structures at the mode rational surfaces resulting from nonadiabatic passing electron dynamics. Although, to our knowledge, such features have not been clearly and comprehensively pointed out in the past literature, one may cite Ref. [62] which has reported the breaking of global mode structure near mode rational surfaces in the presence of the kinetic electrons.

We have presented some features of the electron temperature gradient (ETG) driven mode using the linear, global, gyrokinetic model in toroidal geometry that treats both species, namely, ions and electrons fully gyrokinetically, taking into account all the kinetic effects. The effect of Debye Shielding, breaking of isomorphism of ITG and ETG modes even in the electrostatic limit when the other species is considered fully gyrokinetically are revealed one by one. Also, the global mode structure and stability properties of the low- $n$  (toroidal mode number) toroidal universal mode driven by the density gradient in the presence of finite toroidicity on the intermediate scale in  $k_{\perp}\rho_{Li}$ , along with its coupling to the trapped electrons have been studied perhaps for the first time to our knowledge using the global, linear, gyrokinetic model. The model considers both passing electrons and ions to be fully nonadiabatic incorporating toroidal coupling effects, magnetic drift resonances, Landau resonance effects, transit harmonic resonances, finite Larmor radius to all orders, and orbit width effect for both species. The effect of finite  $\beta$  is also studied in the frame of an electromagnetic model that retains the transverse magnetic perturbation.

The steep density profiles are observed to affect the ITG modes dramatically making the latter unstable even at higher wave number regime. At this higher wave number regime the ITG mode, in general, remains stable. However, if the density gradient is strong enough, the ions can act nonadiabatically at the higher wave number regime giving rise to what is called the short wavelength ion temperature gradient (SWITG) mode. We have presented the features of the SWITG mode in the presence of trapped electrons using EM-GLOGYSTO. A comparison of parametric dependencies for the two cases of the SWITG mode with and

## Chapter 7: Conclusion and Future Direction

without the trapped electrons is presented. In line with the global model, we also compare the results from a local gyrokinetic model for the two cases, with and without the trapped electrons. The trapped electrons have strong effect on the SWITG modes raising the growth rate substantially. The two dimensional mode structure of the SWITG mode has been found to be quite global occupying a considerable fraction of the tokamak cross section for the chosen set of parameters establishing the necessity of a global model to study such a phenomenon. It acquires toroidal like nature in the presence of the trapped electrons. The increased fraction of the trapped electrons with increased toroidicity is the main factor behind this flipping of the mode from the slab nature to toroidal nature. The mode vanishes below a critical  $\eta_i$ ; it transforms itself from the dominantly ion mode to the dominantly trapped electron mode when effects of trapped electrons are taken into account. No significant diffusivity (mixing length estimate) is observed at higher  $k_\theta \rho_{Li}$  where the SWITG mode is strongest for both cases with and without the trapped electrons. This fact is corroborated by the nonlinear simulation using the code Gyrokinetic Electromagnetic Numerical Experiment (GENE). The estimate of relative contribution of the higher  $k_y \rho_s$  part of the heat flux spectrum corresponding to the SWITG mode reveals that the contribution of the SWITG mode to the total heat flux is very low compared to the contribution from the lower  $k_y$  part of the spectrum typically belonging to the standard ITG mode. The zonal flow shearing rate has been found to be much higher than the linear mode frequency and growth rate of the SWITG mode suggesting that the zonal flows are the main saturation mechanisms of the SWITG turbulence. The higher zonal flow shearing rate appears to compensate for the higher growth rate of the mode leading to a minimal contribution to the thermal ion heat flux from the higher  $k_y \rho_s$  part of the spectrum relevant to the SWITG mode irrespective of the density scale length which determines the strength of the SWITG mode with respect to the standard ITG linearly. One may note that in real experiments steep density profiles are often observed during the formation of transport barriers. However, such steep profiles happen to occur in the presence of reverse shear. Therefore, it could be interesting to see how the properties of SWITG mode change in the presence of the nonmonotonic  $q$  profile. It also is equally possible that such steep profiles can affect the TEM and electron temperature gradient (ETG) modes. Such issues remain to be addressed.

## Chapter 7: Conclusion and Future Direction

The physics of energetic ions in the burning plasma is now a topic of immense interest. Their population has been observed to have tremendous impact on the MHD and non-MHD activities in the tokamak plasma. A computationally efficient means to study the effect of these energetic ions on the ITG mode is to incorporate them linearly into the existing global gyrokinetic model of EM-GLOGYSTO. We consider all the three species namely, thermal ions, electrons and energetic ions nonadiabatically, where the density perturbation of the respective species contains all the kinetic effects, such as, Landau resonance, magnetic drift resonance, transit resonance, finite Larmor radius effect, finite orbit width effect, etc. We observe that the energetic ions irrespective of the  $\eta$  profile are stabilizing for the ion temperature gradient driven mode. In the case of He ions the stabilization is further enhanced. The stabilization is thought to be brought about by the dilution of the background thermal ions that drive the ion temperature gradient mode. The stabilization is strongly dependent on the energetic ion population with respect to the thermal ions. The growth rate of the ITG mode decreases almost linearly with the increasing fraction of the energetic ions. He ions on the other hand, have stronger effect on the ITG mode. The stabilization incurred by these energetic ions however is pronounced only at the lower energy region of the energetic ions. Thus, one may anticipate that the He ash in the fusion plasma can play a significant role in the stabilization of the ITG mode and thus in the reduction of ion energy and particle loss from the core of the tokamak. The mixing length estimate of diffusivity is observed to be reduced significantly in the presence of the energetic ions. The He ions are found to have stronger effect on the thermal ion diffusivity. However, nonlinear simulation, although seems to be very expensive computationally, would be required to see the nonlinear evolution of the ITG mode in the presence of energetic ions along with concomitant impact on thermal ion heat flux.

The effect of the microturbulence on the energetic ions, on the other hand, is another issue of great concern. The recent experiments on the redistribution of the energetic ions have given impetus to the investigation of prospective effect of turbulent field on the energetic ions. Inspired by it, the transport of energetic ions induced by the ITG mode and TEM turbulence is studied using the global, nonlinear, gyrokinetic code Gyrokinetic Tokamak Simulation (GTS), and with the aid of the passive tracer method. The energetic ions, treated as passive particles are pushed in the turbulent field using the gyrokinetic equations. The observed

## Chapter 7: Conclusion and Future Direction

transport of energetic ions is found to have strong dependence on the size of the system and their energy. The transport reduces as the energy of the energetic ions increases. Also, the subdiffusive nature of transport for small system size transforms into the diffusive one for bigger system size. The magnitude of transport initially increases with system size and then saturates at larger system size. Radial transport of the isotropic and purely passing hot ions manifests an inverse dependence on their energy, while that of the purely trapped hot ions demonstrates an inverse square dependence on energy in the presence of the TEM turbulence. This means that the higher energy trapped hot ions are less likely to be redistributed by the turbulent field than the passing and isotropic hot ions.

### 7.2 Future Work

In most of the studies using the global, linear, gyrokinetic code EM-GLOGYSTO, we have simplified the model by ignoring many other interesting physics issues. The equilibrium flows as well as electromagnetic and Shafranov shift effects can, in certain cases, be important for the instabilities that were studied in these chapters. One would therefore be curious to see how these factors can change the existing results.

It is also to be pointed out here that the trapped particles model considers deeply trapped particles only. The barely trapped particles or those near the passing trapped boundary have been excluded. Also, the passing particles are considered as fully or deeply passing keeping  $v_{\parallel}$  constant with respect to time.

In the linear model, the numerical solution exists for only the unstable modes, i.e., modes with positive growth rate. This model can be upgraded to be able to find the damped modes also as that of the work detailed in Ref. [22]. It will help to predict the thresholds of the instabilities more correctly.

Chapters 4 and 5 deal with the universal toroidal drift instability and short wavelength ion temperature gradient modes which are unstable in the presence of steep density profiles, i.e, strong density gradient. However, such steep profiles happen to occur in the presence of reverse shear during the formation of transport barriers. Therefore, it could be interesting to see how the properties of these modes change in the presence of the nonmonotonic  $q$  profile. It also is equally possible

## Chapter 7: Conclusion and Future Direction

that such steep profiles can affect the TEM and electron temperature gradient (ETG) modes. Such issues remain to be addressed. The nonlinear results on the SWITG mode are given in the presence of adiabatic electrons. However, addition of trapped electrons in the nonlinear simulation will allow one a broader study on the nonlinear SWITG mode and nonlinear TEM in the presence of steep density profile.

The present linear model equipped with the energetic ions is valid only for the electrostatic case. This can be extended to incorporate electromagnetic perturbations. This would enable one to study the kinetic ballooning mode, energetic particle modes, toroidal Alfvén mode, etc. Also, we have shown the results for only one value of  $a/\rho_i$ . A complete  $a/\rho_i$  scan would help one to project the results to ITER like scales.

The role of microturbulence in the transport of the energetic ions is studied using the nonlinear, global, gyrokinetic code GTS. In the present work, the energetic ions have been considered as *passive* particles, i.e., they do not contribute to the net electric field and hence do not enter the gyrokinetic Poisson equation. This model can be made more consistent and hence more effective by incorporating these energetic ions as a third *active* species that would contribute to the net field. This will allow one to investigate the effect of the energetic ions on the microinstabilities such as ITG mode, TEM, etc., in the nonlinear phase. Moreover, it would be interesting to setup a lower dimensional mathematical model and compare it with the results of our simulations. The particle pinch effect has emerged as an area of intense research in tokamak plasmas. It may be interesting to investigate the effect of energetic particle pinch in the presence of microturbulence while studying nondiffusive transport. Inclusion of nonadiabatic electrons in the ITG turbulence studies will make the investigation more comprehensive.

# Bibliography

- [1] J. Wesson, Tokamaks (Clarendon Press, Oxford, 2004).
- [2] Lindl, J. D., Inertial Confinement Fusion (Springer-Verlag, New York, 1998).
- [3] <http://www.iter.org>.
- [4] W Horton, Rev. Mod. Phys. **71**, 735 (1999).
- [5] P. Terry, Rev. Mod. Phys. **72** (1), 109 (2000).
- [6] Keith H. Burrell, Science **281**, 1816 (1998).
- [7] F. F. Chen, *Introduction to Plasma Physics and Controlled Fusion* Vol. 1.
- [8] L. I. Rudakov and R. Z. Sagdeev, Nuclear Fusion Suppl **2**, 481 (1962).
- [9] B. Coppi, M. N. Rosenbluth, and R. Z. Sagdeev, Phys. Fluids **10**, 582 (1967).
- [10] F. Romanelli, Phys. Fluids B **1**, 1018 (1989).
- [11] S. Brunner, M. Fivaz, T. M. Tran and J. Vaclavik, Phys. Plasmas. **5**(11), 3929 (1998).
- [12] R. D. Sydora, V. K. Decyk and J. M. Dawson, Plasma Phys. Control. Fusion **38**, (1996).
- [13] M. A. Beer and G. W. Hammett, Phys. Plasmas **3**(11), 4018 (1996).
- [14] B. H. Fong and T. S. Hahm, Phys. Plasmas **6**, 188 (1999).
- [15] W. W. Lee, J. L. V. Lewandowski, T. S. Hahm, Z. Lin, Phys. Plasmas **8**, 4435 (2001).

## Bibliography

- [16] Cheng C.Z., Nucl. Fusion **22**, 773 (1982).
- [17] Aaron J. Redd, Arnold H. Kritz, Glenn Bateman, Gregory Rewoldt and W. M. Tang, Phys. Plasmas **6**, 4 (1999).
- [18] P. Malinov and F. Zonca, J. Plasma Physics **71**, 3 (2005).
- [19] P. N. Guzdar, C. S. Liu, J. Q. Dong, and Y. C. Lee, Phys. Rev. Lett. **57**, 2818 (1986).
- [20] Y. C. Lee, J. Q. Dong, P. N. Guzdar, and C. S. Liu, Phys. Fluids **30**, 1331 (1987).
- [21] W. Horton, B. G. Hong, and W. M. Tang, Phys. Fluids **31**, 2971 (1988).
- [22] J. Q. Dong, H. Sanuki, K. Itoh, and Liu Chen, Phys. Plasmas **9**, 4699 (2002).
- [23] W. Dorland, F. Jenko, M. Kotchenreuther, and B. N. Roger, Phys. Rev. Lett. **85**, 5579 (2000).
- [24] R. Singh, P.K. Kaw, J. Weiland, Nuclear Fusion **41**, 1219 (2001).
- [25] M. N. Rosenbluth and M. L. Sloan, Phys. Fluids **14**, 1725 (1971).
- [26] Kadomtsev B.B. and Pogutse O.P., Nucl. Fusion **11**, 67 (1971).
- [27] B. Coppi and G. Rewoldt, Phys. Rev. Lett. **33**, 1329 (1974).
- [28] P. C. Liewer, Nucl. Fusion **25**, 543 (1985)
- [29] A. I. Smolyakov, M. Yagi and Y. Kishimoto, Phys. Rev. Lett. **89**, 125005 (2002).
- [30] S. E. Parker, W. W. Lee, and R. A. Santoro, Phys. Rev. Lett. **71**, 2042 (1993).
- [31] A. M. Dimits, T. J. Williams, J. A. Byers, and B. I. Cohen, Phy. Rev. Lett. **77**, 71 (1996)).
- [32] Tilman Dannert and Frank Jenko, Phys. Plasmas **12**, 072309 (2005).

## Bibliography

- [33] David W. Ross, Ronald V. Bravenec, William Dorland, Michael A. Beer, G. W. Hammett, George R. McKee, Raymond J. Fonck, Masanori Murakami, Keith H. Burrell, Gary L. Jackson, and Gary M. Staebler, *Phys. Plasmas* **9**, 1, (2002).
- [34] D. W. Ross, W. Dorland, *Phys. Plasmas* **9**, 5031 (2002).
- [35] R. E. Waltz, J. M. Candy, and M. N. Rosenbluth, *Phys. Plasmas* **9**, 1938 (2002).
- [36] J. Candy and R. E. Waltz, *J. Comput. Phys.* **186**, 545 (2003).
- [37] J. Candy and R. E. Waltz, *Phys. Rev. Lett.* **91**, 045001 (2003).
- [38] Y. Chen, S.E. Parker, B.I. Cohen, A.M. Dimits, W.M. Nevins, D. Shumaker, V.K. Decyk and J.N. Leboeuf, *Nucl. Fusion* **43**, 1121 (2003).
- [39] A. M. Dimits, G. Bateman, M. A. Beer, B. I. Cohen, W. Dorland, G. W. Hammett, C. Kim, J. E. Kinsey, M. Kotschenreuther, A. H. Kritz, L. L. Lao, J. Mandrekas, W. M. Nevins, S. E. Parker, A. J. Redd, D. E. Shumaker, R. Sydora, and J. Weiland, *Phys. Plasmas* **7**, 969 (2000).
- [40] R. E. Waltz, J. Candy, and M. Faheyc, *Phys. Plasmas* **14**, 056116 (2007).
- [41] F. Jenko, *Comput. Phys. Commun.* **125**, 196 (2000).
- [42] T. Görler and F. Jenko, *Phys. Rev. Lett.* **100**, 185002 (2008).
- [43] A. B. Mikhailovskii, *Nuclear Fusion* **13**, 259 (1973).
- [44] S. Brunner, Ph.D thesis, EPFL, Switzerland, Thesis no: 1701 (1997)
- [45] M. Fivaz, T. M. Tran, L. Villard, K. Appert, S. Brunner, S. E. Parker and J. Vaclavik in *Theory of Fusion Plasmas, Int. Workshop, Varenna, August 1996* (Editrice Compository, Societa Italiana di Fisica, Bologna (1997).
- [46] G. L. Falchetto, J. Vaclavik and L. Villard, *Phys. Plasmas*. **10**, 1424 (2003).
- [47] P. Angelino, A. Bottino, G. Falchetto, R. Ganesh, J. Vaclavik and L. Villard, *Transp. Th. Stat. Phys.* **34**, 333 (2005).

## Bibliography

- [48] R. Ganesh, P. Angelino, J. Vaclavik and L. Villard, *Phys. Plasmas* **11**, 3106 (2004).
- [49] R. Ganesh and J. Vaclavik, *Phys. Rev. Lett.*, **94**, 145002 (2005).
- [50] W. M. Tang, *Nuclear Fusion* **18** 1089 (1978).
- [51] W. M. Tang, J. Connor and R. J. Hastie, *Nuclear Fusion* **21**, 1439 (1980).
- [52] C. Z. Cheng, *Phys. Fluids* **25**, 1020 (1982), C. Z. Cheng, *Physics Reports*, **211** 1 (1992).
- [53] M. Kotschenreuther, *Phys. Fluids* **29** 2898 (1986).
- [54] F. Zonca, L. Chen, J. Q. Dong, R. A. Santoro, *Phys. Plasmas* **6**, 1917 (1999).
- [55] P. Angelino, Ph.D thesis, EPFL, Switzerland, Thesis no: 3559 (2006).
- [56] W. D. Dorland, *Phd Thesis*, Princeton University (1993).
- [57] P. J. Catto, W. M. Tang and D. E. Baldwin, *Plasma Physics* **23**, 639 (1981).
- [58] T. S. Hahm, W. W. Lee and A. Brizard, *Phys. Fluids* **31**, 1940 (1988).
- [59] A. J. Brizard, *Phys. Rev. Lett.* **84** 5768 (2000).
- [60] N. A. Krall and A. W. Trivelpiece, *Principles of Plasma Physics* (San Francisco Press Inc, San Francisco, CA 94101-6800, 1986) p: 396-397.
- [61] P. H. Diamond, S-I. Itoh, K. Itoh and T. S. Hahm, *Plasma Physics and Controlled Fusion* **47**, R35 (2005).
- [62] L. Villard, A. Bottino, S. Brunner, A. Casati, J. Chowdhury, T. Dannert, R. Ganesh, X. Garbet, T. Görler, V. Grandgirard, R. Hatzky, Y. Idomura, F. Jenko, S. Joliet, S. K. Aghdam, X. Lapillonne, G. Latu, B. F. McMillan, F. Merz, Y. Sarazin, T. M. Tran and T. Vernay, *Plasma Phys. Controlled Fusion* **52**, 124038 (2010).
- [63] X. Lapillonne, S. Brunner, O. Sauter, L. Villard, E. Fable, T. Görler, F. Jenko and F. Merz, *Plasma Phys. Control. Fusion* **53**, (2011).

## Bibliography

- [64] M. Kotschenreuther *et al.*, Plasma Physics and Controlled Nuclear Fusion Research **2**, 11 (1993).
- [65] X. Lapillonne, S. Brunner, T. Dannert, S. Jolliet, A. Marinoni, L. Villard, T. Görler, F. Jenko, and F. Merz. Phys. Plasmas **16**, 032308 (2009).
- [66] J. Chowdhury, R. Ganesh, P. Angelino, J. Vaclavik, L. Villard and S. Brunner, Phys. Plasmas **15**, 072117 (2008).
- [67] H. Shirai and JT-60 Team, Phys. Plasmas **5**, 1712 (1998).
- [68] C. M. Greenfield *et al.*, Phys. Plasmas **4**, 1596 (1997).
- [69] F. Ryter, C. Angioni, M. Beurskens, S. Cirant, G. T. Hoang, G. M. D. Hogewij, F. Imbeaux, A. Jacchia, P. Mantica, W. Suttrop, and G. Tardini, Plasma Phys. Controlled Fusion **43**, A323 (2001).
- [70] Ryter, F. Leuterer, G. Pereverzev *et al.*, Phys. Rev. Lett. **86**, 2325 (2001).
- [71] F. Ryter, F. Imbeaux, F. Leuterer, H.-U. Fahrbach, W. Suttrop, and ASDEX Upgrade Team, Phys. Rev. Lett. **86**, 5498 (2001).
- [72] G. T. Hoang, B. Saoutic, L. Guiziou *et al.*, Nucl. Fusion **38**, 117 (1998).
- [73] G. T. Hoang, C. Bourdelle, X. Garbet, G. Giruzzi, T. Aneil, and M. Ottaviani, Phys. Rev. Lett. **87**, 125001 (2001).
- [74] F. Ryter, G. Tardini, F. De Luca, H.-U. Fahrbach, F. Imbeaux, A. Jacchia, K.K. Kirov, F. Leuterer, P. Mantica, A.G. Peeters, G. Pereverzev, W. Suttrop and ASDEX Upgrade Team, Nucl. Fusion **43**, 1396 (2003).
- [75] D. R. Ernst, P. T. Bonoli, P. J. Catto, W. Dorland, C. L. Fiore, R. S. Granetz, M. Greenwald, A. E. Hubbard, M. Porkolab, M. H. Redi, J. E. Rice, K. Zhurovich, and the Alcator C-Mod Group, Phys. Plasmas **11**, 2637 (2004).
- [76] J. C. DeBoo, S. Cirant, T. C. Luce, A. Manini, C. C. Petty, F. Ryter, M. E. Austin, D. R. Baker, K. W. Gentle, C. M. Greenfield, J. E. Kinsey, and G.M. Staebler, Nucl. Fusion **45**, 494 (2005).

## Bibliography

- [77] F. Rytter, C. Angioni, A. G. Peeters, F. Leuterer, H.-U. Fahrbach, W. Sutrop, and ASDEX Upgrade Team, *Phys. Rev. Lett.* **95**, 085001 (2005).
- [78] H. Nordman, J. Weiland, and A. Jarmen, *Nucl. Fusion* **30**, 983 (1990).
- [79] M. A. Beer, G. W. Hammett, G. Rewoldt, E. J. Synakovski, M. C. Zanstorff, and W. Dorland, *Phys. Plasmas* **4**, 1792 (1997).
- [80] T. Dannerta and F. Jenko, *Phys. Plasmas* **12**, 072309 (2005).
- [81] J. Lang, Y. Chen, and S. E. Parker, *Phys. Plasmas* **14**, 082315 (2007).
- [82] E. Z. Gusakov, A. D. Gurchenko, A. B. Altukhov, A. Y. Stepanov, L. A. Esipov, M. Y. Kantor and D. V. Kouprienko, *Plasma Phys. Control. Fusion* **48**, A371 (2006).
- [83] A.D. Gurchenko, E.Z. Gusakov, A.B. Altukhov, A.Yu. Stepanov, L.A. Esipov, M.Yu. Kantor, D.V. Kouprienko, V.V. Dyachenko and S.I. Lashkul *Nucl. Fusion* **47**, 245 (2007).
- [84] F. Jenko, W. Dorland, M. Kotchenreuther, and B. N. Roger, *Phys. Plasmas* **7**, 1904 (2000).
- [85] P. Beyer, S. Benkadda, X. Garbet, and P. H. Diamond, *Phys. Rev. Lett.* **85**, 4892 (2000).
- [86] P. H. Diamond, S. Champeaux, M. Malkov *et al.*, *Nucl. Fusion* **41**, 1067 (2001).
- [87] B. Labit and M. Ottaviani, *Phys. Plasmas* **10**, 126, (2003).
- [88] K. H. Burrell, *Phys. Plasmas* **4**, 1499 (1997).
- [89] M. Maccio, J. Vaclavik, and L. Villard, *Phys. Plasmas* **8**, (2001).
- [90] B. W. Stallard, C. M. Greenfield, G. M. Stabler *et al.*, *Phys. Plasmas* **6**, 1978 (1999).
- [91] T. Görler and F. Jenko, *Phys. Rev. Lett.* **100**, 185002 (2008).
- [92] T. Görler and F. Jenko, *Phys. Plasmas* **15**, 102508 (2008).

## Bibliography

- [93] W. M. Nevins, J. Candy, S. Cowley, T. Dannert, A. Dimits, W. Dorland, C. Estrada-Mila, G. W. Hammett, F. Jenko, M. J. Pueschel, and D. E. Shumaker, *Phys. Plasmas* **13**, 122306 (2006).
- [94] W. M. Nevins, S. E. Parker, Y. Chen, J. Candy, A. Dimits, W. Dorland, G. W. Hammett and F. Jenko, *Phys. Plasmas* **14**, 084501 (2007).
- [95] L. D. Pearlstein and H. L. Berk, *Phys. Rev. Lett.* **23**, 220 (1969).
- [96] N. T. Gladd and W. Horton, Jr. *Phys. Fluids* **16**, 879 (1973).
- [97] D. W. Ross and S. M. Mahajan, *Phys. Rev. Lett.* **40**, 324 (1978).
- [98] K. T. Tsang, P. J. Catto, J. C. Whitson, J. Smith, *Phys. Rev. Lett.* **40**, 327 (1978).
- [99] L. Chen, P. N. Guzdar, R. B. White, P. K. Kaw and C. Oberman, *Phys. Rev. Lett.* **41**, 648 (1978).
- [100] S. P. Hirshman, K. Molvig, *Phys. Rev. Lett.* **42**, 648 (1979).
- [101] C. Z. Cheng, L. Chen, *Phys. Fluids* **23**, 1770 (1980).
- [102] R. Marchand and P. N. Guzdar, *Phys. Fluids* **24**, 2183 (1981).
- [103] T. J. Chep and M. Venema, *Plasma Physics and Controlled Fusion* **27**, 653 (1985).
- [104] H. L. Berk and R. R. Domingues, *J. Plasma Phys* **18**, 31 (1977).
- [105] D. E. Hastings and J. E. McCune, *Phys. Fluids* **25**, 509 (1982).
- [106] A. Hirose, M. Elia, A. I. Smolyakov, and M. Yagi, *Phys. Plasmas* **9**, 1659 (2002).
- [107] Zhe Gao, H. Sanuki, K. Itoh, and J. Q. Dong, *Phys. Plasmas* **10**, 2831 (2003).
- [108] Zhe Gao, H. Sanuki, K. Itoh, and J. Q. Dong, *Phys. Plasmas* **12**, 022502 (2005).
- [109] Zhe Gao, J. Q. Dong, H. Sanuki, *Phys. Plasmas* **11**, 3053 (2004).

## Bibliography

- [110] Zhe Gao, H. Sanuki, K. Itoh, J. Q Dong, *J. Plasma Physics* **72**, 1249 (2006).
- [111] Yi-Kang Pu, Stefano Migliuolo, *Phys. Fluids* **28**, 1722 (1985).
- [112] K.L. Wong, N.L. Bertz, T.S Hahm and E. Synakowski, *Phys. Lett. A* **236**, 339 (1997).
- [113] B. N. Rogers, W. Dorland, and M. Kotschenreuther, *Phys. Rev. Lett.*, **85**, 5336 (2000).
- [114] P. H. Diamond, S. Itoh, K. Itoh and T. S. Hahm, *Plasma Phys. Control. Fusion* **47**, R35 (2005).
- [115] W.W. Heidbrink, G.J. Sadler, *Nucl. Fusion* **34**, 535 (1994).
- [116] S.J. Zweben, R.V. Budny, D.S. Darrow, S.S. Medley, R. Nazikian, B.C. Stratton, E.J. Synakowski, G. Taylor for the TFTR Group, *Nucl. Fusion* **40**, 91 (2000).
- [117] Emanuele Poli, Manuel Garcia-Muioz, Hans-Ulrich Fahrbach, Sibylle Günter, and ASDEX Upgrade Team, *Phys. Plasmas* **15**, 032501 (2008).
- [118] M. Garcia-Munoz, H.-U. Fahrbach, S.D. Pinches, V. Bobkov, M. Brudgam, M. Gobbin, S. Günter, V. Igochine, Ph. Lauber, M.J. Mantsinen, M. Maraschek, L. Marrelli, P. Martin, P. Piovesan, E. Poli, K. Sassenberg, G. Tardini, H. Zohm and the ASDEX Upgrade Team, *Nucl. Fusion* **49**, 085014 (2009).
- [119] Liu Chen, *Phys. Plasmas* **1**, 1519 (1994).
- [120] W. W. Heidbrink, Cris W. Barnes, G. W. Hammett, Y. Kusama, S. D. Scott, M. C. Zarnstorff, L. C. Johnson, D. McCune, S. S. Medley, H. K. Park, A. L. Roquemore, J. D. Strachan, and G. Taylor, *Phys. Fluids B* **3**, 3167 (1991).
- [121] G. Manfredi and R. O. Dendy, *Phys. Rev. Lett.*, **76**, 23 (1996).
- [122] C. Estrada-Mila, J. Candy and R. E. Waltz, *Phys. Plasmas* **13**, 112303, (2006).

## Bibliography

- [123] S. Günter , G. Conway, S. daGraca, H.-U. Fahrbach, C. Forest, M. Garcia Munoz, T. Hauff, J. Hobirk, V. Igochine, F. Jenko, K. Lackner, P. Lauber, P. McCarthy, M. Maraschek, P. Martin, E. Poli, K. Sassenberg, E. Strumberger, G. Tardini, E. Wolfrum, H. Zohm and ASDEX Upgrade Team, Nucl. Fusion **47**, 920 (2007).
- [124] W. W. Heidbrink, J. M. Park, M. Murakami, C. C. Petty, C. Holcomb, and M. A. Van Zeeland, Phys. Rev. Lett. **103**, 175001 (2009).
- [125] W. W. Heidbrink, M. Murakami, J. M. Park, C. C. Petty, M. A. Van Zeeland, J. H. Yu and G. R. McKee, Plasma Phys. Control. Fusion **51**, 125001 (2009).
- [126] Wenlu Zhang, Zhihong Lin and Liu Chen., Phys. Rev. Lett. **101**, 095001 (2008).
- [127] T. Hauff, M. J. Pueschel, T. Dannert, and F. Jenko, Phys. Rev. Lett., **102**, 075004 (2009).
- [128] S. Zhou, W. W. Heidbrink, H. Boehmer, R. McWilliams, T. Carter, S. Vincena, S. K. P. Tripathi, P. Popovich, B. Friedman, and F. Jenko, Phys. Plasmas **17**, 092103 (2010).
- [129] T. Hauff, F. Jenko, A. Shalchi and R. Schlickeiser, The Astrophysical Journal, **711**, 997 (2010).
- [130] G. Tardini, J. Hobirk, V.G. Igochine, C.F. Maggi, P. Martin, D. McCune, A.G. Peeters, A.C.C. Sips, A. Stabler, J. Stober and the ASDEX Upgrade Team, Nucl. Fusion **47** , 280 (2007).
- [131] M Romanelli, A Zocco, F Crisanti and JET-EFDA Contributors, Plasma Phys. Control. Fusion **52**, 045007 (2010).
- [132] J. Chowdhury, R. Ganesh, P. Angelino, J. Vaclavik, L. Villard and S. Brunner, Phys. Plasmas **15**, 072117 (2008).
- [133] J. Chowdhury, R. Ganesh, P. Angelino, J. Vaclavik, L. Villard and S. Brunner, Phys. Plasmas **16**, 052507 (2009).
- [134] Y Idomura, M Wakatani, and S. Tokuda, Phys. Plasmas **7**, 2456 (2000).

## Bibliography

- [135] J. Q. Dong, H. Sanuki, and K. Itoh, *Phys. Plasmas* **8**, 3635 (2001).
- [136] R. Singh, Varun Tangri, H. Nordman and J. Weiland, *Phys. Plasmas* **8**, 4340 (2001).
- [137] F. Jenko, W. Dorland and G. W. Hammett, *Phys. Plasmas* **8**, 4096 (2001).
- [138] W. W. Heidbrink , J. M. Park, M. Murakami, C. C. Petty, C. Holcomb, and M. A. Van Zeeland, *Phys. Rev. Lett.* **103**, 175001 (2009).
- [139] W. X. Wang, Z. Lin, W. M. Tang, W. W. Lee, S. Ethier, J. L. V. Lewandowski, G. Rewoldt, T. S. Hahm, and J. Manickam, *Phys. Plasmas* **13**, 092505 (2006).
- [140] W. X. Wang, P. H. Diamond, T. S. Hahm, S. Ethier, G. Rewoldt, and W. M. Tang, *Phys. Plasmas* **17**, 072511 (2010).
- [141] P. Beyer and S. Benkadda, *CHAOS*, **11**, (2001).
- [142] J. D. Wilson and B. L. Sawford, *Boundary-Layer Meteorology* **78**, 191 (1996).
- [143] J M Dewhurst, B Hnat and R O Dendy, *Plasma Phys. Control. Fusion* **52**, 025004 (2010).
- [144] R. Basu, V. Naulin, J. J. Rasmussen, *Nonlinear Science and Numerical Simulation* **8**, 477 (2003).
- [145] V. Naulin, A. H. Nielsen, and J. J. Rasmussen, *Phys. of Plasmas* **6**, 4575 (1999).
- [146] S. V. Annibaldi, G. Manfredi, R. O. Dendy, *Phys. of Plasmas* **9**, 791 (2002).
- [147] S. V. Annibaldi, G. Manfredi, R. O. Dendy and L. Drury, *Plasma Phys. Control. Fusion* **42**, L13 (2000).
- [148] G. Sánchez Burillo, B. Ph. van Milligen, and A. Thyagaraja, *Phys. of Plasmas* **17**, 052304 (2010).
- [149] T. Hauff and F. Jenko, *Phys. of Plasmas* **14**, 092301 (2007).

## Bibliography

- [150] W. X. Wang, G. Rewoldt, W. M. Tang, F. L. Hinton, J. Manickam, L. E. Zakharov, R. B. White, and S. Kaye, *Phys. of Plasmas* **13**, 082501 (2006).
- [151] Z. Lin, S. Ethier, T. S. Hahm, and W. M. Tang, *Phys. Rev. Lett.*, **88**, 195004 (2002).
- [152] J. Candy, R. E. Waltz and W. Dorland, *Phys. Plasmas* **11**, L25 (2004).
- [153] B. F. McMillan *et al.*, *Phys. Rev. Lett.*, **105**, 155001 (2010).
- [154] R. Sánchez , D. E. Newman, J.N. Leboeuf, V. K. Decyk, and B. A. Carreras, *Phys. Rev. Lett.* **101**, 205002 (2008).
- [155] R. Sánchez *et al.*, *Physics of Plasmas* **16**, 055905(2009).
- [156] K. Hallatschek, W. Dorland, *Phys. Rev. Lett* **95**, 055002 (2005).
- [157] F Jenko, T Dannert and C Angioni, *Plasma Phys. Control. Fusion* **47**, B195 (2005).
- [158] G. Spizzo, R. B. White, S. Cappello, *Phys. Plasmas* **14**, 102310 (2007).
- [159] F. W. Perkins, C. W. Barnes, D. W. Johnson, S. D. Scott, M. C. Zarnstorff, M. G. Bell, R. E. Bell, C. E. Bush, B. Grek, K. W. Hill, D. K. Mansfield, H. Park, A. T. Ramsey, J. Schivell, B. C. Stratton, and E. Synakowski, *Phys. Fluids B* **5**, 477 (1993).
- [160] K. W. Gentle, R. V. Bravenec, G. Cima, H. Gasquet, G. A. Hallock, P. E. Phillips, D. W. Ross, W. L. Rowan, A. J. Wootton, T. P. Crowley, J. Heard, A. Ouroua, P. M. Schoch, and C. Watts, *Phys. Plasmas* **2**, 2292 (1995).
- [161] J. D. Callen and M. W. Kissick, *Plasma Phys. Controlled Fusion* **39**, B173 (1997).
- [162] B. A. Carreras, B. van Milligen, M. A. Pedrosa, R. Balbin, C. Hidalgo, D.E. Newman, E. Sanchez, M. Frances, I. Garcia-Cortes, J. Bleuel, M. Endler, S. Davies, and G. F. Matthews, *Phys. Rev. Lett.* **80**, 4438 (1998).

## Bibliography

- [163] B. A. Carreras, B. P. van Milligen, M. A. Pedrosa, R. Balbin, C. Hidalgo, D. E. Newman, E. Sanchez, R. Bravenec, G. McKee, I. Garcia-Cortes, J. Bleuel, M. Endler, C. Ricardi, S. Davies, G. F. Matthews, E. Martines, and V. Antoni, *Phys. Plasmas* **6**, 1885 (1999).
- [164] G. M. Zaslavsky, M. Edelman, H. Weitzner, B. Carreras, G. McKee, R. Bravenec, and R. Fonck, *Phys. Plasmas* **7**, 3691 (2000).
- [165] S. Jolliet, B. F. McMillan, T. Vernay, L. Villard, A. Bottino, and P. Angelino, *Phys. Plasmas* **16**, 052307 (2009).
- [166] D. Lynden-Bell, *Mon. Not. R. astr. Soc.* **136**, 101 (1967).
- [167] G.M. Zaslavsky, *Physics Reports* **371** (2002) 461.
- [168] Jean-Philippe Bouchaud, Antoine Georges, *Physics Reports* **195** Nos. 4 & 5 (1990).
- [169] R. Metzler, J. Klafter, *Physics Reports* **339**, 1-77 (2000).
- [170] T. Geisel, S. Thomae, *Phys. Rev. Lett* **52**, 1936 (1984).
- [171] D. del-Castillo-Negrete, B. A. Carreras, and V. E. Lynch, *Phys. Rev. Lett.* **94**, 065003 (2005).
- [172] S. Zhou, W. W. Heidbrink, H. Boehmer, R. McWilliams, T. Carter, S. Vincena, S. K. P. Tripathi, P. Popovich, B. Friedman, and F. Jenko, *Phys. Plasmas* **17**, 092103 (2010).
- [173] T. Hauff, F. Jenko, and S. Eule, *Phys. Plasmas* **14**, 102316 (2007).
- [174] R. J. Goldston and P. H. Rutherford, *Introduction to Plasma Physics* (Institute of Physics Publishing, 1995), p. 40.
- [175] Liu Chen, *Journal of Geophysical Research* **104**, 2421, (1999).
- [176] B. Davies, *Journal of Computational Physics* **66**, 36 (1986).
- [177] B. B. Kadomtsev and O. P. Pogutse, in *Reviews of Plasma Physics*, edited by M. A. Leontovich (Consultants Bureau, New York, 1970), Vol. 5, p.249.

## Bibliography

- [178] M. N. Rosenbluth, *Phys. Fluids* **11**, 869 (1968).
- [179] B. D. Fried and S. D. Conte, *The Plasma Dispersion Function* (Academic, New York, 1961).